

Dissertation
submitted to the
Combined Faculties for the Natural Sciences and for Mathematics
of the Ruperto-Carola University of Heidelberg, Germany
for the degree of
Doctor of Natural Sciences

presented by
Diplom-Physicist Michael Stöhr
born in Stuttgart

Oral examination: 22nd July 2003

Analysis of Flow and Transport in Refractive Index Matched Porous Media

Referees: Prof. Dr. Kurt Roth
Prof. Dr. Bernd Jähne

Zusammenfassung

In der vorliegenden Arbeit wurde eine neuartige Methode zur Messung von Strömung und Transport in porösen Medien entwickelt. Durch die Verwendung von speziell geeigneten Feststoffen, Flüssigkeiten und fluoreszierenden Farbstoffen sowie die Anwendung eines hochgenauen Verfahrens zur Anpassung der Brechungsindizes konnte die Dynamik der Farbstoffverteilung in einem dreidimensionalen porösen Medium mittels planarer laser-induzierter Fluoreszenz mit einer sehr hohen zeitlichen und räumlichen Auflösung bestimmt werden. Für die Auswertung der Daten wurden speziell angepasste Algorithmen zur Bildvorverarbeitung entwickelt sowie ein Verfahren zur lokalen Parameterschätzung auf die vorliegende Anwendung übertragen und entscheidend erweitert. Die durchgeführten Messungen stellen die erste gleichzeitige Bestimmung des longitudinalen sowie der beiden transversalen hydrodynamischen Dispersionskoeffizienten dar. Während für die longitudinale Dispersion ein bereits bekanntes Potenzgesetz bestätigt wurde, konnte für die transversale Dispersion erstmals ein deutlich unterschiedliches Verhalten in vertikaler und horizontaler Richtung nachgewiesen werden. Weiterhin konnte mit dem entwickelten Verfahren erstmals der direkte Nachweis für die Existenz nicht konvektiver Zonen, die einen wichtigen Teil zur Dispersion beitragen und eine mögliche Erklärung für das Verhalten gemäß eines Potenzgesetzes bieten, erbracht werden. Schließlich wurde mit dem Verfahren erstmals die Strömung zweier nicht mischbarer Flüssigkeiten in einem dreidimensionalen porösen Medium hochaufgelöst visualisiert.

Abstract

In the present work a novel method for the measurement of flow and transport in porous media has been developed. Through the employment of particularly applicative solids, liquids and fluorescent dyes and the application of a method for the highly precise matching of refractive indices, the dynamics of the dye distribution inside a threedimensional porous medium could be determined with a high temporal and spatial resolution using planar laser-induced fluorescence. For the data analysis specifically adapted algorithms for image preprocessing have been developed and a method for local parameter estimation has been adapted and significantly enhanced for the present application. The performed measurements represent the first simultaneous estimation of the longitudinal and both transversal hydrodynamic dispersion coefficients. Whereas for the longitudinal dispersion a previously known power-law could be confirmed, the significantly different behavior of the transversal dispersion in vertical and horizontal direction has been observed for the first time. Furthermore the measurements provide the first direct evidence for the existence of stagnant zones in the liquid phase, which have an important effect on the dispersion and are a potential explanation for the power-law behavior. Finally the described technique was used for the first highly resolved visualization of the flow of two immiscible liquids in a threedimensional porous medium.

Contents

1	Introduction	7
2	Theory of Hydrodynamic dispersion	9
2.1	Introduction	9
2.2	From kinetic theory to molecular diffusion	9
2.3	From molecular diffusion to hydrodynamic dispersion	12
2.3.1	Taylor dispersion	13
2.3.2	Hydrodynamic dispersion in a homogeneous porous medium	16
2.3.3	Theoretical models	20
2.4	Heterogeneous porous media	22
3	Method of measurement	25
3.1	Introduction	25
3.2	Refractive index matching methods	25
3.3	Experimental setup	26
3.3.1	Imaging devices	26
3.3.2	Light source and optics	27
3.3.3	Personal computer	27
3.3.4	Translation stage	28
3.3.5	Flow cells	28
3.4	Solid properties	29
3.5	Liquid properties	32
3.6	Dye properties	36
3.7	Summary and conclusions	39
4	Method for precise index matching	41
4.1	Introduction	41
4.2	Light propagation in transparent porous media	41
4.3	Experimental technique	43
4.4	Summary and conclusions	45
5	Image Preprocessing	47
5.1	Introduction	47
5.2	Geometric calibration	48
5.3	Brightness correction	50
5.3.1	Correction of spatial inhomogeneity	52
5.3.2	Correction of temporal variations	53

5.4	Correction of scanning time shift	55
5.5	Radiometric camera calibration	57
5.6	Analysis of statistical errors	61
5.7	Verification of the linearity between laser intensity and fluorescence emission	62
5.8	Summary	63
6	Global parameter estimation	65
6.1	Introduction	65
6.2	Averaging	66
6.3	Direct estimation	66
6.4	Fitting of model functions	69
6.5	Confidence bounds for estimated parameters	69
7	Local parameter estimation	71
7.1	Introduction	71
7.2	Total least squares parameter estimation	72
7.2.1	Ordinary least squares	72
7.2.2	Total least squares	73
7.2.3	Equilibration	75
7.2.4	Concluding remarks	76
7.3	Parameter estimation for linear dynamic processes	76
7.3.1	Motion estimation in image sequences	78
7.3.2	Tensor approach	79
7.3.3	Aperture problem	81
7.3.4	Extension to linear models	82
7.3.5	Minimum norm solution	87
7.3.6	Computational aspects	87
7.4	Application to simulated data	90
7.4.1	Choice of filter masks	90
7.4.2	Noise sensitivity	100
7.4.3	Choice of equilibration weight matrix	100
7.4.4	Confidence measure	102
7.4.5	Physically based minimum norm solution	106
7.5	Summary and conclusions	113
8	Single-phase flow in saturated porous media	115
8.1	Introduction	115
8.2	Molecular diffusion	115
8.2.1	Nile Red	116
8.2.2	Alexa Fluor 488	118
8.3	Hydrodynamic dispersion	118
8.3.1	Correlation functions of porous media	121
8.3.2	Longitudinal and transverse dispersion coefficients	126
8.3.3	Temporal evolution of mean and variance	135
8.3.4	Reversibility	137
8.3.5	Holdup dispersion	141
8.3.6	Adsorption	144

8.4	Summary and conclusions	145
9	Flow of two immiscible liquids in a porous medium	149
9.1	Introduction	149
9.2	Immiscible displacement of oil by water	149
9.3	Compensation of spectral overlap	150
9.4	Summary and conclusions	153
10	Summary and conclusions	159
A	Cubic smoothing splines	161
A.1	Introduction	161
A.2	Roughness penalty approach	161
A.3	Estimation of the smoothing parameter λ	162
B	Concentration Profiles	165

Chapter 1

Introduction

The study of flow and transport in porous media is an active field of research, which has applications in many disciplines such as

- forecast of transport and fate of water, dissolved contaminants and non-aqueous phase liquids in hydrology
- heterogeneous catalysis in chemical engineering
- oil recovery in petroleum engineering
- flow of blood and other body tissues in biochemistry and medicine.

The scientific challenge in all these fields is the development of appropriate models for flow and transport, which can then be used e.g. to predict the spreading of a contaminant in an aquifer or to optimize the reaction rate in a packed bed. There is a general agreement among scientists and engineers across the disciplines that further progress in the modeling of these phenomena can only be achieved through the development of enhanced and new experimental techniques.

Earlier studies mostly treated the porous medium as an effectively homogeneous system and neglected the complexity and variability of the local flow processes within the porous medium. It is not surprising that the predictions of models which are based on such simple approaches often proved false. The restriction to the employment of these simple models, mainly caused by the lack of experimental methods for the visualization and quantification of local structure and dynamic processes, could lately be relaxed by the emergence of capable new measurement instrumentation. As a consequence, the models become more sophisticated making use of the contemporaneously growing power of the computers used for their solution.

The spread and fate of water, dissolved contaminants and non-aqueous phase liquids in hydrology is governed by dynamic processes acting on many different scales. From this follows the demand for a variety of experimental methods in order to measure each of these processes on its characteristic scale. Currently progress is made by the development of X-ray tomography, nuclear magnetic resonance (NMR) imaging and refractive index matching techniques on the laboratory scale, ground penetrating radar (GPR) on the field scale and remote sensing with aircrafts and satellites on the global scale.

The objective of this work is the development and application of a planar laser induced fluorescence (PLIF) technique for the spatially and temporally highly resolved measurement

of flow and transport in refractive index matched porous media. Being part of the graduate program 'Modelling and Scientific Computing in Mathematics and Natural Sciences' at the Interdisciplinary Center for Scientific Computing (Interdisziplinäres Zentrum für Wissenschaftliches Rechnen, IWR) of the University of Heidelberg, it benefited from the parallel affiliations to both the soil physics group at the Institute of Environmental Physics and the digital image processing group at the IWR. Followingly it was performed in view of the implications mainly for hydrological models and with the claim to develop sophisticated methods for the processing of the measured data and parameter estimation.

Chapter 2

Theory of Hydrodynamic dispersion

2.1 Introduction

The basic approach to the description of flow and transport in porous media is the introduction of appropriate scales and the derivation of adequate physical models for each scale. This concept is illustrated in figure 2.1: On each scale the respective physical model has a set of intrinsic parameters, which contain structural and material properties. The determination of the correct physical models (like e.g. kinetic theory or Navier-Stokes-equation) for each scale is accomplished through the intuition of (a) scientist(s) from the analysis of experimental observations. Furthermore it is sometimes possible to relate the parameters at a given scale to the model and the parameters at the next smaller scale, a procedure usually referred to as *upscaling*. Such a relation can be an analytical equation obtained from intuition or an empirical law obtained from the analysis of experimental data.

In this sense the theory of hydrodynamic dispersion will be presented in the following sections as a sequence of transitions from the scale of a single molecule to the scale of an aquifer as illustrated in figure 2.1. The first transition presented in section 2.2 goes from kinetic theory to the continuous formulation of molecular diffusion, which was accomplished by Albert Einstein in 1905. The phenomenon of hydrodynamic dispersion is then introduced in section 2.3 as a transition from the transport model for a pure stagnant liquid to a model for the transport in a liquid flowing through a porous medium. This transition is characterized by a strong enhancement of the transport efficiency (typically orders of magnitude), which is caused by a combination of several microscopic physical processes, which are addressed in detail in section

2.2 From kinetic theory to molecular diffusion

The phenomenon of molecular diffusion sketched in figure 2.2a-c is well-known from everyday life: a small pulse of dye (e.g ink) injected into a box of water changes its shape with time towards a broader distribution without any active external stimulation. The first successful explanation of this phenomenon was provided by the kinetic theory developed in the middle of the 19th century by Rudolf Clausius, James Clerk Maxwell, Ludwig Boltzmann and others. At this time a similar phenomenon was known under the name *brownian motion* after the Scottish botanist Robert Brown (1773-1858). In 1827 he observed the zig-zag motion of pollen grains suspended in water under a microscope (Brown, 1828).

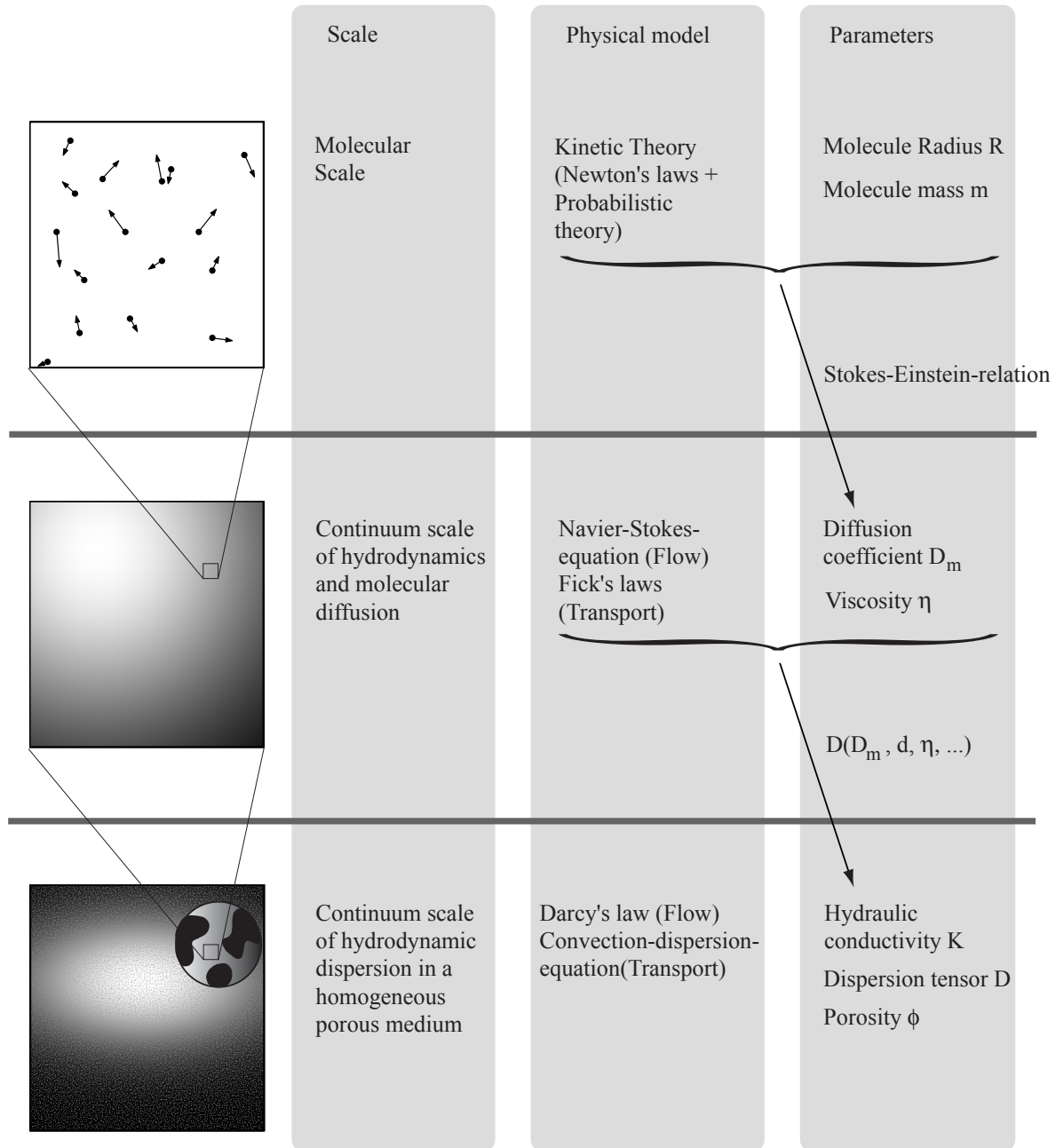


Figure 2.1: Concept of the description of physical processes on different scales. On each scale, the processes are described by an adequate physical model and a set of intrinsic parameters. The major scientific challenge, besides the determination of the correct physical models, is the derivation of the relations between the models and parameters for different scales. The purpose of this illustration is not to provide any complete description (which would have to include temperature dependence, compressibility etc.), but rather to present the conceptual idea of scale transitions.

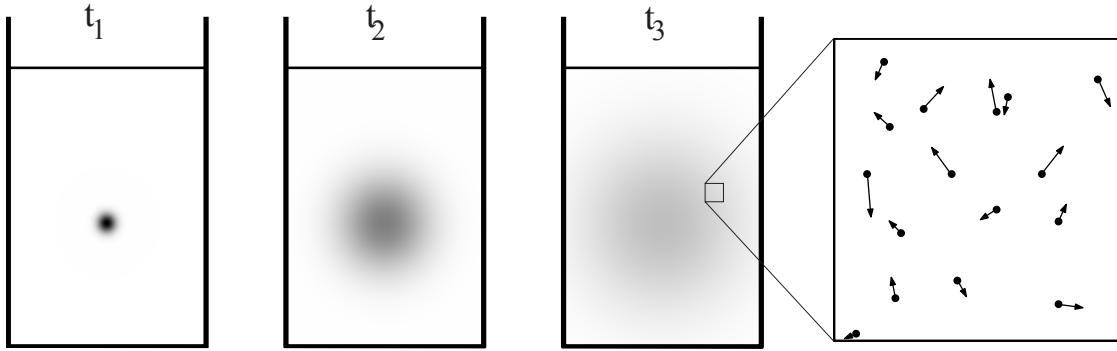


Figure 2.2: Diffusion of a dyed solute pulse in a transparent solvent: the diffusion coefficient D_m for the description of the physical process on the continuum scale (a-c) can be related to the properties of the molecular scale (d) through the Stokes-Einstein-equation 2.8.

Kinetic theory, which is based on the main assumptions

- All matter is composed of small particles.
- The particles are in constant motion according to Newton's law.
- The collisions between the particles are perfectly elastic.

correctly explains these phenomena by the equipartition of thermal energy resulting in a permanent process of movement and collisions of the particles.

During the same time, the young Adolf Fick (1831-1879), a physiologist at the University of Zürich wrote a work entitled "Über Diffusion" (On Diffusion, Fick (1855)). Starting from his interest in diffusion through organic membranes, he addressed himself to the study of diffusion of a solute in its solvent as the elementary physical process. Therefore he performed a series of quantitative measurements of the diffusion of sodium chloride aqueous solutions contained in cylindrical jars together with pure water.

In contrast to kinetic theory, he came up with a phenomenological description based on the empirically obtained assumption that the current \vec{j} is proportional to the concentration gradient,

$$\vec{j} = -D_m \vec{\nabla} c, \quad (2.1)$$

an equation now known as *Fick's first law*. Here c denotes the concentration and D_m is the coefficient of molecular diffusion. The additional assumption that the particles are neither created nor destroyed leads to the continuity equation

$$\frac{\partial c}{\partial t} = -\vec{\nabla} \cdot \vec{j}. \quad (2.2)$$

The combination of Fick's first law and continuity equation leads to Fick's second law

$$\frac{\partial c}{\partial t} = D_m \Delta c. \quad (2.3)$$

Although Fick was aware of the results of kinetic theory, it took about one half of a century to combine the probabilistic, microscopic description of kinetic theory with the macroscopic

phenomenological description introduced by Fick. In 1905 it was Albert Einstein (1879-1955) who derived the diffusion equation 2.3 from the postulates of kinetic theory by realizing that the particle concentration $c(\vec{x}, t)$ is proportional to the probability $p(\vec{x}, t)$ of finding a particle at (\vec{x}, t) (Einstein, 1905). The temporal evolution of $p(\vec{x}, t)$ for a particle initially released at the origin of a d -dimensional space can then be obtained as the normalized solution of equation 2.3,

$$p(\vec{x}, t) = \frac{1}{(4\pi D_m t)^{d/2}} e^{-\frac{r^2}{4D_m t}}, \quad r^2 = \|\vec{x}\|^2, \quad (2.4)$$

and thus the mean squared displacement of the particle grows linearly with time:

$$\langle r^2(t) \rangle = \int r^2 p(\vec{x}, t) d^3 r = 2d D_m t. \quad (2.5)$$

Furthermore Einstein has shown that the diffusion coefficient D_m for a solute is the ratio of the mean thermal energy of the medium kT and the friction f between the solute and the solvent,

$$D_m = \frac{kT}{f}. \quad (2.6)$$

Stokes has shown that the friction of a spherically shaped particle of radius R in a solvent with viscosity η is given by

$$f = 6\pi\eta R. \quad (2.7)$$

From this relation Einstein calculated the diffusion coefficient D_m as

$$D_m = \frac{kT}{6\pi\eta R}, \quad (2.8)$$

which is today called *Stokes-Einstein-relation*. Einstein used this relation to estimate the size of molecules (Einstein, 1906), while at this time the atomistic structure of matter was still a controversial issue (Renn, 1997). In the present work the *Stokes-Einstein-relation* 2.8 is used to estimate the diffusion coefficients and Schmidt numbers for different silicone oil mixtures as described in section 8.2.

In the context of the concept of scale transitions introduced in the previous section and illustrated in figure 2.1, the *Stokes-Einstein-relation* provides an essential link between the description on the molecular scale given by kinetic theory (figure 2.2d), and the description on the continuum scale given by Fick's laws (figure 2.2a-c).

2.3 From molecular diffusion to hydrodynamic dispersion in a homogeneous porous medium

In this section a formalism will be presented for the description of the transport of a solute dissolved in a liquid flowing through a homogeneous porous medium. This is accomplished through an adequate upscaling of the continuous description for the diffusive transport in a pure stagnant liquid given by Fick's laws to an effective description of transport on a properly chosen macroscale. The transport on this macroscale, which is typically caused by a combination of several physical processes, like e.g. diffusion, convection, adsorption or holdup in stagnant zones, is usually referred to as *hydrodynamic dispersion*.

In principle, the temporal evolution of the solute concentration distribution $c(\vec{x}, t)$ in a liquid flowing through a porous medium can be obtained from the velocity field $\vec{v}(\vec{x})$ given by the solution of the *Navier-Stokes-equation* (see e.g. Tritton (1988))

$$\rho\left(\frac{\partial\vec{v}}{\partial t} + \vec{v} \cdot \vec{\nabla}\vec{v}\right) = -\vec{\nabla}p + \eta\Delta\vec{v} + \vec{f}_{\text{external}}. \quad (2.9)$$

For numerical studies of flow in porous media, which is mostly in the range of low Reynolds numbers $\text{Re} < 1$, this equation is often approximated by the linear, and therefore computationally more convenient *Stokes-equation*

$$\rho\frac{\partial\vec{v}}{\partial t} = -\vec{\nabla}p + \eta\Delta\vec{v} + \vec{f}_{\text{external}}. \quad (2.10)$$

Subsequently $c(\vec{x}, t)$ is calculated as the solution of the so-called *convection-diffusion-equation*

$$\frac{\partial c}{\partial t} + \vec{\nabla} \cdot (\vec{v}c) - D_m\Delta c = 0, \quad (2.11)$$

which is a generalization of Fick's second law 2.3 with the additional term $\vec{\nabla} \cdot (\vec{v}c)$ for the convective transport in a flowing liquid.

There are at least two reasons why this approach is not feasible:

- The complex geometry of a porous medium, like e.g. a column filled with sand or an aquifer, can generally not be obtained. Therefore no solution of the Stokes-equation 2.10 can be calculated due to the lack of boundary conditions.
- Even if the boundary conditions were available, no analytical solution of equations 2.10 and 2.11 would be possible, and the computational requirements for a numerical solution would exceed every imaginable dimension.

However, in many cases the exact solution of equations 2.10 and 2.11 is not necessary, and the complex geometry of the porous medium can be represented by a set of few so-called *effective* parameters. In the following this approach will at first be exemplarily introduced for the flow in a capillary tube and then extended to the hydrodynamic dispersion in a homogeneous porous medium.

2.3.1 Taylor dispersion

The description of flow and transport in a capillary tube is an illustrative example for the scale transition from molecular diffusion to hydrodynamic dispersion. Due to its simplicity an exact analytical solution for the velocity field $\vec{v}(\vec{x})$ is available, and it is further possible to derive exact analytical relations between the microscopic and the effective macroscopic parameters.

The laminar flow field in a capillary tube of length L is given by the solution of the Navier-Stokes-equation 2.9 (the so-called *Hagen-Poiseuille's law*) as

$$v(r) = \frac{\Delta p}{L} \frac{R^2}{4\eta} \left(1 - \frac{r^2}{R^2}\right) \stackrel{v_0 = \frac{\Delta p R^2}{4\eta L}}{=} v_0 \left(1 - \frac{r^2}{R^2}\right), \quad (2.12)$$

where R denotes the tube radius, $r = \sqrt{y^2 + z^2}$ the distance from the central axis of the tube, Δp the pressure difference between the tube ends, η the viscosity of the liquid and v_0

the velocity in the center ($r = 0$) of the tube. The temporal evolution of the concentration distribution $c(\vec{x}, t)$ for a dissolved solute with the molecular diffusion coefficient D_m is then described by the convection-diffusion-equation 2.11.

Figure 2.3 shows the evolution of $c(\vec{x}, t)$ for a solute pulse which was initially uniformly distributed at $x = 0$ ($c(\vec{x}, 0) = c_0\delta(x)$). In this numerical simulation the concentration c is represented by the density of the tracer particles, which are translated by an additive superposition of convective and diffusive transport according to

$$\vec{x}_{t+1} = \vec{x}_t + \vec{v}(\vec{x}_t) + \varepsilon \quad \text{with} \quad \langle \varepsilon \rangle = 0, \quad \langle \varepsilon^2 \rangle = 2D_m. \quad (2.13)$$

From the examination of the images in figure 2.3b-g and the analysis of the governing equations 2.12 and 2.11, the qualitative behavior of solute transport can be separated into two different regimes. The transition between these two regimes is characterized by the time τ a particle needs to diffuse a distance equal to the tube diameter $d = 2R$:

$$\tau = \frac{d^2}{2D_m} = \frac{2R^2}{D_m}. \quad (2.14)$$

For the simulation shown in figure 2.3 the value of this characteristic time is $\tau = 40000$. For $t < \tau$, the initial transverse positions of the particles have moved less than the tube diameter, and thus the shape of the parabolic flow profile $v(r)$ is still more or less identifiable from the particle distribution. For $t > \tau$ molecular diffusion has led to a complete transverse mixing of the tracer particles and consequently the particle distribution is independent of the transverse position.

Another qualitative change between the behaviors for $t < \tau$ and $t > \tau$ can be recognized from the temporal evolution of the particle distributions in flow direction, which are represented by the gray lines in figure 2.3b-g: the transition from $t < \tau$ to $t > \tau$ is accompanied by a transition of the particle distribution in flow direction towards a gaussian distribution. This important finding is a direct consequence of the so-called *central limit theorem* (CLT). It essentially states that the sum Ω of n statistically independent random variables ε_i characterized by their means μ_i and variances σ_i^2

$$\mu_i = \langle \varepsilon_i \rangle \quad \text{and} \quad \sigma_i^2 = \langle (\varepsilon_i - \mu_i)^2 \rangle \quad (2.15)$$

is a random variable whose probability distribution converges for $n \rightarrow \infty$ to a gaussian distribution with mean μ_Ω and variance σ_Ω^2 :

$$\Omega = \sum_{i=1}^n \varepsilon_i \xrightarrow{n \rightarrow \infty} \mu_\Omega = \sum_{i=1}^n \mu_i, \quad \sigma_\Omega^2 = \sum_{i=1}^n \sigma_i^2. \quad (2.16)$$

For a detailed discussion and a proof of this theorem see Grimmert & Stirzaker (2001).

Consequently the 3D microscopic convection-diffusion-equation 2.11 converges for $t > \tau$ to the 1D macroscopic, so-called *convection-dispersion-equation*

$$\frac{\partial \bar{c}}{\partial t} + \bar{v} \frac{\partial \bar{c}}{\partial x} - D \Delta \bar{c} = 0. \quad (2.17)$$

The parameters \bar{v} and D of this macroscopic equation can be directly related to the microscopic flow field $v(r)$ and diffusion coefficient D_m :

$$\bar{v} = \frac{v_0}{2}, \quad D = D_m + \frac{R^2 v_0^2}{48 D_m}. \quad (2.18)$$

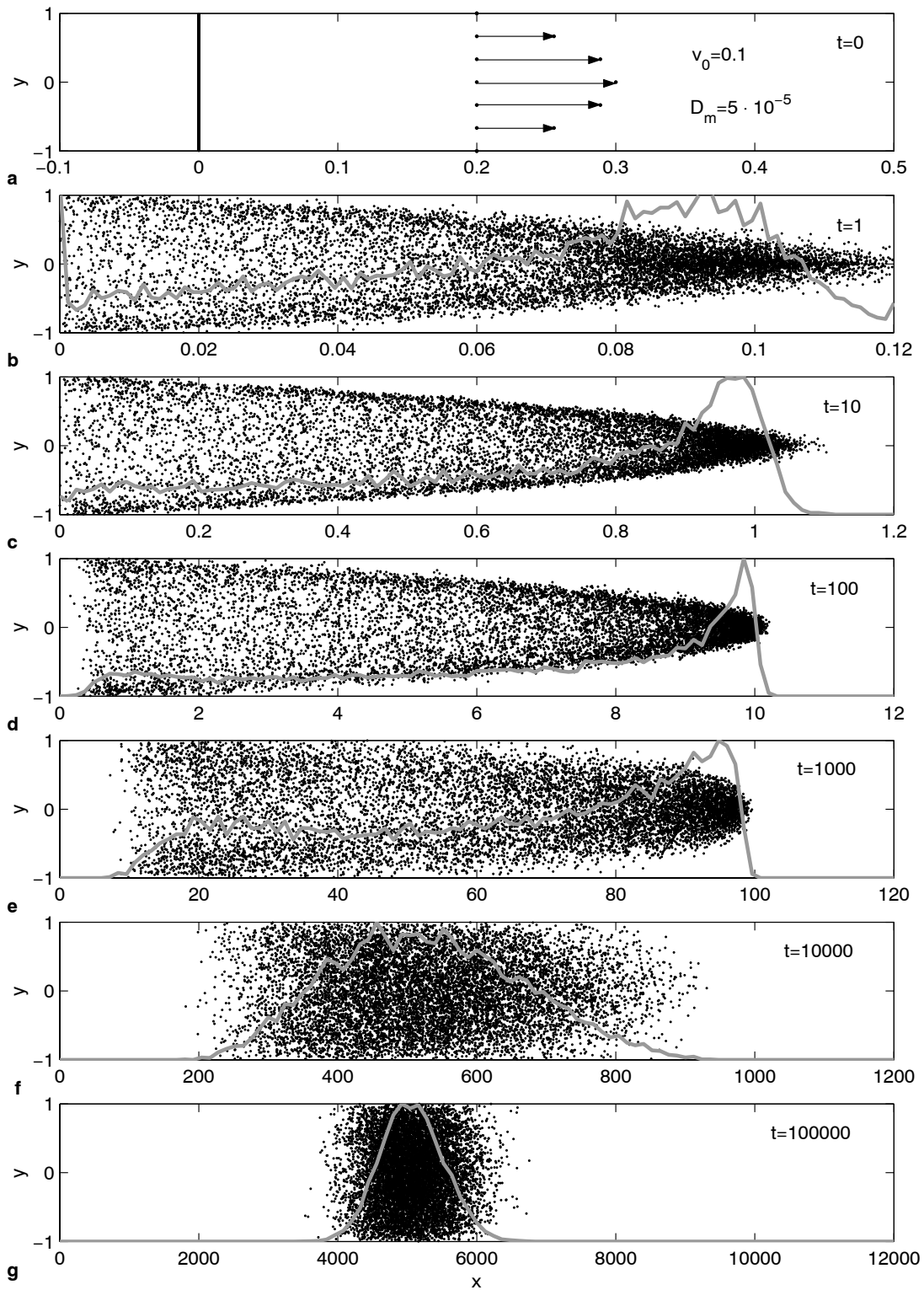


Figure 2.3: Dispersion of a solute pulse in the flow field of a capillary tube: for $t > \tau = 40000$ the particle distribution in flow direction (indicated by the gray lines) approaches a gaussian distribution according to the central limit theorem. The images represent the 2D projections of the 3D particle distributions.

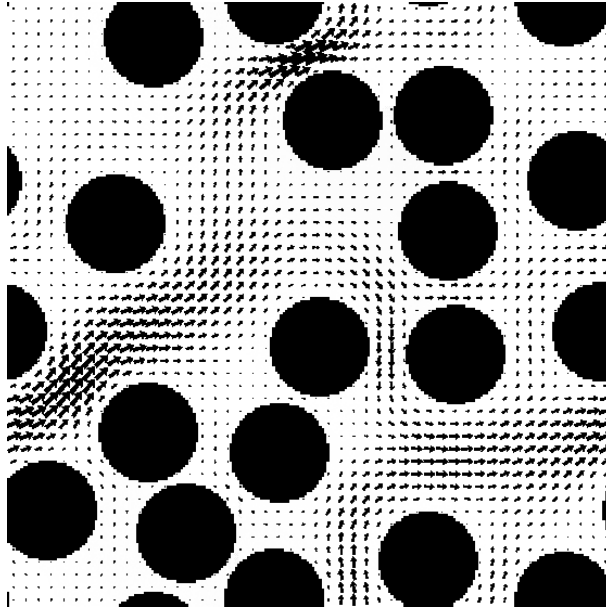


Figure 2.4: Steady flow field in an array of spheres obtained from the solution of the Stokes-equation 2.10 using a finite difference method (reprinted from Ruge (1996)).

In recognition of Sir Geoffrey Taylor, who found these relations in 1953 (Taylor, 1953), the dispersion of a solute in a capillary tube is today usually referred to as *Taylor-dispersion*.

The transport on the macroscale, which is caused by a combination of microscopic convection and diffusion, is quantified by the *dispersion coefficient* D . According to equation 2.18, the value of D is typically significantly higher than D_m . At first view it is surprising that D decreases with increasing D_m . This is a result of the effect that a high value of D_m increases transverse mixing and therefore reduces the broadening of the particle distribution in flow direction due to convection.

Although the flow in a capillary tube is mostly not an adequate model for the flow in a porous medium, the observed mechanisms and the resulting description by a macroscopic convection-dispersion-equation provide the conceptual basis for the following description of flow and transport in a porous medium.

2.3.2 Hydrodynamic dispersion in a homogeneous porous medium

In contrast to the flow in a capillary tube, the exact flow field in a porous medium is typically not known. Numerical solutions like that shown in figure 2.4 are only feasible for small domains and only under the condition that the boundary conditions, i.e. the shape of the solid surfaces, are known. However, even if these conditions are not fulfilled and the detailed velocity profile is not available, the *central limit theorem*, which was applied for the macroscopic description of transport in a capillary tube, is in principle similarly applicable to the flow in a porous medium.

The transition from the microscopic description based on the Navier-Stokes-equation 2.9 and the convection-diffusion-equation 2.11 to the macroscopic description of flow and transport in homogeneous porous medium based on the central limit theorem then leads to the 3D

convection-dispersion-equation

$$\frac{\partial \bar{c}}{\partial t} + \bar{\nabla} \cdot (\bar{v}\bar{c}) - \bar{\nabla} \cdot (D\bar{\nabla}\bar{c}) = 0. \quad (2.19)$$

Here \bar{v} denotes the macroscopic averaged velocity in the liquid phase and

$$D = \begin{pmatrix} D_{xx} & D_{xy} & D_{xz} \\ D_{xy} & D_{yy} & D_{yz} \\ D_{xz} & D_{yz} & D_{zz} \end{pmatrix} \quad (2.20)$$

denotes the symmetric so-called *dispersion tensor*. For the flow in x-direction ($\bar{v} = (\bar{v}_x, 0, 0)^T$) in an isotropic porous medium, D is given by

$$D = \begin{pmatrix} D_L & 0 & 0 \\ 0 & D_T & 0 \\ 0 & 0 & D_T \end{pmatrix}, \quad (2.21)$$

where D_L and D_T are the so-called *longitudinal* and *transversal* dispersion coefficients. The value of \bar{v} can be obtained from the solution of the *Darcy equation*

$$\bar{v} = -\frac{K}{\eta}\bar{\nabla}p, \quad (2.22)$$

where η denotes the liquid viscosity and K is the *hydraulic conductivity* of the porous medium.

For many practical applications of flow and transport in porous media (like e.g. the spread and fate of contaminants in an aquifer) the values of D_L , D_T and K are an essential information. However, unlike the above discussed flow in a capillary tube, no analytical relations are available here due to the complexity of the porous medium. Whereas K is only a function of the porous structure, the dispersion coefficients D_L and D_T potentially depend on many different parameters of the porous matrix, the solvent and the solute, like e.g. the macroscopic velocity \bar{v} , the particle diameter d (as a first-order representation the pore geometry), the density ρ and viscosity η of the solvent and the diffusion coefficient D_m :

$$D_{L/T} = D_{L/T}(\bar{v}, d, \rho, \eta, D_m, \dots) \quad (2.23)$$

The analysis of the geometrical and dynamical similarity of the functional dependence 2.23 according to the *Buckingham-Pi-theorem* (Buckingham, 1914) leads to the conclusion that the dimensionless dispersion coefficients $\frac{D_L}{D_m}$ and $\frac{D_T}{D_m}$ can be written as a function of two dimensionless variables:

$$\frac{D_{L/T}}{D_m} = \frac{D_{L/T}}{D_m} \left(\frac{\bar{v}d}{D_m}, \frac{\eta}{\rho D_m}, \dots \right) = \frac{D_{L/T}}{D_m} (\text{Pe}, \text{Sc}, \dots) \quad (2.24)$$

Although in principle other dimensionless variables could be chosen, the above used *Peclet number* Pe and *Schmidt number* Sc are the by far most common. Intuitively the Peclet number represents the relative magnitudes of convective and diffusive transport over the typical length d of the porous medium, and the Schmidt number represents the ratio of the coefficients of momentum diffusion and mass diffusion:

$$\text{Peclet number } \text{Pe} = \frac{\bar{v}d}{D_m} = \frac{\text{"convective transport"}}{\text{"diffusive transport"}}. \quad (2.25)$$

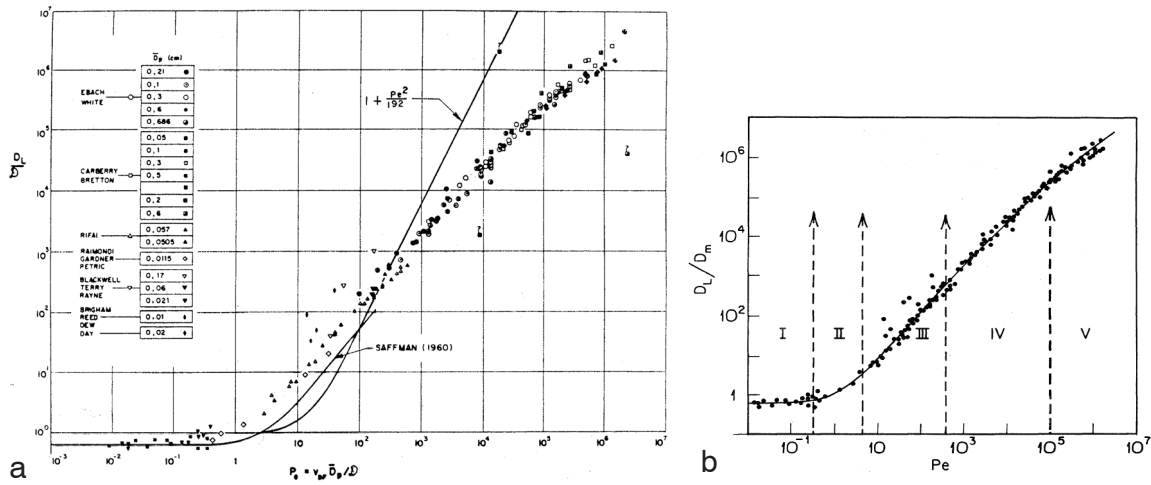


Figure 2.5: Dependence of the dimensionless longitudinal dispersion coefficient $\frac{D_L}{D_m}$ on the Peclet number Pe represented by a compilation of measurements from several authors reprinted from **a** Dullien (1992) and **b** Sahimi (1993) including a classification of different Pe ranges.

$$\text{Schmidt number } Sc = \frac{\eta}{\rho D_m} = \frac{\text{"momentum diffusion"}}{\text{"molecular diffusion"}}. \quad (2.26)$$

The transformation of constitutive equations into a dimensionless form is a commonly used method to reduce a physical process to its intrinsic complexity, especially in hydrodynamics. A more detailed discussion of this concept is given in Tritton (1988).

For several decades it is the objective of both theoretical and experimental scientists to determine the dependencies of the dispersion coefficients on the Peclet number and Schmidt number. For the experimental studies substantial use is made of the dimensionless formulation 2.24: the existence of this formulation provides the opportunity to study the (Pe, Sc) -dependence of the dispersion coefficients through comparatively inexpensive laboratory experiments. The values of the dispersion coefficients can then in principle be transformed to any other scale, like e.g. the field scale in hydrology.

Figure 2.5 shows two compilations of experimentally determined longitudinal dispersion coefficients plotted versus the Peclet number Pe . According to Sahimi (1993) the dependence of $\frac{D_L}{D_m}$ on Pe can be broken down into five different regimes as indicated in figure 2.5b:

$Pe < 0.3$

In this regime convection is so slow that dispersion is controlled almost completely by diffusion. Consequently the dispersion is isotropic with the dispersion coefficients given by

$$\frac{D_L}{D_m} = \frac{D_T}{D_m} = \frac{1}{F\phi}, \quad (2.27)$$

where F is the so-called *formation factor* and ϕ the porosity of the porous medium. The value of $\frac{1}{F\phi}$, which is determined by the pore structure, is typically in the range between 0.15 and 0.7.

0.3 < Pe < 5

This regime is characterized by the transition from the diffusion-dominated regime to a regime mostly controlled by convection. In this transition zone, where both diffusion and convection contribute significantly to the dispersion, the dispersion coefficients start to increase with increasing Pe. However, no universally valid formula for $\frac{D_{L/T}}{D_m}(\text{Pe})$ has yet been obtained for this transitional regime.

5 < Pe < 300

In this range of Peclet numbers, the so-called *power-law regime*, the measured dispersion coefficients are best described by the empirical relations

$$\frac{D_L}{D_m} = \alpha_L \text{Pe}^{n_L} \quad \text{and} \quad (2.28)$$

$$\frac{D_T}{D_m} = \alpha_T \text{Pe}^{n_T}. \quad (2.29)$$

A comparison of experimentally obtained values for α_L , α_T , n_L and n_T is given in section 8.3.2. A theoretical consideration of this behavior is presented in section 2.3.3.

300 < Pe < 10⁵

For a porous medium without any stagnant zones, like e.g. dead-end pores (see section 2.3.3), the transport in this Pe range is completely dominated by convection (usually referred to as *mechanical dispersion*) and thus the dependence on the Peclet number must be linear:

$$\frac{D_L}{D_m} = \alpha_L \text{Pe} \quad \text{and} \quad (2.30)$$

$$\frac{D_T}{D_m} = \alpha_T \text{Pe}. \quad (2.31)$$

However, there are strong indications that stagnant zones are much more prevalent in porous media than intuitively expected (see section 8.3.5). This leads to an extension of the power-law relations 2.28 and 2.29 into the present Pe range, which is confirmed by the results of several authors given in section 8.3.2.

Pe > 10⁵

Whereas for the previous Pe regimes a laminar flow field was assumed, in this regime turbulence starts to contribute to the dispersion process. Consequently the dispersion coefficients are supposed to depend not only on the Peclet number Pe, but also on the Reynolds number $\text{Re} = \frac{\rho \bar{v} d}{\eta}$.

The plot of the longitudinal dispersion coefficients versus the Peclet number in figure 2.5a, which is compiled from measurements using a large variety of porous media, solvents and solutes and therefore covering a large range of values for d , ρ , η and D_m , suggests that the dispersion coefficients depend solely on the Peclet number, and the dependence on the Schmidt number can be neglected. In one of the few quantitative studies of the Schmidt number dependence of dispersion coefficients, Delgado & Guedes de Carvalho (2001) have found that $\frac{D_T}{D_m}$ shows a dependence on Sc only for $\text{Sc} < 550$.

2.3.3 Theoretical models

The following paragraphs are designed to provide a more detailed analysis of the microscopic physical processes that lead to the empirical laws for the respective Pe ranges which have been discussed above. Koch & Brady (1985) have developed a quantitative theory which states that the dispersion coefficients are resulting from a combination of the following physical phenomena:

- In the absence of convection, the dispersion coefficients are given by the *tortuosity* τ of the porous medium, which is defined as the ratio of $D_{L/T}$ at $Pe=0$ and the diffusion coefficient in the pure solvent D_m .
- Pure convection results in a contribution to $D_{L/T}$ which scales linearly with Pe. This so-called *mechanical dispersion* comes from the velocity fluctuations in the liquid phase of the porous medium as illustrated in figure 2.4.
- The diffusive boundary-layers near the solid surface lead to the so-called *boundary-layer dispersion* which scales as $Pe \ln Pe$.
- Regions in the liquid phase with zero velocity (so-called *stagnant zones*), where the solute can enter or exit solely through diffusion, lead to a contribution which grows quadratically with Pe. This effect is called *holdup dispersion*.

Finally the dispersion coefficients are given by the linear superposition

$$\frac{D_{L/T}}{D_m} = \tau + \alpha Pe + \beta Pe \ln Pe + \gamma Pe^2. \quad (2.32)$$

According to Koch & Brady (1985), boundary-layer dispersion and holdup dispersion can be neglected for the transverse dispersion coefficients, so that $\beta = 0$ and $\gamma = 0$ for D_T . The individual contributions are specified in the next paragraphs.

Tortuosity

As discussed above, the tortuosity τ determines the dispersion $D_0 = D_{L/T}(Pe = 0)$ of a solute in the absence of convection, and consequently itself is determined by the structure of the pore space. Millington & Quirk (1960) (cited by Roth (1996a)) have found different empirical models for the dependence of D_0 on the volumetric content of the liquid phase θ and the porosity ϕ ($\theta = \phi$ for saturated porous media). According to Jin & Jury (1996) (cited by Roth (1996a)), Millington-Quirk's first model

$$\tau = \frac{D_0(\theta)}{D_m} = \frac{\theta}{\phi^{2/3}} \quad (2.33)$$

agrees best with experimental data.

Mechanical dispersion

Mechanical dispersion is the result of the velocity fluctuations in the liquid phase. If the velocity profile $\vec{v}(\vec{x})$ in the porous medium is described statistically by its mean $\bar{\vec{v}}$ and its velocity autocorrelation function (VACF)

$$C_{vv}(t) = \langle (\vec{v}(0) - \bar{\vec{v}})(\vec{v}(t) - \bar{\vec{v}})^T \rangle, \quad (2.34)$$

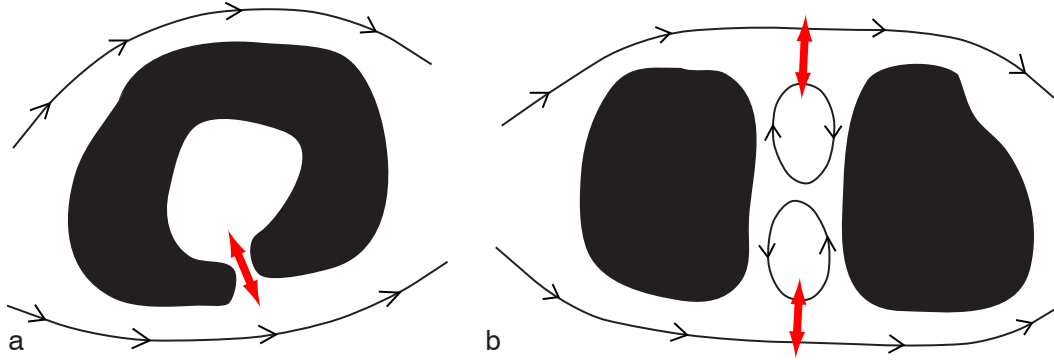


Figure 2.6: Different types of regions in the liquid phase which are accessible solely by diffusion: **a** dead-end pore and **b** circulation pattern.

the time-dependent dispersion tensor D can be calculated as

$$D(t) = \int_0^t C_{vv}(t') dt'. \quad (2.35)$$

Obviously the asymptotic dispersion tensor $D(t \rightarrow \infty)$ only exists if the integral in equation 2.35 converges, i.e. if the VACF decays at least with $1/t$. Lowe & Frenkel (1996) have found from numerical simulations using a lattice boltzmann method that at high Peclet numbers the dispersion coefficient is diverging. However, the results of the comparative study of Maier *et al.* (2000) was contrary to this finding, and the statement was relinquished by Capuani *et al.* (2003).

Holdup dispersion

The effect of holdup dispersion results from stagnant zones in the liquid phase of the porous medium, which are accessible from the convective part of the flow field only by diffusion. Since its contribution to the dispersion coefficient grows quadratically with Pe , holdup dispersion is an important mechanism for high Peclet numbers. Intuitively it seems that such stagnant zones like e.g. so-called *dead-end pores* (figure 2.6a) should hardly occur in unconsolidated bead packings, which are commonly used for laboratory experiments. There are however several studies (including this work) which indicate that holdup dispersion plays an important role in solute transport. A detailed discussion of this issue is given in section 8.3.5.

A possible explanation for the unexpectedly strong influence of holdup dispersion might be the existence of closed loops in the convective flow field. Figure 2.6b shows a potential constellation for the formation of such closed loops. Furthermore Azzam & Dullien (1977) have shown that closed loops can emerge also in rectangular pockets as shown in figure 2.7a. Dentz *et al.* (2003) showed analytically that in any incompressible Gaussian random field there is finite probability for closed streamlines (see figure 2.7b).

Boundary-layer dispersion

The following description of boundary-layer dispersion is adopted from Koch & Brady (1985): "Saffman (1959) modelled the microstructure of a porous medium as a network of capillary

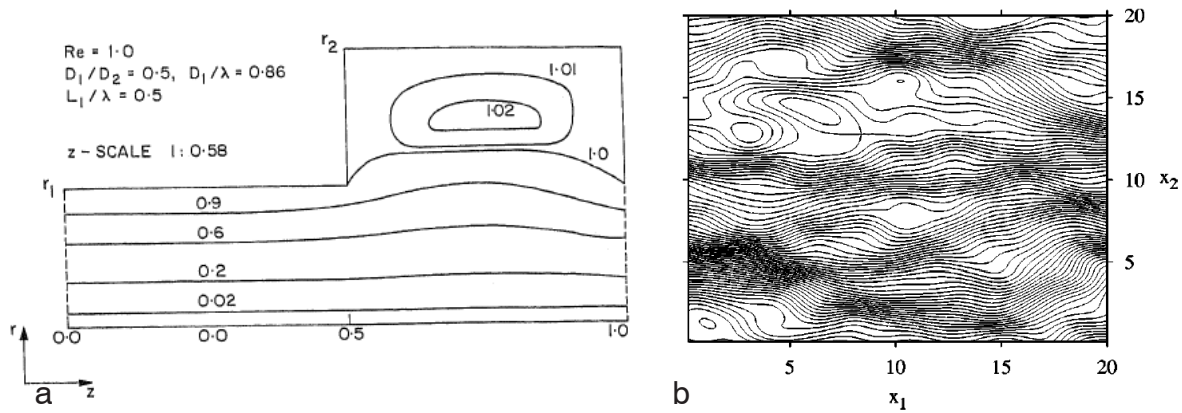


Figure 2.7: **a** Formation of closed streamlines in a rectangular pocket adjacent to a capillary tube (reprinted from Azzam & Dullien (1977)). **b** Closed streamlines obtained by Dentz *et al.* (2003) from a linearized solution of the Darcy equation for a 2D Gaussian-distributed velocity field.

tubes of random orientation. At high Peclet number and at very long time, Saffman found that the dispersion never becomes truly mechanical, the effective diffusivity growing as $Pe \ln Pe$. The logarithmic dependence results from the zero velocity of the fluid at the capillary walls. The time required for a tracer particle to leave a capillary would become infinite as its distance from the walls goes to zero, if molecular diffusion did not allow the tracer to escape the region of low velocity near the wall. This phenomenon is similar to the 'holdup' dispersion mentioned above, although in this case there is no finite region of zero velocity."

Boundary wall effects

The presence of the boundary walls of the laboratory columns used for the measurements of dispersion coefficients leads to inhomogeneities of the pore structure near the walls. Maier *et al.* (2002) found that these inhomogeneities lead to a significant increase of the effective longitudinal dispersion coefficient compared to the bulk. Consequently this effect is a possible explanation for deviations between the measured dispersion coefficients from different experiments. Furthermore the adequate consideration of this effect is mandatory for the correct upscaling of the laboratory measurements to the field scale.

2.4 Heterogeneous porous media

The homogeneity of the porous medium was a stringent requirement for the description of flow and transport given in the previous section. This requirement is fulfilled if there exists a finite representative elementary volume (REV) for which the average of the relevant microscopic quantities, like e.g. the velocity $\bar{\vec{v}} = \frac{1}{V} \int \vec{v}(\vec{x}) dV$ or the porosity $\bar{\phi} = \frac{1}{V} \int \phi(\vec{x}) dV$, becomes independent of the position \vec{x} in the porous medium. While the assumption of homogeneity is approximately justified for most unconsolidated bead packings used for laboratory experiments (for a fundamental discussion of this issue see Torquato *et al.* (2000)), natural porous media like soil are typically heterogeneous on every scale.

Chapter 3

Method of measurement

3.1 Introduction

This chapter describes the setup of an experimental apparatus for the non-invasive optical measurement of 3D pore-scale flow and transport in porous media. The method uses a planar laser-induced fluorescence (PLIF) technique in combination with a system of transparent solids and liquids with highly precise matched refractive indices. In PLIF a fluorescent substance is excited by a planar laser sheet with its wavelength tuned to the absorption band of the substance. The light is absorbed by the substance and re-emitted at characteristic wavelengths. A 2D image of the concentration distribution can be obtained by a CCD camera mounted with its optical axis perpendicular to the laser sheet. Due to the fact that the absorption and emission bands of the fluorescent dye have no or only little overlap, the dye distribution between the laser sheet and the camera does not affect the measurement. Therefore a consecutive displacement of the laser plane in the out-of-plane direction results in a set of 2D images representing the 3D concentration distribution. This technique gives access to 3D information without any challenging tomographic reconstruction. The main features of the method, i.e. its high spatial and temporal resolution and the simultaneous visualisation of two immiscible liquids, are attained by the employment of capable illumination and imaging devices and the composition of a proper combination of solids, liquids and fluorescent dyes.

At first the next section gives a short overview of previously employed refractive index matching methods. Then section 3.3 describes the general arrangement of the setup and the technical specifications of the single components used in this work. The physical and chemical properties of the utilised solids, liquids and dyes are specified in section 3.4, 3.5 and 3.6 respectively. Finally a summary and conclusions are given in section 3.7

3.2 Refractive index matching methods

The difficulties of many experimental methods to probe flow and transport on the pore scale of a porous medium, stemming from the opaqueness of the medium, can be overcome by the application of a transparent porous matrix and liquids with their refractive index matched to that of the matrix. Refractive index matching methods are used for some decades to gain 3D optical access to liquid flow phenomena (for an overview see Budwig (1994)). The application of these methods to porous media has been accomplished by Burdett *et al.* (1981) using a light absorption technique, Montemagno & Gray (1995) and Rashidi *et al.* (1996) using PLIF

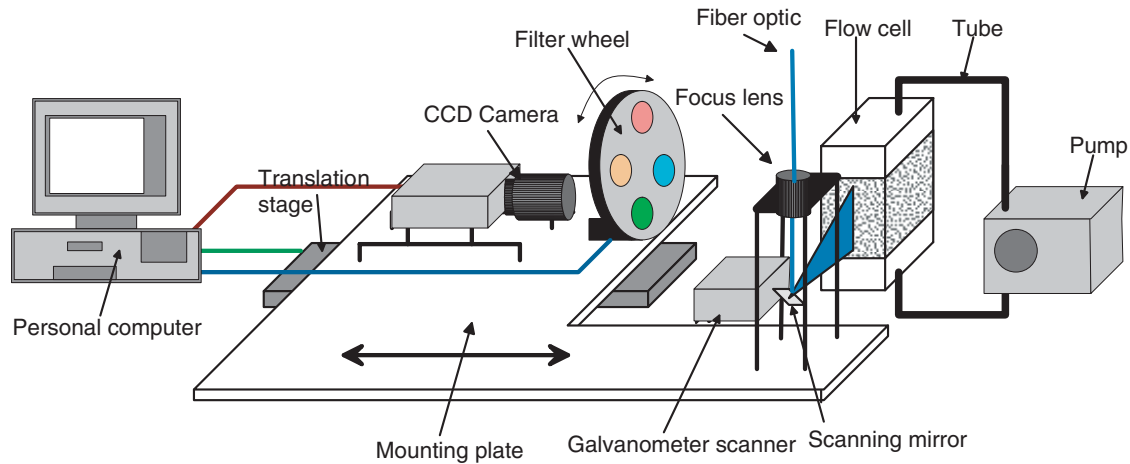


Figure 3.1: Layout of the experimental setup for the PLIF method.

and Peurrung *et al.* (1995) and Moroni & Cushman (2001) using particle tracking velocimetry (PTV). In contrast to these previous works, the PLIF technique presented in the following sections has a much higher spatial and temporal resolution and is the first to simultaneously visualize the dynamics of two immiscible liquids.

3.3 Experimental setup

The layout of the setup components, which are detailed in the following subsections, is shown in figure 3.1, and a corresponding photograph is pictured in figure 3.2. The imaging devices (CCD camera and optical bandpass filters) are mounted on a plate together with the optical devices for illumination (fiber, focus lens and galvanometer scanner). During the experiments, the mounting plate is shifted consecutively in z-direction by a motorized translation stage in order to scan the volume of the flow cell, which stands at a fixed position. A personal computer (PC) controls the translation stage, filter wheel and CCD camera and receives and stores the image data to a hard disk.

3.3.1 Imaging devices

A high resolution progressive scan camera (Basler A113P, Basler (1998)) is used to record the images. It employs a CCD sensor chip with a resolution of 1300×1030 pixels providing features like electronic exposure time control and partial scan, which can be controlled by the connected PC. Thereby the exposure time is adjusted continuously in steps of 20 ms (the scanning duration of the laser beam) to obtain maximum signal-to-noise ratio and the scan area on the CCD chip is adapted to the geometry of the flow cell. In horizontal flow, a partial scan area of 1300×600 pixels is used, resulting in a resolution of circa $70 \mu\text{m}$ in x- and y-direction. Optical bandpass filters ($550 \pm 20 \text{ nm}$ and/or $600 \pm 20 \text{ nm}$, the transmittance curves are shown in figure 3.11) are used to limit the imaging to these emission wavelengths of the fluorescent dye, where the refractive indices are closely matched (see chapter 4), and also to screen scattered light e.g. from imbedded air bubbles. In two-phase flow, where two dyes with different emission wavelengths are used, a PC-controlled filter wheel (see figures 3.1

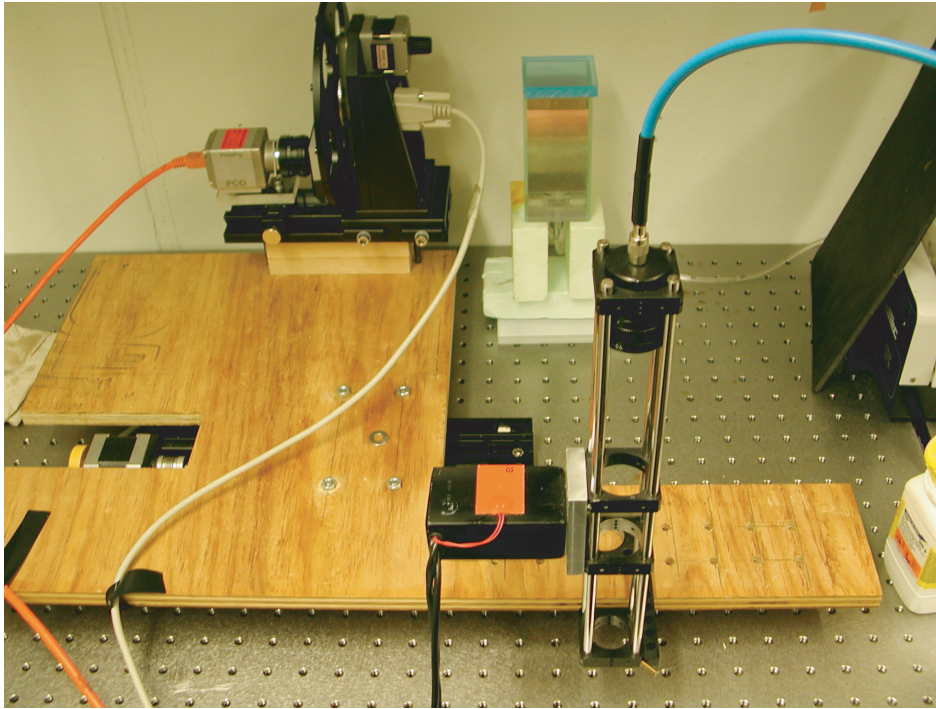


Figure 3.2: Photograph of the experimental setup corresponding to figure 3.1.

and 3.2) is deployed to change between the two filters. The switch is done after each complete volume scan.

3.3.2 Light source and optics

The light source for illumination is an argon ion laser (Spectra-Physics Stabilite 2017) operating at 488 nm with an output of 1.5 W. The beam is coupled to an optical fiber and then focused on the flow cell to a diameter between 0.5 and 1 mm. It is expanded to a vertical sheet by reflection on the mirror of a galvanometer scanner oscillating at 50 Hz.

3.3.3 Personal computer

The personal computer, equipped with a 500 MHz Intel pentium 3 processor and 1GB RAM, is the central control unit of the measurement setup. It drives the translation stage and the filter wheel via a ISA stepper motor card (Owis SM30). Synchronously it sets the camera parameters (exposure time, partial scan area, gain and offset) and triggers the readout of the CCD via the RS 232 interface. The camera transfers an 8 bit video data stream to a FPGA framegrabber (Silicon Software microenable equipped with a Xilinx XC4085XLA), which is received by the PC at its PCI interface and stored to a hard disk. For a representative experiment (90 images à 1300×600 pixel every 30 s) the averaged data rate is circa 2.3 MB/s.

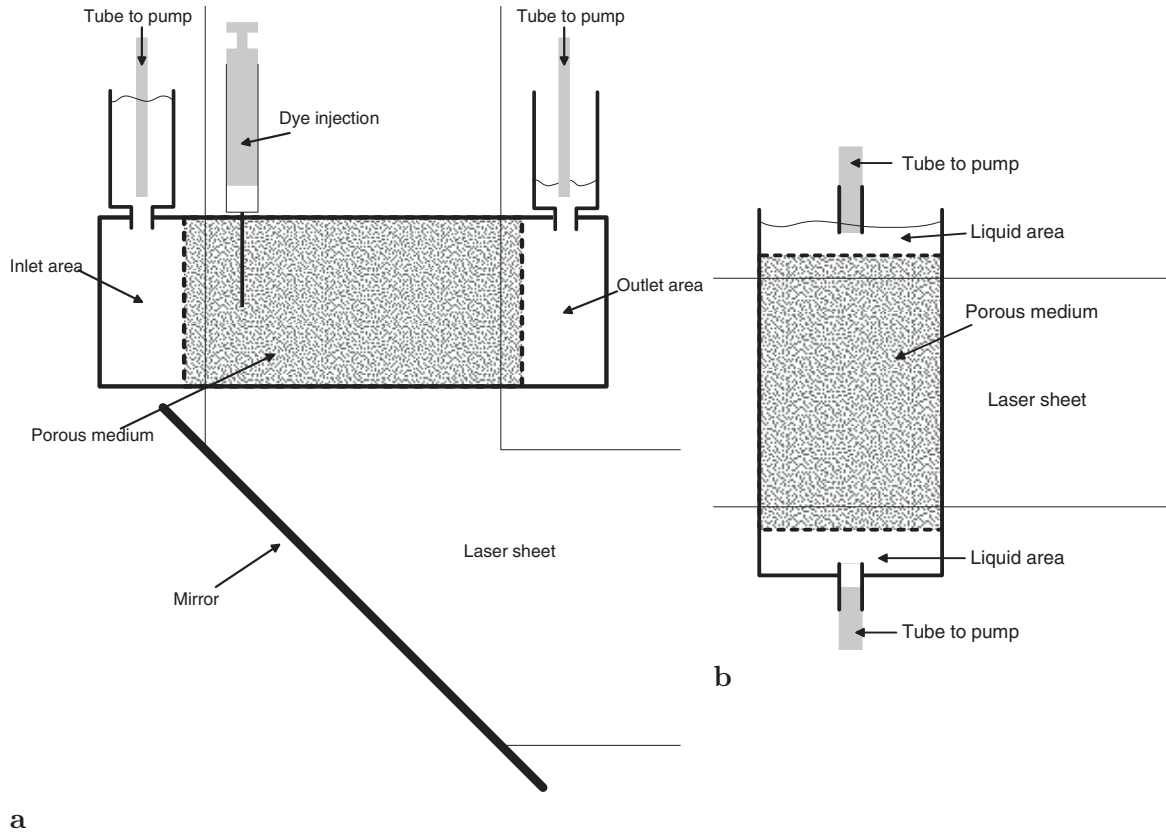


Figure 3.3: Flow cells for **a** horizontal and **b** vertical flow.

3.3.4 Translation stage

For the displacement of the mounting plate and the devices mounted on it a motorized translation stage (Owis VTM 80) was employed. Its 2-phase stepping motor performs at a maximum traverse speed of 8 mm/s over a maximum distance of 300 mm. The resolution is specified as $2.5 \mu\text{m}$ and the repeatability as $10 \mu\text{m}$, which is adequate for increments of $400 \mu\text{m}$ used in the experiments. In a typical experiment 90 parallel planes have been recorded every 30 seconds. During the first 14 seconds the actual scanning and data acquisition take place whereas the remaining 16 seconds are used to drive back the translation stage and store the data to the harddisk.

3.3.5 Flow cells

The flow cells are rectangular parallelepipeds made of plexiglass. The solid granulate material is clamped between two metal grids which adjoin to liquid-filled inlet and outlet areas. A tubing pump conveys the fluids through a tube from the outlet to the inlet with adjustable flow rate and direction. Two versions of the flow cells for horizontal and vertical flow direction are sketched in figure 3.3.

The vertical flow cell is mainly used for two-phase flow experiments, like imbibition or drainage processes, where the two liquids have significantly different densities. Its volume for the porous matrix, which is penetrated by a laterally entering laser sheet, has a size of $5 \times$

$10 \times 5 \text{ cm}^3$. The tubing pump is directly connected to the lower liquid area, so that its flow rate is directly coupled to the average liquid velocity in the porous medium. A sketch of the vertical flow cell is shown in figure 3.3b and a photograph is shown in figure 3.4.

The horizontal flow cell is employed for single-phase flow experiments, where the liquid density throughout the medium is approximately constant. The volume of the porous matrix is sized $8 \times 4 \times 4 \text{ cm}^3$. Here the liquid is not pumped directly through the porous medium but from and into two containers mounted above the outlet and inlet area, so that the hydraulic heads in these containers reach an equilibrium according to the flow rate given by the pump. The hydraulic heads can be calculated from the heights of the liquid levels in the containers in order to determine the hydraulic conductivity of the porous medium. The upper coverage of the cell has a hole with a set-in piece of rubber, through which an injection containing dyed liquid is introduced at the beginning of an experiment and the desired quantity of dye is injected. Since the cell is not laterally accessible for the laser sheet, it is placed upon a mirror mounted at 45° so that the laser sheet enters the cell from the bottom. The layout of the horizontal flow cell is shown in figure 3.3a and figure 3.5 shows a corresponding photograph.

3.4 Solid properties

For the solid constituting the porous matrix, a transparent, rigid and inert material is required. Because the number of suitable liquids decreases rapidly with increasing refractive index, the refractive index of the solid should be as low as possible. The two classes of applicable materials are plastics and glasses. Since the refractive index should not depend on the orientation of the grains, which would be the case for birefringent materials, no crystalline but only amorphous materials can come into consideration. The refractive indices of plastics are in a range from 1.49 (acrylic, e.g. Plexiglass or Perspex) to 1.58 (polycarbonate, e.g. Lexan or Makrolon), those of optical glasses from 1.46 (fused silica) to 1.87 (Schott LaSFN9). Since one aim of the present work was to investigate the influence of different surface properties (e.g. contact angle or adsorption rate), one material of each class was used, Plexiglass and fused silica. The refractive index of a solid is a function of temperature and wavelength, which is quantified for the two materials in table 3.1 and figure 3.6. The dependence on the wavelength is used for the precise matching of the refractive indices of solids and liquids as described in chapter 4. The two solids further differ significantly regarding their densities and water/air contact angles as specified in table 3.1. Whereas plexiglass is only moderately acid resistant, fused silica is extremely resistant owing to the very strong silicon-oxygen bonds.

The fused silica was delivered by the manufacturer (Schott Lithotec) as blocks with diameters of a few centimeters. They were crushed making use of a jaw crusher which allowed the adjustment of the gap size that the crushed material must pass before leaving. However, the resulting size distribution proved to be very broad and therefore the outcome was further sieved to sizes of 0.6 - 1 mm. The result is shown in figure 3.7b.

The plexiglass was obtained from the manufacturer (Goodfellow GmbH) in a granulation of 0.6 mm mean diameter. Unfortunately, a big portion of the grains had air bubbles included, which make them unusable for the present application. The separation of the pure grains was performed by immersing them into a NaCl solution with density hardly smaller than that of plexiglass, where the pure grains accumulated at the bottom.

The shape of the grains differs significantly for the two materials. Whereas the fused silica grains have many sharp edges, the shape of the plexiglass is close to spherical as shown in

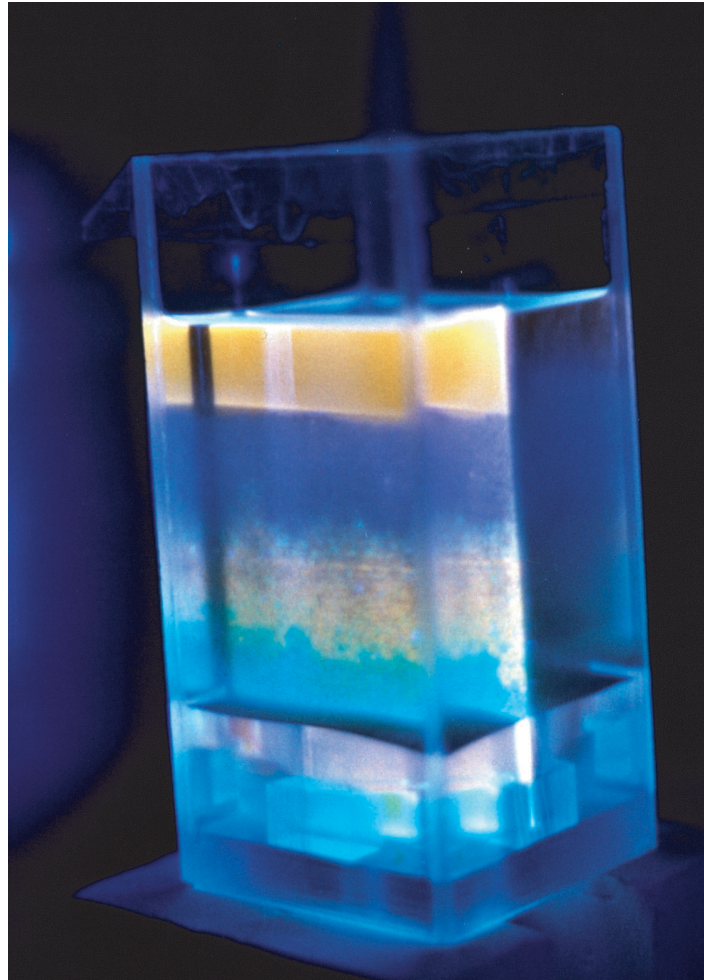


Figure 3.4: Photograph of the vertical flow cell sketched in figure 3.3b. In the present experiment the oil (marked with an orange fluorescing dye) in the upper part is displaced by water (marked with a green fluorescing dye) which is injected from the bottom of the cell. The distribution of the two liquids is visible in the section illuminated by the laser sheet.

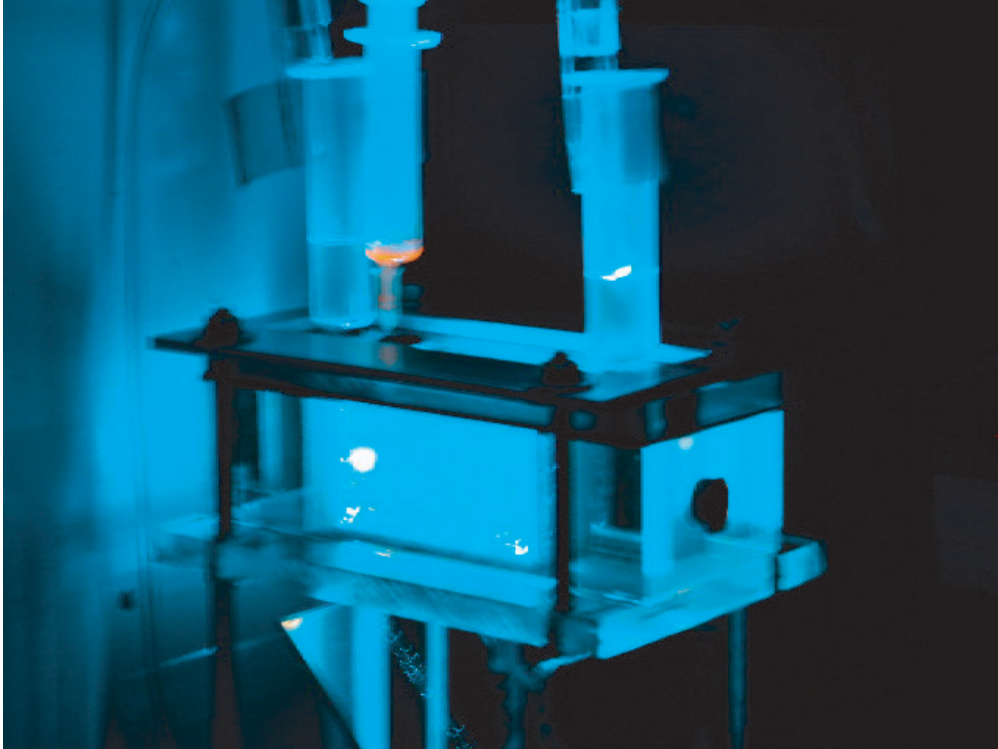


Figure 3.5: Photograph of the horizontal flow cell sketched in figure 3.3a. The volume with the porous matrix and the liquid containers are filled with silicone oil, and the injection with the dyed, orange fluoresceing oil is introduced from the top.

Solid	refractive index n	dn/dT [$^{\circ}\text{C}^{-1}$]	density ρ [g/cm^3]	water/air contact angle	mean diameter \bar{d}	porosity ϕ [cm^3/cm^3]
Fused silica	1.46 ^a	$9.8 \cdot 10^{-6}$ ^a	2.2 ^a	≈ 0 ^b	0.8 mm	0.48
Plexiglass	1.495 ^c	$-105 \cdot 10^{-6}$ ^c	1.19 ^d	59.3 ^b	0.6 mm	0.37

Table 3.1: Properties of solids for use as the porous matrix.

^afrom Schott (2001) at $T = 20^{\circ}\text{C}$ and $\lambda = 588\text{nm}$

^bfrom Adamson (1997)

^cfrom Waxler *et al.* (1979) at $\lambda = 589\text{nm}$

^dfrom Goodfellow (1999)

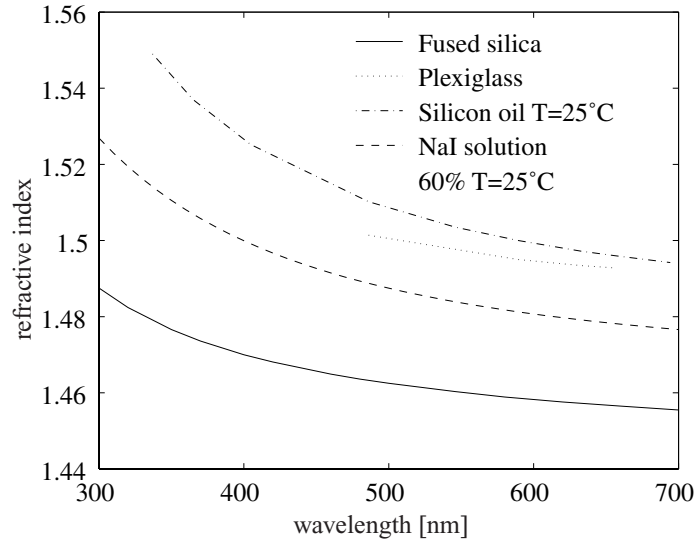


Figure 3.6: Refractive index as a function of wavelength for fused silica (from Schott (2001)), plexiglass (from Waxler *et al.* (1979)), silicone oil (from Cargille (1999)) and sodium iodide aqueous solution (from Narrow *et al.* (2000)).

figure 3.7a. In contrast to the plexiglass grains, the fused silica grains are considerably oblate, which is hardly visible from figure 3.7b since they are mostly lying on the flat side. These differences in grain morphology and size distribution effectuate the different porosity values given in table 3.1. They were calculated from the weight of a predefined volume V filled with the porous media and their respective densities:

$$\phi = 1 - \frac{m_{\text{solid}}}{\rho_{\text{solid}}V}. \quad (3.1)$$

3.5 Liquid properties

For the present technique two immiscible and transparent liquids matching the refractive index of the solids are required. Additionally they are demanded to be inert, nontoxic, nonvolatile

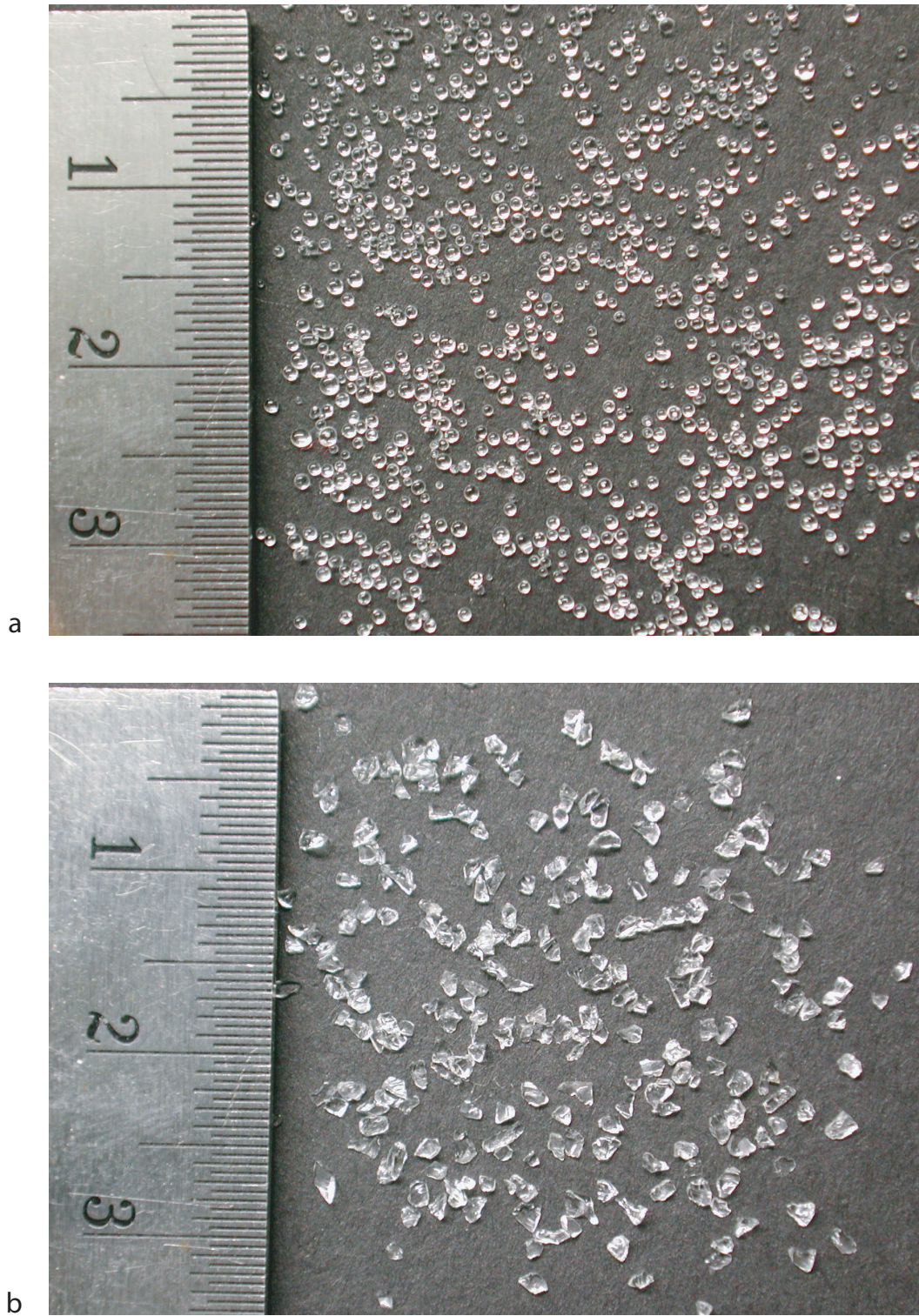


Figure 3.7: Granular materials for use as transparent porous matrix: **a** plexiglass **b** fused silica. The numbers on the ruler denote centimeter.

Liquid	refractive index n	dn/dT [$^{\circ}\text{C}^{-1}$]	density ρ [g/cm^3]	viscosity ν [mm^2/s]	surface tension σ [mN/m]
DC 200	1.375 ^a	-	0.761 ^a	0.65 ^a	15.9 ^a
DC 550	1.4935 ^b	$-3.97 \cdot 10^{-4c}$	1.068 ^b	125 ^b	24.5 ^b
DC 556	1.46 ^d	-	0.98 ^d	22.5 ^d	-
DC 710	1.533 ^e	-	1.11 ^e	500 ^e	28.5 ^e
water	1.333 ^f	$-0.9 \cdot 10^{-4f}$	0.998 ^f	1.004 ^f	73 ^f

^a from Dow Corning (1999d) at $T = 25^{\circ}\text{C}$

^b from Dow Corning (1996a) at $T = 25^{\circ}\text{C}$

^cvalue taken from Cargille (1999) for a silicone oil similar to DC 550

^d from Dow Corning (1998b) at $T = 25^{\circ}\text{C}$

^e from Dow Corning (1996c) at $T = 25^{\circ}\text{C}$

^ffrom Weast (1974) at $T = 20^{\circ}\text{C}$ and $\lambda = 589 \text{ nm}$

Table 3.2: Properties of pure liquids for different Dow Corning silicone oils and water.

and nonflammable. Although in general there can exist more than two immiscible liquids in contact with each other, there are mainly two classes that can be divided by the polarity of their molecules. The first class are liquids on the basis of water as a solvent and additional water soluble substances (e.g. salts), where the molecules of both solvent and solute are polar. The other class of liquids typically consist of unpolar organic molecules (e.g. hydrocarbons) which have no or only a small solubility in water. In the terminology of hydrology these classes are called aqueous phase liquids (APL) and non-aqueous phase liquids (NAPL).

As a NAPL a group of Dow Corning silicone oils was used, whose properties are given in table 3.2. They are all miscible with each other so that the refractive index of the mixture can be adjusted between 1.375 (DC 200) and 1.533 (DC 710). For the determination of the ratio of two liquids so that their mixture has a desired refractive index the following formula given by Kerr (1977) can be used:

$$V_1 n_1 + V_2 n_2 = V_{\text{mix}} n_{\text{mix}}, \quad (3.2)$$

where V_1 , V_2 and V_{mix} denote the volumes and n_1 , n_2 and n_{mix} denote the refractive indices of the two liquids and their mixture. The values obtained by this formula served as starting values for the more precise method described in chapter 4, which matches the index at a certain wavelength. The mixing behaviour for the viscosity of a mixture of two silicone oils is specified in a data sheet which was supplied by the manufacturer (Dow Corning (1999d)). The according specification is reprinted and translated in figure 3.8. Under the assumption that the volume V_{mix} of a mixture of two liquids is the sum of their volumes ($V_{\text{mix}} = V_1 + V_2$), the density of the mixture is given by

$$\rho_{\text{mix}} = \frac{m_1 + m_2}{\frac{m_1}{\rho_1} + \frac{m_2}{\rho_2}}. \quad (3.3)$$

Mixtures of silicone oils have been prepared for use with both plexiglass and fused silica, and the resulting properties are given in table 3.3.

For the aqueous phase, a zinc chloride solution was taken. Due to deprotonation of the hydrated zinc ions the pH of a solution with refractive index 1.46 is around 2.0. It is therefore not compatible with plexiglass and with many fluorescent dyes. Though sodium iodide

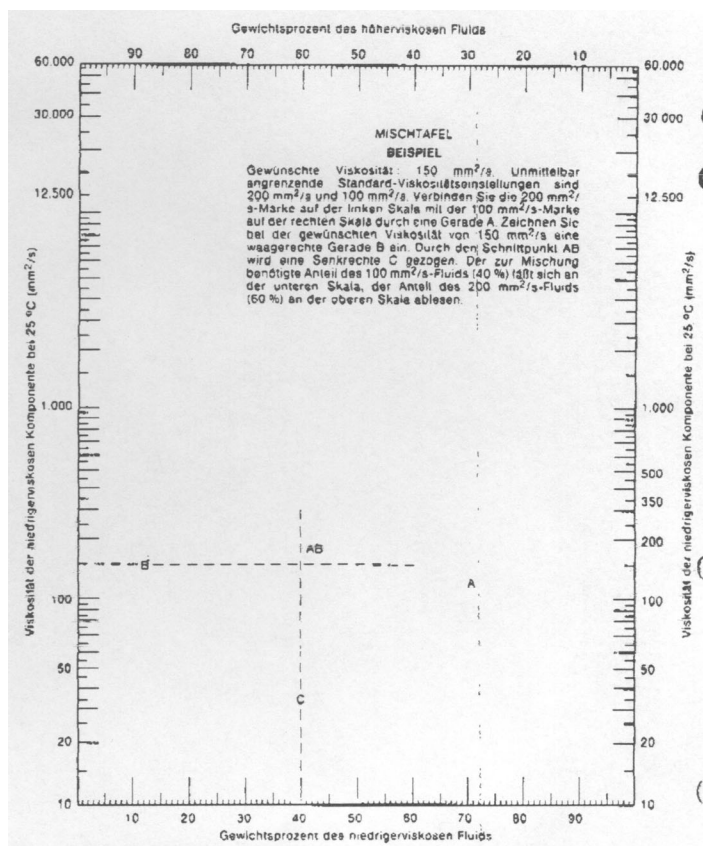


Figure 3.8: Viscosity of a mixture of two Dow Corning silicone oils (from Dow Corning (1999d)). The left and right vertical axes denote the viscosities of the higher and lower viscous fluid respectively. The upper and lower horizontal axes denote the weight percent of the higher and lower viscous fluid. The viscosity of the mixture is obtained by connecting the points on the left and right vertical axis by a straight line and then reading off the viscosity at the desired mixing ratio.

solutions as a possible alternative have a significantly higher pH, the number of compatible dyes is even lower due to reaction with iodide. The properties of the 58 wt.% solution for use with fused silica are shown in table 3.3. The values for density and viscosity plotted in figure 3.9 are taken from a product sheet of an industrial manufacturer (Madison (1999)).

As noted in section 3.4 for the solids, the refractive index of the liquids also depends on temperature and wavelength. As a consequence, the indices of solids and liquids can be matched only for one certain wavelength, which is described in chapter 4. The temperature and wavelength dependences of silicone oils shown in table 3.2 and figure 3.6 are taken from a data sheet for a silicone oil similar to DC 550 (Cargille (1999)). Due to the lack of data for zinc chloride solutions, its wavelength dependence is exemplified in figure 3.6 by the model for sodium iodide solutions given in Narrow *et al.* (2000). The modification of the mixing ratio of the silicone oils and the weight percentage of zinc chloride solution approximately leads to a up- or down-shift of the corresponding dispersion curves in figure 3.6, so that the curves of the solid and liquid intersect at a certain wavelength. The differences in temperature dependence

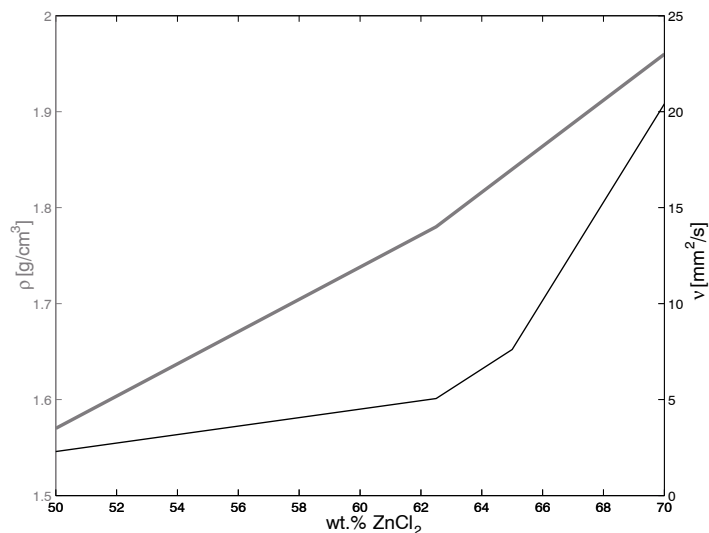


Figure 3.9: Density and viscosity of a ZnCl_2 aqueous solution as a function of ZnCl_2 weight percent (from Madison (1999)).

of the solids and liquids results in the necessity to keep the temperature constant during an experiment. Although no active temperature control was performed, no effects from changes of temperature were found as described in chapter 4.

3.6 Dye properties

For the measurement of flow and transport and the visualization of two-phase displacement processes two fluorescent dyes have to be found that fulfil the following requirements:

- in order to allow for the distinction between solid, non-aqueous and aqueous phase in an immiscible displacement experiment, both dyes must be soluble exclusively in one of the liquid phases.
- a high quantum efficiency and high absorption rate at the laser excitation wavelength (488 nm) are necessary for a high intensity of the emitted light.
- for a clear separation of the two liquid phases the dyes must have a significantly different stokes shift, i.e. the overlap of the emission spectra must be minimal.
- the dye for the zinc chloride aqueous solution must be compatible with a pH-value of 2.0.

The fluorescein substitute Alexa Fluor 488 (Molecular Probes) was found to satisfy these requirements as a dye for the zinc chloride aqueous solution. It exhibits high absorbance, quantum yields and photostability as well as low sensitivity to pH. Table 3.4 shows its molecular weight and structure. Its fluorescence spectra shown in figures 3.10 and 3.11 are almost identical to those of fluorescein.

Liquid	84 wt.% DC 550 + 16 wt.% DC 556	98 wt.% DC 556 + 2 wt.% DC 200	58 wt.% ZnCl ₂ solution
Refractive index n	1.49	1.46	1.46
Density ρ [g/cm ³]	1.05 ^a	0.97 ^a	1.70 ^b
Kinematic viscosity ν [mm ² /s]	95 ^c	21 ^c	4 ^b
Dynamic viscosity $\eta = \nu\rho$ [g/(cm · s)]	1.00	0.20	0.07
molecular diffusivity D_m [mm ² /s]	$1.96 \cdot 10^{-5}$ (Nile red)	$9.58 \cdot 10^{-5}$ (Nile red)	$5.36 \cdot 10^{-5}$ (Alexa Fluor 488)
Schmidt number $Sc = \nu/D_m$	$5 \cdot 10^6$ (Nile red)	$2 \cdot 10^5$ (Nile red)	$7 \cdot 10^4$ (Alexa Fluor 488)

Table 3.3: Properties of liquid mixtures and solutions with their refractive index matched to fused silica and plexiglass. The properties of the corresponding dyes in these liquids have been determined as described in section 8.2.

^acalculated with equation 3.3

^bfrom Madison (1999)

^cdetermined with the specification shown in figure 3.8

For the silicone oils the phenoxazine dye Nile Red proved to be well applicative. It features a sufficient absorbance at the laser wavelength and a considerably higher stokes shift than the Alexa Fluor 488. Its molecular weight and structure are given in table 3.4.

In figures 3.10 the absorption spectra of these dyes given in Haugland (2001) are plotted together with the laser excitation wavelength. The corresponding emission spectra and the transmittance curves of the optical bandpass filters (550 ± 20 nm and 600 ± 20 nm) are shown in figure 3.11. The filters were chosen to be each selective to one dye and to obtain maximal signal amplitude and optimal spatial accuracy. The spatial accuracy is optimal if the transmission bands are narrow and close together (see chapter 4), whereas the signal amplitude is maximal for broad transmission bands centered at the maxima of the emission curves. The chosen transmission bands shown in figure 3.11 are a compromise between these two oppositional demands. As noted in Haugland (2001), the emission spectrum of Nile Red shown in figure 3.11 undergoes blue shifts in nonpolar environments. This explains that the maximum fluorescence in the present case was found to be around 600 nm. Figures 3.10 and 3.11 also show that the emission spectrum of Alexa Fluor 488 and the absorption spectrum of Nile Red overlap. This will increase the fluorescence intensity of a Nile Red solution in the vicinity of a fluorescent Alexa Fluor 488 solution.

The coefficients of molecular diffusion D_m and Schmidt numbers Sc for the dyes in the index matched liquids are given in table 3.3. They were estimated from the dispersion of the dyes in the porous medium with the fluid at rest as described in section 8.2.

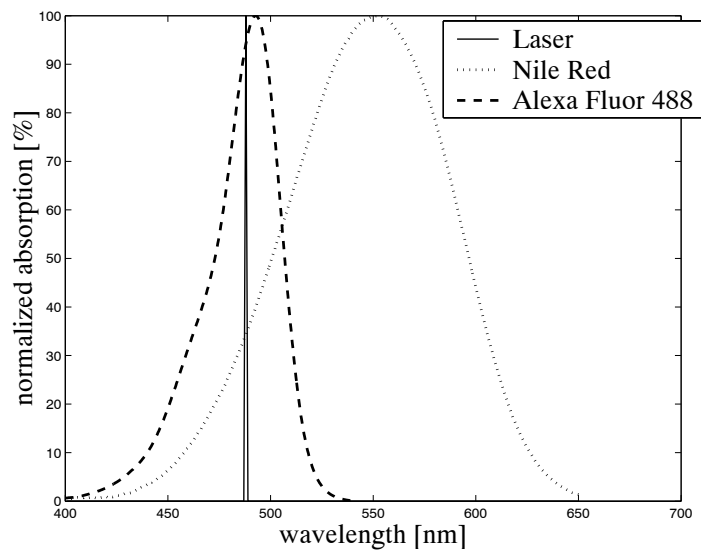


Figure 3.10: Normalized absorption spectra of Alexa Fluor 488 and Nile Red (from Haugland (2001)) and laser excitation line.

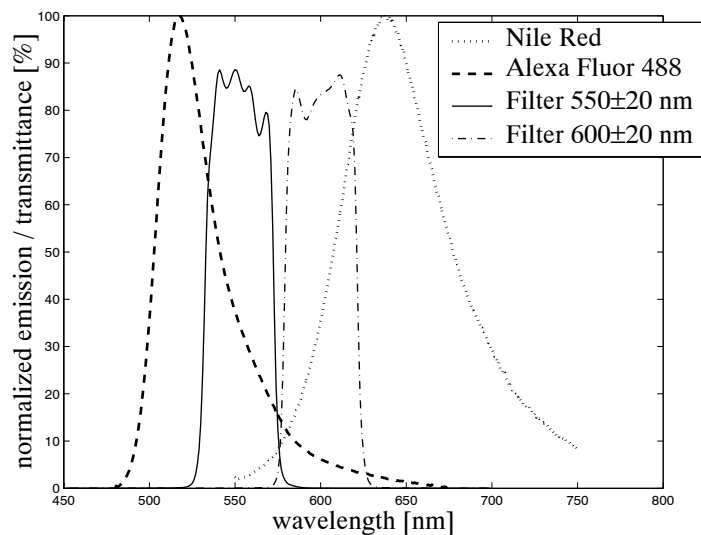


Figure 3.11: Normalized emission spectra of Alexa Fluor 488 and Nile Red (from Haugland (2001)) and transmittance curves of optical bandpass filters. In the present application the maximal emission of Nile Red was found to be shifted to around 600 nm in accordance with Haugland (2001).

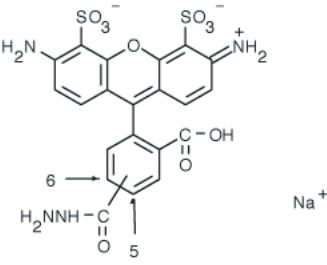
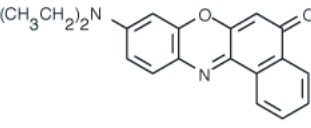
	Alexa Fluor 488	Nile Red
Molecular Formula	$C_{21}H_{15}N_4NaO_{10}S_2$	$C_{20}H_{18}N_2O_2$
Molecular Weight	570.48	318.37
Structure		

Table 3.4: Molecular properties of fluorescent dyes (from Haugland (2001)).

3.7 Summary and conclusions

In the present chapter the configuration and functionality of an experimental method for the measurement of flow and transport in porous media has been described. The high performance of this method has been accomplished by the following two major achievements:

- The composition of capable devices for the spatially and temporally highly resolved measurement of the local dye concentrations in a 3D flow cell using laser-induced fluorescence. The system is able to measure $1300 \times 600 \times 100$ local concentrations every 30 s.
- The selection of an appropriate set of solids, liquids and fluorescent dyes for the formation of a transparent and optically homogeneous porous medium. The availability of two immiscible liquids with the same refractive index, and two corresponding fluorescent dyes which are each soluble in only one of these liquid phases, allows for the investigation of two-phase flow in porous media. Due to the availability of two different solid materials it is possible to study the influence of solid-liquid interactions on the dye transport.

Together with the method for the precise matching of refractive indices described in chapter 4, these capabilities result in the high qualification of the presented technique for the investigation of flow and transport in porous media on different scales.

Chapter 4

Method for precise index matching

4.1 Introduction

The spatial precision of the measured data is mainly determined by the amount of refraction caused by mismatched refractive indices of solid and liquid(s), and it is therefore necessary to match these indices as close as possible. Due to the differences in optical dispersion of each phase, the refractive indices can be matched at only one wavelength. This chapter describes a method which was used for the highly precise matching of the refractive indices at a given wavelength. The method has already been used for a long time in materials science for the characterization of the homogeneity of glass and was successfully adopted for the present application. In the next section the fundamental principles of light propagation in a porous medium with transparent solid and liquid phases are described, including some historical notes based on the comprehensive review Hense (1987). Section 4.3 then presents the experimental technique used in this work. The chapter is finished by a summary and conclusions given in section 4.4.

4.2 Light propagation in transparent porous media

In 1884 the danish physicist Christian Christiansen published a paper (Christiansen (1884) cited by Hense (1987)) where he demonstrated the behaviour of immersed plate glass grains in a benzene-CS₂ mixture of the same refractive index as the glass. He correctly explained the effect that the powder became indistinguishable from the mixture and simultaneously the whole system became coloured by the different dependence of the refractive indices of the liquid and the glass on wavelength.

The same effect occurs in the index-matched porous media used in this work: The dispersion curves of the liquids shown in figure 3.6 are changed by variation of mixing ratio or solute weight percentage so that the refractive indices match at one certain wavelength. Light with a different wavelength is refracted at the solid-liquid interfaces, with the angle of refraction growing with distance from the matching wavelength. The qualitative behaviour of a white light beam passing through a porous medium is illustrated in figure 4.1. The refractive indices are matched for green light. The multiplied effect of a single sphere sketched in figure 4.1a leads to a wavelength dependent broadening of a light beam in porous media. In figure 4.1b the qualitative behaviour of a white light beam passing through a porous medium is outlined. A photograph of a porous medium corresponding to this situation, consisting of plexiglass

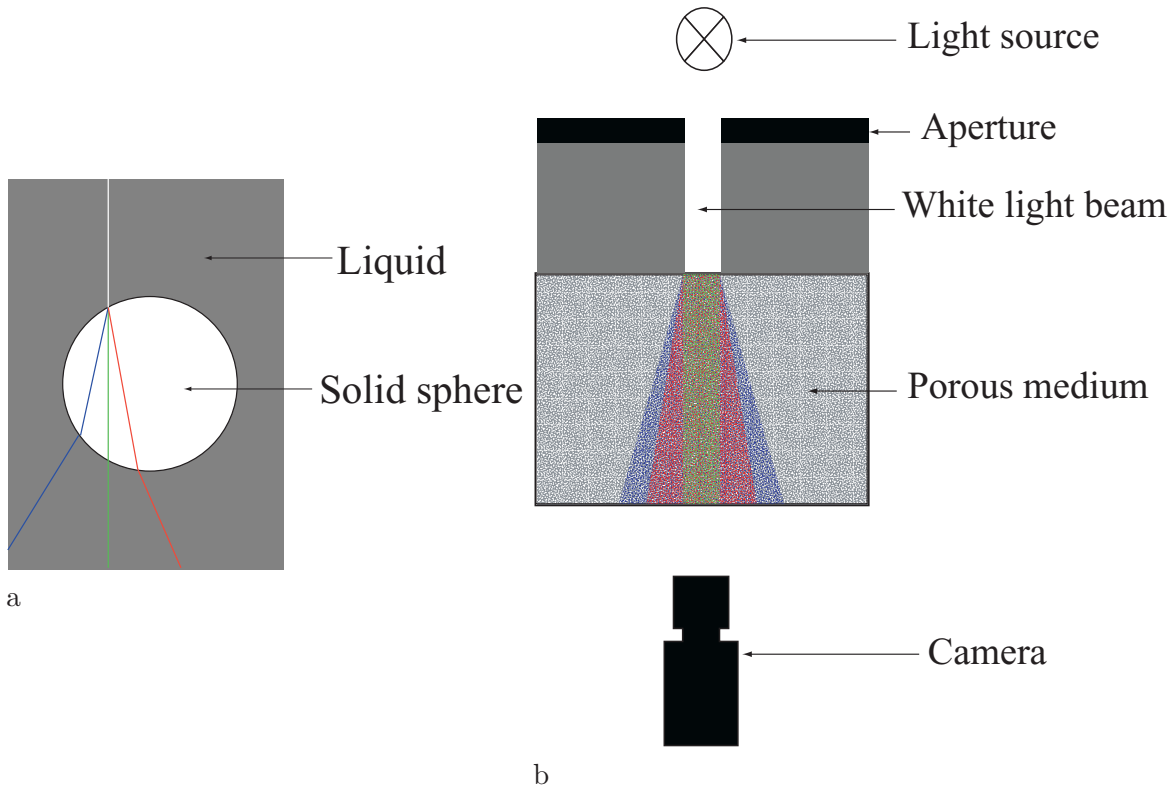


Figure 4.1: Qualitative behaviour of a white light beam passing through **a** a sphere and **b** a porous medium with the refractive indices of the solid and liquid matched for the green portion of the light.

and silicone oil matched at 550 nm, was taken with this setup and is shown in figure 4.2a. The broadening of the red and blue portion of the light beam is obvious. The porous medium shown in figure 4.2b contained plexiglass and silicone oil matched at 500 nm, so that the broadening occurs mainly in the red portion of the spectrum.

Christiansen suggested that this behaviour of light propagation in such systems makes them applicable as a band-pass filter or monochromator. He further made several other suggestions for the application of this phenomenon, which all became realized in practice, like e.g. the use as a thermometer or as a polarizer / depolarizer (using birefringent powders). He also studied the dependence of this effect on grain size, noticing that it only occurs for relatively large grains (120 μm - 600 μm), whereas a system with fine grains (10 μm - 30 μm) behaves as an optically homogeneous medium for almost the whole visible spectrum, with the refractive index given by $n = q_{\text{solid}}n_{\text{solid}} + q_{\text{liquid}}n_{\text{liquid}}$ (q_{solid} and q_{liquid} denoting the respective volume fractions). Today the Christiansen filter has been replaced by others (e.g. interference filters) in the ultraviolet and visible range, but is still used in the infrared. The main application today is the only one that Christiansen did not anticipate - the characterization of glass homogeneity.

Many efforts have been made for the theoretical description of the transmittance of a Christiansen filter as a function of wavelength, starting with a work of Strutt (later Lord Rayleigh) in 1899 (Strutt (1899) cited by Hense (1987)). Until now no formula has been derived that is valid over the whole range of the spectrum, but there is a large number of

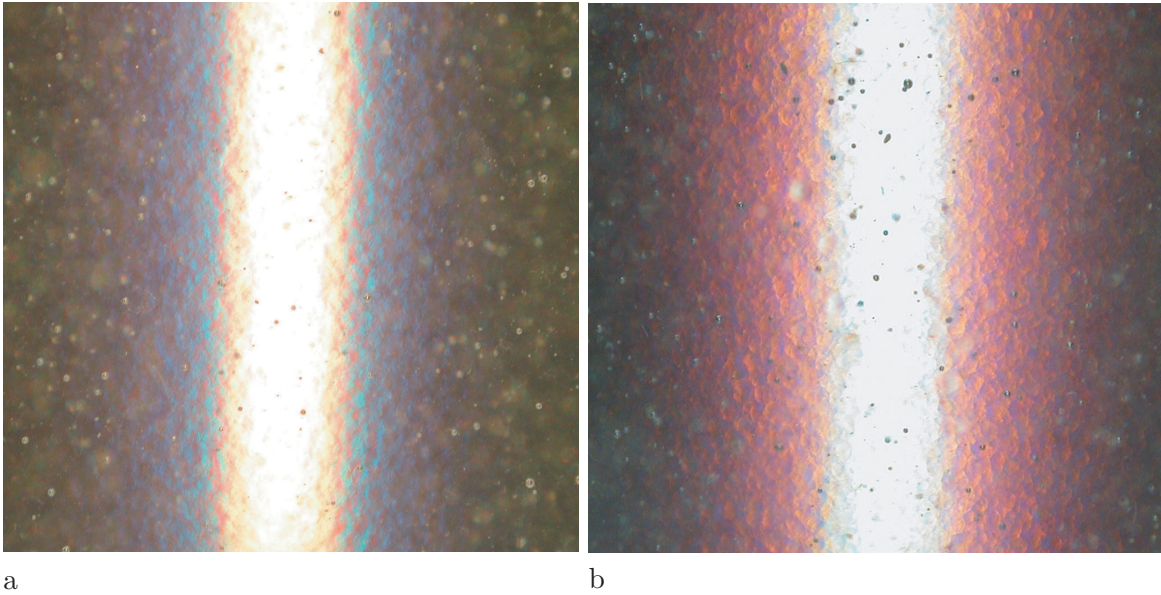


Figure 4.2: Photographs taken with the configuration shown in figure 4.1b and a porous medium consisting of plexiglass and a mixture of silicone oils whose refractive indices were matched at **a** 550 nm and **b** 500 nm. The colours of the broadened light depict the variation of light propagation for different wavelengths.

equations which are valid in a certain range of wavelengths. While the effects of wave optics (phase change and interference) become important for small sized dispersed particles and small $\Delta n = |n_{\text{solid}} - n_{\text{liquid}}|$, geometrical optics is applicable for $d \cdot \Delta n > \lambda$ (d denoting the particle size). The theories reviewed in Hense (1987) mainly differ by the use of one or a combination of these approaches. For the present application, i.e. the determination of the wavelength where the refractive indices of solid and liquid are matched, only the maximum and not the detailed shape of the transmittance curve is of interest. All theories predict the intuitively expected behaviour that the transmittance is maximal at the matched wavelength.

4.3 Experimental technique

As described in the last section, only light with one certain wavelength, where the refractive indices of solid and liquid are matched, can propagate through the medium without interference. For all other wavelengths, the propagation is modified and thus the recorded image is corrupt. This problem is addressed by the use of optical bandpass filters, which restrict the imaging to a range of approximately 40 nm (see chapter 3). In order to obtain optimal spatial accuracy for the images, the matched wavelength must coincide with the center wavelength of the bandpass filter. Therefore a HP 8453 spectrophotometer was used as shown in figure 4.3. As the broadening of the light beam increases, the screening effect of the slit leads to a decrease of light intensity on the photodiode array. Thus, the phenomena described in the last section result in transmittance curves with a maximum at the matched wavelength. As an example, the curve for two different porous media are shown in figure 4.4 together with the curve for the corresponding optical filter. For the present application this method offers the possibility to easily match the refractive indices with an accuracy of 1 nm. This corresponds

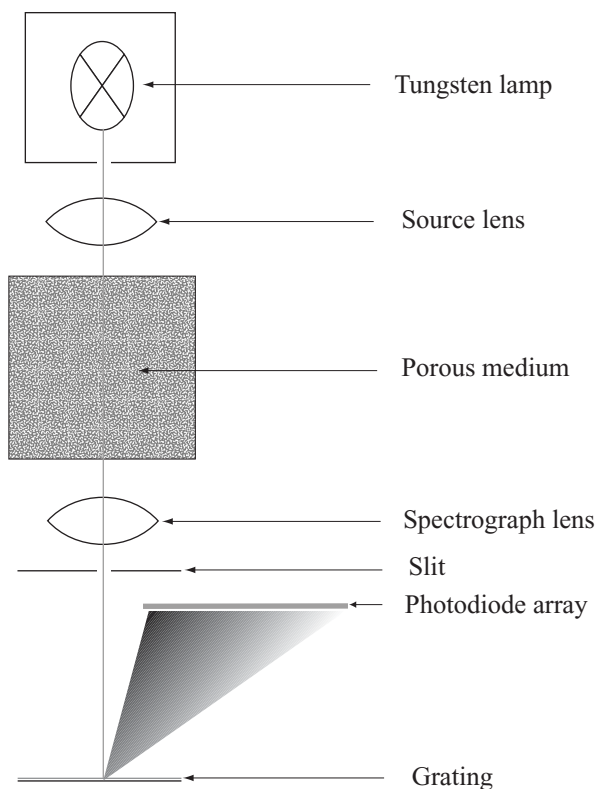


Figure 4.3: Optical system of the HP 8453 spectrophotometer used for the determination of the matched wavelength.

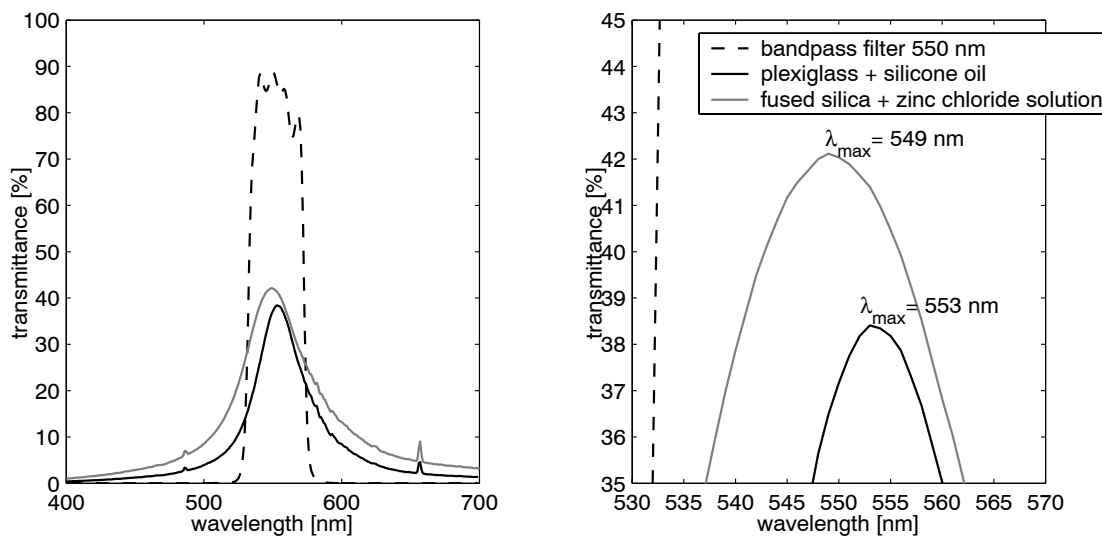


Figure 4.4: **a** Transmittance curves obtained with the setup shown in figure 4.3 for two porous media (plexiglass+silicone oil and fused silica+zinc chloride solution) matched at approximately 550 nm and for a bandpass filter with a transmittance range of $550 \pm 20 \text{ nm}$. **b** Magnified area of maximum transmittance.

to a difference in the refractive index of the liquid phase of about $5 \cdot 10^{-5}$.

Due to the different $\frac{dn}{dT}$ of the liquids (table 3.2) and solids (table 3.1), changes in temperature during the experiment must be avoided. Therefore the refractive index matching was done directly before the experiments, with all components of the flow cell being in equilibrium with room temperature ($T \approx 25^\circ C$). Although no temperature control was performed, no significant changes in the transmittance curve were found after the experiments.

4.4 Summary and conclusions

In section 4.2 the principles of light propagation in transparent porous media have been presented and their applicability to the media used in this work has been qualitatively validated. Consequently these principles have been employed in section 4.3 for the development of a method for the precise matching of the refractive indices of the solids and liquids used in the PLIF method described in chapter 3 at a certain wavelength. This easily applicable method is the basis for the high spatial resolution of the flow and transport measurements presented in this work. Furthermore the method provides the opportunity to accurately detect a possible mismatch of the refractive indices due to temperature changes.

Chapter 5

Image Preprocessing

5.1 Introduction

This chapter describes the processing of the acquired data, i.e. the digital images, in order to remove systematic and statistical errors. The first outcome of the flow measurements is a time series of 3D image stacks with 8 bits per pixel. The aim of image preprocessing is to transform this information back into a corresponding set of dye concentration values at well-defined positions inside the flow cell, which is then the basis for further evaluations. The quality of these transformations is the decisive factor for the accuracy of the final results.

The purpose of this chapter is to provide an accurate and complete presentation of the methods that lead to the results in later chapters. Its content may not be mandatory for the understanding of the final results, but for the exact traceability of the data flow in order to allow for a comparison of the results with other work in the future.

Measurement data is always subject to statistical error, caused e.g. by quantum fluctuations, which results in an uncertainty of the data characterised by its variance. Often the data is additionally modified by systematic errors, i.e. a shift between the mean value and the true value.

Both types of errors can in principle be corrected. The first approach should always be to optimise the experimental setup in terms of error minimization. Statistical errors can be reduced by repeating the measurement or by applying statistical models which exploit correlations in the data. Systematic errors can be corrected by performing a calibration before or after the measurement, or sometimes also directly out of the data.

Since the correction of systematic errors is a possible source for the introduction of artefacts, it is obligatory to quantitatively understand the physical process that leads to the error in order to find the proper correction. In particular it is not allowed to simply fit the data to any expected values. Thus any discrepancies in the results which lack explanation must not be removed.

In the following sections the individual sources of error are described followed by the method for their correction. Then the statistical errors are analysed and quantified in section 5.6. A verification of the linearity of the measurements is performed in section 5.7. In the last section the whole proceeding of image preprocessing is put together out of these individual methods.

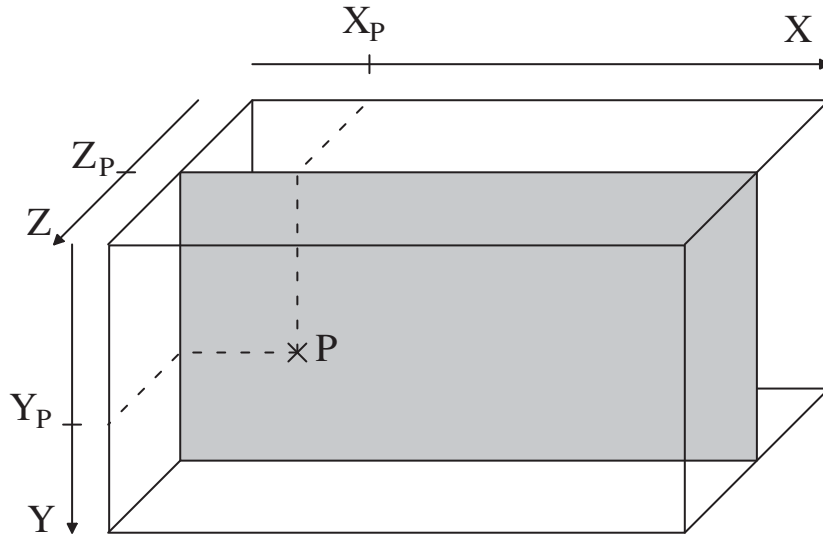


Figure 5.1: Definition of world coordinates $(X, Y, Z)^T$ inside the horizontal flow cell.

5.2 Geometric calibration

The purpose of the geometric calibration is to give a relation between the 3D world coordinates $\vec{X} = (X, Y, Z)^T$ (see figure 5.1) of the measured object and their corresponding 2D image coordinates $\vec{x} = (x, y)^T$.

$$\begin{pmatrix} x \\ y \end{pmatrix} = \vec{f}(X, Y, Z) \quad (5.1)$$

The transformation \vec{f} from world to image coordinates typically consists of a linear projection plus additional aberrations and distortions caused e.g. by lens impairments or refractions at interfaces between media with different refractive indices. According to the experimental setup an appropriate model is chosen and the models parameters are estimated from a calibration procedure. Normally one is interested in the inverse of the transformation which is in general not available because the problem is under-determined, so additional efforts have to be made like e.g. the use of a stereo camera system.

In the present application only the part of the 3D world is visible that is illuminated by the laser sheet, which is a plane perpendicular to the optical axis (see figure 5.2). Thus the transformation \vec{f}_Z for a given Z position of the laser sheet goes from 2D world to 2D image coordinates:

$$\begin{pmatrix} x \\ y \end{pmatrix} = \vec{f}_Z(X, Y) \quad (5.2)$$

It is composed of a refraction at the glass-air interface of the flow cell and a projection by the camera optics. For small angles θ the snellius law $n_{\text{air}} \sin \theta_{\text{air}} = n_{\text{glass}} \sin \theta_{\text{glass}}$ can be approximated by $n_{\text{air}} \theta_{\text{air}} = n_{\text{glass}} \theta_{\text{glass}}$ (see figure 5.2). For common camera lenses aberrations can be neglected so the resulting transformation is linear

$$\begin{pmatrix} x \\ y \end{pmatrix} = \begin{pmatrix} a_{xx}(Z) & 0 \\ 0 & a_{yy}(Z) \end{pmatrix} \begin{pmatrix} X \\ Y \end{pmatrix} + \begin{pmatrix} b_x(Z) \\ b_y(Z) \end{pmatrix} \quad (5.3)$$

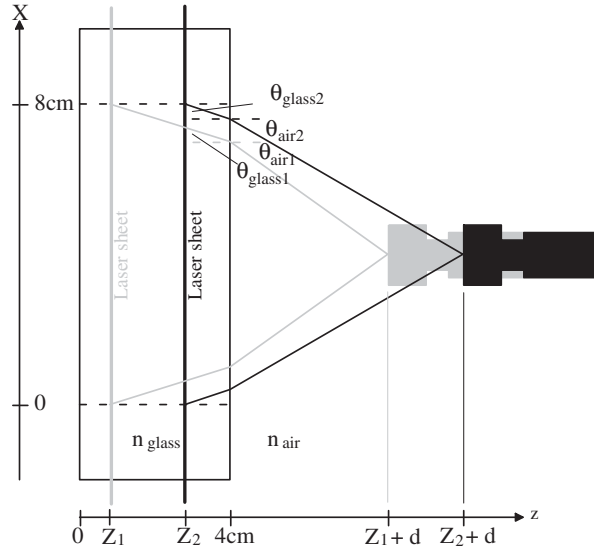


Figure 5.2: Image distortion for two different Z caused by the glass-air interface.

and thus the requested inverse transformation is given by:

$$\begin{pmatrix} X \\ Y \end{pmatrix} = \begin{pmatrix} \frac{1}{a_{xx}(Z)} & 0 \\ 0 & \frac{1}{a_{yy}(Z)} \end{pmatrix} \begin{pmatrix} x - b_x(Z) \\ y - b_y(Z) \end{pmatrix} \quad (5.4)$$

The matrix elements $a_{xy}(Z)$ and $a_{yx}(Z)$ have been set to zero since the camera is mounted so that the (x, y) and (X, Y) axes are orthogonal. The third world coordinate Z is given by the position of the translation stage z :

$$Z = (z - 1)\Delta Z, \quad z = 1 \dots n_z, \quad (5.5)$$

with n_z and ΔZ denoting the number of steps and the stepwidth.

Consequently the task of geometric camera calibration is to find the parameters $\vec{p}(z) = (a_{xx}(z), a_{yy}(z), b_x(z), b_y(z))^T$ for every position z . Even though the Z -distance d between the laser sheet and principal plane of the camera optics is constant, the optical paths change with the distance between the laser sheet and the air-glass interface (see figure 5.2) and for this reason also the parameters $\vec{p}(z)$ depend on Z .

Since it is not practicable to introduce any calibration target into the flow cell, for the determination of the parameters $\vec{p}(z)$ advantage was taken of the finding that the area between the grids appears slightly brighter than the areas outside (mostly due to small concentrations of uniformly distributed dye or scattering at impurities). In order to enhance the contrast between the inner and outer area the volume images for all times of a sequence were summed up. Then for every Z the left, right, lower and upper boundaries ($x_l(z), x_r(z), y_u(z)$ and $y_l(z)$) of the inner area were chosen at the position of maximum gradient. This is exemplified in figure 5.3. To further reduce noise, the boundary positions $\bar{x}_l(z), \bar{x}_r(z), \bar{y}_u(z)$ and $\bar{y}_l(z)$ were approximated by a straight line as shown in figure 5.4. Subsequently the images for $z > 1$ were stretched so that the lines are parallel to the Z axis and the parameters $\vec{p}(z) = \vec{p}(1)$ are constant over Z . Finally the parameters a_{xx}, a_{yy}, b_x and b_y can be evaluated to associate these

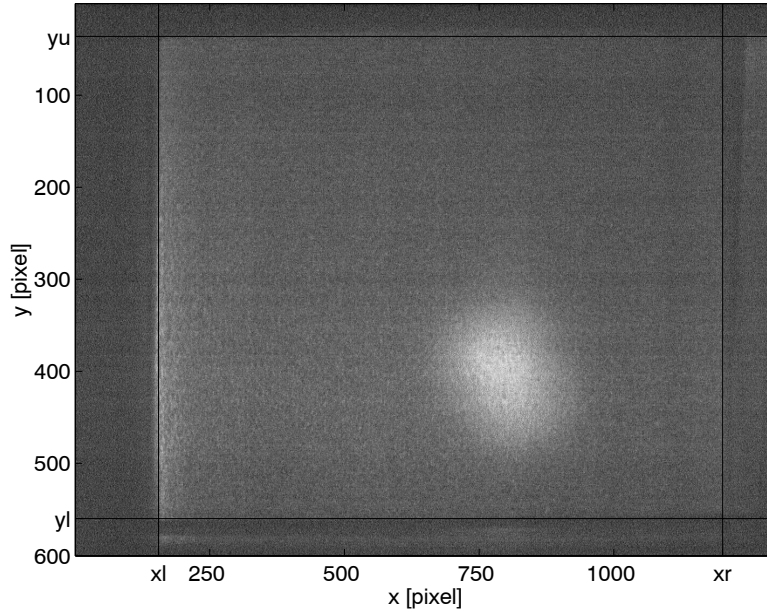


Figure 5.3: Determination of the flow volume boundaries x_l , x_r , y_u and y_l for a single z-image.

lines to their corresponding world coordinates $X=0\text{cm}$, $X=8\text{cm}$, $Y=0\text{cm}$ and $Y=4\text{cm}$:

$$a_{xx} = \frac{\bar{x}_r(1) - \bar{x}_l(1)}{8\text{cm}}, b_x = \bar{x}_l(1), a_{yy} = \frac{\bar{y}_l(1) - \bar{y}_u(1)}{4\text{cm}}, b_y = \bar{y}_u(1). \quad (5.6)$$

5.3 Brightness correction

This section deals with the relation between the emitted light intensity $I(X, Y, Z, t)$ and the dye concentration $c(X, Y, Z, t)$. For sufficiently low excitation light intensities (below saturation) $s(X, Y, Z, t)$ these quantities are related linearly through a constant of proportionality k :

$$I(X, Y, Z, t) = k \cdot s(X, Y, Z, t) \cdot c(X, Y, Z, t) \quad (5.7)$$

Thus for a correct determination of $c(X, Y, Z, t)$ from measured $I(X, Y, Z, t)$ it is necessary to know the spatial distribution of $s(X, Y, Z, t)$. The constant k is mainly a function of the sampling volume and the quantum efficiency. As we do not aim at measuring absolute concentrations, we set $k = 1$. The objective of the experimental design is to make the illumination $s(X, Y, Z, t)$ as uniformly distributed as possible. Nevertheless there are some effects that can hardly be avoided:

- the laser light intensity is unequally distributed in X-direction because the waveform of the galvanometer scanner is not perfectly triangular
- the light intensity decreases while passing through the medium due to scattering at small bubbles or impurities

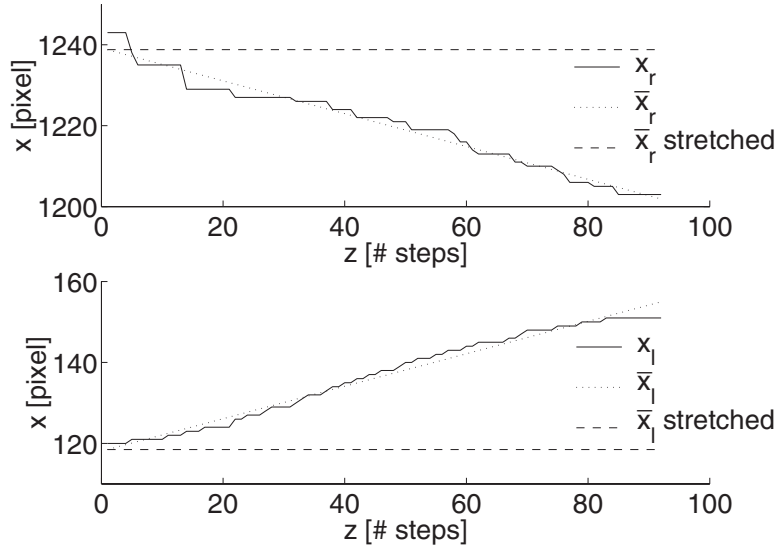


Figure 5.4: Variation of x_l and x_r for different z (solid lines), after fitting a straight line (dotted lines) and after image stretching (dashed lines).

- while the illumination itself is constant for different Z , two phenomena provoke a decrease of the measured intensity with increasing Z .

Firstly, with increasing Z an increasing amount of emitted light is reflected at the air-glass interface (see figure 5.5a). This is due to the fact that, for a given X_1 , θ_{air} and θ_{glass} are decreasing with increasing Z . As a result, also the angular-dependent transmittance $T = \frac{I_{\text{trans}}(\theta_{\text{glass}}, \theta_{\text{air}})}{I_{\text{inc}}}$ for the respective polarisation

$$T_{\parallel} = \frac{I_{\text{trans}\parallel}}{I_{\text{inc}\parallel}} = \frac{2n_{\text{glass}} \cos \theta_{\text{glass}}}{n_{\text{glass}} \cos \theta_{\text{air}} + n_{\text{air}} \cos \theta_{\text{glass}}} \quad (5.8)$$

$$T_{\perp} = \frac{I_{\text{trans}\perp}}{I_{\text{inc}\perp}} = \frac{2n_{\text{glass}} \cos \theta_{\text{glass}}}{n_{\text{glass}} \cos \theta_{\text{glass}} + n_{\text{air}} \cos \theta_{\text{air}}} \quad (5.9)$$

is decreasing with increasing Z .

Secondly, the element of solid angle subtended by the camera optics $\Omega(Z)$ is decreasing with increasing Z as illustrated in figure 5.5b. Since the measured intensity is proportional to Ω , it decreases in the same manner.

A numerical computation of these phenomena considering the geometrical proportions of the setup and integrating over the (X, Y) -plane resulted in an approximately linear decrease for the normalised nonpolarised light transmittance $f_{\text{trans}} = \frac{T(z)}{T(1)}$ as well as for the normalised solid angle $f_{\Omega} = \frac{\Omega(z)}{\Omega(1)}$. As shown in figure 5.6, the effect due to the solid angle exceeds the effect of transmissivity by far.

- the temporal behaviour of the laser light intensity is characterised by short-time fluctuations as well as slow shifts of the mean intensity (e.g. due to temperature changes).

As these effects apparently don't have any interactions, they can be separated:

$$s(X, Y, Z, t) = s_X(X) \cdot s_Y(Y) \cdot s_Z(Z) \cdot s_t(t) \quad (5.10)$$

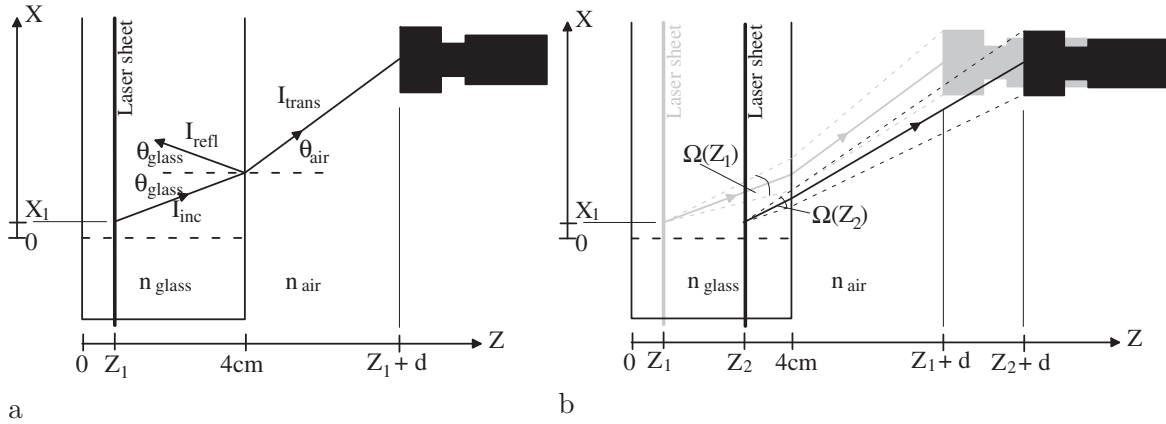


Figure 5.5: Two effects caused by the glass-air interface resulting in a Z -dependence of the measured light intensity: (a) variation of $I_{\text{trans}}(Z)$ with $\theta_{\text{glass}}(Z)$ and $\theta_{\text{air}}(Z)$ (b) variation of solid angle $\Omega(Z)$.

In the following subsections the correction for the spatial distribution and the temporal behaviour, and a check of the linearity assumed in equation `refeqillumlin` are described.

5.3.1 Correction of spatial inhomogeneity

For the determination of the spatial distribution advantage was taken of the presence of small bubbles and impurities inherent in the bead packing. Under the assumption that they are uniformly distributed inside the flow cell, which is legitimated by the extensive mixing of the grains before filling, the amount of scattered light is a measure of the local illumination. Therefore a volume image of the flow domain was recorded without using a bandpass filter (which would screen the scattered light) before every flow measurement. An example of such an image is shown in figure 5.7a. The volume image is then calibrated and geometrically transformed as described in section 5.2 (the geometrical calibration is particularly applicable here since it makes use of the scattered light). From the geometrically calibrated volume image the spatial distribution functions can then be obtained by averaging over the corresponding areas:

$$s_X(X) = \frac{1}{I_{\text{tot}}} \sum_{YZ} I(X, Y, Z) \quad (5.11)$$

$$s_Y(Y) = \frac{1}{I_{\text{tot}}} \sum_{XZ} I(X, Y, Z) \quad (5.12)$$

$$s_Z(Z) = \frac{1}{I_{\text{tot}}} \sum_{XY} I(X, Y, Z) \quad (5.13)$$

$$I_{\text{tot}} = \sum_{XYZ} I(X, Y, Z). \quad (5.14)$$

However, these averaged distributions are still characterised by individual peaks at the positions of the scattering particles and therefore deserve further smoothing. The x - and y -distributions were smoothed using cubic smoothing splines (see Green & Silverman (1994) and appendix A) as shown in figure 5.7b,c. As described above, a linear decrease of $s_z(z)$ is expected, and consequently the z -distribution was fitted with a straight line. This is shown

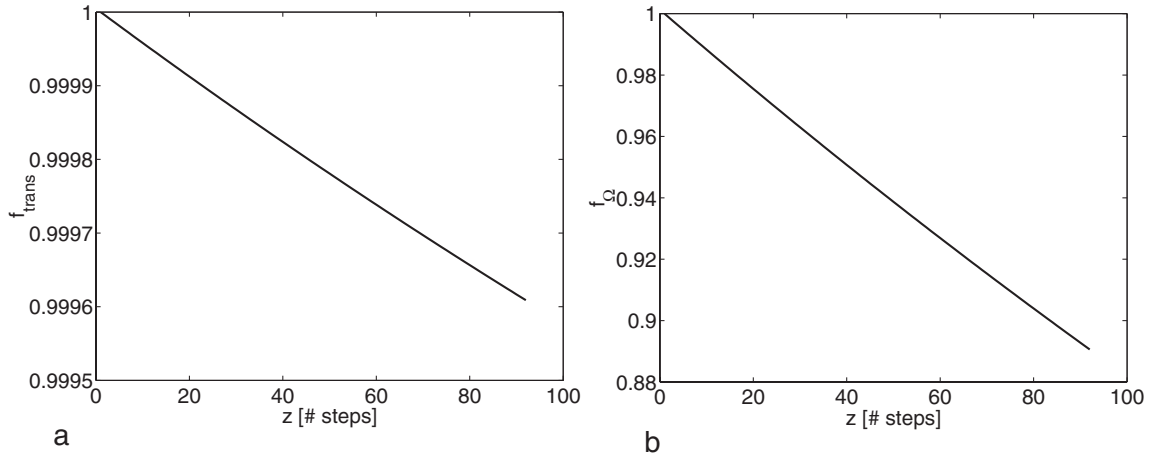


Figure 5.6: Computational results of the decrease in measured light intensity caused by the effects shown in figure 5.5: **a** variation of transmittance and **b** variation of solid angle.

in figure 5.7d together with the above explained numerically simulated result $s_{z,\text{sim}}(z) = f_{\text{trans}}(z)f_{\Omega}(z)$ from figure 5.6, showing a very good consistency. Finally the correction is done by the division

$$c''(X, Y, Z, t) = \frac{I(X, Y, Z, t)}{s_X(X)s_Y(Y)s_Z(Z)}, \quad (5.15)$$

where $c''(X, Y, Z, t) = c(X, Y, Z, t)s_t(t)$ still has to be corrected for the temporal variations, which is described in the next section.

5.3.2 Correction of temporal variations

The laser was found to exhibit temporal light intensity variations. These variations appeared on all timescales from μs to hours. Typically the long-time variations after activation of the laser are characterised by a rapid rise of the light intensity followed by a slow decay. In figure 5.8 the grayvalue timesequences of different pixels in an image where a static object was illuminated with laser light. The transition from rise to decay after about 1 hour and also additional short-time variations are evident. Furthermore, intensity variations can be caused by manual changes of the laser intensity. In the experimental setup employed a volume image was taken every 30 seconds. Thus, every variation taking longer than 30 seconds was considered as a long-time variation $\bar{s}_t(t_i)$, and the faster variations as short-time variations or noise ε_s :

$$s_t(t_i) = \bar{s}_t(t_i) + \varepsilon_s, i = 1..n_t \quad (5.16)$$

with $\langle \varepsilon_s \rangle = 0$.

Correction of long-time variations

The value of the long-time variation $\bar{s}_t(t_i)$ can then be calculated out of the data with use of the assumption that the total amount of concentration inside the flow cell remains constant over time, what can be expected since the dyes are photostable and inert. Then we can attribute every change of the volumetric concentration sum to a change of laser light intensity and thus

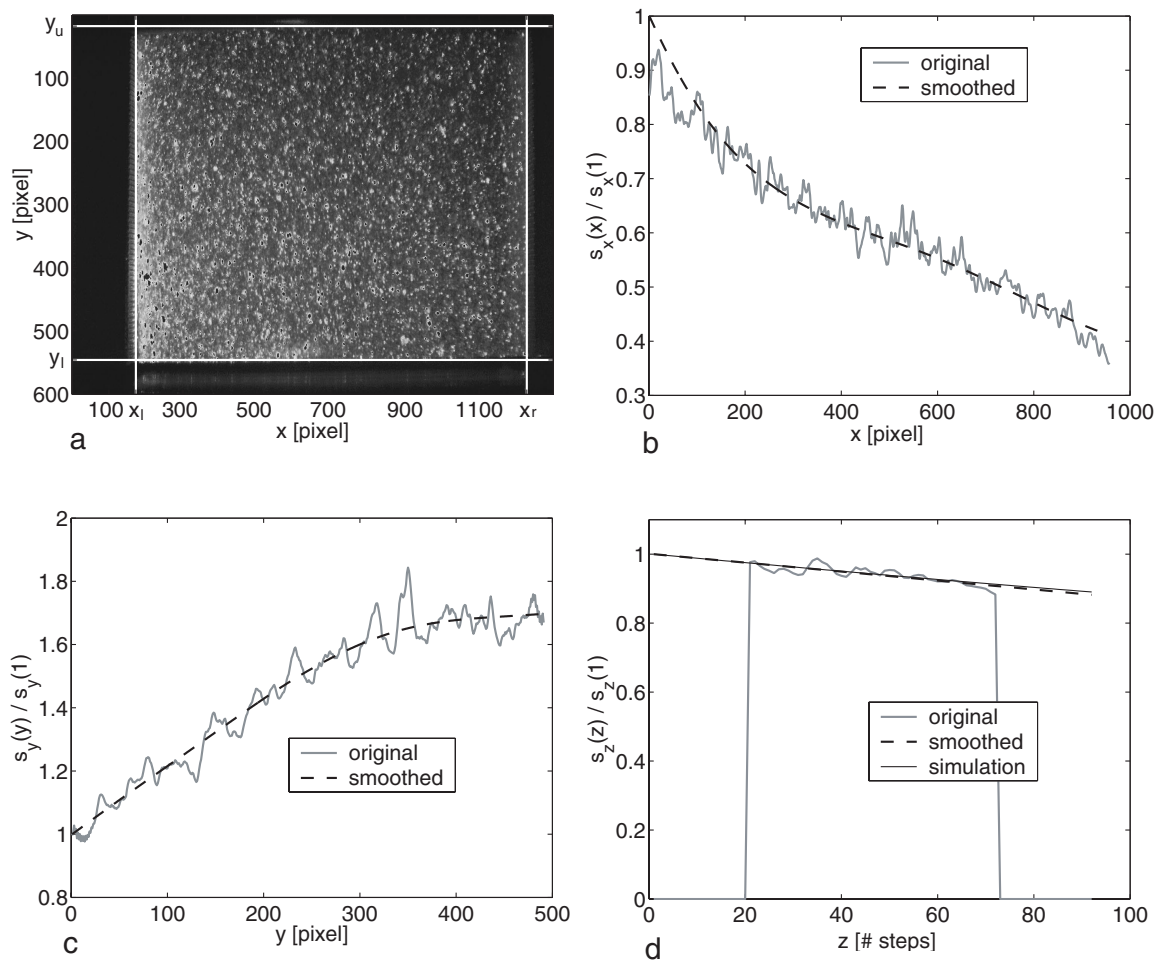


Figure 5.7: **a** Distribution of scattered light intensity in a x-y-plane **b,c** original and smoothed distributions of scattered light intensities in x and y direction, respectively **d** original, smoothed and simulated distributions of scattered light intensity in z direction.

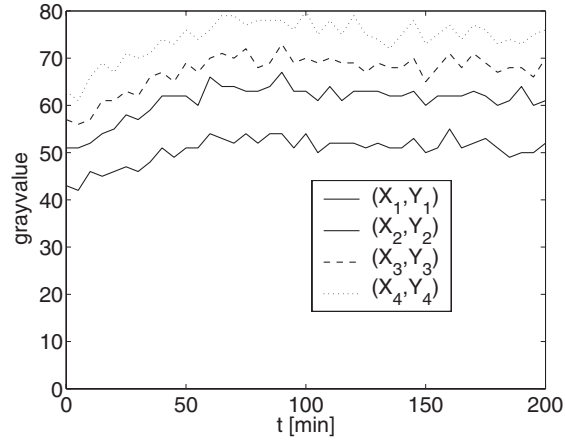


Figure 5.8: Temporal grayvalue changes in a time series of images of a static object illuminated with an argon ion laser (for four different pixel), indicating a change of laser light intensity.

calculate $\bar{s}_t(t_i)$ by spatial averaging over the flow cell volume (which is actually a temporal averaging over the 30s volume acquisition time due to the sequential acquisition):

$$\bar{s}_t(t_1) = 1, \bar{s}_t(t_i) = \frac{\sum_{klm} c''(X_k, Y_l, Z_m, t_i)}{\sum_{klm} c''(X_k, Y_l, Z_m, t_1)}, k = 1..n_x, l = 1..n_y, m = 1..n_z, i = 2..n_t \quad (5.17)$$

For normalisation $\bar{s}_t(t_1) = 1$ was chosen. Figure 5.9a shows $\bar{s}_t(t)$ for an experiment without any manual intensity changes, indicating a similar behaviour as the static object in figure 5.8. Figure 5.9b shows an experiment with a manual change of laser light intensity at $t = 248$ min. The normalised concentration $c'(X, Y, Z, t)$ after correction for the long-time variations is given by

$$c'(X, Y, Z, t) = \frac{c''(X, Y, Z, t)}{\bar{s}_t(t)}. \quad (5.18)$$

The effect of this correction is exemplified for both experiments in figure 5.9c,d.

Correction of short-time variations

After the correction for the long-time variations, the signal $c'(X, Y, Z, t)$ is still contaminated with short-time fluctuations and also camera noise (see section 5.5). In order to remove them, an appropriate smoothing filter has to be selected. Since we don't want to make any restrictive a priori assumption of an explicit parametric model here, a nonparametric model known as cubic smoothing splines was applied. The details of this filter are described in appendix A. Then the concentration $c(X, Y, Z, t)$ is given by

$$c(X, Y, Z, t) = h(c'(X, Y, Z, t)), \quad (5.19)$$

where h denotes the smoothing filter. The effect of smoothing is depicted in figure 5.9e,f.

5.4 Correction of scanning time shift

In PLIF a volume image is not recorded simultaneously, but by a consecutive displacement of the laser plane in the Z -direction. Thus the parts of the volume with different Z are recorded

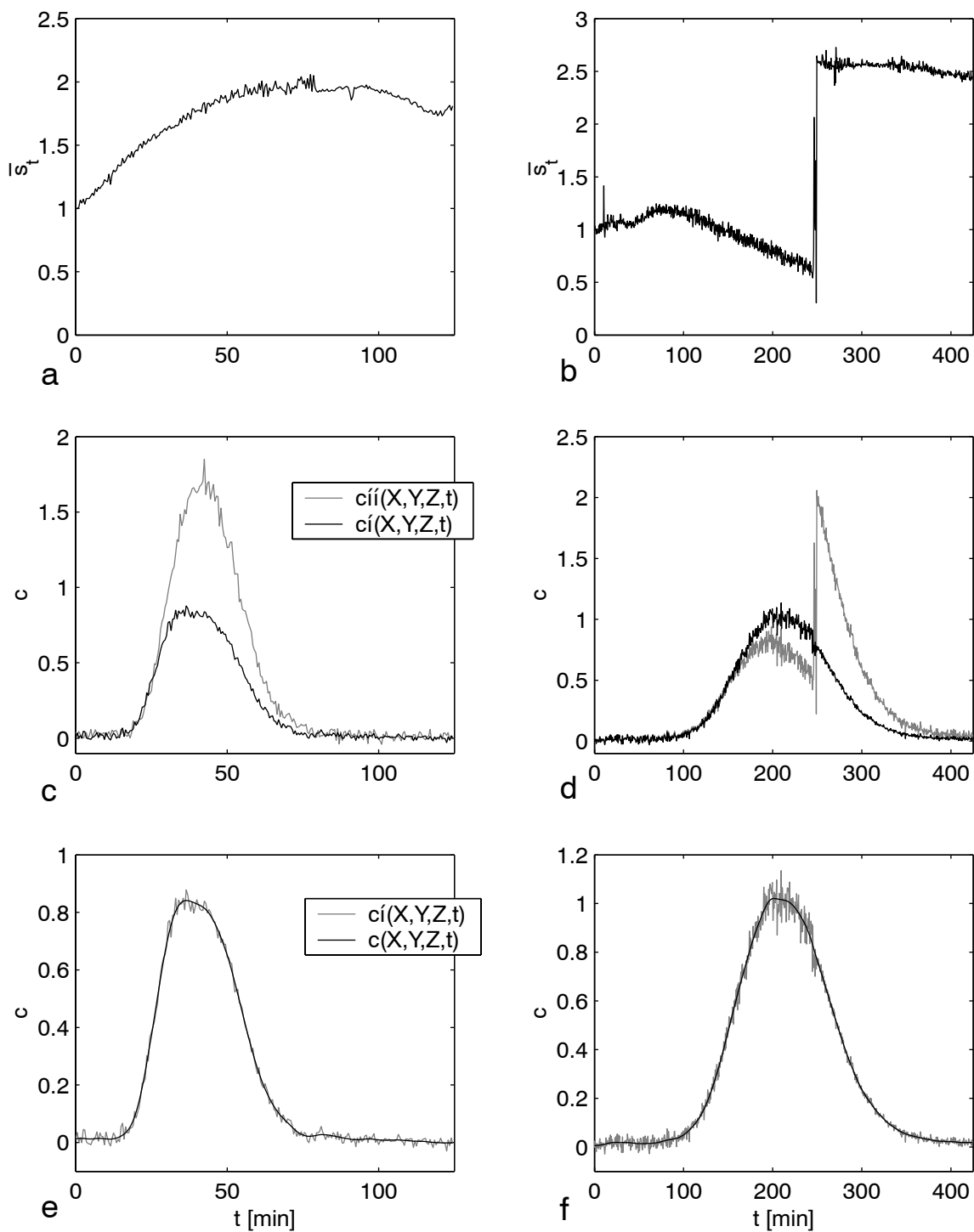


Figure 5.9: Correction of the temporal variation of concentration $c(X, Y, Z, t)$ at fixed positions (X, Y, Z) for two different experiments: **a,b** long-time variation $\bar{c}_t(t)$, **c,d** concentrations $c''(X, Y, Z, t)$ before and $c'(X, Y, Z, t)$ after correction for long-time variation, **e,f** concentrations $c'(X, Y, Z, t)$ before and $c(X, Y, Z, t)$ after correction for short-time variation

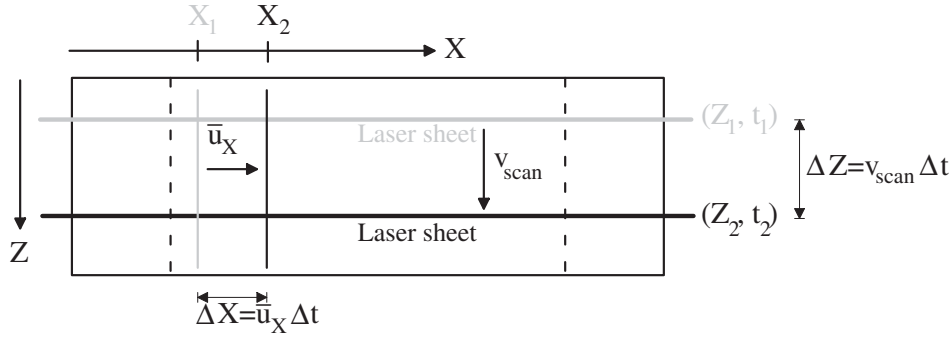


Figure 5.10: Effect of scanning time shift.

later with growing Z , as shown in figure 5.10. The relation between the scanning time t_Z at a position $Z > 0$ and the scanning time t_0 at $Z = 0$ is given by

$$t_Z = t_0 + \frac{Z}{v_{\text{scan}}}, \quad (5.20)$$

where v_{scan} is the scanning velocity of the translation stage. In order to relate all measurements for different Z to the same time t_0 , the respective timeseries have to be shifted by

$$\Delta t(Z) = -\frac{Z}{v_{\text{scan}}}. \quad (5.21)$$

v_{scan} is typically $\frac{4 \text{ cm}}{14 \text{ s}} \approx 0.29 \frac{\text{cm}}{\text{s}}$. Since the timeseries $c(X, Y, Z, t)$ are available as continuous spline functions (see appendix A), this is simply done by a resampling at the shifted times. Figure 5.11a shows an example of this correction for a point at $(X_0, Y_0, Z = 24 \text{ mm})$ and $\Delta t = 24 \text{ mm} \cdot \frac{14 \text{ s}}{40 \text{ mm}} = 8.4 \text{ s}$. Whereas $\Delta t(Z)$ is constant for experiments with different flow rates, the resulting shift in X -direction

$$\Delta X(Z) = \bar{u}_X \Delta t(Z) \quad (5.22)$$

is proportional to the mean X -velocity in the liquid phase \bar{u}_X . In figure 5.11b the resulting X -shift for the experiment in figure 5.11a with $\bar{u}_X = 0.032 \frac{\text{mm}}{\text{s}}$, $\Delta X = 0.032 \frac{\text{mm}}{\text{s}} \cdot 8.4 \text{ s} = 0.27 \text{ mm}$ is shown in form of Y -Sum at $Z = 24 \text{ mm}$ and $t = 1020 \text{ s}$, $\sum_i c(X, Y_i, 24 \text{ mm}, 1020 \text{ s})$.

5.5 Radiometric camera calibration

In this section the relation between incident light intensity $I(x, y)$ and grayvalue output $g(x, y)$ of the CCD camera is investigated and the origin and correction of systematic errors are described. The camera electronics consists of three major components as described in Basler: sensor, amplifier and ADC (Analog Digital Converter). The sensor output provides a voltage signal which is then amplified and converted to a digital output signal. By adjusting gain and offset of the amplifier, the CCD sensor signal can be shaped to optimally match the ADC input voltage range for a given application as shown in figure 5.12. The characteristic curve is guaranteed to be linear for a certain range of light intensity and gain. Then, the relation between grayvalue g and light intensity I can be described by:

$$g = g_0 + \alpha \eta \tau_{\text{exp}} I, \quad (5.23)$$

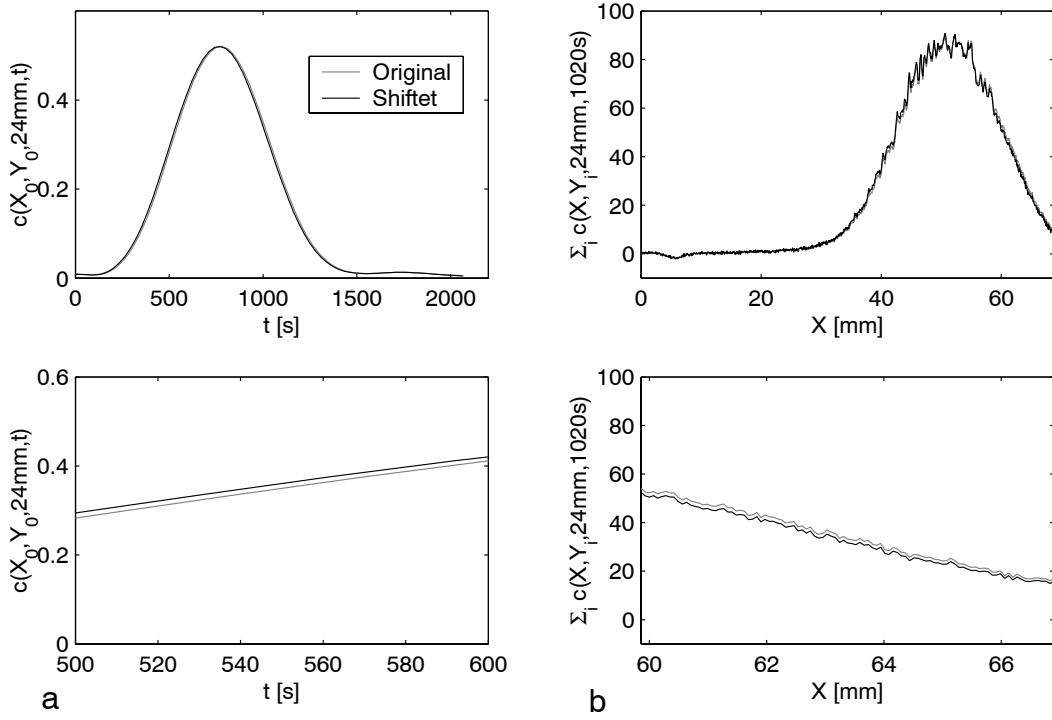


Figure 5.11: Correction of scanning time shift in **a** t -direction and **b** X -direction.

with η denoting the quantum efficiency, α the amplification factor, τ_{exp} the exposure time and g_0 a constant offset. However, there are some effects resulting in statistical and systematic errors:

- The grayvalue is contaminated with additive CCD chip noise, stemming from mainly these sources: thermal noise (can be avoided by cooling the chip), photon noise and electronics noise (e.g. amplifier). Therefore the variance of g is the sum of a constant σ_0^2 (mainly due to thermal noise) and a contribution due to photon and electronics noise which grows linearly with I and quadratically with α (see e.g. Jähne (2002)):

$$\sigma_g^2 = \sigma_0^2 + \alpha^2 \eta \tau_{\text{exp}} I \quad (5.24)$$

- CCD chips typically exhibit blooming effects, i.e. charges spilling out into surrounding pixels. Even though the employed CCD chip features special anti-blooming circuits which reduce this effect by a factor of at least 100 (Basler), the effect was still found to be considerable. As an example, figure 5.13 shows the average of 460 images of a LED in a dark environment. The effect of blooming is appearing evidently in the right image with the zoomed grayvalue range in the form of a horizontal bar beneath the LED.
- The grayvalue offset g_0 in equation 5.23, mainly caused by the generation of thermal electrons, is found to be a non-uniform distribution $g_0(x, y)$. The shape of this dark signal non-uniformity is shown in figure 5.14a. As can be seen from figure 5.13b, its amplitude is approximately comparable to that of the blooming. Figure 5.14b shows

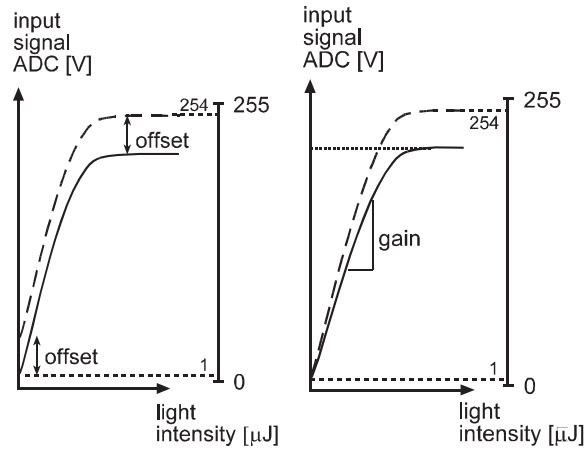


Figure 5.12: Effect of the amplifier: offset and gain (from Basler (1998)).

that the mean amplitude of the dark signal is increasing with time, probably due to a rise of temperature.

For the correction of these effects, the following methods were used:

- At first, the images were corrected for non-uniform dark signal $g_0(x, y)$ by the subtraction of an averaged dark image $\overline{g_0}(x, y)$:

$$g(x, y) \rightarrow g(x, y) - \overline{g_0}(x, y) \quad (5.25)$$

This dark image was obtained as the mean of a sequence of typically 500 dark images which were recorded before the experiments. Figure 5.14a shows an example of an averaged dark image, and figure 5.15a shows the LED image from figure 5.13 after the dark signal correction. From now on, the image data is no more represented as 8-bit values but as double-precision floating-point numbers.

- Next the effect of blooming is corrected. To this end the image area of the camera was chosen to be slightly larger than the flow cell, with the left part of the image (approximately 50 pixel) recording a dark background. Then, the blooming correction is done by the subtraction of the mean of left 50 pixels:

$$g(x, y) \rightarrow g(x, y) - \frac{1}{50} \sum_{i=1}^{50} g(x_i, y) \quad (5.26)$$

Figure 5.15b shows this correction for the LED image in figures 5.15a and 5.13.

- Finally the image data is still contaminated with additive noise. This statistical error is carried through the following geometric calibration and is then corrected together with other statistical errors as described in section 5.3.2.

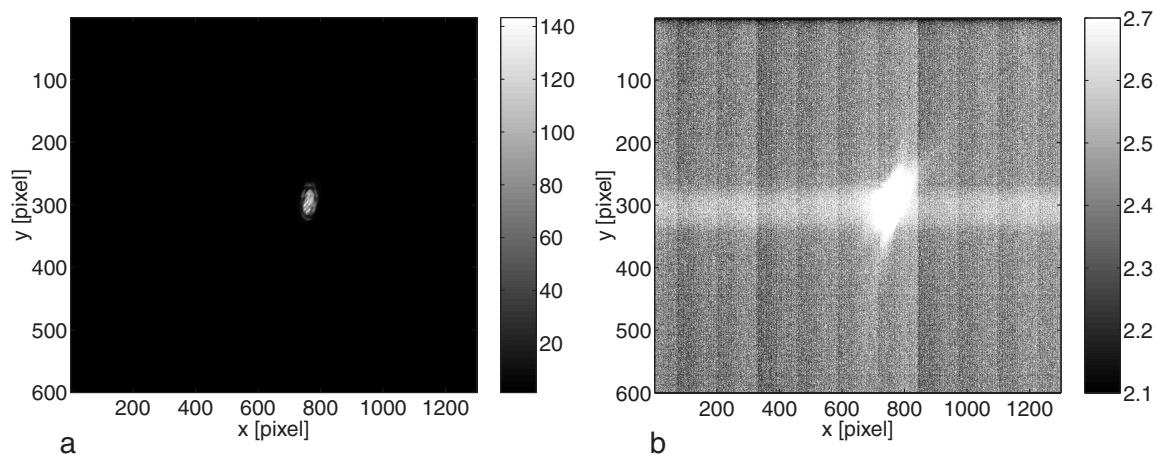


Figure 5.13: Blooming in the image of a LED on a dark background: **a** full grayvalue range and **b** zoomed grayvalue range exhibiting the dark signal and blooming.

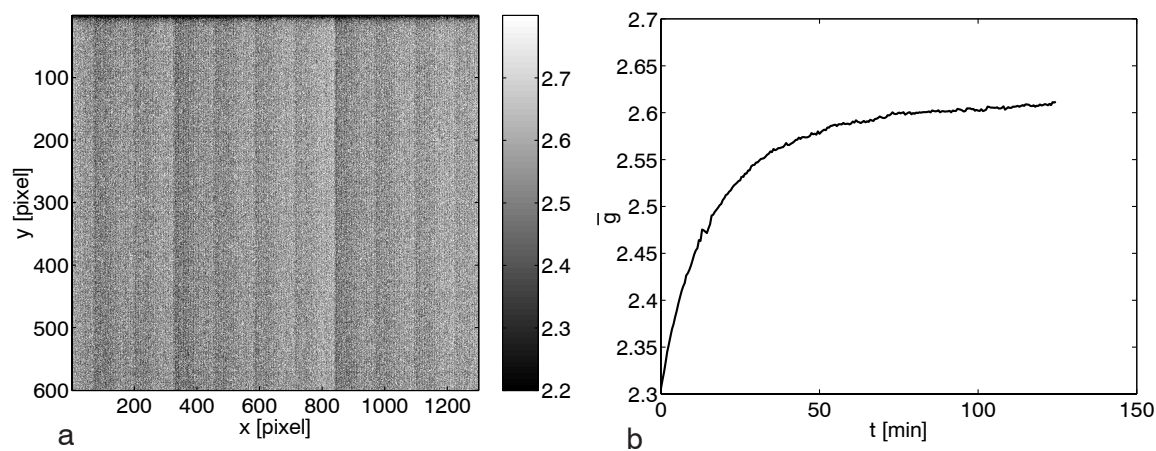


Figure 5.14: **a** Dark image $g_0(x, y)$ in a zoomed grayvalue range and **b** mean amplitude of the dark image \bar{g}_0 as a function of time.

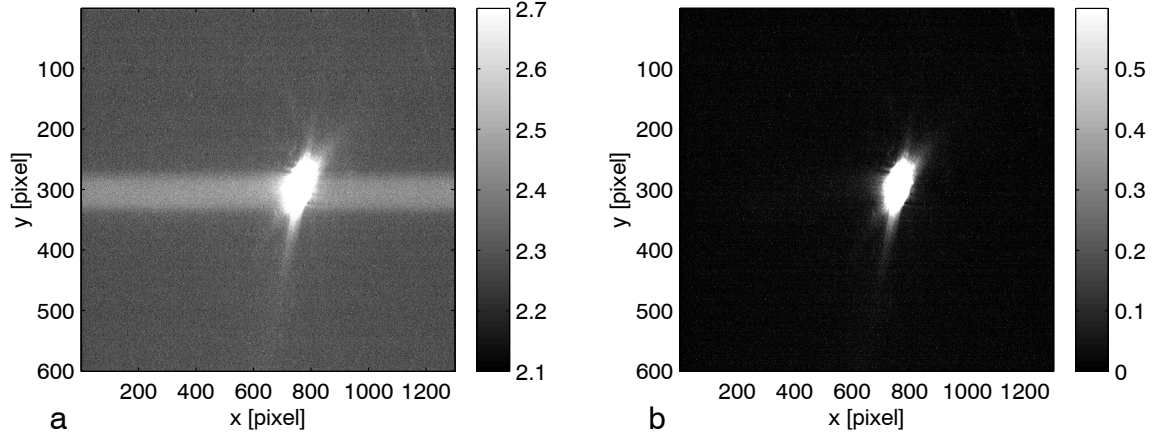


Figure 5.15: Correction of the LED image in figure 5.13: **a** for dark signal and **b** for blooming.

5.6 Analysis of statistical errors

There are two sources which induce statistical uncertainty to the measured concentrations. The first, the short-time fluctuations of laser light intensity described in section 5.3, result in a quadratic increase of the variance σ_c^2 with the normalised concentration c due to the linearity of the measurement shown in section 5.7:

$$\sigma_{c,\text{laser}}^2 = k_{\text{laser}}c^2 \quad (5.27)$$

The second source, the noise of the camera electronics (see section 5.5), results in a constant plus a linear increase of σ_c^2 :

$$\sigma_{c,\text{CCD}}^2 = \sigma_0^2 + k_{\text{CCD}}c \quad (5.28)$$

Then, the resulting variance σ_c^2 is given by the sum

$$\sigma_c^2 = \sigma_0^2 + k_{\text{CCD}}c + k_{\text{laser}}c^2, \quad (5.29)$$

with the constant σ_0^2 dominating for low and the laser light fluctuations dominating for high concentrations. In order to determine the sought parameters σ_0^2 , k_{CCD} and k_{laser} , the statistical errors have been calculated from the differences between the normalised concentrations $c'(X, Y, Z, t)$ before and $c(X, Y, Z, t)$ after the noise removal (see section 5.3.2) and plotted against c . Figure 5.16a shows the result for a sequence of 1000 images with 1000 x 500 pixel. The curve exhibits the expected quadratic progression, and the constant σ_0^2 can be read off from the limit $c \rightarrow 0$ to $\sigma_0^2 \approx 2 \cdot 10^{-4}$. Figure 5.16b shows the same data plotted as the signal-to-noise ratio $\text{SNR} = \frac{c}{\sigma_c}$. From this curve the constant k_{laser} can be read off from the limit $c \rightarrow 1$ as $1/\sqrt{k_{\text{laser}}} \approx 22.5 \rightarrow k_{\text{laser}} \approx 0.002$. The relative error $\frac{\sigma_c}{c}$ is lower than $1/20 = 5\%$ for $c > 0.4$.

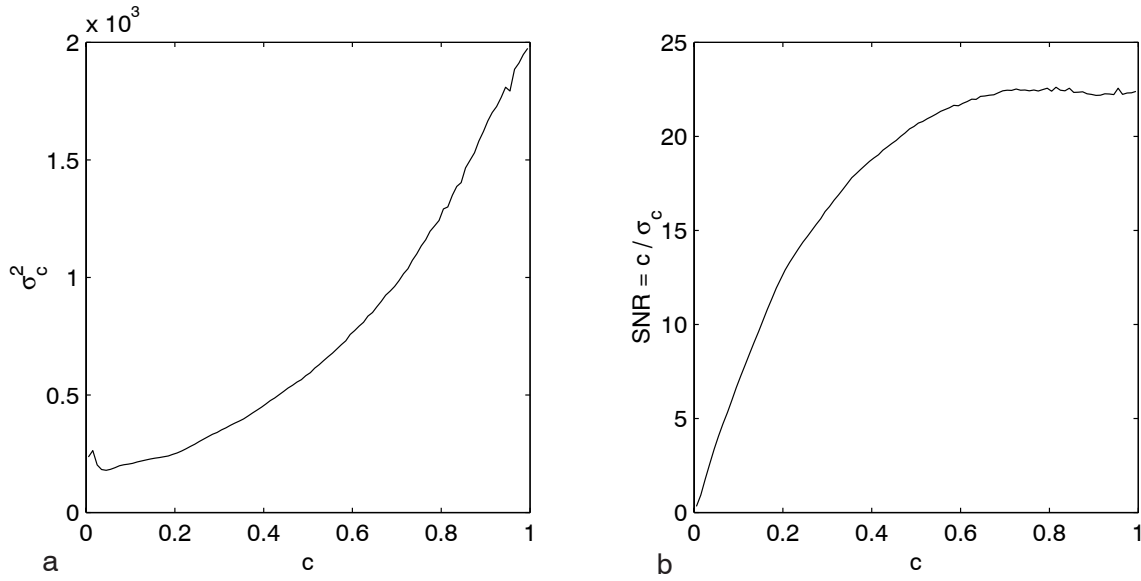


Figure 5.16: Statistical error for the measurement of normalised concentration: **a** Increase of variance σ_c^2 with c and **b** increase of the signal-to-noise ratio with c .

5.7 Verification of the linearity between laser intensity and fluorescence emission

With the present technique the result of a measurement of the local concentration $c(X, Y, Z, t)$ is an 8-bit grayvalue $g(x, y, z, t)$. In the previous sections the inverse transform from $g(x, y, z, t)$ to $c(X, Y, Z, t)$ (except for a constant of proportionality) was described. For this transformation the following assumptions of linearity were made:

- The intensity of emitted light $I(X, Y, Z, t)$ is proportional to the dye concentration $c(X, Y, Z, t)$ and the laser light intensity $s(X, Y, Z, t)$:

$$I(X, Y, Z, t) \propto c(X, Y, Z, t) \cdot s(X, Y, Z, t) \quad (5.30)$$

The linearity between I and s is only valid below a certain light intensity, where saturation effects are negligible, i.e. where the major fraction of the dye molecules is not in an excited state. Since the degree of saturation depends strongly on the relative magnitude of the rates of excitation and deexcitation, this intensity varies significantly for different dyes (Ghauharali *et al.*, 1997).

- The grayvalue output of the CCD camera is proportional to the incident light intensity:

$$g(x, y, z, t) \propto I(x, y, z, t) \quad (5.31)$$

This linearity is guaranteed by the camera manufacturer within a certain range of I as described in section 5.5.

In this section a verification of these two linearities is performed through a check of the linearity between g and s , which follows from equations 5.30 and 5.31:

$$g(x, y, z, t) \propto s(x, y, z, t) \quad (5.32)$$

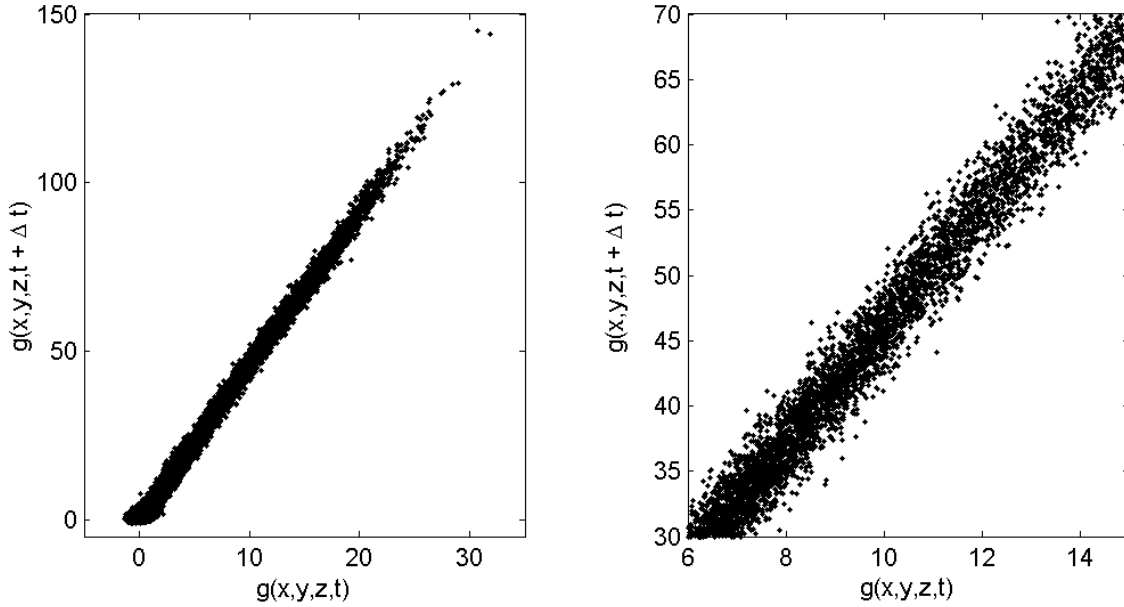


Figure 5.17: Grayvalues of a volume image before ($g(x, y, z, t)$) and after ($g(x, y, z, t + \Delta t)$) abrupt increase of laser intensity. The linearity of the curve confirms the linearity of the measurement.

Any nonlinear deviation from the relations 5.30 and 5.31 would result in a corresponding nonlinear deviation in equation 5.32 and thus a validation of the linearity 5.32 will confirm the assumptions. The validation was performed by abruptly changing the laser light intensity during an experiment:

$$s(x, y, z, t + \Delta t) = ks(x, y, z, t). \quad (5.33)$$

Then, the grayvalues must show the same abrupt change:

$$g(x, y, z, t + \Delta t) = kg(x, y, z, t). \quad (5.34)$$

Figure 5.17 shows the result of this validation, with the grayvalues corrected for dark signal and blooming (see section 5.5). The curve is linear over the whole range and passing through the origin and thus confirms the linearity of the measurement.

5.8 Summary

In this chapter the transformation from the grayvalue output of the camera $g(x, y, z, t)$ (in image coordinates (x, y, z)) to normalized concentration values $c(X, Y, Z, t)$ (in world coordinates (X, Y, Z)), which are the basis for further analysis was described. The transformation consists of several steps which are summarized in figure 5.18. The accuracy of these transformations is of essential importance for the further analysis. Through the employment of appropriate smoothing filters statistical errors could be largely reduced, leading to a higher signal-to-noise ratio. Furthermore two basic requirements for the measurement process, the linearity between incident laser light and emitted fluorescence intensity and the linearity between incident light intensity and grayvalue output of the CCD camera have been validated.

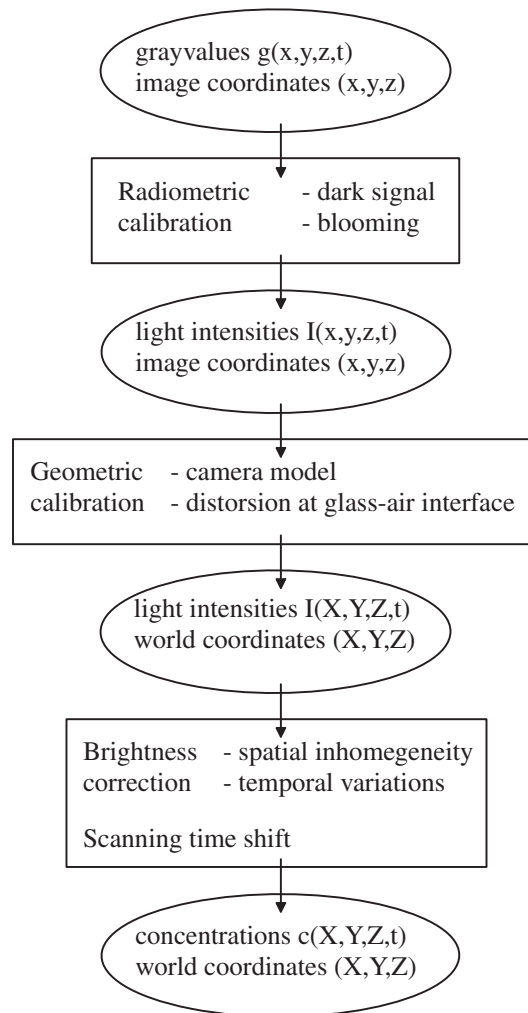


Figure 5.18: Data flow through the single steps of image preprocessing.

Chapter 6

Global parameter estimation

6.1 Introduction

This chapter is a description of the methods used for the estimation of the parameters of different transport models from the measured data. Even though the experimental method used in this work (see chapter 3) provides data with a high spatial resolution, in this chapter the sought parameters are assumed to be global, i.e. independent of the position in the porous medium. If this assumption is relaxed, the methods for local parameter estimation described in chapter 7 are employed. As explained in section 2.4, the respective parameters potentially depend on the scale, i.e. the size of the averaging REV which is used for their estimation. This is especially important for the comparison of results from different experimental methods. Since many techniques for the investigation of hydrodynamic dispersion are so-called breakthrough experiments where concentrations are measured only at the outlet of a flow cell, the global parameter estimation methods described in this chapter are used for the comparison with their results.

The parameters regarded in this chapter are the mean velocity \bar{u}_x and the dispersion coefficients D_{xx} , D_{yy} and D_{zz} in the 3D convection dispersion equation (CDE)

$$\frac{\partial \bar{c}}{\partial t} + \bar{u}_x \frac{\partial \bar{c}}{\partial x} + \bar{u}_y \frac{\partial \bar{c}}{\partial y} + \bar{u}_z \frac{\partial \bar{c}}{\partial z} - D_{xx} \frac{\partial^2 \bar{c}}{\partial x^2} - D_{yy} \frac{\partial^2 \bar{c}}{\partial y^2} - D_{zz} \frac{\partial^2 \bar{c}}{\partial z^2} = 0 \quad (6.1)$$

and the mobile pore space fraction f and the rate constant K in the 1D differential capacitance model according to Coats & Smith (1964)

$$f \frac{\partial \bar{c}}{\partial t} + (1 - f) \frac{\partial \bar{c}^*}{\partial t} + \bar{u}_x \frac{\partial \bar{c}}{\partial x} - D_{xx} \frac{\partial^2 \bar{c}}{\partial x^2} = 0 \quad (6.2)$$

$$(1 - f) \frac{\partial \bar{c}^*}{\partial t} = K(\bar{c} - \bar{c}^*). \quad (6.3)$$

This model is used to describe dispersion in case of the presence of stagnant zones in the liquid phase of the porous medium (see section 2.3.3). Since the flow direction is parallel to the x-axis the off-diagonal dispersion coefficients D_{xy} , D_{xz} and D_{yz} are set to zero.

In the next section the process of upscaling the measured microscopic concentration $c(x, y, z, t)$ to the macroscopic concentration $\bar{c}(x, y, z, t)$ by averaging over an appropriate REV is described. Then different methods for the parameter estimation are presented and their performances on synthetic data are compared in section 6.3 and 6.4. Finally section 6.5 deals with the calculation of confidence bounds for the estimated parameters.

6.2 Averaging

The initial data for the parameter estimation is a time series of volume images of normalized microscopic concentration values $c(x, y, z, t)$, which has been corrected for different systematic and statistical errors as described in chapter 5. The task of averaging then is to transform this data to macroscopic concentrations $\bar{c}(x, y, z, t)$ for which the macroscopic equations 6.1-6.3 provide a valid description. Certainly this task is ambiguous, and the parameters of the equation will depend on the size of the REV used for averaging as discussed in section 2.4. Here we use the full xy -, xz - and yz -planes as an REV for the respective parameter estimation: equation 6.1 then separates into the 3 components

$$\frac{\partial \bar{c}(x, t)}{\partial t} + \bar{u}_x \frac{\partial \bar{c}(x, t)}{\partial x} - D_{xx} \frac{\partial^2 \bar{c}(x, t)}{\partial x^2} = 0 \quad \text{with} \quad \bar{c}(x, t) = \sum_{yz} c(x, y, z, t) \quad (6.4)$$

$$\frac{\partial \bar{c}(y, t)}{\partial t} + \bar{u}_y \frac{\partial \bar{c}(y, t)}{\partial y} - D_{yy} \frac{\partial^2 \bar{c}(y, t)}{\partial y^2} = 0 \quad \text{with} \quad \bar{c}(y, t) = \sum_{xz} c(x, y, z, t) \quad (6.5)$$

$$\frac{\partial \bar{c}(z, t)}{\partial t} + \bar{u}_z \frac{\partial \bar{c}(z, t)}{\partial z} - D_{zz} \frac{\partial^2 \bar{c}(z, t)}{\partial z^2} = 0 \quad \text{with} \quad \bar{c}(z, t) = \sum_{xy} c(x, y, z, t). \quad (6.6)$$

Analogously the averages over the yz -plane $\bar{c}(x, t) = \sum_{yz} c(x, y, z, t)$ and $\bar{c}^*(x, t) = \sum_{yz} c^*(x, y, z, t)$ are used for the 1D differential capacitance model 6.2-6.3.

The effect of averaging performed in such a manner is exemplified for an initial microscopic data set shown in figure 6.1a together with the macroscopic functions $\bar{c}(x, t)$, $\bar{c}(y, t)$ and $\bar{c}(z, t)$ in figure 6.1b-d.

6.3 Direct estimation

A first approach for the estimation of the mean velocity \bar{u}_x and the dispersion coefficient D_{xx} is their relation to the first and second moment of the concentration distribution:

$$\bar{u}_x = \frac{d\bar{x}}{dt} \quad \text{with} \quad \bar{x} = \langle x \rangle = \frac{\sum_{xyz} xc(x, y, z, t)}{\sum_{xyz} c(x, y, z, t)} \quad (6.7)$$

$$D_{xx} = \frac{1}{2} \frac{d\sigma^2}{dt} \quad \text{with} \quad \sigma^2 = \langle (x - \bar{x})^2 \rangle = \frac{\sum_{xyz} (x - \bar{x})^2 c(x, y, z, t)}{\sum_{xyz} c(x, y, z, t)} \quad (6.8)$$

However, these estimates, especially that for D_{xx} are very sensitive to additive constants or noise. To demonstrate this, estimates have been performed on a simulated test sequence with $D_{xx} = 50$ and $\bar{u}_x = 18$ shown in figure 6.2a and two variants, one with a small additional constant $\Delta \bar{c} = 1$ and the second with additional noise η ($\langle \eta \rangle = 0.5$ and $\langle (\eta - \langle \eta \rangle)^2 \rangle = 1/12$). Figure 6.2b shows $\sigma^2(t)$ for these three test sequences, indicating the huge impact of small additions on the estimation of σ^2 . This huge sensitivity can be overcome to some degree by using a more robust estimator for the variance, the median absolute deviation (mad):

$$\text{mad} = 1.4826 \quad \text{median}(|x - \text{median}(x)|) \quad (6.9)$$

As can be seen from figure 6.2c, this provides significantly better results, but still exhibits considerable deviations from the correct results. As a conclusion, these direct estimates can be used only in the complete absence of any additive constants or noise.

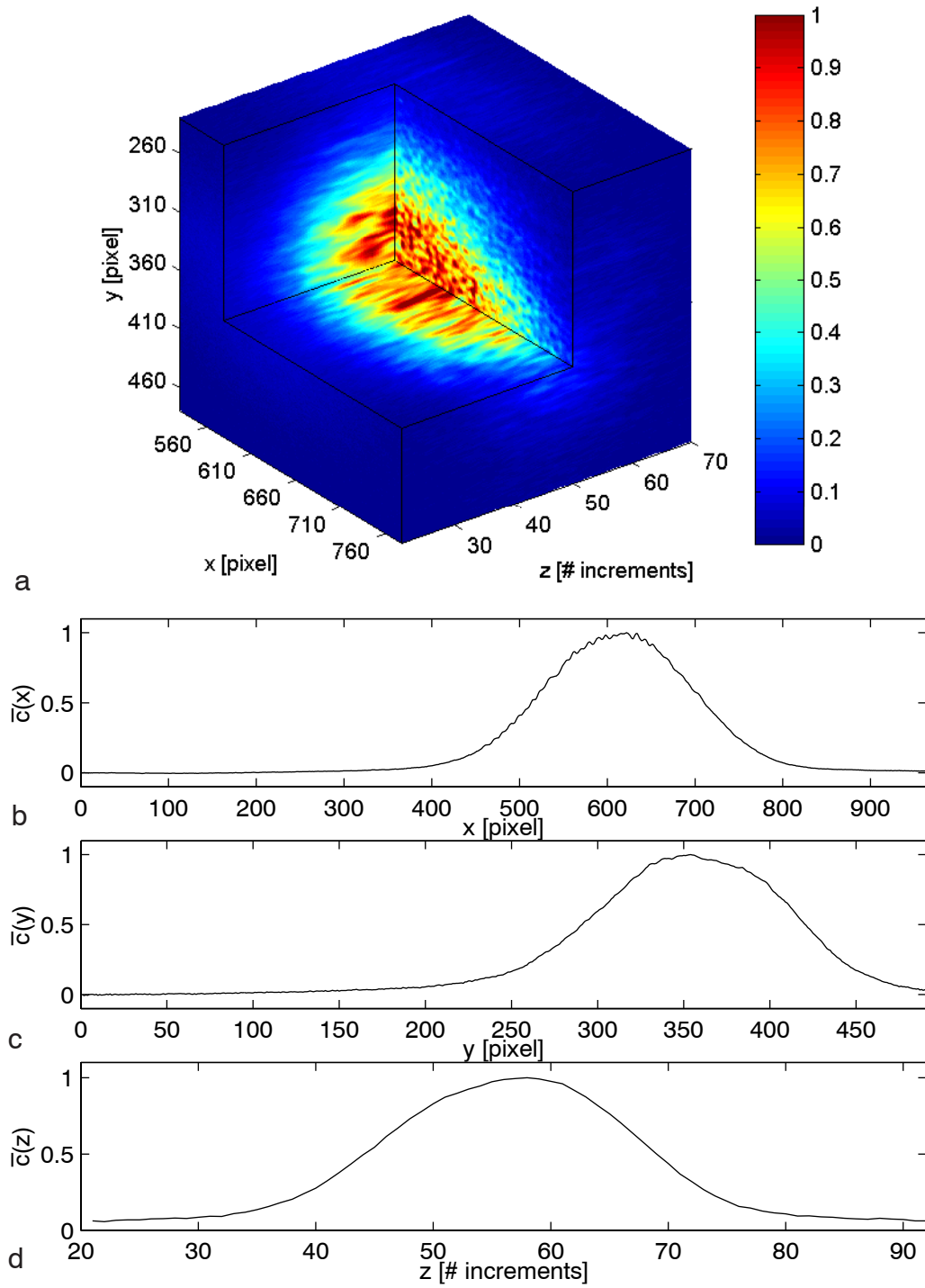


Figure 6.1: Effect of averaging: **a** microscopic dye concentration $c(x, y, z)$ in a $250 \times 250 \times 50$ voxel volume subset and the corresponding averaged macroscopic concentrations in **b** x-direction, **c** y-direction and **d** z-direction.

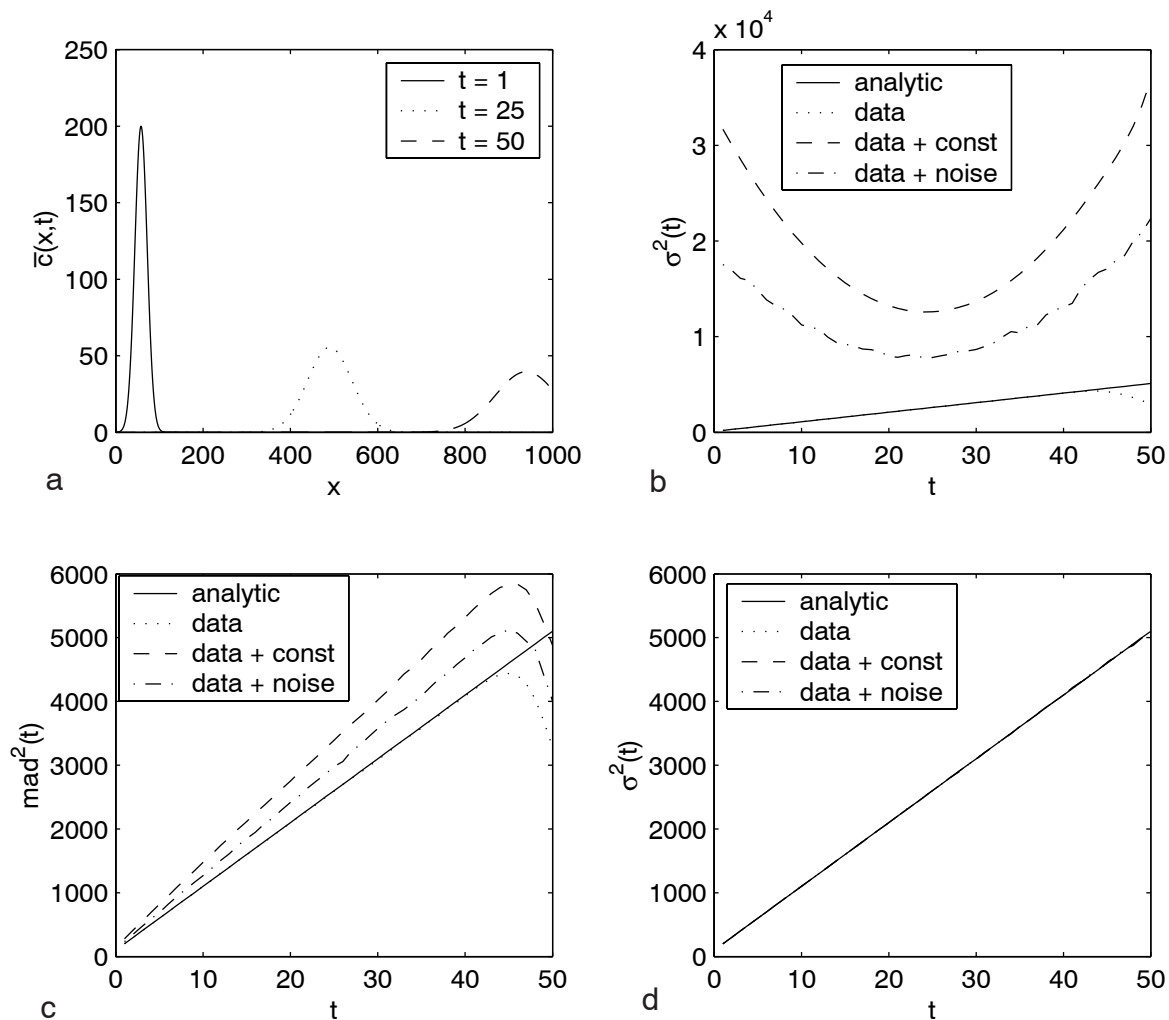


Figure 6.2: Parameter estimation for a simulated test sequence: **a** concentration distribution for three different times; temporal evolution of **b** variance, **c** squared median absolute deviation (mad) and **d** variance from a fitted gaussian for the original data, additive constant and additive noise respectively.

6.4 Fitting of model functions

A possible solution to the problem of additive constants and noise is the use of parameterized models, whose parameters are estimated by the minimization of the sum of squared differences between the model function and the data. If the solutions of the model are assumed to be gaussians, an additive constant \bar{c}_0 can be explicitly included in the solution of the model given by equation 6.4:

$$\bar{c}_{\text{mod}}(x; \bar{c}_0, a, \bar{x}, \sigma^2) = a \frac{1}{\sqrt{2\pi\sigma^2}} e^{-\frac{(x-\bar{x})^2}{2\sigma^2}} + \bar{c}_0 \quad (6.10)$$

For the case that the observed macroscopic concentrations $\bar{c}(x_i)$ are contaminated with independent and normally distributed noise

$$\bar{c}(x_i) = \bar{c}_{\text{true}}(x_i) + \eta(x_i) \quad \text{with} \quad \langle \eta(x_i) \rangle = 0, \langle \eta(x_i)\eta(x_j) \rangle = \delta_{ij}\sigma_i^2, \quad (6.11)$$

the maximum likelihood estimation \vec{p}_{est} of the parameter set $\vec{p} = (\bar{c}_0, a, \bar{x}, \sigma^2)$ is given by

$$\min_{\bar{c}_0, a, \bar{x}, \sigma^2} \chi^2 = \sum_{i=1}^N \frac{(\bar{c}(x_i) - \bar{c}_{\text{mod}}(x_i; \bar{c}_0, a, \bar{x}, \sigma^2))^2}{\sigma_i^2}. \quad (6.12)$$

The standard algorithm for such nonlinear minimization problems is the Levenberg-Marquardt-method (Press *et al.*, 1992). The results of this method for σ^2 shown in figure 6.2d are in excellent agreement with the analytic values. This approach has become the standard method for the estimation of dispersion coefficients. For the present work, the *transport analysis package* (Roth, 1996b) was employed. It features the availability of different initial conditions (dirac pulse, step, finite pulse) as well as different interaction models (equilibrium adsorption and rate-limited adsorption), and therefore allows to additionally estimate the mobile pore space fraction f and the rate constant K for the 1D differential capacitance model.

However, this method is only applicable if the initial condition $\bar{c}(x, t_0)$ is known exactly and the sought parameters are constant throughout the medium. Furthermore this method is relying on an informed guess about the starting values of the minimization. In chapter 7 a method is presented which allows the estimation of local, and therefore heterogeneous parameters \bar{u}_x and D_{xx} for arbitrary initial conditions and with no starting values necessary.

6.5 Confidence bounds for estimated parameters

The estimated parameters are worthless without information about their statistical significance. This information is given by the probability distribution of the difference between the estimated and true parameters $\Delta\vec{p} = \vec{p}_{\text{est}} - \vec{p}_{\text{true}}$. For the case of independent and normally distributed noise as in equation 6.11, and if the model is linear or can be linearized near the minimum of χ^2 , the errors in the parameters are also normally distributed and the probability distribution is defined by its covariance matrix $\text{cov}_{\vec{p}} = \langle (\Delta\vec{p})^2 \rangle$:

$$p(\Delta\vec{p}) = \frac{|\text{cov}_{\vec{p}}|^{-1/2}}{(2\pi)^{n/2}} e^{-\frac{1}{2}\Delta\vec{p}^T \text{cov}_{\vec{p}}^{-1} \Delta\vec{p}} \quad (6.13)$$

The value of $\text{cov}_{\vec{p}}$ is the inverse of the half of the hessian matrix D , which is typically returned by the Levenberg-Marquardt-algorithm together with \vec{p}_{est} :

$$\text{cov}_{\vec{p}} = \left(\frac{1}{2}D\right)^{-1} \quad \text{with} \quad D_{ij} = \frac{\partial^2 \chi^2}{\partial p_i \partial p_j}. \quad (6.14)$$

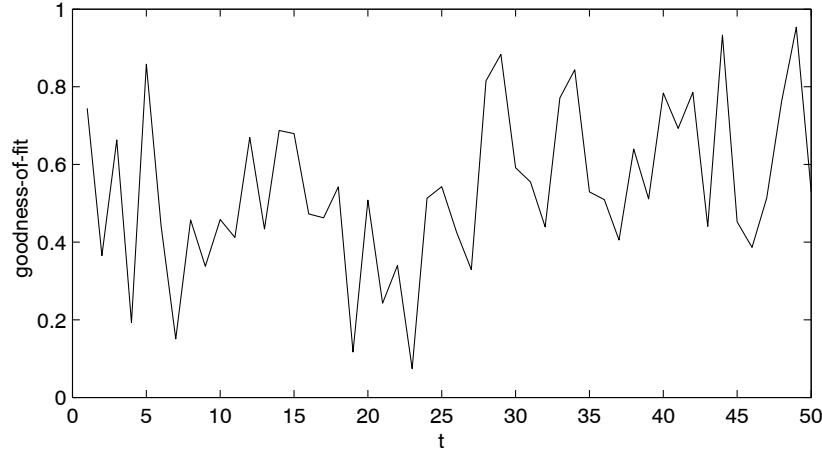


Figure 6.3: Goodness-of-fit calculated with equation 6.17 for the simulated test sequence with additive noise shown in figure 6.2a.

As an example the results of the estimation of $\vec{p} = (\bar{c}_0, a, \bar{x}, \sigma^2)$ for the simulated test sequence with additive noise at $t = 25$ shown in figure 6.2a are given:

$$\vec{p}_{\text{est}} = \begin{pmatrix} 0.4857 \\ 55.5207 \\ 490.0112 \\ 2.5976 \cdot 10^3 \end{pmatrix}, \quad \text{cov}_{\vec{p}} = \begin{pmatrix} 0.0014 & -0.0011 & -0.0000 & -0.1715 \\ -0.0011 & 0.0170 & -0.0000 & -0.8558 \\ -0.0000 & -0.0000 & 0.0187 & 0.0007 \\ -0.1715 & -0.8558 & 0.0007 & 209.0147 \end{pmatrix} \quad (6.15)$$

The covariance matrix $\text{cov}_{\vec{p}}$ provides information about the accuracy and correlations of the estimated parameters. The latter are more obvious from the matrix of correlation coefficients

$$\text{corr}_{ij} = \frac{\text{cov}_{ij}}{\sqrt{\text{cov}_{ii}\text{cov}_{jj}}} \Rightarrow \text{corr}_{\vec{p}} = \begin{pmatrix} 1.0000 & -0.2206 & -0.0002 & -0.3221 \\ -0.2206 & 1.0000 & -0.0006 & -0.4537 \\ -0.0002 & -0.0006 & 1.0000 & 0.0004 \\ -0.3221 & -0.4537 & 0.0004 & 1.0000 \end{pmatrix}. \quad (6.16)$$

However, these quantities give no information if the model fitting was successful, i.e. if the model chosen is correct to describe the data. Usually this so-called goodness-of-fit is measured by the value of χ^2 at the minimum and the number of degrees of freedom (the difference between the number of data points N and the number of parameters n) $\nu = N - n$. The goodness-of-fit is then given by the value of the incomplete gamma function

$$P\left(\frac{\nu}{2}, \frac{\chi_{\min}^2}{2}\right) = \frac{1}{\Gamma(\chi_{\min}^2/2)} \int_0^{\nu/2} e^{-t} t^{\chi_{\min}^2/2-1} dt. \quad (6.17)$$

Typically the goodness-of-fit is believable for values larger than 0.1 (Press *et al.*, 1992). This is supported by the results from the estimations with the simulated test sequence with additive noise shown in figure 6.2a+d, whose goodnesses-of-fit (calculated with $\nu = 1000 - 4 = 996$) are shown in figure 6.3. In the range between 0.1 and 0.001 the fit may be acceptable if the model omits small effects in the data or the errors have been slightly underestimated. For values less than 0.001, the assumptions about the model and/or the errors must be flawed and therefore have to be reconsidered.

Chapter 7

Local parameter estimation

7.1 Introduction

The following chapter presents a method for the local parameter estimation of linear dynamic processes. The aim is to overcome a number of disadvantages occurring with the methods used for the global parameter estimation as described in chapter 6, namely:

- the estimated parameters are assumed to be constant throughout the medium, and there is no direct way to allow for heterogeneity in the estimation. Since a main feature of the experimental technique developed in this work is its high spatial and temporal resolution, the detailed information about the local variability of flow and transport contained in the measured data can only be retrieved with an adequate local parameter estimation.
- an explicit assumption on the initial distribution $\bar{c}(x, t_0)$ (typically a dirac pulse or a step function) is needed and has to be accurately realized in the experiment.
- an informed guess about the initial values is necessary for the estimation in order to avoid running into local minima.
- the results become instable if there are significant linear dependencies between the parameters.

Towards this end, a total least squares (TLS) parameter estimation method is presented and further developed in the following sections. At first the framework of the subsequent estimations, the method of total least squares is introduced in section 7.2. The application of this framework to the parameter estimation for dynamic processes which can be modeled by linear differential equations is then presented in section 7.3. While sections 7.2 and 7.3 are mainly a survey and adaption of established methods, further analysis was performed in order to enhance the accuracy of the estimated parameters and to identify a suitable confidence measure. Therefore the method is first applied to different simulated test data sets, as described in section 7.4. This allows to evaluate the performance of the method under different conditions and to optimize its accuracy through the variation of certain free parameters. The findings of these investigations are then used in the application of the method to the experimental data obtained with the technique presented in chapter 3. Finally, a summary is given and conclusions are made in section 7.5.

7.2 Total least squares parameter estimation

The technique for the local parameter estimation presented in this chapter belongs to the class of so-called *subspace methods* (Mühlich & Mester, 1999). These methods, which have several applications in digital signal processing and computer vision (see Mühlich & Mester (1999) for an overview) achieve the separation of data and noise from a measurement through dividing the vector space of an overdetermined set of measurements into a data space and an error space. In other words the rank of the measurement matrix (which typically has full rank due to noise) is reduced to that of the lower dimensional data space. One of these methods, the so-called *total least squares method* has gained growing interest in computer vision over the last decade (Mühlich & Mester, 1999) and will be used in the present application. Therefore its basic theory will be introduced below for the example of a straight line fit.

7.2.1 Ordinary least squares

Suppose you want to fit a straight line

$$y = ax + b \quad (7.1)$$

to a set of noisy measurements

$$y_i = y_{i0} + \varepsilon_i \quad \text{with } i = 1..n, \quad (7.2)$$

where the y_{i0} denote the undisturbed values which are contaminated by independent and normally distributed additive noise ε_i with zero mean ($\langle \varepsilon_i \rangle = 0$) and variance σ^2 ($\langle \varepsilon_i^2 \rangle = \sigma^2$). An example of this situation is illustrated in figure 7.1 for $n = 50$, $a = 3/2$, $b = 10$ and $\sigma = 5$.

Together with the given x_i this results for $n > 2$ in an overdetermined set of equations

$$y_i = ax_i + b \quad \text{with } i = 1..n. \quad (7.3)$$

The maximum likelihood solution for the sought parameters a and b is then given by those parameters that yield the minimum sum of squared differences

$$\sum_{i=1}^n (ax_i + b - y_i)^2 \stackrel{!}{=} \min. \quad (7.4)$$

With

$$A = \begin{pmatrix} x_1 & 1 \\ x_2 & 1 \\ \vdots & \vdots \\ x_n & 1 \end{pmatrix}, \quad \vec{p} = \begin{pmatrix} a \\ b \end{pmatrix}, \quad \vec{b} = \begin{pmatrix} y_1 \\ y_2 \\ \vdots \\ y_n \end{pmatrix} \quad (7.5)$$

the set of equations 7.3 can be written as

$$A\vec{p} = \vec{b} \quad (7.6)$$

and the least sum of squared differences 7.4 is defined as

$$\|A\vec{p} - \vec{b}\|^2 \stackrel{!}{=} \min. \quad (7.7)$$

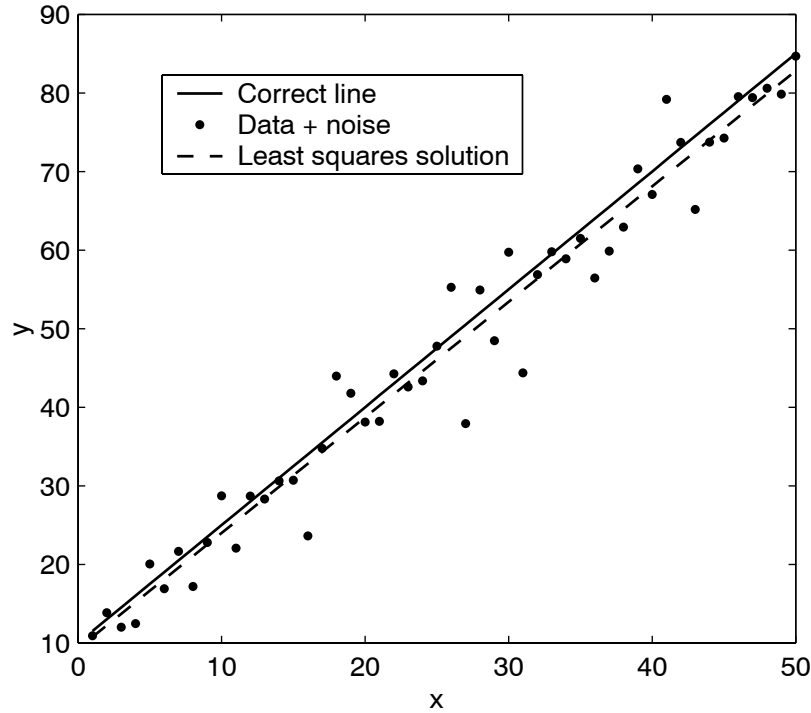


Figure 7.1: Least squares solution for a straight line fit: The data (\bullet) was calculated from equation 7.1 with $a = 3/2$ and $b = 10$ (—) and contaminated with additive white gaussian noise according to equation 7.2 with $n = 50$ and $\sigma = 5$. The least squares estimation (- -) was obtained using equation 7.10 ($a = 1.46$ and $b = 9.5$).

The minimum can then be found by setting the partial derivatives to zero:

$$\frac{\partial}{\partial a} \|A\vec{p} - \vec{b}\|^2 = 0 \qquad \frac{\partial}{\partial b} \|A\vec{p} - \vec{b}\|^2 = 0 \qquad (7.8)$$

$$\Leftrightarrow A^T(A\vec{p} - \vec{b}) = 0 \qquad (7.9)$$

$$\Leftrightarrow \vec{p} = (A^T A)^{-1} A^T \vec{b} \qquad (7.10)$$

$(A^T A)^{-1} A^T$ is the so-called Pseudoinverse. For white gaussian noise ε_i this solution for a and b is the estimator with minimal quadratic error and maximum likelihood. The result of equation 7.10 for the example given above is shown in figure 7.1.

7.2.2 Total least squares

The ordinary least squares estimation presented above is based on the assumption that the x_i are error-free and only the y_i contain noise. What if both the x_i and the y_i are contaminated with errors?

$$x_i = x_{i0} + \eta_i \quad \langle \eta_i \rangle = 0 \quad \langle \eta_i^2 \rangle = \sigma_x^2 \qquad (7.11)$$

$$y_i = y_{i0} + \varepsilon_i \quad \langle \varepsilon_i \rangle = 0 \quad \langle \varepsilon_i^2 \rangle = \sigma_y^2 \qquad (7.12)$$

This situation is exemplified in figure 7.2 for $n = 50$, $a = 3/2$, $b = 10$, $\sigma_x = 2$ and $\sigma_y = 4$.

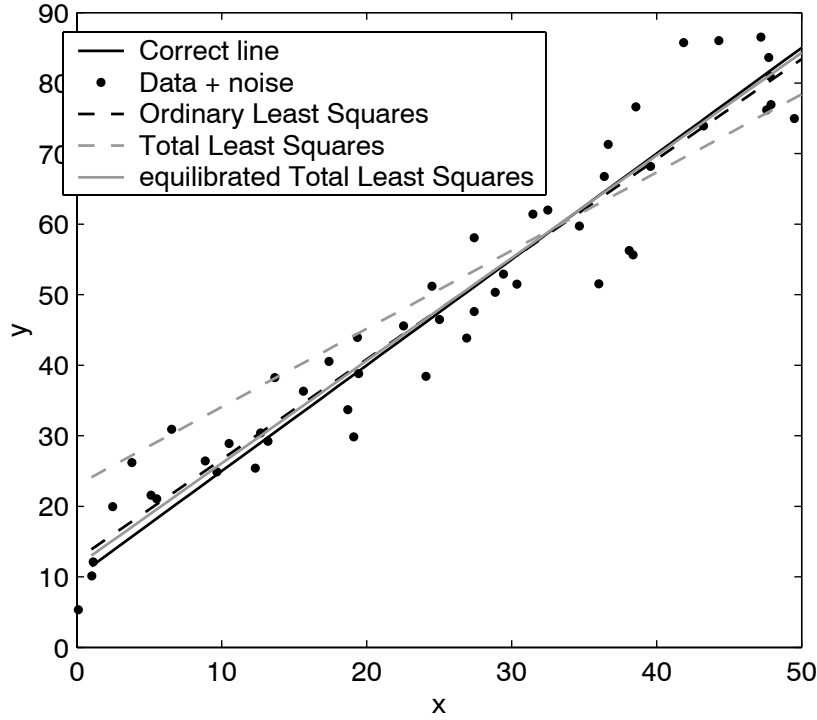


Figure 7.2: Different Least squares solutions for a straight line fit: The data (\bullet) was calculated from equation 7.1 with $a = 3/2$ and $b = 10$ (—) and then both the x_i and y_i were contaminated with additive white gaussian noise according to equations 7.11 and 7.12 ($\sigma_x = 2$ and $\sigma_y = 4$). The ordinary least squares estimation $a_{\text{OLS}} = 1.42$ and $b_{\text{OLS}} = 12.5$ (- -) was obtained using equation 7.10. The total least squares estimation without equilibration $a_{\text{TLS}} = 1.11$ and $b_{\text{TLS}} = 23.0$ (- · -) is considerably worse than OLS. The maximum likelihood estimator for this problem, the equilibrated TLS estimation $a_{\text{eq TLS}} = 1.46$ and $b_{\text{eq TLS}} = 11.6$ (—) is slightly better than OLS.

Again, the maximum likelihood solution is given by the minimal quadratic error:

$$\sum_{i=1}^n (ax_i + b - y_i)^2 \stackrel{!}{=} \min. \quad (7.13)$$

With

$$A = \begin{pmatrix} -y_1 & x_1 & 1 \\ -y_2 & x_2 & 1 \\ \vdots & \vdots & \vdots \\ -y_n & x_n & 1 \end{pmatrix} \quad \vec{p} = \begin{pmatrix} 1 \\ a \\ b \end{pmatrix} \quad (7.14)$$

the set of equations 7.3 can be written as

$$A\vec{p} = 0 \quad (7.15)$$

and the least sum of squared differences 7.13 is defined as

$$\|A\vec{p}\|^2 \stackrel{!}{=} \min. \quad (7.16)$$

In order to avoid the trivial solution $\vec{p} = 0$, the additional constraint

$$\|\vec{p}\|^2 = 1 \tag{7.17}$$

is required. Here, the difference between this so-called *total least squares* (TLS) approach and the ordinary least squares (OLS) estimation described above becomes obvious: In OLS the minimum is found in the 2D vector space of the 2D vector \vec{p} , while in TLS \vec{p} is a 3D vector and the minimum is lying on the unit sphere of the according 3D vector space. The TLS minimization 7.16 with the constraint 7.17 is then carried out with the method of Lagrange multipliers:

$$\|A\vec{p}\|^2 + \lambda(1 - \|\vec{p}\|^2) \stackrel{!}{=} \min \tag{7.18}$$

or with $J = A^T A$

$$\vec{p}^T J \vec{p} + \lambda(1 - \vec{p}^T \vec{p}) \stackrel{!}{=} \min. \tag{7.19}$$

The minimum is found by setting the partial derivatives with respect to the elements of \vec{p} to zero, which leads to the eigenvalue equation

$$J\vec{p} = \lambda\vec{p}. \tag{7.20}$$

From the properties of J :

- symmetric \rightarrow real eigenvalues
- non-negative definite \rightarrow non-negative eigenvalues

follows that the minimum is given by the eigenvector to the smallest eigenvalue λ_{\min} of J :

$$J\vec{p}_{\min} = \lambda_{\min}\vec{p}_{\min}. \tag{7.21}$$

The values for a and b are then obtained by scaling \vec{p}_{\min} to satisfy $p_1 = 1$ in equation 7.14:

$$a = \frac{p_{\min 2}}{p_{\min 1}}, \quad b = \frac{p_{\min 3}}{p_{\min 1}}. \tag{7.22}$$

The result for the above given example is shown in figure 7.2.

7.2.3 Equilibration

It can be shown (Van Huffel & Vandewalle, 1991) that \vec{p}_{\min} given by equation 7.21 is the maximum likelihood estimator if the errors of the elements of A are independent random variables with zero mean and equal standard deviation σ_A :

$$A = A_0 + \Delta A \quad \langle \Delta A_{ij} \rangle = 0 \quad \langle \Delta A_{ij}^2 \rangle = \sigma_A^2 \tag{7.23}$$

Typically this is not the case and each column of A has a different error variance:

$$A = \begin{pmatrix} -y_1 & x_1 & 1 \\ -y_2 & x_2 & 1 \\ \vdots & \vdots & \vdots \\ -y_n & x_n & 1 \end{pmatrix} \tag{7.24}$$

$$\begin{matrix} \uparrow & \uparrow & \uparrow \\ \sigma_y^2 & \sigma_x^2 & \sigma_1^2 \end{matrix}$$

In the example shown in figure 7.2 for instance these values are $\sigma_x = 2$, $\sigma_y = 4$ and $\sigma_1 = 0$. Therefore the requirement 7.23 is violated which is the reason for the erroneous TLS estimation in figure 7.2.

To fulfil the requirement 7.23 the columns of A have to be scaled with a weight matrix W_R :

$$AW_R W_R^{-1} \vec{p} = 0 \quad (7.25)$$

$$W_R = \begin{pmatrix} 1/\sigma_y & 0 & 0 \\ 0 & 1/\sigma_x & 0 \\ 0 & 0 & 1/\sigma_1 \end{pmatrix} \quad (7.26)$$

$$\Rightarrow A_{\text{eq}} \vec{p}_{\text{eq}} = 0 \quad A_{\text{eq}} = AW_R \quad \vec{p}_{\text{eq}} = W_R^{-1} \vec{p} \quad (7.27)$$

with A_{eq} fulfilling the condition 7.23. This transformation towards a matrix A_{eq} with equal standard deviations of the elements is called *equilibration*.

For the final optimal solution \vec{p}_{min} the eigenvector \vec{p}_{eqmin} to the smallest eigenvalue λ_{eqmin} of $J_{\text{eq}} = A_{\text{eq}}^T A_{\text{eq}}$ has then to be rescaled:

$$\vec{p}_{\text{min}} = W_R \vec{p}_{\text{eqmin}} \quad \Rightarrow \quad a = \frac{p_{\text{min}2}}{p_{\text{min}1}} \quad b = \frac{p_{\text{min}3}}{p_{\text{min}1}}. \quad (7.28)$$

As expected the result for the example shown in figure 7.2 proves to be better than OLS and non-equilibrated TLS.

If one column of A is assumed to be error-free, like in the present example $\sigma_1 = 0$, the corresponding element in W_R becomes infinite and therefore A_{eq} is undefined. This problem can be circumvented by approximating σ_1 by the smallest possible value according to the machine precision or by using the mixed OLS-TLS method given in Van Huffel & Vandewalle (1991).

7.2.4 Concluding remarks

The presented total least squares method is a generalization of the commonly used (ordinary) least squares method. Its application is mandatory for the case that several variables are contaminated with errors. The knowledge of the correct variances for the equilibration is necessary to obtain the optimal, i.e. maximum likelihood solution. For the demonstrated example of a straight line fit an instructive geometric interpretation is given in figure 7.3.

7.3 Parameter estimation for linear dynamic processes

The total least squares estimation procedure introduced in the last section has gained much interest in the field of computer vision over the last decade (Mühlich & Mester (1999), Haußecker *et al.* (1999)). After describing how the method of TLS can be applied to one of the classical challenges of computer vision, i.e. the estimation of motion, the framework is extended to the analysis of any dynamic process that can be modeled by a linear partial differential equation.

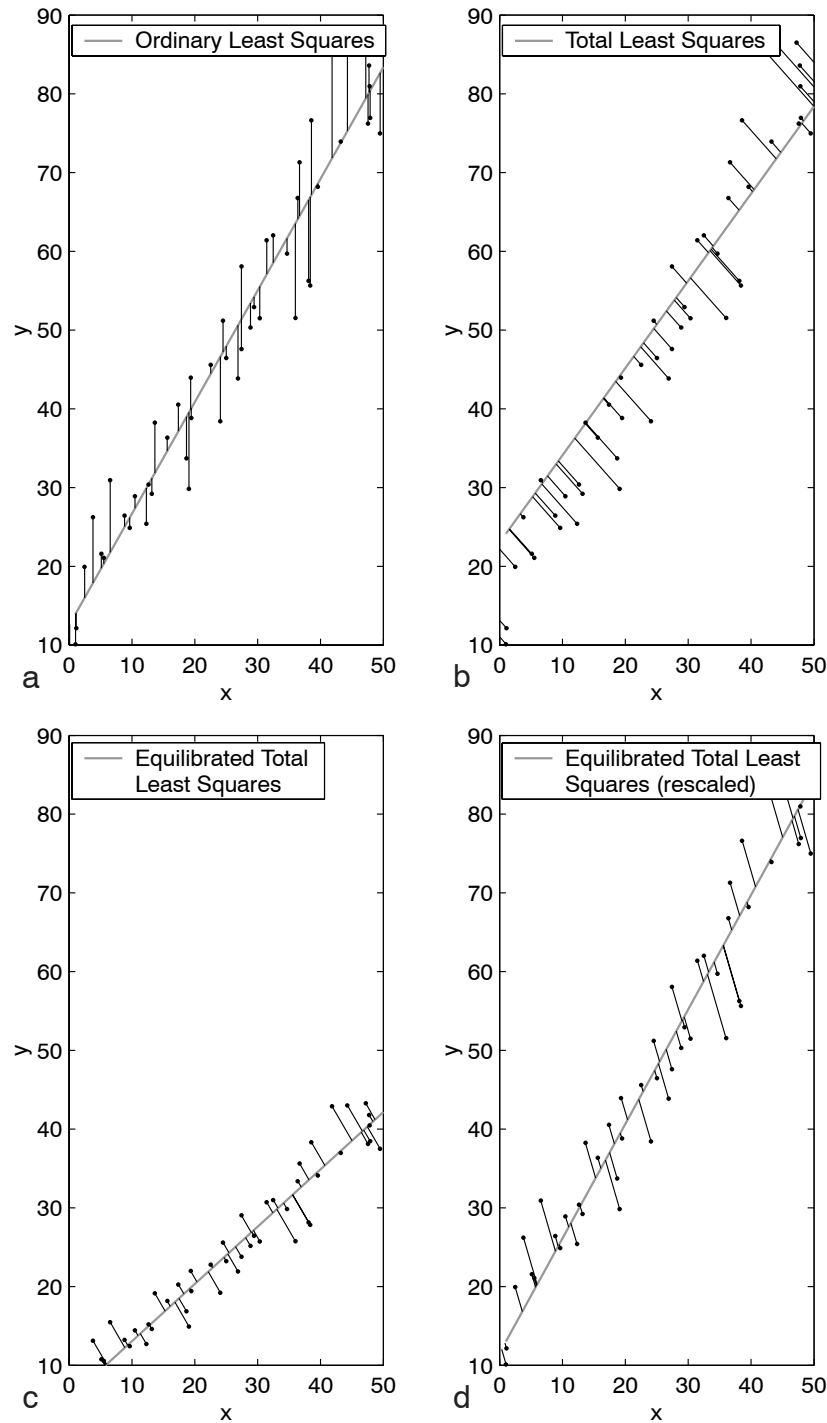


Figure 7.3: Geometric interpretation of different least squares estimators used for a straight line fit to data with errors in x and y ($\sigma_x = 2$ and $\sigma_y = 4$): **a** OLS minimizes the deviations in y -direction to the estimated line, while **b** TLS minimizes the Euclidean distances. This is only correct for $\sigma_x = \sigma_y$, which is achieved by an equilibration, i.e. scaling of y with a factor $1/2$ (**c**). The so obtained solution has then to be rescaled for the correct result (**d**).

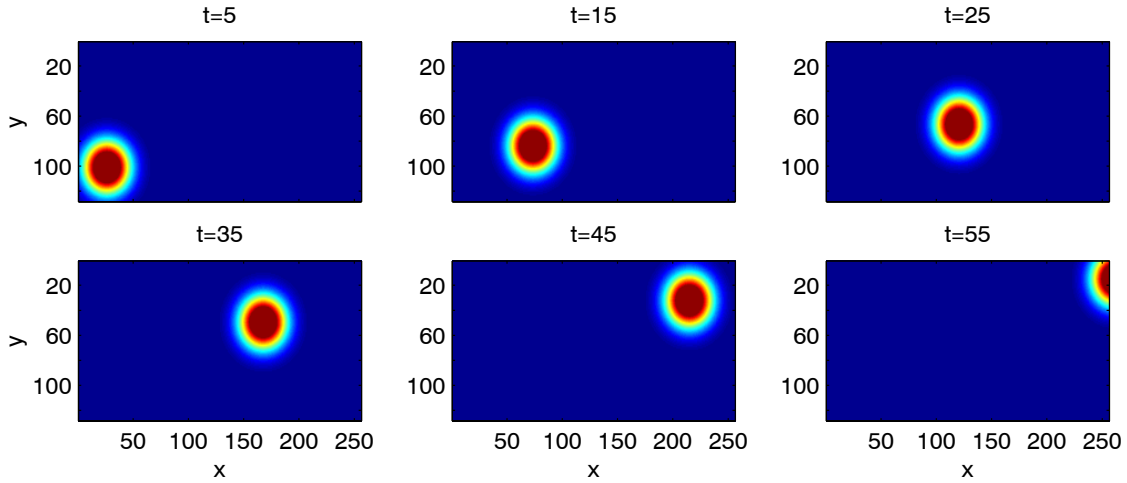


Figure 7.4: Example of a time-series $t = 1..64$ of 2D images ($n_x = 256$, $n_y = 128$) with a gaussian distribution moving with $\vec{u} = (4.7, -1.7)^T$ shown for six different times.

7.3.1 Motion estimation in image sequences

Suppose you want to estimate the motion of an object from a discrete set of intensity values $g(x, y, t)$ of a time-series $t = 1, 2, \dots, n_t$ of 2D image arrays $g(1..n_x, 1..n_y, t)$, as illustrated in figure 7.4. If the two assumptions

- the object is moving with constant velocity
- the brightness of the object is constant

are fulfilled, the temporal evolution of $g(x, y, t)$ can be described by the so-called *brightness constancy constraint equation* (BCCE)

$$\frac{dg}{dt} = \frac{\partial g}{\partial t} + \frac{\partial g}{\partial x} \frac{\partial x}{\partial t} + \frac{\partial g}{\partial y} \frac{\partial y}{\partial t} = 0 \quad (7.29)$$

$$= \frac{\partial g}{\partial t} + \vec{u} \vec{\nabla} g = 0 \quad (7.30)$$

$$\text{with } \vec{u} = \begin{pmatrix} u_x \\ u_y \end{pmatrix} = \begin{pmatrix} \frac{\partial x}{\partial t} \\ \frac{\partial y}{\partial t} \end{pmatrix} \text{ and } \vec{\nabla} g = \begin{pmatrix} \frac{\partial g}{\partial x} \\ \frac{\partial g}{\partial y} \end{pmatrix}. \quad (7.31)$$

Since the BCCE gives only one constraint for the two unknown velocities u_x and u_y for every pixel, additional assumptions have to be made. A commonly used solution for this problem is the extension to a local neighborhood, assuming that \vec{u} is constant in this neighborhood. This can be formulated as the following minimization problem:

$$E = \int_{-\infty}^{\infty} w(x - x', y - y', t - t') \left(\frac{\partial g}{\partial t} + \vec{u} \vec{\nabla} g \right)^2 dx' dy' dt' \stackrel{!}{=} \min. \quad (7.32)$$

The shape of the local neighborhood is defined by the weighting function $w(x-x', y-y', t-t')$. Then the local velocities u_x and u_y can be found by setting the partial derivatives to zero:

$$\frac{\partial E}{\partial u_x} = 2 \int_{-\infty}^{\infty} w(x-x', y-y', t-t') \frac{\partial g}{\partial x} \left(\frac{\partial g}{\partial t} + \vec{u} \vec{\nabla} g \right) dx' dy' dt' = 0 \quad (7.33)$$

$$\frac{\partial E}{\partial u_y} = 2 \int_{-\infty}^{\infty} w(x-x', y-y', t-t') \frac{\partial g}{\partial y} \left(\frac{\partial g}{\partial t} + \vec{u} \vec{\nabla} g \right) dx' dy' dt' = 0 \quad (7.34)$$

With the notation $\bar{g} = \int_{-\infty}^{\infty} w(x-x', y-y', t-t') g dx' dy' dt'$ for the weighted averaging this leads to the set of equations

$$\begin{pmatrix} \overline{\frac{\partial g}{\partial x} \frac{\partial g}{\partial x}} & \overline{\frac{\partial g}{\partial x} \frac{\partial g}{\partial y}} \\ \overline{\frac{\partial g}{\partial y} \frac{\partial g}{\partial x}} & \overline{\frac{\partial g}{\partial y} \frac{\partial g}{\partial y}} \end{pmatrix} \begin{pmatrix} u_x \\ u_y \end{pmatrix} = - \begin{pmatrix} \overline{\frac{\partial g}{\partial x} \frac{\partial g}{\partial t}} \\ \overline{\frac{\partial g}{\partial y} \frac{\partial g}{\partial t}} \end{pmatrix} \quad (7.35)$$

$$\Leftrightarrow A \vec{u} = \vec{b} \quad \Rightarrow \quad \vec{u} = A^{-1} \vec{b}. \quad (7.36)$$

This differential method can be used in principle to estimate \vec{u} , it has however two drawbacks:

- the solution for \vec{u} becomes undefined or instable for $\det A$ equal or close to zero.
- the estimate of \vec{u} takes only errors in $\frac{\partial g}{\partial t}$ into account, but not in $\frac{\partial g}{\partial x}$ and $\frac{\partial g}{\partial y}$.

These issues will be adressed in the following paragraph.

7.3.2 Tensor approach

The example of a time-series of 2D images shown in figure 7.4 can be represented alternatively as a 3D intensity distribution with the third axis denoting time as illustrated in figure 7.5. From this point of view the motion of an object in a 2D image can be understood as a 3D orientation in the corresponding 3D spatiotemporal intensity distribution. As shown in figure 7.5 the velocities can then be calculated as

$$u_x = \tan \varphi_x = \frac{\Delta x}{\Delta t} \quad \text{and} \quad u_y = \tan \varphi_y = \frac{\Delta y}{\Delta t} \quad (7.37)$$

or from the normalized vector of 3D orientation

$$\vec{p} = \begin{pmatrix} p_x \\ p_y \\ p_t \end{pmatrix} \quad \text{with} \quad \vec{p}^T \vec{p} = 1 \quad (7.38)$$

$$\Rightarrow \quad u_x = \frac{p_x}{p_t} \quad \text{and} \quad u_y = \frac{p_y}{p_t} \quad (7.39)$$

The orientation \vec{p} in the neighborhood of the spatiotemporal position $\vec{x} = (x, y, t)^T$ is defined as the direction of minimal intensity changes and is therefore given by the solution of the minimization problem

$$E = \int_{-\infty}^{\infty} w(x-x', y-y', t-t') (\vec{\nabla} g^T \vec{p})^2 dx' dy' dt' \stackrel{!}{=} \min, \quad (7.40)$$

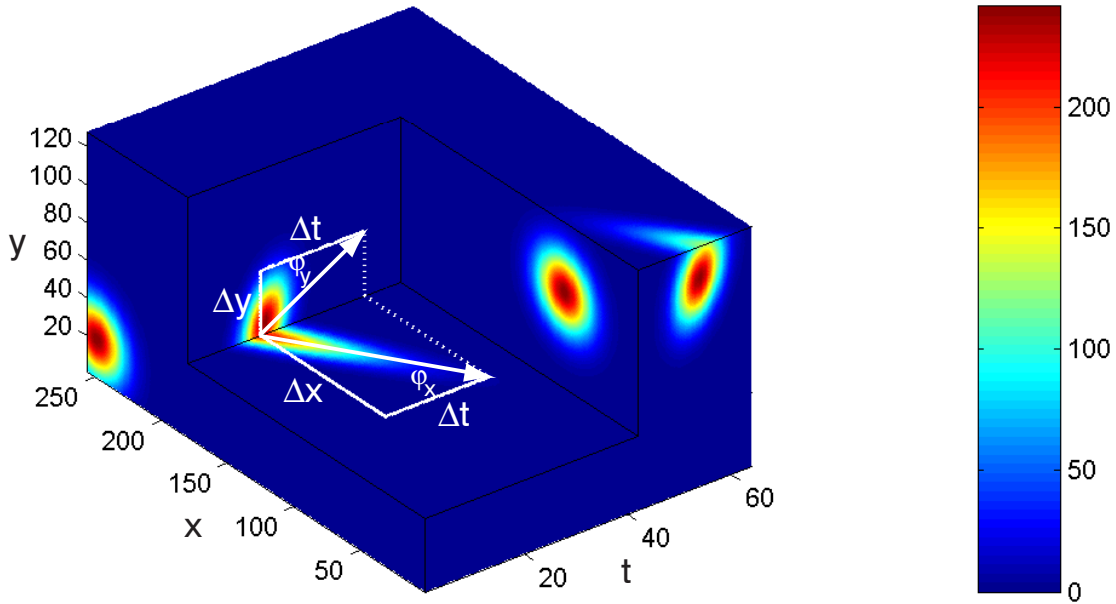


Figure 7.5: 3D representation of the time-series of 2D images with a moving gaussian distribution shown in figure 7.4. The velocities u_x and u_y can be estimated from the orientation of the 3D spatiotemporal intensity distribution according to equation 7.39.

$$\text{where } \vec{\nabla}g = \begin{pmatrix} \frac{\partial g}{\partial x} \\ \frac{\partial g}{\partial y} \\ \frac{\partial g}{\partial t} \end{pmatrix} \quad (7.41)$$

denotes the 3D spatiotemporal gradient vector. The average over the local neighborhood defined by w is made under the assumption that $(u_x, u_y)^T = \text{const.}$ within the neighborhood. With

$$J = \int_{-\infty}^{\infty} w(x - x', y - y', t - t') (\vec{\nabla}g^T \vec{\nabla}g) dx' dy' dt' = \begin{pmatrix} \frac{\partial g}{\partial x} \frac{\partial g}{\partial x} & \frac{\partial g}{\partial x} \frac{\partial g}{\partial y} & \frac{\partial g}{\partial x} \frac{\partial g}{\partial t} \\ \frac{\partial g}{\partial y} \frac{\partial g}{\partial x} & \frac{\partial g}{\partial y} \frac{\partial g}{\partial y} & \frac{\partial g}{\partial y} \frac{\partial g}{\partial t} \\ \frac{\partial g}{\partial z} \frac{\partial g}{\partial x} & \frac{\partial g}{\partial z} \frac{\partial g}{\partial y} & \frac{\partial g}{\partial z} \frac{\partial g}{\partial t} \end{pmatrix} \quad (7.42)$$

this can be written as

$$E = \vec{p}^T J \vec{p} \stackrel{!}{=} \min. \quad (7.43)$$

With the additional constraint $\vec{p}^T \vec{p} = 1$ the minimization problem can then be solved analogously to equation 7.19 with the method of Lagrange multipliers:

$$\vec{p}^T J \vec{p} + \lambda(1 - \vec{p}^T \vec{p}) \stackrel{!}{=} \min. \quad (7.44)$$

Again this results in an eigenvalue problem for J

$$J \vec{p} = \lambda \vec{p} \quad (7.45)$$

and the optimal solution \vec{p}_{\min} is given by the eigenvector to the smallest eigenvalue λ_{\min} :

$$J \vec{p}_{\min} = \lambda_{\min} \vec{p}_{\min} \quad (7.46)$$

and the local velocity \vec{u} at the spatiotemporal position $\vec{x} = (x, y, t)^T$ can be calculated as

$$\vec{u}_{\min} = \begin{pmatrix} u_x \\ u_y \end{pmatrix} = \begin{pmatrix} \frac{p_x}{p_t} \\ \frac{p_y}{p_t} \end{pmatrix}. \quad (7.47)$$

In contrast to the OLS motion estimation 7.36, this TLS estimation allows for errors in all variables $\frac{\partial g}{\partial t}$, $\frac{\partial g}{\partial x}$ and $\frac{\partial g}{\partial y}$. In the case of independent errors with zero mean and equal variance this is the maximum likelihood solution. If the variables have different errors, the tensor J must be equilibrated in analogy to section 7.2.3 using a weight matrix W_R :

$$J_{\text{eq}} = \int_{-\infty}^{\infty} w(x - x', y - y', t - t') (W_R^T \vec{\nabla} g^T \vec{\nabla} g W_R) dx' dy' dt' \quad (7.48)$$

and the solution of the eigenvalue problem then has to be rescaled according to $\vec{p}_{\min} = W_R \vec{p}_{\min \text{ eq}}$. For the proper choice of the elements of W_R see section 7.3.6.

7.3.3 Aperture problem

In practical applications it is often the case that a moving 2D object has structure only in one direction, e.g. a moving edge. This situation is illustrated in figure 7.6. Now the solution of the minimization problem 7.40 is not a single orientation vector, but a 2D vector space corresponding to the planes of constant intensity spanned by the vectors \vec{p}_1 and \vec{p}_2 shown in the 3D representation figure 7.7. In the eigenvalue problem 7.45 there will be two eigenvalues λ_1 and λ_2 equal or close to zero and the 2D space of possible solutions is spanned by the corresponding eigenvectors \vec{e}_1 and \vec{e}_2 :

$$\vec{p} = a_1 \vec{e}_1 + a_2 \vec{e}_2. \quad (7.49)$$

The problem that the solution of equation 7.46 is no longer unique if a 2D object has structure in only one direction is known as the *aperture problem*.

It is important to realize that the ambiguity of the solution is not a deficiency but a feature of the estimation method. Whereas the OLS solution 7.36 would simply become divergent, the eigenvalue spectrum of the TLS estimator directly reveals the problem and a numerically stable solution can be calculated as described in section 7.3.5. The different cases of the eigenvalue spectrum of J can be classified as follows:

- $\lambda_1 = \lambda_2 = \lambda_3 = 0$: constant grayvalue \rightarrow no further analysis.
- $\lambda_1 > 0, \lambda_2 = \lambda_3 = 0$: spatial orientation and constant motion \rightarrow only one velocity component can be estimated.

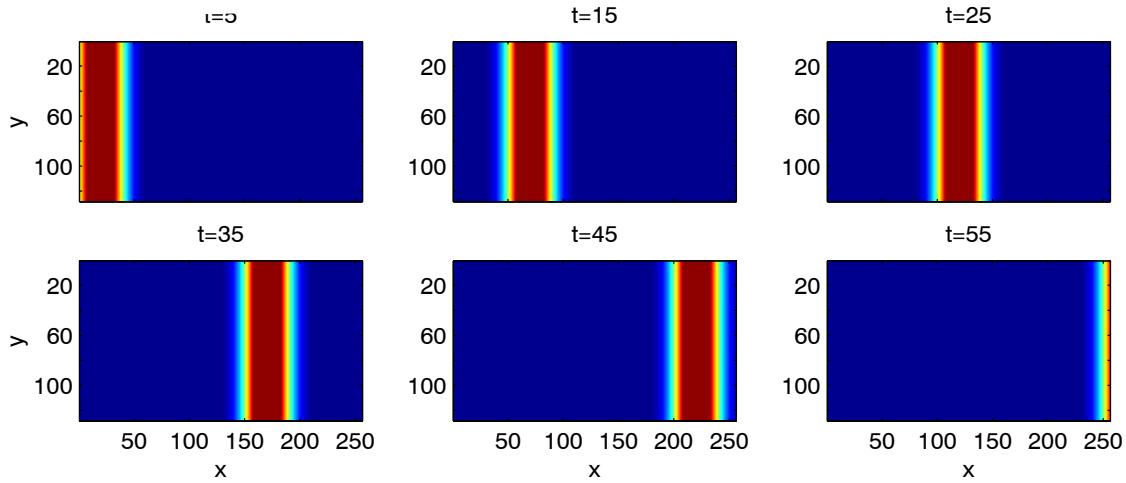


Figure 7.6: Example of a time-series $t = 1..64$ of 2D images ($n_x = 256$, $n_y = 128$) with an object moving in x-direction with $u_x = 5$ shown for six different times. Since the object has structure only in x-direction, no information about its movement in y-direction can be obtained from this image sequence.

- $\lambda_1, \lambda_2 > 0$, $\lambda_3 = 0$: distributed spatial structure and constant motion \rightarrow both velocity components can be estimated.
- $\lambda_1, \lambda_2, \lambda_3 > 0$: distributed spatial structure and non-constant motion \rightarrow no further analysis.

This possibility to directly recognize what kind of information can be obtained from the data is a very attractive feature of the TLS estimation technique.

7.3.4 Extension to linear models

Until now it was assumed that the temporal change of intensity $\frac{\partial g}{\partial t}$ was caused only by movement. This led to the BCCE 7.30 and to the further conclusion that movement corresponds to the direction of minimal intensity changes defined by equation 7.40. However this assumption is often violated by additional dynamic processes causing intensity changes, like e.g. diffusion, exponential decay or changes of illumination. For the case of isotropic diffusion this is exemplified in figures 7.8 and 7.9.

The presence of such processes must then be included in the BCCE. For the above examples the resulting extended BCCE's are as follows.

Isotropic diffusion As presented in section 2.2 the process of isotropic diffusion can be described by the differential equation

$$\frac{dg}{dt} = D \Delta g = D \left(\frac{\partial^2 g}{\partial x^2} + \frac{\partial^2 g}{\partial y^2} \right). \quad (7.50)$$

with D denoting the diffusion coefficient. Together with constant movement the BCCE extends to

$$\frac{dg}{dt} = \frac{\partial g}{\partial t} + u_x \frac{\partial g}{\partial x} + u_y \frac{\partial g}{\partial y} - D \left(\frac{\partial^2 g}{\partial x^2} + \frac{\partial^2 g}{\partial y^2} \right) = 0. \quad (7.51)$$

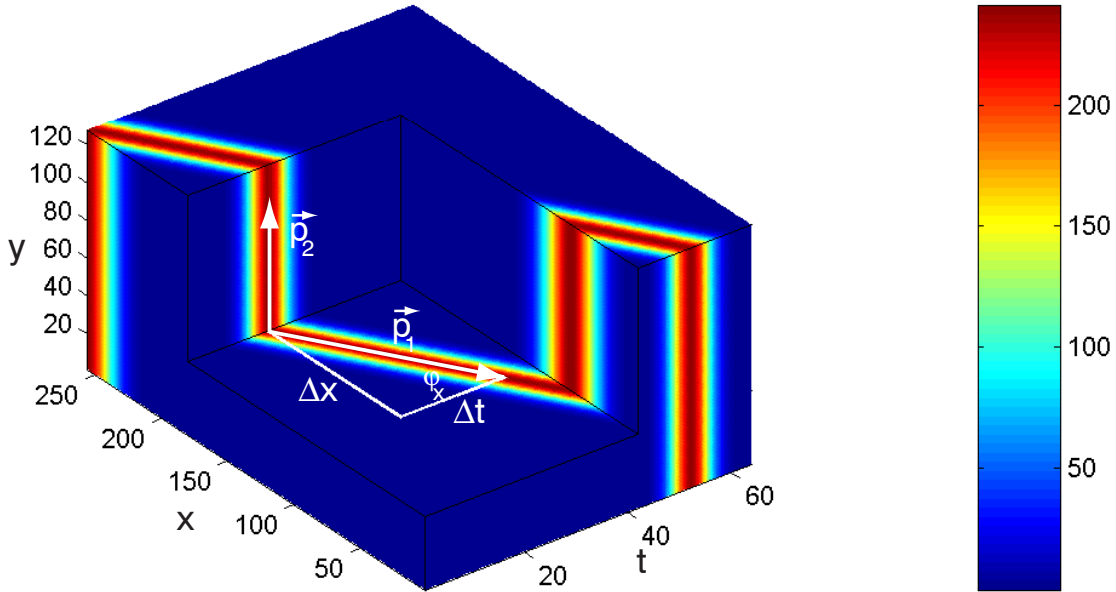


Figure 7.7: 3D representation of the image sequence shown in figure 7.6. Contrary to the situation shown in figure 7.5, where a unique local orientation could be estimated, this situation is characterized by the so-called aperture problem: The directions of minimal intensity changes are lying in a plane spanned by \vec{p}_1 and \vec{p}_2 and consequently the velocity u_y cannot be estimated. The velocity in x-direction u_x can be estimated from the minimum norm solution 7.67.

Anisotropic diffusion Anisotropic diffusion is a generalization of isotropic diffusion which can be used e.g. to model dispersion in a porous medium. It is described by the differential equation

$$\begin{aligned} \frac{dg}{dt} &= \vec{\nabla} (D \vec{\nabla} g) = \begin{pmatrix} \frac{\partial}{\partial x} \\ \frac{\partial}{\partial y} \end{pmatrix} \begin{pmatrix} D_{xx} & D_{xy} \\ D_{xy} & D_{yy} \end{pmatrix} \begin{pmatrix} \frac{\partial g}{\partial x} \\ \frac{\partial g}{\partial y} \end{pmatrix} \\ &= D_{xx} \frac{\partial^2 g}{\partial x^2} + 2D_{xy} \frac{\partial^2 g}{\partial x \partial y} + D_{yy} \frac{\partial^2 g}{\partial y^2} = 0. \end{aligned} \quad (7.52)$$

Here D denotes the symmetric 2×2 diffusion tensor. The resulting extended BCCE is then given by:

$$\frac{dg}{dt} = \frac{\partial g}{\partial t} + u_x \frac{\partial g}{\partial x} + u_y \frac{\partial g}{\partial y} - D_{xx} \frac{\partial^2 g}{\partial x^2} - 2D_{xy} \frac{\partial^2 g}{\partial x \partial y} - D_{yy} \frac{\partial^2 g}{\partial y^2} = 0. \quad (7.53)$$

Exponential decay A process, where the probability for the decay within the time dt of a substance is constant, like e.g. for radioactive substances, follows the law of exponential

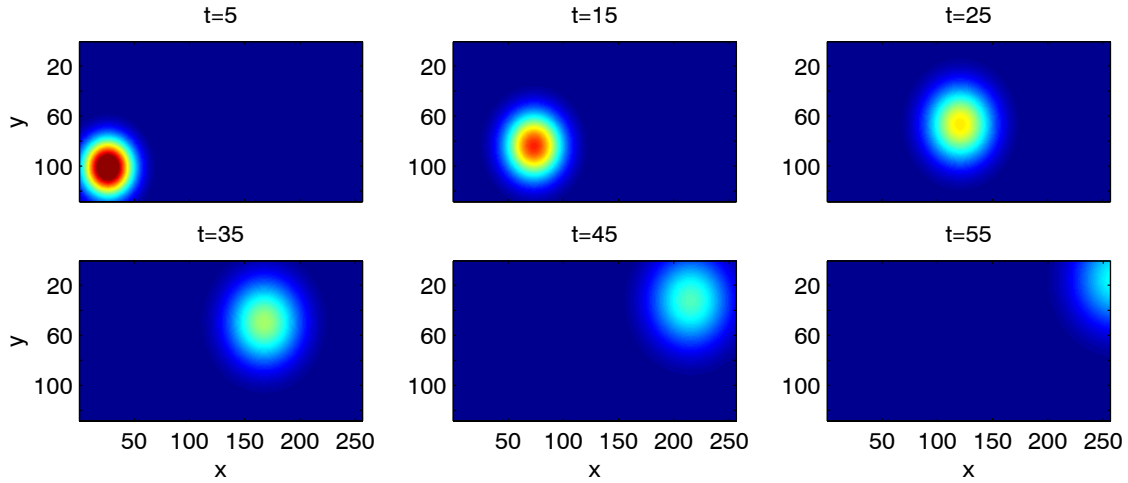


Figure 7.8: Example of a time-series $t = 1..64$ of 2D images ($n_x = 256$, $n_y = 128$) showing a gaussian distribution moving with $\vec{u} = (4.7, -1.7)^T$, which is additionally subject to diffusion, for six different times. In contrast to the situation in figure 7.4, brightness changes are caused by a combination of movement and diffusion, and therefore the BCCE must be extended according to equation 7.51.

decay which is described by the differential equation

$$\frac{dg}{dt} = -\kappa g \quad (7.54)$$

with κ denoting the decay constant. Here the resulting extended BCCE is given by

$$\frac{dg}{dt} = \frac{\partial g}{\partial t} + u_x \frac{\partial g}{\partial x} + u_y \frac{\partial g}{\partial y} + \kappa g = 0. \quad (7.55)$$

Linear changes of intensity The process of a linear change of intensity, caused e.g. by a change of illumination or by external sources or sinks, can be described by the differential equation

$$\frac{dg}{dt} = q, \quad (7.56)$$

where q denotes the source strength. Then the BCCE extends to

$$\frac{dg}{dt} = \frac{\partial g}{\partial t} + u_x \frac{\partial g}{\partial x} + u_y \frac{\partial g}{\partial y} - q = 0. \quad (7.57)$$

3D anisotropic diffusion Although the above examples are all formulated for 2D image sequences, the presented formalism can be applied in any dimension. As an example the differential equation for a 3D anisotropic diffusion process is given by

$$\frac{dg}{dt} = \vec{\nabla} (D \vec{\nabla} g) = \begin{pmatrix} \frac{\partial}{\partial x} \\ \frac{\partial}{\partial y} \\ \frac{\partial}{\partial z} \end{pmatrix} \begin{pmatrix} D_{xx} & D_{xy} & D_{xz} \\ D_{xy} & D_{yy} & D_{yz} \\ D_{xz} & D_{yz} & D_{zz} \end{pmatrix} \begin{pmatrix} \frac{\partial g}{\partial x} \\ \frac{\partial g}{\partial y} \\ \frac{\partial g}{\partial z} \end{pmatrix} =$$

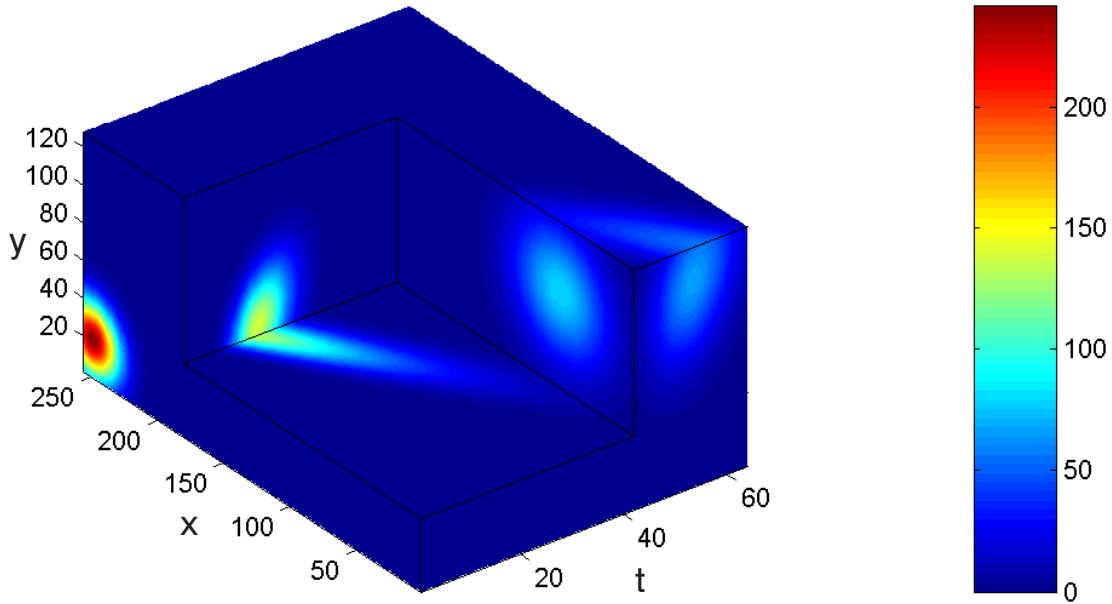


Figure 7.9: 3D representation of the image sequence shown in figure 7.8. In opposition to the situation shown in figure 7.5, the velocity of the object cannot be estimated from the direction of minimal intensity changes. Here the velocities are part of a 4D parameter vector \vec{p} which is estimated from an extended tensor J given by equation 7.61, with \vec{p} and \vec{d} given by the 2D isotropic diffusion model in table 7.1.

$$= D_{xx} \frac{\partial^2 g}{\partial x^2} + D_{yy} \frac{\partial^2 g}{\partial y^2} + D_{zz} \frac{\partial^2 g}{\partial z^2} + 2D_{xy} \frac{\partial^2 g}{\partial x \partial y} + 2D_{xz} \frac{\partial^2 g}{\partial x \partial z} + 2D_{yz} \frac{\partial^2 g}{\partial y \partial z}, \quad (7.58)$$

where D now denotes the symmetric 3×3 diffusion tensor. This results in the extended BCCE

$$\begin{aligned} \frac{dg}{dt} &= \frac{\partial g}{\partial t} + u_x \frac{\partial g}{\partial x} + u_y \frac{\partial g}{\partial y} + u_z \frac{\partial g}{\partial z} - D_{xx} \frac{\partial^2 g}{\partial x^2} - D_{yy} \frac{\partial^2 g}{\partial y^2} - D_{zz} \frac{\partial^2 g}{\partial z^2} \\ &\quad - 2D_{xy} \frac{\partial^2 g}{\partial x \partial y} - 2D_{xz} \frac{\partial^2 g}{\partial x \partial z} - 2D_{yz} \frac{\partial^2 g}{\partial y \partial z} = 0. \end{aligned} \quad (7.59)$$

In principle, for every process that can be described by a linear differential equation, and for any combination of these, a corresponding differential equation for optical flow, i.e. an extended BCCE, can be formulated and its parameters can be estimated. For that purpose the minimization problem 7.40 is reformulated in the generalized form

$$E = \int_{-\infty}^{\infty} w(x - x', y - y', t - t') (\vec{d}^T \vec{p})^2 dx' dy' dt' \stackrel{!}{=} \min. \quad (7.60)$$

The corresponding pairs of data vector \vec{d} and parameter vector \vec{p} are given in table 7.1. Analogous to equation 7.40 it is assumed that the parameters \vec{p} are constant within the local neighborhood defined by w . With the extended tensor J defined by

$$J = \int_{-\infty}^{\infty} w(x - x', y - y', t - t') (\vec{d} \vec{d}^T) dx' dy' dt' \quad (7.61)$$

model	\vec{d}	\vec{p}
2D translation	$\left(\frac{\partial g}{\partial x}, \frac{\partial g}{\partial y}, \frac{\partial g}{\partial t}\right)^T$	$(u_x, u_y, 1)^T$
2D translation + isotropic diffusion	$\left(\frac{\partial g}{\partial x}, \frac{\partial g}{\partial y}, \frac{\partial^2 g}{\partial x^2} + \frac{\partial^2 g}{\partial y^2}, \frac{\partial g}{\partial t}\right)^T$	$(u_x, u_y, -D, 1)^T$
2D translation + anisotropic diffusion	$\left(\frac{\partial g}{\partial x}, \frac{\partial g}{\partial y}, \frac{\partial^2 g}{\partial x^2}, \frac{\partial^2 g}{\partial x \partial y}, \frac{\partial^2 g}{\partial y^2}, \frac{\partial g}{\partial t}\right)^T$	$(u_x, u_y, -D_{xx}, -2D_{xy}, -D_{yy}, 1)^T$
2D translation + exponential decay	$\left(\frac{\partial g}{\partial x}, \frac{\partial g}{\partial y}, g, \frac{\partial g}{\partial t}\right)^T$	$(u_x, u_y, \kappa, 1)^T$
2D translation + linear change	$\left(\frac{\partial g}{\partial x}, \frac{\partial g}{\partial y}, 1, \frac{\partial g}{\partial t}\right)^T$	$(u_x, u_y, -q, 1)^T$
3D translation + anisotropic diffusion	$\left(\frac{\partial g}{\partial x}, \frac{\partial g}{\partial y}, \frac{\partial g}{\partial z}, \frac{\partial^2 g}{\partial x^2}, \frac{\partial^2 g}{\partial y^2}, \frac{\partial^2 g}{\partial z^2}, \frac{\partial^2 g}{\partial x \partial y}, \frac{\partial^2 g}{\partial x \partial z}, \frac{\partial^2 g}{\partial y \partial z}, \frac{\partial g}{\partial t}\right)^T$	$(u_x, u_y, u_z, -D_{xx}, -D_{yy}, -D_{zz}, -2D_{xy}, -2D_{xz}, -2D_{yz}, 1)^T$

Table 7.1: Associated pairs of data vector \vec{d} and parameter vector \vec{p} for the TLS parameter estimation with different extended linear models. The n elements of \vec{p} are always ordered so that $p_n = 1$.

this leads to the analogous eigenvalue problem

$$J\vec{p} = \lambda\vec{p}. \quad (7.62)$$

The application of particular models then differs only in the choice of the corresponding vectors \vec{d} and \vec{p} , which are given for the above models in table 7.1. For simplicity the following formulations are often restricted to 2D models.

With the extension of the BCCE also the classification of the eigenvalue spectrum of J has to be extended. In general the TLS estimation divides the n dimensional vector space of \vec{p} into a p dimensional data space and a $n - p$ dimensional nullspace or error space (in the presence of noise). The nullspace is spanned by the eigenvectors to the eigenvalues equal or (in the presence of noise) close to zero. Every vector in the nullspace is a possible solution. As a consequence, only p parameters can be estimated. For a reasonable solution the nullspace must have at least dimension 1. If the dimension is equal to 1, the parameters p_1, p_2, \dots, p_{n-1} have a unique solution due to the additional constraint $p_n = 1$ (see table 7.1). If no eigenvalue is close to zero, either a wrong model was chosen or the level of noise is too high.

If the elements of \vec{d} are contaminated with errors of different variance, \vec{d} has to be properly equilibrated in analogy to sections 7.3.2 and 7.2.3

$$\vec{d}_{\text{eq}} = \vec{d}W_R \quad \text{with} \quad W_R = \begin{pmatrix} 1/\sigma_1 & 0 & \cdots & 0 \\ 0 & 1/\sigma_2 & & \vdots \\ \vdots & & \ddots & 0 \\ 0 & \cdots & 0 & 1/\sigma_4 \end{pmatrix} \quad (7.63)$$

and the solution $\vec{p}_{\min \text{eq}}$ of the following eigenvalue problem $J_{\text{eq}}\vec{p}_{\text{eq}} = \lambda_{\text{eq}}\vec{p}_{\text{eq}}$ then must be rescaled according to $\vec{p}_{\min} = W_R\vec{p}_{\min \text{eq}}$.

7.3.5 Minimum norm solution

As stated above, any vector in the nullspace is a possible solution of the minimization problem 7.60. If its dimension is higher than 1, the most reasonable choice is often that with minimal (euclidean) norm. In the example of a moving edge shown in figure 7.6 for instance, the minimum norm solution would give the velocity vector perpendicular to the edge.

If the eigenvalues are arranged in descending order, $\lambda_1 > \dots > \lambda_p > \lambda_{p+1} \approx \dots \approx \lambda_n \approx 0$, the nullspace is spanned by the eigenvectors \vec{e}_i with $i > p$, and every linear combination

$$\vec{p} = \sum_{i=p+1}^n r_i \vec{e}_i = E\vec{r} \quad \text{with} \quad E = (\vec{e}_{p+1} \cdots \vec{e}_n) = \begin{pmatrix} e_{(p+1)1} & \cdots & e_{n1} \\ \vdots & \ddots & \vdots \\ e_{(p+1)n} & \cdots & e_{nn} \end{pmatrix} \quad (7.64)$$

is a possible solution to the minimization problem 7.60. The minimum norm solution \vec{p}_{\min} is then given by

$$\|\vec{p}\|^2 = \vec{r}^T E^T E \vec{r} = \vec{r}^T \vec{r} = \sum_{i=p+1}^n r_i^2 \stackrel{!}{=} \min \quad (7.65)$$

and the additional constraint $p_n = 1$ can be written as

$$p_n = \sum_{i=p+1}^n r_i e_{in} = \vec{v}^T E \vec{r} = 1 \quad \text{with} \quad \vec{v} = (0, \dots, 0, 1)^T. \quad (7.66)$$

The solution of this constrained minimization problem is given by

$$\vec{p}_{\min} = \frac{E E^T \vec{v}}{\vec{v}^T E E^T \vec{v}}. \quad (7.67)$$

For a complete derivation of the solution see Spies (2001). It is noted that the demand for the minimal norm 7.65 is not always justified. As an alternative, a variational method using a smoothness constraint presented in Spies (2001) can be used. In section 7.4.5, a modified minimization criterion based on physical constraints is introduced which is adapted for the parameter estimation in a 2D anisotropic diffusion process.

7.3.6 Computational aspects

Nothing has yet been said about some important aspects of the computational implementation of the TLS parameter estimation. While the formalism presented until here was given in its continuous form, a suitable discretization is needed to account for the discrete form of the image data.

Calculation of derivatives

The estimation of the derivatives $\frac{\partial g}{\partial t}$, $\frac{\partial g}{\partial x}$, $\frac{\partial g}{\partial y}$, $\frac{\partial^2 g}{\partial x^2}$, $\frac{\partial^2 g}{\partial x \partial y}$ etc. from the given image data set $g(x_1 \dots x_{n_x}, y_1 \dots y_{n_y}, t_1 \dots t_{n_t})$ at discrete times t_k and positions $(x_i, y_j)^T$ is implemented as

a discrete convolution with an appropriate filter mask $h(-R_x..R_x, -R_y..R_y, -R_t..R_t)^T$ (see Jähne (2002)):

$$g'(x_i, y_j, t_k) = h * g = \sum_{x_l=-R_x}^{R_x} \sum_{y_m=-R_y}^{R_y} \sum_{t_n=-R_t}^{R_t} h(x_l, y_m, t_n) g(x_i - x_l, y_j - y_m, t_k - t_n). \quad (7.68)$$

Scharr (2000) has compared different choices for the filter mask h with regard to systematic errors, i.e. deviations from the corresponding analytical derivative, and to their stability in the presence of noise. It was found that the choice of the filter mask has appreciable influence on the accuracy of a subsequent TLS parameter estimation. A comprehensive analysis and discussion of this issue is given in section 7.4.1.

Averaging over a local neighborhood

For the calculation of the $n \times n$ tensor J the values of $\vec{d}\vec{d}^T$ have to be averaged over a local neighborhood according to equation 7.61. This is necessary to increase the rank of J and therefore decrease the ambiguity of the resulting solution. Uniqueness of the result is reached if the rank of J is equal to $n - 1$. Therefore the size of the local neighborhood must be chosen carefully: It must be large enough to avoid ambiguity and to reduce the uncertainty of the estimated parameters, resulting from noise in the image data, to an acceptable level. On the other hand it also must be small enough to fulfill the assumption of locally constant parameters made with equation 7.60. The extensions of the neighborhood in x-, y- and t-direction can be chosen separately. For the analysis of a stationary flow field for instance it is reasonable to extend the neighborhood over the whole temporal range and use a small spatial neighborhood. For a discrete set of image data, the integral describing the average in equation 7.61 is replaced by a convolution with an appropriate (mostly binomial or box shaped) averaging filter mask B according to equation 7.68. The elements of J are then calculated as

$$J_{pq} = B * (D_p * g \cdot D_q * g), \quad p, q = 1..n, \quad (7.69)$$

where D_p and D_q denote the respective derivative filters and \cdot denotes the pointwise multiplication.

Equilibration weight matrix

As noted in section 7.3.4, for the correct solution the elements of \vec{d} must be scaled with a weight matrix W_R in order to equilibrate their error variances σ_i^2 as expressed by equation 7.63. Consequently the relative magnitudes of the errors for the elements of \vec{d} must be known a priori. Under the assumption that the image data g is contaminated with independent and identically distributed gaussian noise with variance $\sigma_d^2 = \langle (g - \bar{g})^2 \rangle$, the variances $\sigma_i^2 = \langle (d_i - \bar{d}_i)^2 \rangle$ constituting the elements of W_R can be calculated as

$$\sigma_i^2 = \text{var}(D_i * g) = \sigma_d^2 \sum_{x_j=-R_x}^{R_x} \sum_{y_k=-R_y}^{R_y} \sum_{t_l=-R_t}^{R_t} D_i^2(x_j, y_k, t_l) \quad (7.70)$$

from the elements of the filter mask D_i . As an example, the variance for a derivative obtained with the 1D filter mask $D = (-1/8 \ 6/8 \ 0 \ -6/8 \ 1/8)$ is $\sigma_D^2 = \frac{74}{64}\sigma_d^2$. A numerical validation of this relation is presented in section 7.4.3. The knowledge of σ_d^2 is not necessary for the

equilibration and can be set to $\sigma_d^2 = 1$ because only the relative magnitudes are needed. It is however necessary for the classification of the eigenvalue spectrum as described below. For a characterization of noise in the image data obtained with the experimental technique used in this work see section 5.6.

Classification of eigenvalue spectra and confidence measures

In an ideal situation there would be one eigenvalue of J exactly zero and the sought parameters could be readily obtained from the corresponding eigenvector. However, since image data always contains noise (at least the quantization noise), the smallest eigenvalue will hardly become exactly zero. If aperture problems occur, more eigenvalues will be close to zero. From this the question arises how the term *close to zero* can be quantified, i.e. which eigenvectors belong to the nullspace and which to the data space.

After the equilibration according to equation 7.63 the errors of the elements of \vec{d}_{eq} are assumed to be independent with zero mean and same variance σ_d^2 :

$$\langle d_i d_j \rangle = \sigma_d^2 \delta_{ij}. \quad (7.71)$$

Then noise simply results in an additive diagonal matrix $J'_{\text{eq}} = J_{\text{eq}} + k_B \sigma_d^2$, where $k_B = \sqrt{\sum_{i=1}^{N_B} B_i^2}$ is given by the elements B_i of the averaging filter B and consequently the eigenvalues of J_{eq} are shifted according to

$$\lambda'_i = \lambda_i + k_B \sigma_d^2 \quad (7.72)$$

(Spies, 2001). On this basis, an eigenvector can be attributed to the nullspace if its eigenvalue is smaller than a threshold τ_1 of about $\tau_1 \approx k_B (3\sigma_d)^2$. The value of σ_d^2 can be evaluated by trial and error or by a separate analysis as described in section 5.6. If the smallest eigenvalue is higher than τ_1 , either the noise is higher than assumed, or the model is not compatible with the data, and the parameters estimated from the associated eigenvector should be handled with care.

Apart from the smallest eigenvalue as a measure of noise the trace of J can be used to determine the amount of structure in the data. Often the parameters can only be estimated reliably if the amount of structure is above a certain level. Therefore it makes sense to check if the trace of J is above a certain threshold τ_2 before the following eigenvalue problem 7.62 is solved. Again the value of τ_2 is preferably found by trial and error. Spies (2001) found a value of $\tau_2 \approx 15$ if a normalized averaging filter B is used.

For the remaining estimates that have passed the thresholds τ_1 and τ_2 it is often desirable to quantify their reliability by an appropriate confidence measure, like e.g. the goodness-of-fit 6.17 for the global parameter estimation in chapter 6. The determination of suitable confidence measures is an object of ongoing research (Nestares *et al.*, 2000), which is complicated by the nonlinearity of the eigenvalue problem. Spies (2001) suggests a quantity that measures how close the smallest eigenvalue λ_n came to the threshold τ_1 :

$$\omega_c = \begin{cases} 0 & \text{if } \lambda_n > \tau_1 \text{ or } \text{tr}(J) < \tau_2 \\ \left(\frac{\tau_1 - \lambda_n}{\tau_1 + \lambda_n} \right)^2 & \text{else} \end{cases} \quad (7.73)$$

For $\lambda_n = 0$ the confidence is one and for $\lambda_n \rightarrow \tau_1$ the confidence goes to zero. Another confidence measure used in this work, which will be introduced in section 7.4.4, is the ratio

of λ_n to the product of the trace of J and the size N_B of the averaging filter B , which can be interpreted as an noise-to-signal ratio:

$$\omega_{\text{NSR}} = \frac{\lambda_n}{N_B \text{tr}(J)}, \quad (7.74)$$

The performances of different confidence measures are evaluated and compared in section 7.4.4.

7.4 Application to simulated data

As explained in section 7.3.6, the presented technique has several critical issues which can have strong influences on the accuracy of the results and therefore have to be chosen carefully. In detail these are

- the choice of the filters D for the calculation of the elements of the tensor J with equation 7.69.
- the shape of the averaging filter mask B used in equation 7.69.
- the weight matrix W_R used to equilibrate the elements of \vec{d} according to equation 7.63.
- the choice of appropriate thresholds τ_1 and τ_2 for λ_n (see section 7.3.6) or the use of other methods to estimate the dimension of the nullspace of J .
- a suitable confidence measure for the quantification of the accuracy of the estimated parameters.

With simulated test data it is possible to study their influences on the accuracy of the estimated parameters making use of the a priori known results (the so-called ground truth), which have been used to generate the data. The optimal choice of the parameters listed above depends on properties of the data (amplitudes of signal and noise) and the model that is fitted to the data. In the following subsections the impact and optimal choice is investigated separately for each of the above listed parameters.

7.4.1 Choice of filter masks

It is obvious that the accuracy of the parameters estimated from the tensor J depends strongly on the accuracy of its elements J_{pq} , which are obtained from the image data through the application of appropriate linear filters D according to equation 7.69. Since the eigenvalue analysis is a highly nonlinear operation, no analytical relation between errors of the elements J_{pq} and errors of the estimated parameters \vec{p} can be given, and therefore a numerical analysis is employed. This subsection deals with the choice of optimal, i.e. most accurate, linear filters D for the estimation of the corresponding derivatives. In the case of a 2D CDE described by the BCCE 7.53 for example, these are the first order derivatives $\frac{\partial g}{\partial t}$, $\frac{\partial g}{\partial x}$ and $\frac{\partial g}{\partial y}$ and the second order derivatives $\frac{\partial^2 g}{\partial x^2}$, $\frac{\partial^2 g}{\partial x \partial y}$ and $\frac{\partial^2 g}{\partial y^2}$.

The accuracy of linear filters can be defined with respect to two different criteria. The first is the amount of systematic errors, which can be defined by the deviations between the responses of the examined filter and an ideal filter. The second criterium is the statistical error of the filter response if the signal, i.e. the image data, is contaminated with noise.

At first an analysis of systematic errors of different filters will be given in the following. Therefore the response of a discrete linear shift-invariant 1D filter h_x ($x=0..N-1$) is characterized by its so-called *transfer function*, i.e. its discrete fourier transform

$$\tilde{h}_k = \frac{1}{\sqrt{N}} \sum_{x=0}^{N-1} h_x \exp\left(-\frac{2\pi i k x}{N}\right), \quad k = 1..N-1. \quad (7.75)$$

The inverse discrete fourier transform is given by

$$h_x = \frac{1}{\sqrt{N}} \sum_{k=0}^{N-1} \tilde{h}_k \exp\left(\frac{2\pi i k x}{N}\right), \quad x = 1..N-1. \quad (7.76)$$

The importance of this fourier space representation comes from the fact that the convolution of a 1D signal g_x ($x=0..N-1$) with the filter h_x , $g' = h * g$, corresponds to a pointwise multiplication in fourier space:

$$g'_x = \sum_{x'=0}^{N-1} h_{x'} g_{x-x'} \Leftrightarrow \tilde{g}'_k = \tilde{h}_k \cdot \tilde{g}_k \quad (7.77)$$

Furthermore, also the partial derivatives $\partial/\partial x$, $\partial^2/\partial x^2$ etc. can be written as a multiplication in fourier space:

$$g'_x = \partial g / \partial x \Leftrightarrow \tilde{g}'_k = 2\pi i k \tilde{g}_k \quad (7.78)$$

$$g''_x = \partial^2 g / \partial x^2 \Leftrightarrow \tilde{g}''_k = -4\pi^2 k^2 \tilde{g}_k \quad (7.79)$$

$$g^{(n)}_x = \partial^n g / \partial x^n \Leftrightarrow \tilde{g}^{(n)}_k = (2\pi i k)^n \tilde{g}_k \quad (7.80)$$

This formalism can easily be extended to analogous formulations in higher dimensions (see Jähne (2002)). From this it is now possible to evaluate the systematic errors of different first and second order derivative filters by comparing their transfer functions with the reference functions 7.78 and 7.79. Table 7.2 shows the definitions of the first order derivative filters h_{x1} , h_{x2} , h_{x3} and $h_{xcutoff}$ and of the corresponding second order derivative filters h_{xx1} , h_{xx2} , h_{xx3} and $h_{xxcutoff}$. h_{x1} and h_{x3} are the 3- and 5-element filters that have been optimized by Scharf (2000) with respect to minimum deviation from the reference function. h_{x2} is a 5-element filter which is damped at high frequencies. $h_{xcutoff}$ is defined by its fourier transform $\tilde{h}_{xcutoff}$, and therefore it is applied to the fourier transform of a signal by pointwise multiplication according to equation 7.77. It is equal to the reference function 7.78 for $k < k_{cutoff}$ and zero for $k \geq k_{cutoff}$. The corresponding second order filters h_{xx1} , h_{xx2} , h_{xx3} and $h_{xxcutoff}$ are defined analogously (see table 7.2). Figure 7.10a shows the absolute value of the transfer functions of the first order derivative filters together with the reference function, and figure 7.10c shows the deviations from the reference function. The same is shown for the second order filters in figure 7.10b+d. Obviously all filters are close to the reference for low frequencies. For higher frequencies, the optimized 5-/9-element filters h_{x3}/h_{xx3} are the best, followed by the optimized 3-/5-element filters h_{x1}/h_{xx1} . The filters h_{x2}/h_{xx2} show the highest damping at high frequencies. For further analysis a test signal g_{gauss} was generated as

$$g_{gauss}(x) = 250 \cdot e^{-\frac{(x-x_0)^2}{2\sigma^2}}, \quad x_0 = 100, \sigma = 12, x = 1..256. \quad (7.81)$$

The signal and the absolute value of its fourier transform are shown in figure 7.10e+f. The filters were then used to estimate the derivatives from the data. Figure 7.10g+h show the

First order derivative filters		
Notation	Definition	Comments
$h_{x\text{ref}}$	$\tilde{h}_{x\text{ref}}(k) = ik$	Reference function.
h_{x1}	$h_{x1} = [-1\ 0\ 1]/2$	Optimal 3-element filter (Scharr, 2000).
h_{x2}	$h_{x2} = [-2\ -1\ 0\ 1\ 2]/10$	5-element filter with damping for high frequencies.
h_{x3}	$h_{x3} = [1\ -6\ 0\ 6\ -1]/8$	Optimal 5-element filter (Scharr, 2000).
$h_{x\text{cutoff}}$	$\tilde{h}_{x\text{cutoff}} = \begin{cases} ik & k < k_{\text{cutoff}} \\ 0 & k \geq k_{\text{cutoff}} \end{cases}$	Reference function with cut-off at $k = k_{\text{cutoff}}$.
$h_{x\text{Wiener}}$	see equation 7.83	Wiener filter calculated with equation 7.83 using the spectral density $\ \tilde{g}_{\text{gauss}}(k)\ ^2$ and assuming white noise with $\sigma^2 = 1$.
Second order derivative filters		
Notation	Definition	Comments
$h_{xx\text{ref}}$	$\tilde{h}_{xx\text{ref}} = -k^2$	Reference function.
h_{xx1}	$h_{xx1} = h_{x1} * h_{x1}$ $= [1\ 0\ -2\ 0\ 1]/4$	Optimal 5-element filter.
h_{xx2}	$h_{xx2} = h_{x2} * h_{x2}$ $= [4\ 4\ 1\ -4\ -10\ -4\ 1\ 4\ 4]/100$	9-element filter with damping for high frequencies.
h_{xx3}	$h_{xx3} = h_{x3} * h_{x3}$ $= [1\ -12\ 36\ 12\ -74\ 12\ 36\ -12\ 1]/64$	Optimal 9-element filter.
$h_{xx\text{cutoff}}$	$\tilde{h}_{xx\text{cutoff}} = \begin{cases} -k^2 & k < k_{\text{cutoff}} \\ 0 & k \geq k_{\text{cutoff}} \end{cases}$	Reference function with cut-off at $k = k_{\text{cutoff}}$.
$h_{xx\text{Wiener}}$	see equation 7.83	Wiener filter calculated with equation 7.83 using the spectral density $\ \tilde{g}_{\text{gauss}}(k)\ ^2$ and assuming white noise with $\sigma^2 = 1$.

Table 7.2: Definitions of first and second order derivative filters.

results together with the analytical solution, and figure 7.10i+j show the deviations from the analytical solution. Since the signal is restricted to low frequencies (see figure 7.10f), it is no surprise that $h_{x\text{cutoff}}$ and $h_{xx\text{cutoff}}$ coincide with the analytical solution, and also the other filters perform reasonably well. As expected, h_{x3}/h_{xx3} show the smallest deviations, followed by h_{x1}/h_{xx1} and h_{x2}/h_{xx2} .

In the following now the statistical error of the derivative filters, i.e. the statistical error of the estimated derivatives if the data is contaminated with noise, will be examined. Typically image data is always affected by noise from various sources, at least from quantization noise due to the restriction to 8-bit integer values, and further e.g. from thermal CCD noise or electronics noise (see section 5.5). Typically it is assumed as a first approximation that the noise $n(x)$ of adjacent pixels x and $x + 1$ is not correlated, which leads to a constant so-called *white* noise spectrum

$$\|\tilde{n}\|^2(k) = \sigma_n^2, \quad \text{with} \quad \sigma_n^2 = \langle n^2 \rangle. \quad (7.82)$$

For the following examinations the test signal g_{gauss} (equation 7.81) was contaminated firstly with quantization noise, i.e. rounded to integer values and secondly with white gaussian noise

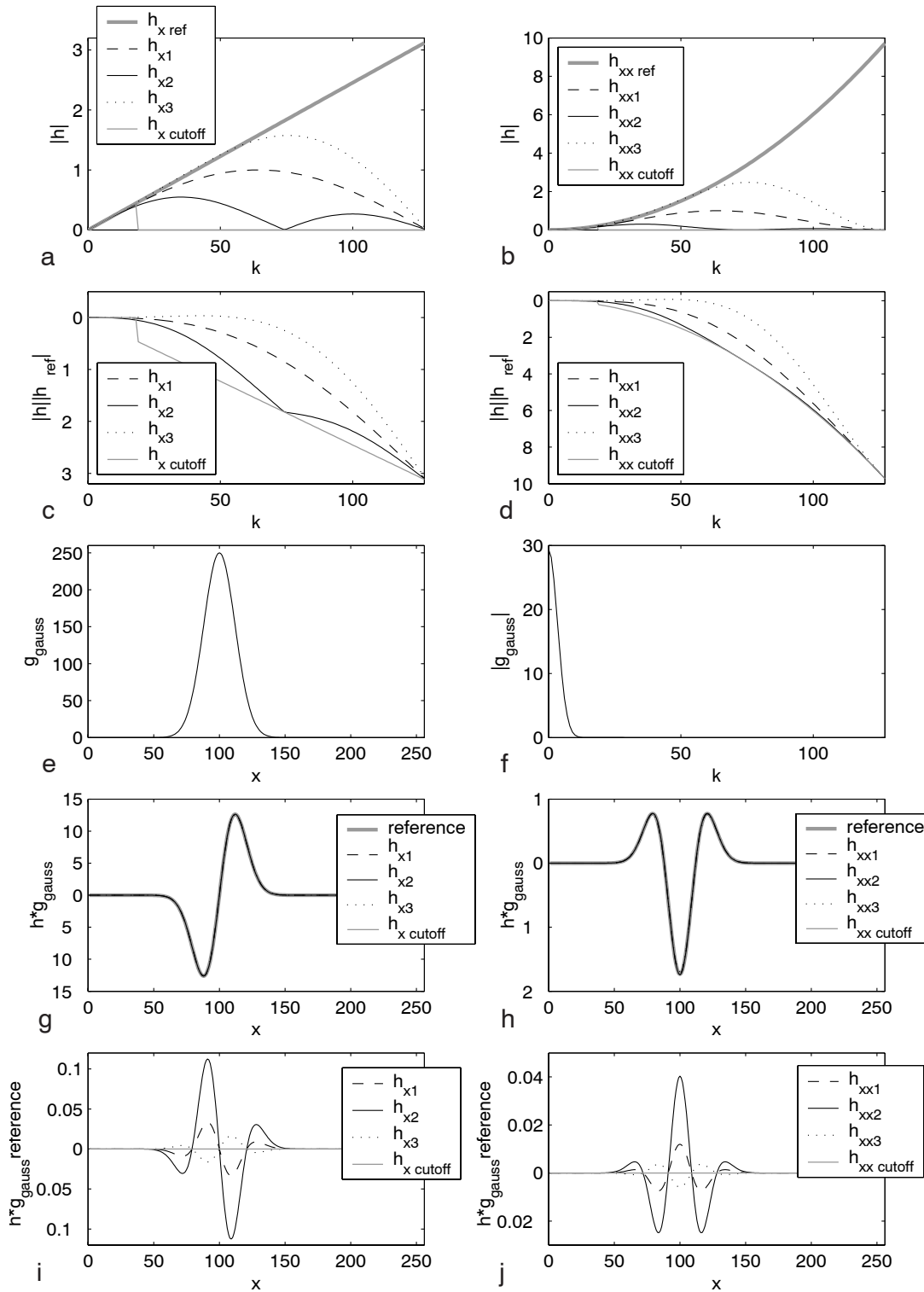


Figure 7.10: Comparison of 1D derivative filters with respect to systematic error: Transfer functions of **a** first order and **b** second order filters. Deviations from reference for **c** first order and **d** second order filters. **e** Test signal (gaussian curve) and **f** corresponding fourier spectrum. Estimation of **g** first order and **h** second order derivative and **i+j** deviations from reference.

with $\sigma_n^2 = 1$ as shown in figure 7.11c+d. The corresponding logarithmized absolute values of the fourier spectra are given in figure 7.11e+f, showing that for high k the spectra are fully dominated by noise close to the analytical values $\log(\|\tilde{n}\|_{\text{quant}}) = \log(\frac{1}{\sqrt{12}}) = -1.24$ and $\log(\|\tilde{n}\|_{\text{white}}) = \log(\sigma) = 1$. The problem of finding an optimal filter in the presence of noise was firstly solved independently by Wiener (1942) and Kolmogoroff (1941). If the spectra of the unperturbed signal g and the noise n are known, the filter h_{Wiener} which is optimal in the sense of minimum squared deviations from the unperturbed result $h * g$ is given by (see e.g. Hänsler (2001)):

$$\tilde{h}_{\text{Wiener}}(k) = \tilde{h}(k) \frac{\|\tilde{g}(k)\|^2}{\|\tilde{g}(k)\|^2 + \|\tilde{n}(k)\|^2}. \quad (7.83)$$

This relation was used to calculate $h_{x\text{Wiener}}$ and $h_{xx\text{Wiener}}$ for $\tilde{h}(k) = \tilde{h}_{x\text{ref}}(k)/\tilde{h}_{xx\text{ref}}(k)$, $\|\tilde{g}(k)\|^2 = \|\tilde{g}_{\text{gauss}}(k)\|^2$ and $\|\tilde{n}(k)\|^2 = 1$. The results are shown together with the reference functions and $h_{x\text{cutoff}}/h_{xx\text{cutoff}}$ in figure 7.11a+b. As expected the Wiener filters are close to the reference function where the signal is stronger than noise and otherwise close to zero. Then the estimated first order derivatives of the signal with white noise ($\sigma_n^2 = 1$), obtained by the filters h_{x2} , h_{x3} , $h_{x\text{cutoff}}$ and $h_{x\text{Wiener}}$ are compared to the analytical reference function as shown in figure 7.11g+i. As expected the Wiener filter shows the smallest deviations from the reference. The deviations of the cutoff filter are only little higher. Both h_{x2} and h_{x3} show considerable deviations, but those of h_{x3} are significantly higher. Similar results were obtained for the corresponding second order derivatives shown in figure 7.11h+j. Here the deviations of h_{xx2} and most notably those of h_{xx3} are even higher.

The results discussed above lead to some important conclusions concerning the prospective choice of optimal filters for the TLS parameter estimation technique described in section 7.2. The results have shown that already a small amount of noise ($\sigma^2 = 1$, see figure 7.11c+d) can have large impact on the estimation of the first order, and even more on the second order derivative. The filters that were optimized for minimal systematic error, h_{x3} and h_{xx3} , proved to be most susceptible to noise. Thus the optimization with respect to statistical errors is much more important than to systematic error in practical applications. It is therefore necessary to take into account the spectral properties of the signal and noise for suitable choice of derivative filters. Often the spectrum of the signal is not a priori known, so that the optimal Wiener filter given by equation 7.83 cannot be used. However, if the spectrum is known to be restricted to a range $k < k_{\text{cutoff}}$, a corresponding cutoff filter can be used which gives results that are comparable to those of the Wiener filter as shown in figure 7.11i+j. Since the example of the gaussian signal g_{gauss} used above is quite similar to the data measured in this work (i.e. solutions of a convection-dispersion equation), the employment of cutoff filters seems reasonable. For other applications, where the spectrum of the data is not bandlimited, other methods are available to reduce noise before estimating the derivatives, like e.g. anisotropic diffusion (Scharf, 2000), cubic smoothing splines (Green & Silverman (1994) and appendix A), wavelets or simulated annealing.

Until now only 1D filters were considered. If the data has two or more dimensions, the derivative filters discussed above can be extended accordingly. This offers the possibility to further reduce noise by the application of a smoothing filter perpendicular to the direction of the derivative. As an example the 2D so-called *Sobel operator*

$$h_{x\text{Sobel}} = \frac{1}{2} \begin{pmatrix} 1 & 0 & -1 \end{pmatrix} * \frac{1}{4} \begin{pmatrix} 1 \\ 2 \\ 1 \end{pmatrix} = \frac{1}{8} \begin{pmatrix} 1 & 0 & -1 \\ 2 & 0 & -2 \\ 1 & 0 & -1 \end{pmatrix} \quad (7.84)$$

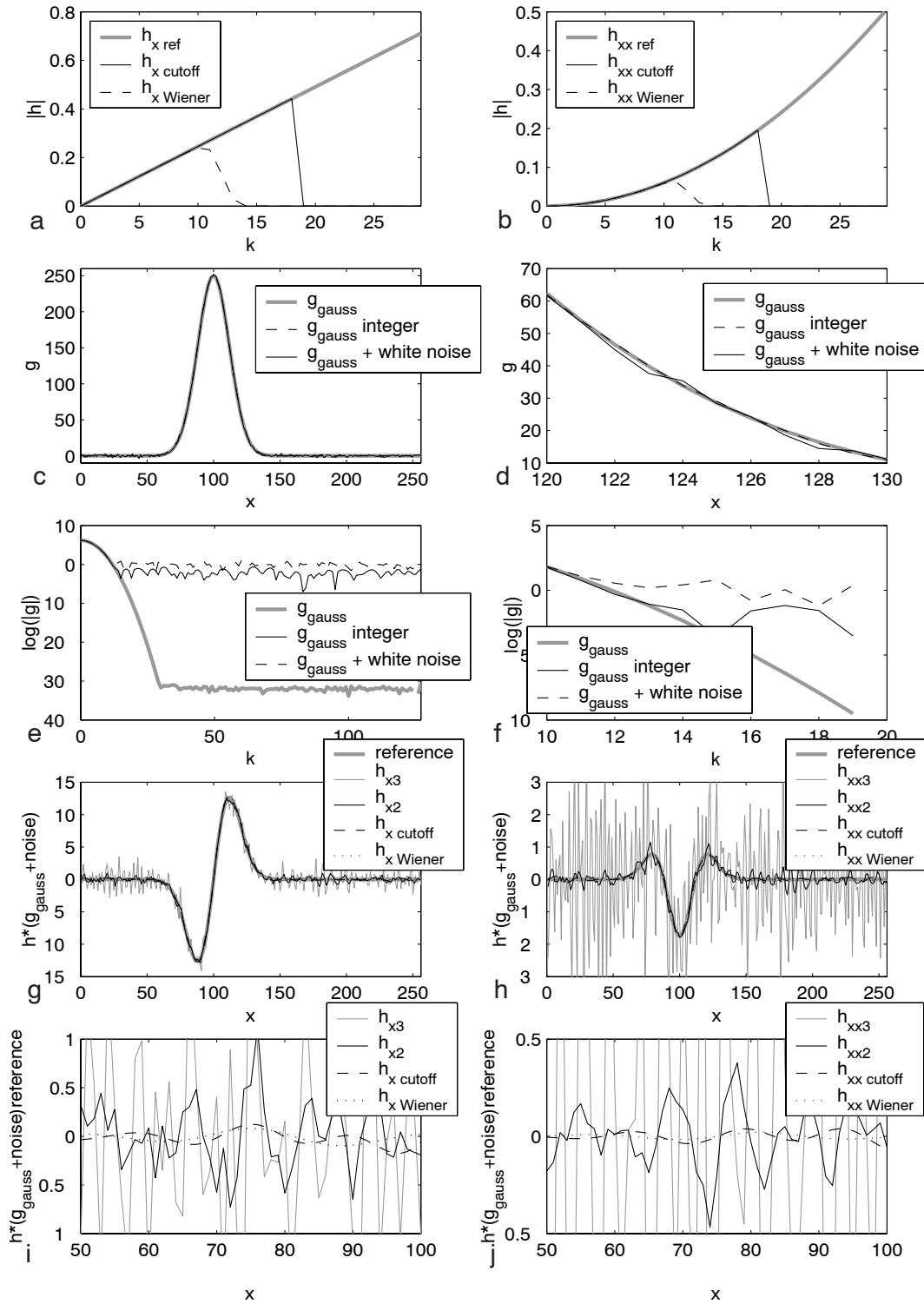


Figure 7.11: Comparison of 1D derivative filters with respect to statistical error: Transfer functions of **a** first order and **b** second order filters. **c+d** Test signal (gaussian curve) with quantization noise and white noise ($\sigma^2 = 1$). **e+f** Corresponding fourier spectra. Estimation of **g** first order and **h** second order derivatives from the test signal with white noise and **i+j** deviations from reference.

3D filter set	1D first order derivative ($i \in \{x, y, t\}$)
h_2	$h_{2i\ 1D} = [-2\ -1\ 0\ 1\ 2]/10$
h_3	$h_{3i\ 1D} = [1\ -6\ 0\ 6\ -1]/8$
h_{cutoff}	$\tilde{h}_{\text{cutoff}i\ 1D} = \begin{cases} ik & k < k_{\text{cutoff}} \\ 0 & k \geq k_{\text{cutoff}} \end{cases}$
3D filter set	1D second order derivative ($i \in \{xx, yy\}$)
h_2	$h_{2i1D} = [4\ 4\ 1\ -4\ -10\ -4\ 1\ 4\ 4]/100$
h_3	$h_{3i1D} = [1\ -12\ 36\ 12\ -74\ 12\ 36\ -12\ 1]/64$
h_{cutoff}	$\tilde{h}_{\text{cutoff}i\ 1D} = \begin{cases} -k^2 & k < k_{\text{cutoff}} \\ 0 & k \geq k_{\text{cutoff}} \end{cases}$
3D filter set	1D smoothing ($i \in \{x, y, t\}$)
h_2	$h_{2\ \text{smooth}i} = [1\ 4\ 6\ 4\ 1]/16$
h_3	$h_{3\ \text{smooth}i} = [1\ 4\ 6\ 4\ 1]/16$
h_{cutoff}	$\tilde{h}_{\text{cutoff}\ \text{smooth}i} = \begin{cases} 1 & k < k_{\text{cutoff}} \\ 0 & k \geq k_{\text{cutoff}} \end{cases}$

Table 7.3: 3D derivative filter sets used for the TLS parameter estimation. Each set is composed of 1D first and second order derivatives and perpendicular 1D smoothing filters in x-, y-, and t-direction respectively.

uses the filter $[1, 0, -1]/2$ for the horizontal derivative and the $[1, 2, 1]/4$ filter mask for smoothing in the vertical direction. For the selection of the filters for perpendicular smoothing the above considerations apply correspondingly. For data with bandlimited spectra for instance cutoff filters can be used.

In the following now the above discussed sets of derivative filters will be applied in a TLS parameter estimation in order to investigate the influence of the filter accuracy on the accuracy of the TLS parameters. Therefore a synthetic image sequence of a simulated 2D convection-dispersion process according to equation 7.53 was generated as shown in figure 7.12. The parameters used for the simulation,

$$\vec{v} = \begin{pmatrix} v_x \\ v_y \end{pmatrix} = \begin{pmatrix} 4.70 \\ -1.71 \end{pmatrix} \Leftrightarrow \|\vec{v}\| = 5, \quad (7.85)$$

$$D = \begin{pmatrix} D_{xx} & D_{xy} \\ D_{xy} & D_{yy} \end{pmatrix} = \begin{pmatrix} 7.03 & -1.29 \\ -1.29 & 3.97 \end{pmatrix} \Leftrightarrow D_L = 7.5, D_T = 3.5, \quad (7.86)$$

were constant over space and time, resulting in a constant true parameter vector (see table

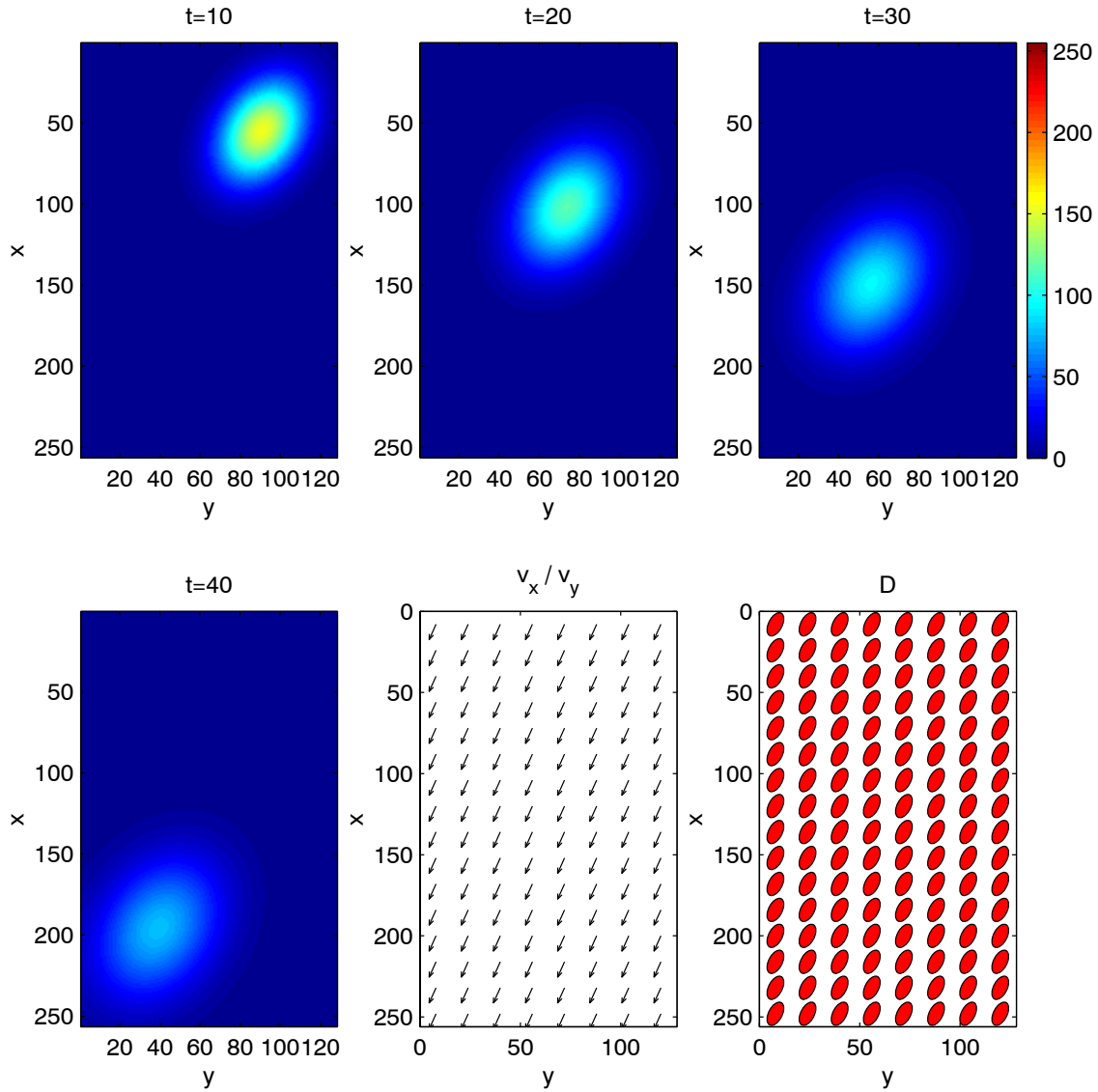


Figure 7.12: Synthetic test data set of a simulated 2D convection-dispersion process used for the performance analysis of TLS parameter estimation. The data set, which consists of 50 2D images ($x = 1..256$, $y = 1..128$, $t = 1..50$), is shown for $t = 10, 20, 30$ and 40 . The parameters $v_x = 4.70$, $v_y = -1.71$ (plotted as vectors), $D_{xx} = 7.03$, $D_{xy} = -1.29$ and $D_{yy} = 3.97$ (represented as ellipses) used for the simulation are constant in space and time. For better visibility the velocity vectors in the illustration are scaled with a factor 2.

7.1)

$$\vec{p}_{\text{true}} = \begin{pmatrix} 4.70 \\ -1.71 \\ -7.03 \\ 2.57 \\ -3.97 \\ 1 \end{pmatrix}. \quad (7.87)$$

Three different sets of derivative filters, based on the 1D filter sets h_2 , h_3 and h_{cutoff} given in table 7.2 were chosen for a comparison. The 1D derivative filters were extended to 3D filters using appropriate perpendicular 1D smoothing filters, in analogy to equation 7.84 for the 2D sobel operator. The utilized 1D filters for the three filter sets are given in table 7.3. As an example, the resulting 3D first derivative in y-direction for the filter set h_2 is given by

$$h_{2y3D} = h_{2y1D} * h_{2\text{smooth } x} * h_{2\text{smooth } t}. \quad (7.88)$$

For the comparison of the different filter sets the simulated test data shown in figure 7.12 was contaminated with additive white gaussian noise with variance $\sigma^2 = 1$. For the following TLS parameter estimation the equilibration weight matrix W_R was calculated according to equation 7.70, and a box shaped averaging filter mask B with a window size of (15 15 21) in x-, y-, and t-direction was applied according to equation 7.69. Figure 7.13 shows the estimated parameters \vec{p}_{est} and the logarithmic relative error given by

$$\log\left(\frac{\|\Delta\vec{p}\|}{\|\vec{p}\|}\right) = \log\left(\frac{\|\vec{p}_{\text{est}} - \vec{p}_{\text{true}}\|}{\|\vec{p}_{\text{est}}\|}\right) \quad (7.89)$$

for each filter set at $t = 20$ and $x = 8, 24, 40, \dots, 248/y = 8, 24, 40, \dots, 120$. The vectors and ellipses representing the velocities and dispersivities and only plotted for $\log(\frac{\|\Delta\vec{p}\|}{\|\vec{p}\|}) < 1$. As expected from the above discussed noise sensitivities of the corresponding 1D filters (see figure 7.11), the filter set h_{cutoff} leads to the best results, while h_2 gives only few and h_3 gives no results within the given error range. The following conclusions can be drawn from these results:

- the choice of filters for the estimation of the derivatives has an immense, i.e. orders of magnitude, influence on the accuracy of the estimated parameters. If filters are not chosen carefully, a big part of the information contained in the data is not accessible!
- the differences in accuracy for the three filter sets mostly come from their different susceptibilities to noise, which can be directly seen from their transfer functions in figures 7.10 and 7.11. The systematic errors of the filter sets in contrast have only minor influences here. It is therefore absolutely necessary that the chosen filters are optimized with respect to statistical error!
- obviously the errors in dispersivity are significantly higher than those for the velocities. This can be readily explained by the higher uncertainties of the second order derivatives as shown in figure 7.11g+h.

Finally it is noted that the choice of optimal filters strongly depends on the properties of the data. If the images e.g. contain sharp edges or discontinuous motion, the systematic

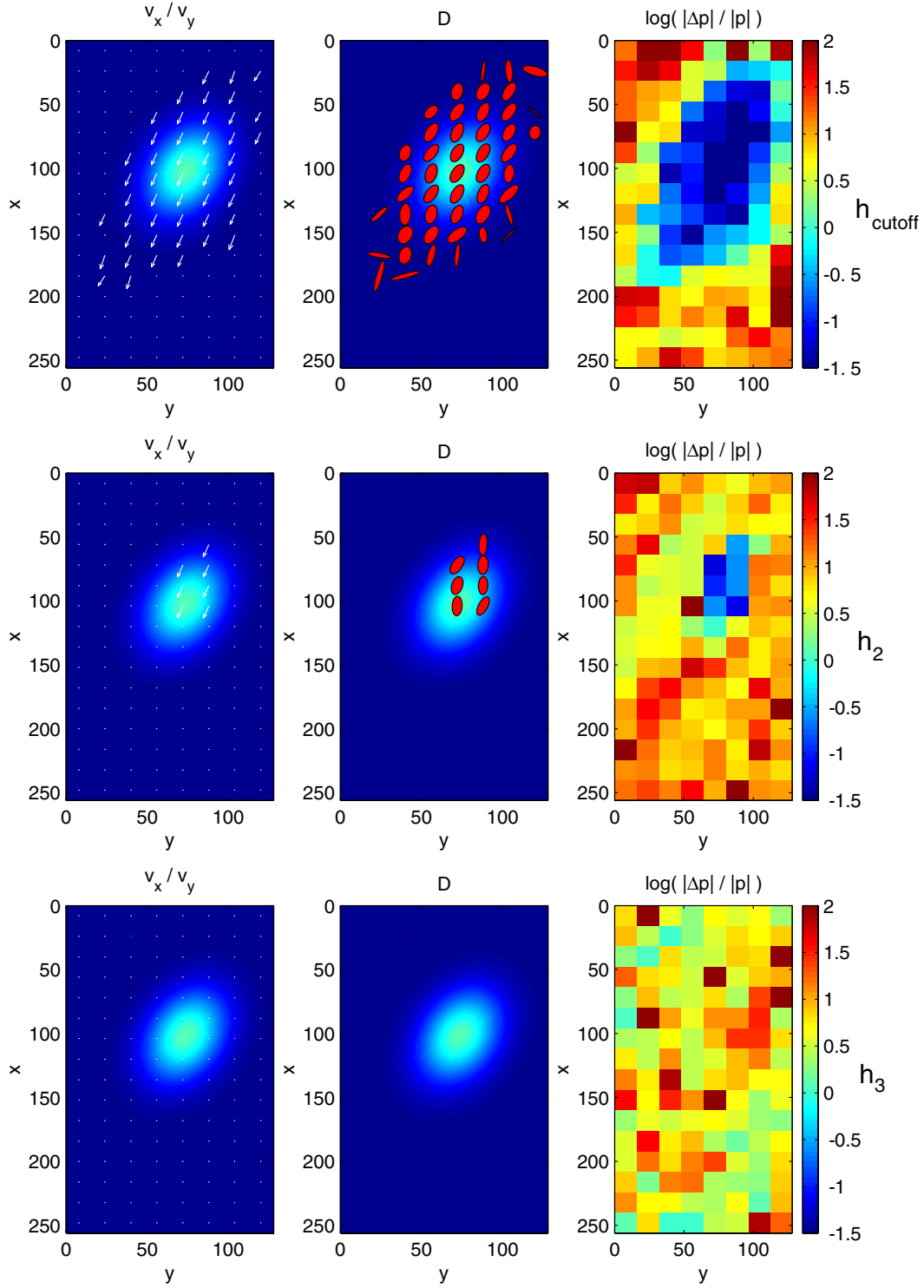


Figure 7.13: Velocities and dispersion tensors estimated from the simulated test data (shown in figure 7.12) contaminated with white noise of variance $\sigma^2 = 1$. Each row shows the results for one of the derivative filter sets given in table 7.3. The right column shows the logarithmic relative error as defined in equation 7.89.

error at high frequencies will become significant, and a cutoff filter will not be a good solution. However, there are other methods to reduce noise in these situations, like the above mentioned anisotropic diffusion (Schar, 2000), wavelets, simulated annealing or smoothing splines (Green & Silverman (1994) and appendix A).

7.4.2 Noise sensitivity

Whereas for parameter estimation problems solved with OLS methods the error in the estimated parameters can be directly related to the error in the data through a covariance matrix as defined in equations 6.13 and 6.14, no such direct relation exists for the TLS parameter estimation. As stated in Mühlich & Mester (1999), subspace methods are relatively insensitive against low noise levels, whereas higher noise levels can change the order of the eigenvalues and the associated eigenvectors. If this happens, the impairment of the result is very severe, since the eigenvectors are pairwise orthogonal.

The simulated test data shown in figure 7.12 offers the opportunity to numerically evaluate the relation between errors in the data and the estimated parameters. In figure 7.14, the parameters (estimated with the cutoff derivative filters at $t = 20$) and their relative error are shown for different noise levels σ_d^2 . As discussed in section 7.4.1, the accuracy of the estimated parameters strongly depends on the choice of the derivative filters. Therefore the relative error of the estimated parameters at the position $x = 104$, $y = 72$ has been computed with the three filter sets given in table 7.3 for different noise levels, as shown in figure 7.15. For $\sigma_d^2 < 0.01$ all filter sets have relative errors smaller than one, with those of h_2 and h_3 proving to be very insensitive to the noise level. At $\sigma_d^2 \approx 0.02$, the relative errors of h_2 and h_3 abruptly increase to significantly higher values. h_2 shows a second transition at $\sigma_d^2 \approx 1$. For h_{cutoff} , the relative errors are smaller than one for $\sigma_d^2 < 100$, and then a transition occurs to a rather common level with h_2 and h_3 .

7.4.3 Choice of equilibration weight matrix

As mentioned in section 7.3.6 the different magnitudes of statistical error σ_i^2 for the elements d_i of the data \vec{d} must be taken into account for the correct estimation of the parameters \vec{p} through the application of an equilibration matrix W_R . Therefore the elements $1/\sigma_i$ of W_R must be known prior to the estimation. Under the assumption that the data is contaminated with additive white noise, the σ_i^2 can be calculated from a given filter mask according to equation 7.70. If the filter is defined by its transfer function $\tilde{h}_i(k)$ (like a Wiener filter or the cutoff filters in table 7.3), the σ_i^2 can be determined from the noise spectrum of the image data $\tilde{n}(k)$ ($\tilde{n}(k) = \sigma_d$ for white noise) through the use of the inverse discrete fourier transform 7.76:

$$\sigma_i^2 = \frac{1}{N} \sum_{k=0}^{N-1} \|\tilde{h}_i(k)\tilde{n}(k)\|^2 \stackrel{\tilde{n}(k)=\sigma_d}{=} \frac{1}{N} \sigma_d^2 \sum_{k=0}^{N-1} \|\tilde{h}_i(k)\|^2 \quad (7.90)$$

In order to validate the weight matrices W_R used for the TLS estimation, the values of σ_i^2 calculated analytically from equations 7.70 and 7.90 were compared to the effective values obtained numerically from the differences $\Delta\vec{d} = \vec{d} - \vec{d}_{\text{true}}$ between the estimated derivatives \vec{d} and the a priori known analytical derivatives \vec{d}_{true} . Table 7.4 compares the analytically calculated covariance matrices $C_{ij} = \sigma_i^2 \delta_{ij}$ with the numerically obtained covariance matrices $C = \langle (\vec{d} - \vec{d}_{\text{true}})(\vec{d} - \vec{d}_{\text{true}})^T \rangle$ for each of the three filter sets. For the filter sets h_{cutoff} and

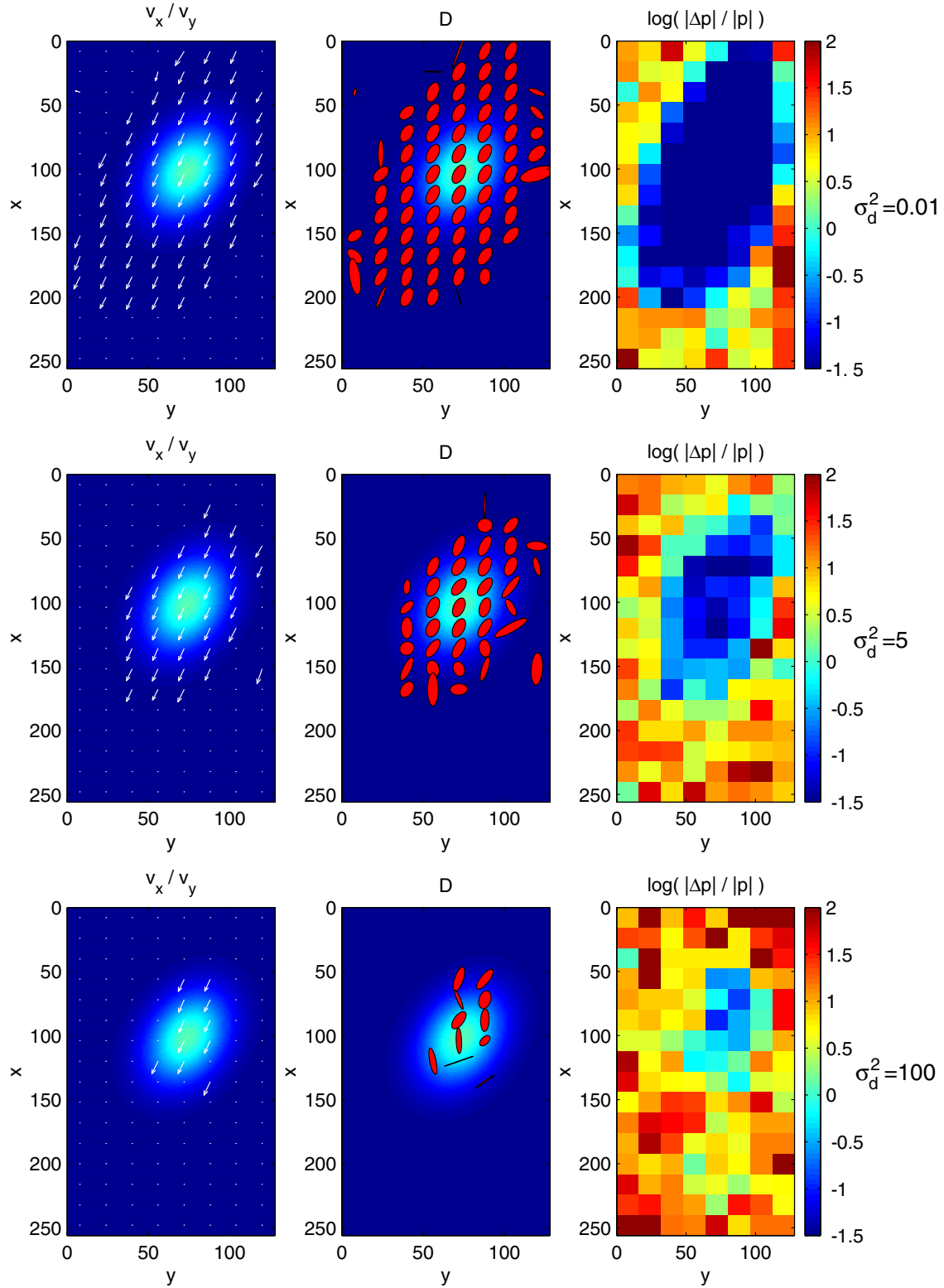


Figure 7.14: Estimated velocities and dispersion tensors calculated from the simulated test data shown in figure 7.12 contaminated with different noise levels $\sigma_d^2 = 0.01, 5$ and 100 , using the filter set h_{cutoff} . The results for $\sigma_d^2 = 1$ are given in figure 7.13.

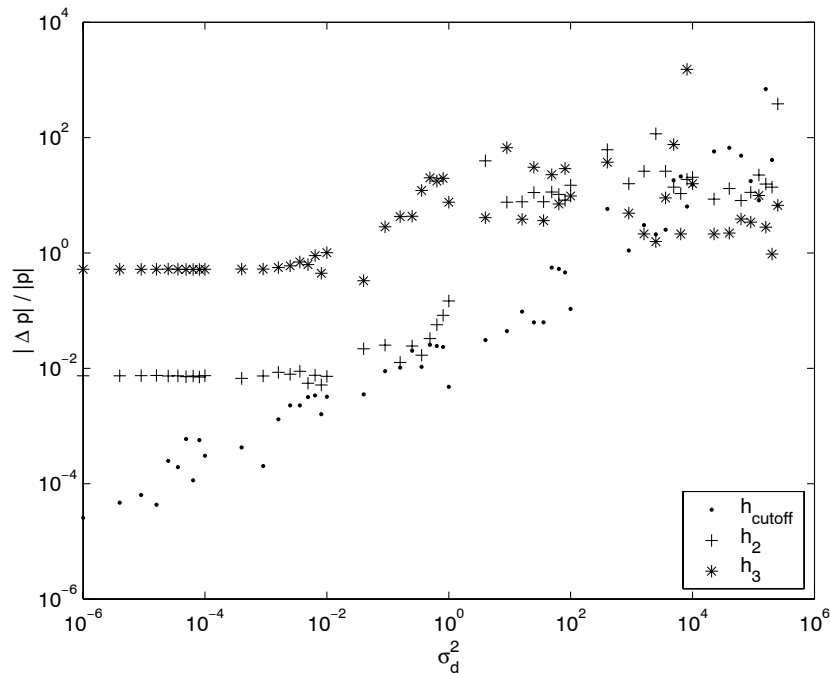


Figure 7.15: Accuracy of estimated parameters as a function of noise level in the data. The parameters have been estimated from the simulated test data shown in figure 7.12 using three different sets of derivative filters given in table 7.3.

h_3 the comparison shows a satisfactory agreement between analytical and numerical values. For the filter set h_2 , some of the numerically obtained errors are higher than the analytically predicted values. This is caused by systematic errors: whereas h_{cutoff} and h_3 are close to the reference function and therefore systematic errors are low (see figure 7.10), the systematic errors become significant for h_2 . Here now the question arises if the accuracy can be further enhanced by including the systematic errors into the equilibration matrix W_R . Therefore the estimation for the filter set h_2 was recalculated using the numerically obtained variances shown in table 7.4, which include systematic errors. The result shown in figure 7.16 indicates primarily an enhancement of accuracy, although few values slightly lost accuracy. However, it is generally not possible to directly quantify the error caused by the systematic deviations of the transfer function. But even if there is only some rough estimate available, it may be reasonable to take it into account. Finally the importance of a careful choice of W_R is further emphasized by the loss of accuracy in the results obtained for $W_R = \mathbb{1}$ shown in figure 7.16.

7.4.4 Confidence measure

The presented TLS parameter estimation technique still lacks a measure of confidence for the estimated parameters. The values of the estimated parameters are of no use if no information about their uncertainty is available. It would therefore be desirable to have a quantity which correlates as strong as possible with the relative error $\frac{\|\Delta\hat{p}\|}{\|\hat{p}\|}$ of the estimation. Obviously the quality of the estimation will depend both on the noise and on the amount of structure in the data. In section 7.3.6 two relevant quantities, the smallest eigenvalue λ_n and the trace $\text{tr}(J)$

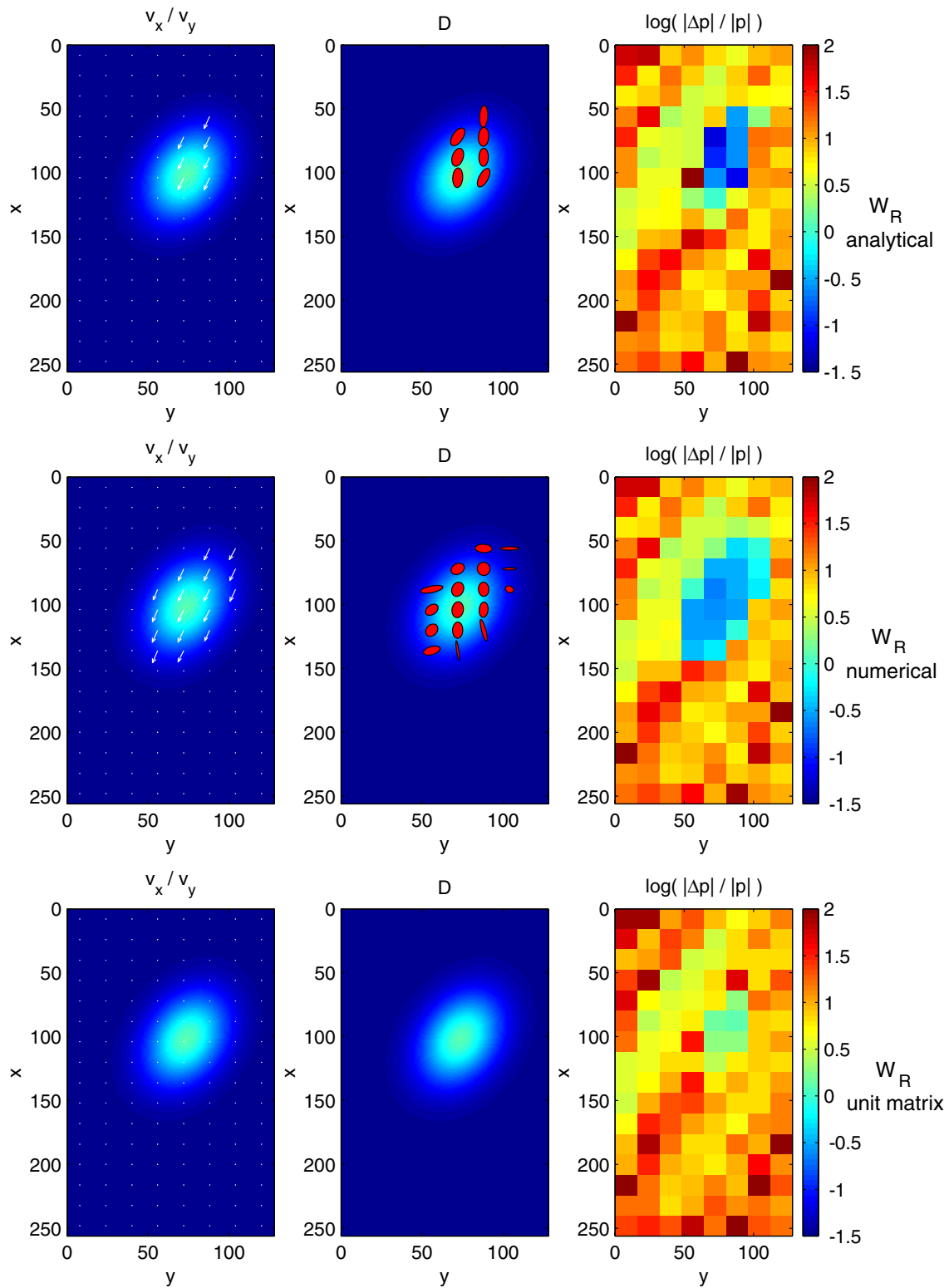


Figure 7.16: TLS parameter estimation with the filter set h_2 using different equilibration weight matrices: The results obtained with the analytical W_R (upper row) can be further enhanced by using a numerically estimated W_R which contains all types of error (middle row). The TLS estimation without equilibration ($W_R = \mathbb{I}$, lower row) strongly reduces accuracy.

filter set	$C_{\text{analytical}}$	$C_{\text{numerical}}$
h_{cutoff} [$\cdot 10^{-3}$]	$\begin{pmatrix} 0.9799 & 0 & 0 & 0 & 0 & 0 \\ 0 & 0.0600 & 0 & 0 & 0 & 0 \\ 0 & 0 & 0.1821 & 0 & 0 & 0 \\ 0 & 0 & 0 & 0.0021 & 0 & 0 \\ 0 & 0 & 0 & 0 & 0.0190 & 0 \\ 0 & 0 & 0 & 0 & 0 & 0.0035 \end{pmatrix}$	$\begin{pmatrix} 0.9338 & 0.0025 & 0.0454 & -0.0018 & 0.0088 & -0.0068 \\ 0.0025 & 0.0741 & 0.0091 & -0.0019 & -0.0067 & -0.0002 \\ 0.0454 & 0.0091 & 0.2089 & 0.0021 & 0.0010 & -0.0002 \\ -0.0018 & -0.0019 & 0.0021 & 0.0027 & 0.0047 & 0.0001 \\ 0.0088 & -0.0067 & 0.0010 & 0.0047 & 0.0223 & 0.0004 \\ -0.0068 & -0.0002 & -0.0002 & 0.0001 & 0.0004 & 0.0037 \end{pmatrix}$
h_2	$\begin{pmatrix} 0.0075 & 0 & 0 & 0 & 0 & 0 \\ 0 & 0.0075 & 0 & 0 & 0 & 0 \\ 0 & 0 & 0.0075 & 0 & 0 & 0 \\ 0 & 0 & 0 & 0.0015 & 0 & 0 \\ 0 & 0 & 0 & 0 & 0.0015 & 0 \\ 0 & 0 & 0 & 0 & 0 & 0.0027 \end{pmatrix}$	$\begin{pmatrix} 0.2160 & -0.0332 & 0.0117 & 0.0008 & 0.0001 & -0.0003 \\ -0.0332 & 0.0136 & -0.0020 & -0.0000 & 0.0002 & 0.0001 \\ 0.0117 & -0.0020 & 0.0092 & -0.0001 & 0.0000 & -0.0001 \\ 0.0008 & -0.0000 & -0.0001 & 0.0017 & 0.0010 & -0.0001 \\ 0.0001 & 0.0002 & 0.0000 & 0.0010 & 0.0016 & -0.0001 \\ -0.0003 & 0.0001 & -0.0001 & -0.0001 & -0.0001 & 0.0030 \end{pmatrix}$
h_3	$\begin{pmatrix} 0.0865 & 0 & 0 & 0 & 0 & 0 \\ 0 & 0.0865 & 0 & 0 & 0 & 0 \\ 0 & 0 & 0.0865 & 0 & 0 & 0 \\ 0 & 0 & 0 & 0.1578 & 0 & 0 \\ 0 & 0 & 0 & 0 & 0.1578 & 0 \\ 0 & 0 & 0 & 0 & 0 & 0.3656 \end{pmatrix}$	$\begin{pmatrix} 0.0856 & 0.0011 & -0.0009 & -0.0009 & -0.0007 & -0.0005 \\ 0.0011 & 0.0933 & -0.0019 & 0.0008 & -0.0007 & -0.0003 \\ -0.0009 & -0.0019 & 0.0799 & -0.0018 & 0.0003 & -0.0008 \\ -0.0009 & 0.0008 & -0.0018 & 0.1623 & 0.0187 & -0.0007 \\ -0.0007 & -0.0007 & 0.0003 & 0.0187 & 0.1542 & -0.0017 \\ -0.0005 & -0.0003 & -0.0008 & -0.0007 & -0.0017 & 0.3359 \end{pmatrix}$

Table 7.4: Comparison of analytically calculated covariance matrices C used for the TLS equilibration with the corresponding covariances obtained numerically from the differences between data and analytical solution. The numerical values are taken from the estimations shown in figure 7.13 at the position $x = 104$, $y = 72$.

of the tensor J have already been introduced. The value of λ_n is an indicator for the noise in the data \vec{d} , $\lambda_n \approx \sigma_d^2$, whereas $\text{tr}(J)$ indicates the amount of structure in the data.

The problem with these two quantities is that they are typically not invariant under a scaling of the data with a factor k :

$$\vec{d}' = k \vec{d} \quad \Rightarrow \quad \lambda'_n = k \lambda_n, \quad \text{tr}(J)' = k \text{tr}(J). \quad (7.91)$$

Since this scaling does not change the estimated parameters, it is clear that a suitable measure of confidence also must be invariant under this scaling. The reason for the scale dependence is that the value of σ_d for the calculation of the equilibration weight matrix W_R according to equations 7.70 and 7.90 is typically not a priori known, and is then set to an arbitrary value, e.g. $\sigma_d = 1$. The lacking knowledge of σ_d does not affect the estimated parameters, since these are scale invariant, but the values of λ_n and $\text{tr}(J)$ are scaled according to equation 7.91.

From this discussion, the ratio $\frac{\lambda_n}{\text{tr}(J)}$ seems to be an appropriate measure of confidence: It fulfils the requirement of scale invariance, and can easily be interpreted as a ratio of noise to signal strength. However, it does not take into account the shape of the window for the averaging over a local neighborhood, which is defined by the shape of the averaging filter mask B in equation 7.69. As shown below, the shape of B has an effect on the noise-to-signal ratio. The correct confidence measure which can be interpreted as the ratio of signal to noise is then given by

$$\omega_{\text{NSR}} = \frac{\lambda_n}{N_B \text{tr}(J)}, \quad (7.92)$$

where N_B denotes the size of the normalized, box-shaped averaging filter B . In the next paragraphs the choice of this confidence measure will be motivated theoretically and validated by numerical results.

The following derivation is based on the assumption that the relative error $\frac{\|\Delta \bar{p}\|}{\|\bar{p}\|}$ of the estimated parameters is correlated with the relative error of the tensor elements J_{ij} . For a box shaped averaging filter mask with N_B elements the tensor elements are given by

$$J_{ij} = \frac{1}{N_B} \sum_{k=1}^{N_B} d_{ik} d_{jk} \quad (7.93)$$

$$= \frac{1}{N_B} \sum_{k=1}^{N_B} (d_{ik0} + \epsilon_{ik})(d_{jk0} + \epsilon_{jk}), \quad (7.94)$$

where the d_{ik0} denote the true data elements, which are contaminated with noise ϵ_{ik} ($\langle \epsilon_{ik} \rangle = 0$, $\langle \epsilon_{ik} \epsilon_{jl} \rangle = \sigma_d^2 \delta_{ij} \delta_{kl}$). The expectation of J_{ij} then becomes

$$\langle J_{ij} \rangle = \frac{1}{N_B} \sum_{k=1}^{N_B} d_{ik0} d_{jk0} + \sigma_d^2 \delta_{ij}. \quad (7.95)$$

The variance of J_{ij} is then given by

$$\langle (J_{ij} - \langle J_{ij} \rangle)^2 \rangle = \langle \left(\frac{1}{N_B} \sum_{k=1}^{N_B} d_{ik0} \epsilon_{jk} + d_{jk0} \epsilon_{ik} + \epsilon_{ik} \epsilon_{jk} - \sigma_d^2 \delta_{ij} \right)^2 \rangle \quad (7.96)$$

$$= \frac{1}{N_B^2} \langle \sum_{k=1}^{N_B} d_{ik0}^2 \epsilon_{jk}^2 + d_{jk0}^2 \epsilon_{ik}^2 + \epsilon_{ik}^2 \epsilon_{jk}^2 + \sigma_d^4 \delta_{ij} \rangle \quad (7.97)$$

$$\sigma_d^2 \ll d_{ik0}^2 \approx \frac{1}{N_B^2} \sigma_d^2 \sum_{k=1}^{N_B} d_{ik0}^2 d_{jk0}^2 \quad (7.98)$$

For the diagonal elements ($i = j$) this transforms into

$$\langle (J_{ii} - \langle J_{ii} \rangle)^2 \rangle \approx \frac{1}{N_B^2} \sigma_d^2 2 \sum_{k=1}^{N_B} d_{ik0}^2 \quad (7.99)$$

and the squared relative error is given by

$$\frac{\sigma_{J_{ii}}^2}{J_{ii}^2} = \frac{\frac{1}{N_B^2} \sigma_d^2 2 \sum_{k=1}^{N_B} d_{ik0}^2}{\left(\frac{1}{N_B} \sum_{k=1}^{N_B} d_{ik0}^2 \right)^2} = \frac{1}{N_B} \frac{2\lambda_n}{J_{ii}}. \quad (7.100)$$

In order to equally account for all elements of $\text{tr}(J)$, the value of J_{ii} is replaced by the mean of the diagonal elements

$$\overline{J_{ii}} = \frac{1}{n} \sum_{i=1}^n J_{ii} = \frac{1}{n} \text{tr}(J), \quad (7.101)$$

so that the squared relative error of the mean diagonal element is given by

$$\frac{\sigma_{\overline{J_{ii}}}^2}{\overline{J_{ii}}^2} = \frac{2n\lambda_n}{N_B \text{tr}(J)}. \quad (7.102)$$

If the above assumption, that the relative error of the estimated parameters is correlated with the relative error of the tensor elements J_{ij} is correct, this result leads to the confidence measure ω_{NSR} given by equation 7.92 (the value of n is treated as a constant in the present application).

In order to validate the significance of ω_{NSR} , its correlation with the relative error $\frac{\|\Delta\vec{p}\|}{\|\vec{p}\|}$ of the estimated parameters is evaluated for the simulated test data set shown in figure 7.12. Five sets of parameters have been estimated at the positions $t = 20, x = 8, 24, 40, \dots, 248$ and $y = 8, 24, 40, \dots, 120$ using the cutoff derivative filters. Four sets have been calculated with an averaging window size of $15 \times 15 \times 21$ in x-, y-, and t-direction ($N_B = 15 \cdot 15 \cdot 21 = 4725$) and different noise levels in the data of $\sigma_d^2 = 1, \sigma_d^2 = 5$ and $\sigma_d^2 = 0.01$. The last set is calculated with a window size of $5 \times 5 \times 7$ ($N_B = 175$) and a noise level of $\sigma_d^2 = 0.01$. In figure 7.17a the logarithmic relative error is plotted against the smallest eigenvalue λ_n . It is obvious that λ_n correlates with the noise level, but as expected it does not correlate with the relative error. The relative error plotted against $\text{tr}(J)$ in figure 7.17b in contrast shows correlations within each data set, with the relative error decreasing with increasing $\text{tr}(J)$. However the correlations of the particular data sets do not coincide, so that no global relation between $\text{tr}(J)$ and relative error can be given. If instead the relative error is plotted against the ratio $\frac{\lambda_n}{\text{tr}(J)}$ as shown in figure 7.17c, the first four data sets with the $15 \times 15 \times 21$ averaging window show a satisfactory coincidence. The data set with the $5 \times 5 \times 7$ averaging window however is significantly shifted to lower $\frac{\lambda_n}{\text{tr}(J)}$. In figure 7.17d finally all data sets show an acceptable coincidence when the relative error is plotted against $\omega_{\text{NSR}} = \frac{\lambda_n}{N_B \text{tr}(J)}$. A rough threshold for ω_{NSR} can be read off to $\tau_{\text{NSR}} \approx 10^{-8}$ for a relative error $\frac{\|\Delta\vec{p}\|}{\|\vec{p}\|} < 1$. The spatial distributions of $\lambda_n, \text{tr}(J), \frac{\lambda_n}{N_B \text{tr}(J)}$ and $\log\left(\frac{\|\Delta\vec{p}\|}{\|\vec{p}\|}\right)$ are depicted in figure 7.18. The apparent correlation between ω_{NSR} and $\log\left(\frac{\|\Delta\vec{p}\|}{\|\vec{p}\|}\right)$ further confirms the applicability of ω_{NSR} as a measure of confidence.

Finally the following concluding remarks can be made from the above results:

- the quantity $\omega_{\text{NSR}} = \frac{\lambda_n}{N_B \text{tr}(J)}$ has proven to be a suitable confidence measure for the present TLS parameter estimation.
- In agreement with theoretical considerations, it is invariant under scaling of the data, different noise levels and different averaging window sizes.
- A value of $\tau_{\text{NSR}} \approx 10^{-8}$ has been found for $\frac{\|\Delta\vec{p}\|}{\|\vec{p}\|} < 1$.
- from this analysis the applicability is limited to the parameter estimation of a 2D convection dispersion model. Further analysis is necessary for an extension to other models given e.g. in table 7.1.

7.4.5 Physically based minimum norm solution

As already discussed previously in sections 7.3.3 and 7.3.5, in certain situations, usually referred to as aperture problems, it is in principle not possible to estimate the entire parameter set, but only a particular subset of the parameters. In the example of the moving edge shown in figure 7.6 for instance, only the velocity perpendicular to the edge can be estimated. These situations can be identified from the eigenvalue spectrum of J , $\lambda_1 > \lambda_2 > \dots > \lambda_n$, through the number $n-p$ of eigenvalues close to zero: $\lambda_i \approx 0$ for $i = p+1..n$. Any vector in the $(n-p)$ -dimensional nullspace spanned by the corresponding eigenvectors \vec{e}_i is then a possible solution.

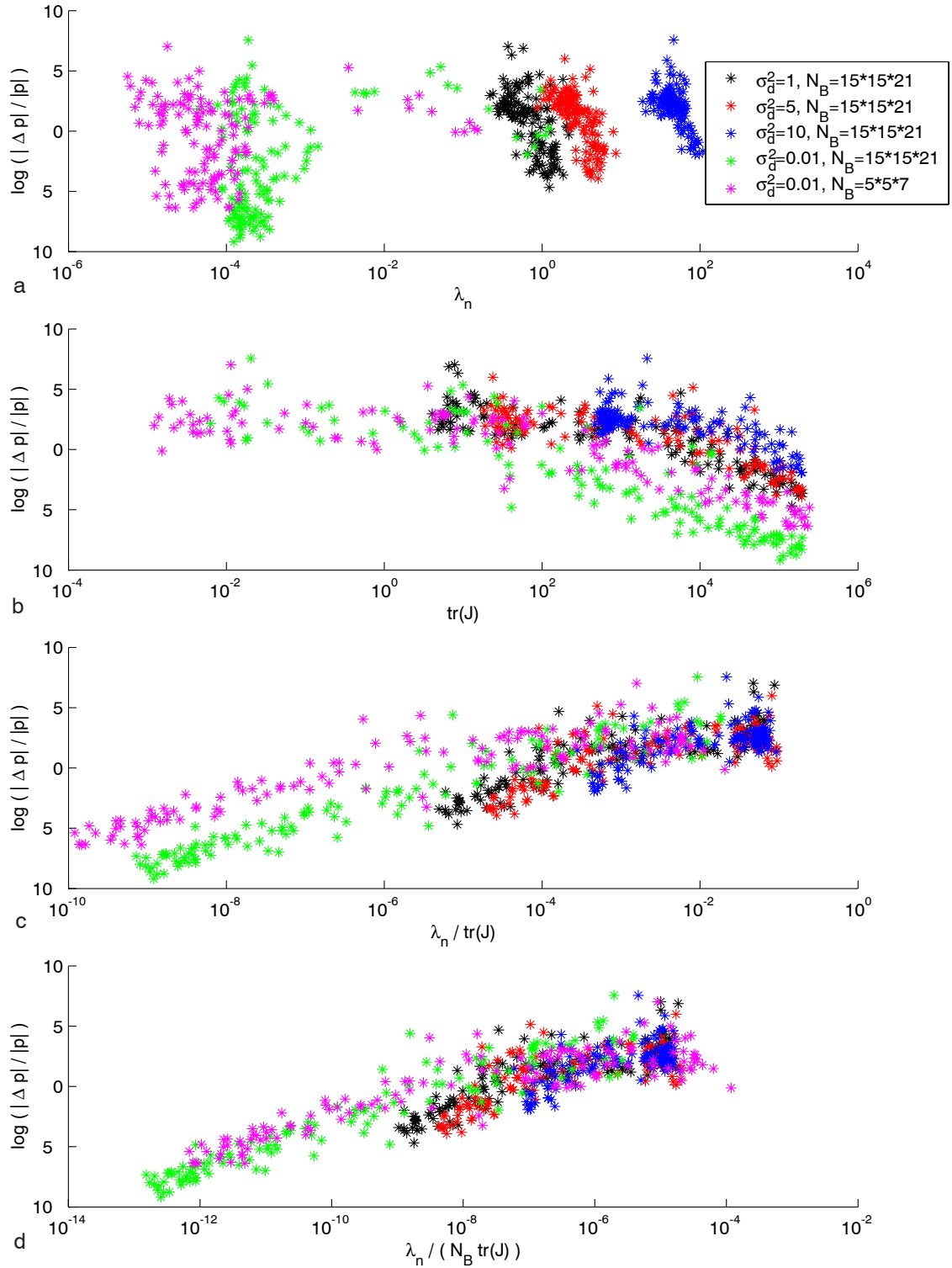


Figure 7.17: Dependence of the logarithmic relative error $\frac{\|\Delta \vec{p}\|}{\|\vec{p}\|} < 1$ on **a** the smallest eigenvalue λ_n , **b** the trace $\text{tr}(J)$, **c** the ratio $\frac{\lambda_n}{\text{tr}(J)}$ and **d** the confidence measure $\omega_{\text{NSR}} = \frac{\lambda_n}{N_B \text{tr}(J)}$.

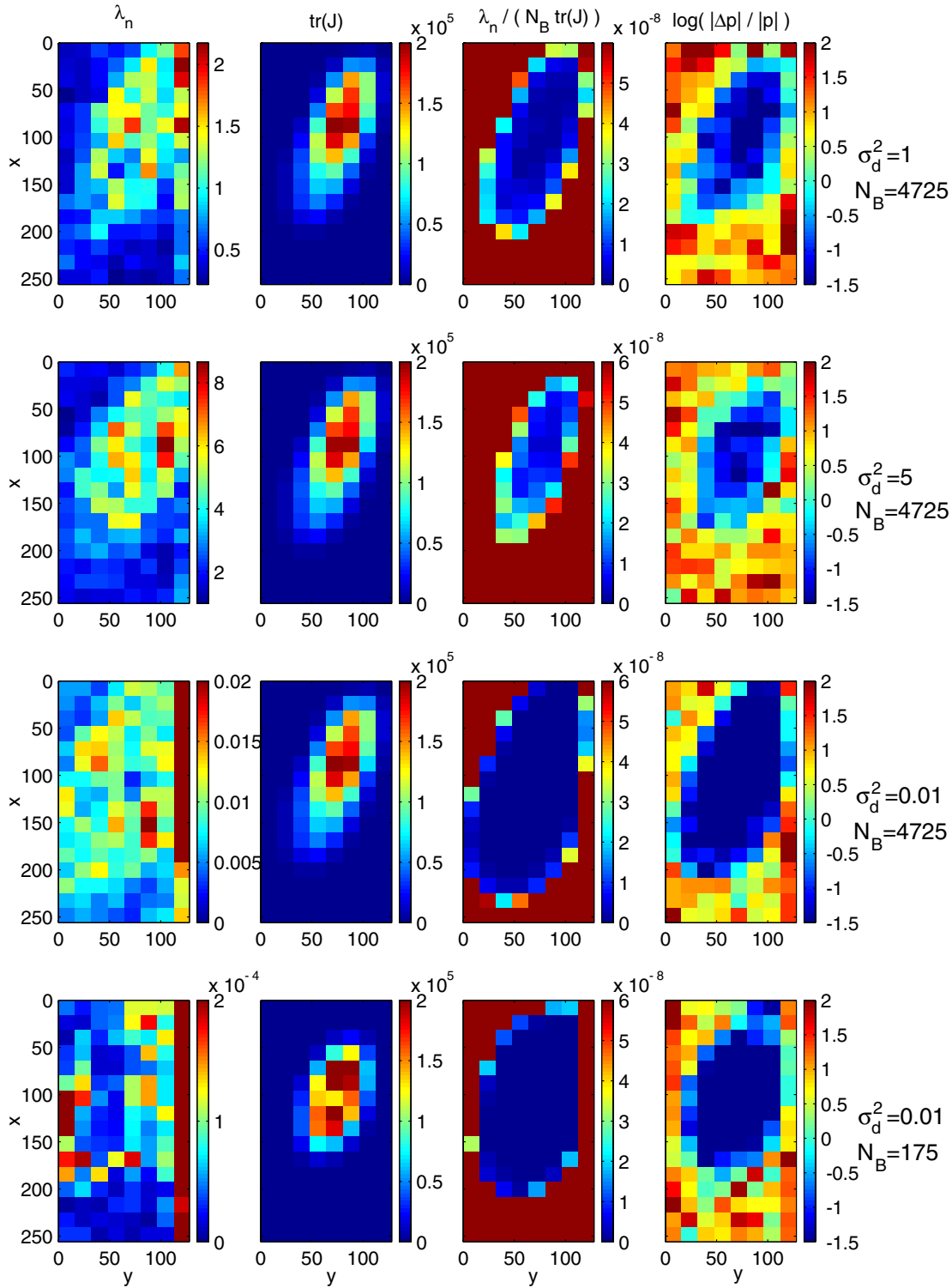


Figure 7.18: Spatial distributions of the smallest eigenvalue λ_n , trace $\text{tr}(J)$, confidence measure $\omega_{\text{NSR}} = \frac{\lambda_n}{N_B \text{tr}(J)}$ and logarithmic relative error $\frac{\|\Delta \hat{p}\|}{\|\hat{p}\|} < 1$ for the TLS parameter estimation with the simulated test data shown in figure 7.12. The results are shown for four data sets with different noise levels σ_d^2 and different averaging window size N_B .

A unique solution to this ill-posed problem can then only be found through regularization with one or more additional constraints. Often the solution with minimal euclidean norm defined by equation 7.65 gives reasonable results: in the example of the moving edge, the result would be the velocity perpendicular to the edge.

In the following it will be shown that the minimum norm solution 7.65 does not lead to reasonable results for aperture problems in the parameter estimation of a 2D convection dispersion model. This problem will then be overcome by the introduction and application of a specially adapted minimization criterion.

An example of an aperture problem for a 2D convection dispersion process is presented in figure 7.19. Additional to the movement, the image sequence indicates dispersion of the edge in the direction of movement. Due to the lack of gradients parallel to the edge, neither the velocity nor the dispersion in the parallel direction can be estimated. Since apparently only two parameters, namely the velocity and the dispersion perpendicular to the edge, can be estimated, a four-dimensional nullspace indicated by four eigenvalues close to zero is expected. The following paragraphs will now describe the separation of nullspace and data space and the appropriate determination of velocity and dispersion tensor from the manifold of possible solutions. For the calculation of the derivatives the filter set h_2 (see table 7.3) is used, since the cutoff filters are not applicable here due to the sharp edges at the image boundaries. A box shaped filter mask B of size (15 15 21) in x-, y- and t-direction is used for the local averaging according to equation 7.69. The image sequence was contaminated with gaussian white noise with variance $\sigma_d^2 = 1$.

The first step is the determination of the nullspace dimension at each position from the according eigenvalue spectra. In figure 7.20a the eigenvalue spectrum at the position $x = 104 / y = 72 / t = 20$ is plotted exemplarily. For each eigenvalue then the corresponding confidence measure ω_{NSR} given by equation 7.92 can be calculated as shown in figure 7.20b. The gray line indicates the threshold $\tau_{\text{NSR}} \approx 10^{-8}$ which was found in section 7.4.4. Consequently the estimated number of nullspace dimensions at this position is four. Figure 7.20c shows the such estimated nullspace dimensions for all x/y-positions. As expected, the dimension is four in the area marked by the edge and zero in the areas without structure as e.g. $x > 200$. The fact that the border between these two areas is characterized by a stepwise transition from zero to four instead of a sharp transition is caused by the noise which leads to uncertainties of the eigenvalues.

The expectation that the parameters estimated exclusively from the smallest eigenvalue will not give useful results is confirmed by figure 7.21, where all results have relative errors higher than 100 %. The first candidate for a reasonable solution is that with the minimal euclidean norm as described in section 7.3.5. The results calculated with the nullspace dimensions from figure 7.20c are shown in figure 7.21. Although the logarithmic relative error in the area of the edge of circa -0.5 could in principle be accepted, the constancy of the errors already indicates that the results are systematically biased.

This motivates a closer look at the minimization criterion which was applied here. For a 2D convection dispersion model equation the minimum norm criterion 7.65 can be written as

$$v_x^2 + v_y^2 + D_{xx}^2 + (2D_{xy})^2 + D_{yy}^2 \stackrel{!}{=} \min. \quad (7.103)$$

From this formulation the problem becomes apparent: whereas the minimization of the norm of the velocity vector $\vec{v} = \begin{pmatrix} v_x \\ v_y \end{pmatrix}$ is physically reasonable, the minimization of the sum of

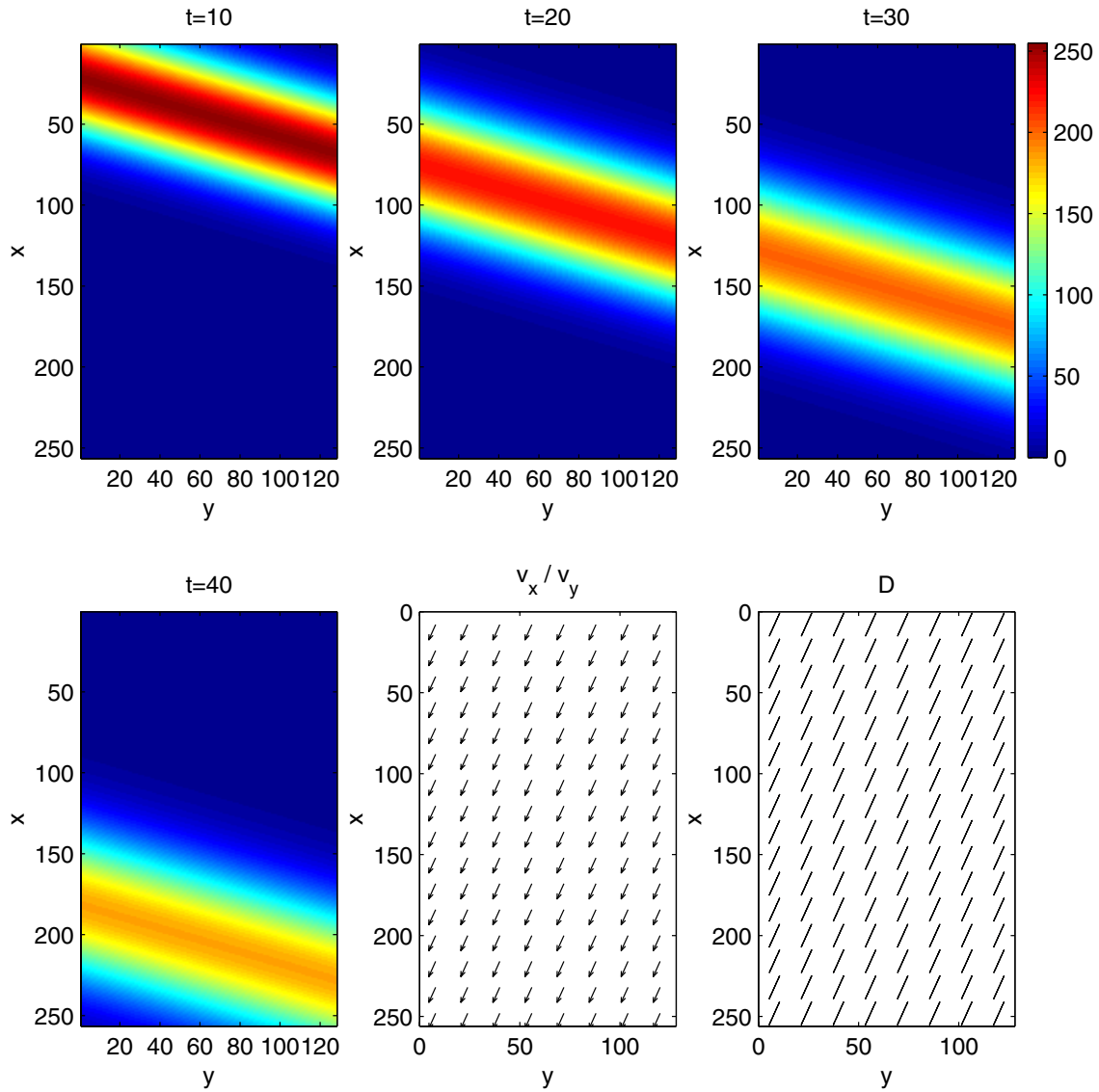


Figure 7.19: Synthetic test data set of a simulated 2D convection-dispersion process used for the performance analysis of TLS parameter estimation in the presence of aperture problems. Due to the lack of gradients parallel to the moving edge, no velocity or dispersion in the parallel direction can be estimated. The data set consisting of 50 2D images ($x = 1..256$, $y = 1..128$, $t = 1..50$) is shown for $t = 10, 20, 30$ and 40 . The velocities ($v_x = 4.70$, $v_y = -1.71$) plotted as vectors and dispersion tensors ($D_{xx} = 6.62$, $D_{xy} = -2.41$ and $D_{yy} = 0.88$) represented as ellipses are constant in space and time and directed perpendicular to the edge. For better visibility the velocity vectors in the illustration are scaled with a factor 2.

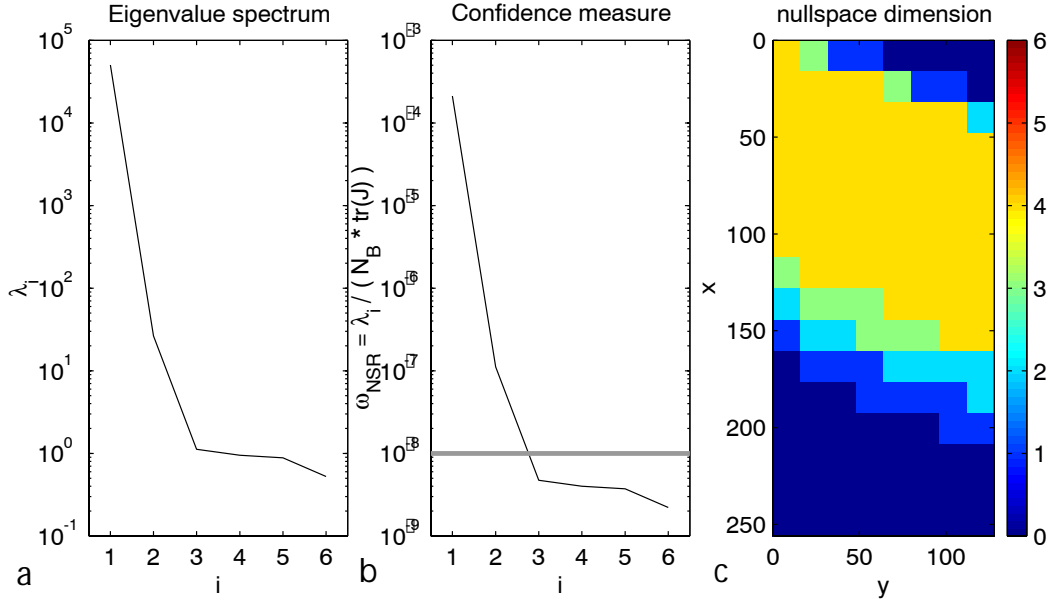


Figure 7.20: Determination of the nullspace dimension from the eigenvalue spectrum: **a** eigenvalue spectrum at the position $x = 104 / y = 72 / t = 20$ **b** values of the corresponding confidence measure ω_{NSR} and threshold τ_{NSR} (represented by the gray line) defined in section 7.4.4. The nullspace dimension is estimated from the number of $\omega_{\text{NSR}} < \tau_{\text{NSR}}$. **c** spatial distribution of such estimated nullspace dimensions for $t = 20$.

the squared elements of the dispersion tensor $D = \begin{pmatrix} D_{xx} & D_{xy} \\ D_{xy} & D_{yy} \end{pmatrix}$ has no physical reason.

This can be readily recognized from the lack of rotational invariance of the term $D_{xx}^2 + (2D_{xy})^2 + D_{yy}^2$, whereas the norm of \vec{v} is rotationally invariant. A measure which quantifies the total amount of dispersion and which is in addition rotationally invariant is the trace of D , $\text{tr}(D) = D_{xx} + D_{yy}$. This leads to the following modified minimization criterion

$$v_x^2 + v_y^2 + (D_{xx} + D_{yy})^2 \stackrel{!}{=} \min. \quad (7.104)$$

A second physical requirement is the non-negative definiteness of D , which is necessary to fulfil the second thermodynamic law. This requirement can be formulated by the additional, rotationally invariant constraint

$$\det D = D_{xx}D_{yy} - D_{xy}^2 \stackrel{!}{\geq} 0. \quad (7.105)$$

The minimization of 7.104 subject to 7.105 can be carried out using standard iterative optimization techniques (see e.g. Coleman & Li (1996)) with the solution of equation 7.65 used as an initial value.

The results of this physically based regularization approach are shown in figure 7.21. The increase of accuracy compared to the non-physically motivated approach is significant. The facts that the accuracies are comparable to those of the corresponding direct estimation shown in figure 7.13, and that no systematic bias is identifiable confirm the hypothesis that the presented criterion is optimal for aperture problems in 2D convection dispersion models.

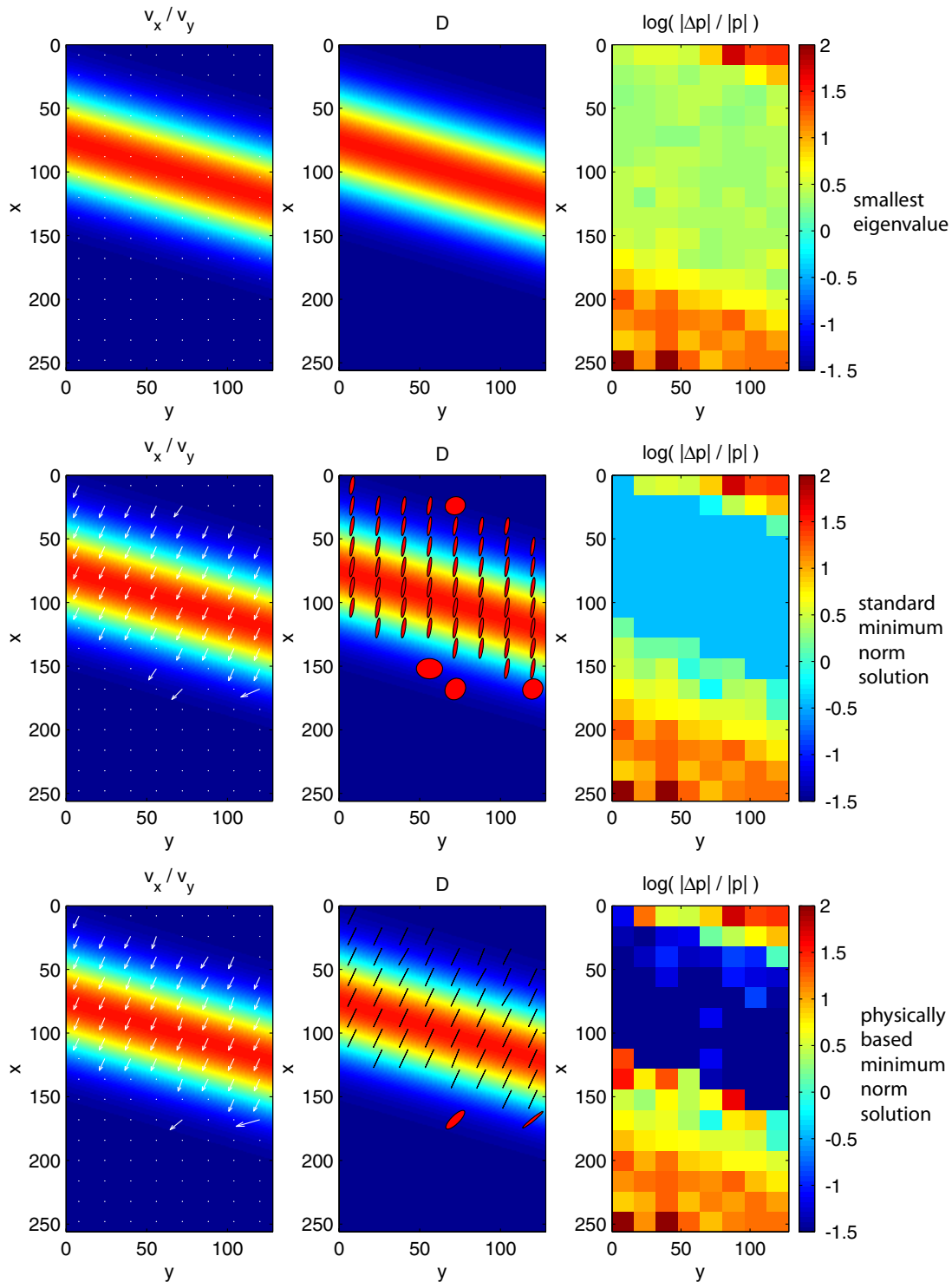


Figure 7.21: Velocities, dispersion tensors and logarithmic relative errors estimated from the image sequence shown in figure 7.19. The parameters were estimated from the smallest eigenvalue (upper row), as a standard minimum norm solution (middle row) and a minimum norm solution based on physical constraints (lower row). The vectors and ellipses representing the velocities and dispersivities are only plotted for $\log(\frac{\|\Delta p\|}{\|p\|}) < 1$.

At last the results of this section lead to the following concluding remarks:

- the confidence measure ω_{NSR} introduced in section 7.4.4 can be used in combination with an appropriate threshold τ_{NSR} to estimate the dimension of the nullspace.
- if this dimension is higher than one, a unique, physically reasonable solution can be obtained by the application of one or more additional criteria.
- the standard minimum norm solution presented in section 7.3.5 does not generally lead to physically reasonable results. It is therefore necessary to verify the applied minimization criteria with respect to physical constraints like e.g. rotation invariance.

7.5 Summary and conclusions

In this chapter a method was presented for the local parameter estimation of linear dynamic processes. At first an outline was given of the basic theory of the underlying TLS parameter estimation framework and its application to linear dynamic processes. The following features lead to the conclusion that the method is an excellent tool for the analysis of flow and transport in porous media:

- the dynamic process which is to be estimated can be directly integrated into the estimation procedure in the form of a differential equation. A solution to this equation is not necessary.
- the formalism allows for a direct specification of the location and size of the estimate in space and time. Any assumption about heterogeneities, as defined e.g. by an REV, can easily be incorporated into the estimation.
- the method yields a direct non-iterative maximum likelihood estimate with no need of any initial values.
- the cause of a failure of the estimation, like e.g. a low signal-to-noise ratio or an aperture problem, can be readily detected from an eigenvalue spectrum and potentially be corrected by adapted additional constraints.

Thereafter the performance and accuracy of the method was evaluated in detail through application to synthetic image data sets of a 2D convection-dispersion process. These investigations resulted in a number of important insights:

- typically the noise in the image data is the limiting factor for the accuracy of the estimated parameters. There the noise susceptibility of the filters used for the computation of derivatives has a tremendous impact on the resulting accuracy and consequently the filters must be chosen very carefully.
- the resulting accuracy can be significantly reduced if the relative magnitudes of errors in the data are not correctly taken into account and equilibrated with a proper weight matrix.
- for a suitable measure of confidence, it is necessary to correctly take into account the smallest eigenvalue λ_n and the trace of J as well as the size N_B of the local averaging volume. The resulting measure $\omega_{\text{NSR}} = \frac{\lambda_n}{N_B \text{tr}(J)}$ proved reliable in the present application.

- aperture problems can be detected from the eigenvalue spectrum via the corresponding spectrum of ω_{NSR} and a proper threshold τ_{NSR} .
- for processes other than pure translation the standard minimum norm solution in case of an aperture problem does typically not lead to reasonable results and has to be replaced by a physically based solution.

Although these results are obtained exclusively from the analysis of a 2D convection-dispersion process, no qualitative changes of the drawn conclusions are expected for the application to higher dimensions or other models given in table 7.1. However, values of quantities like the threshold τ_{NSR} or the choice of proper constraints for the case of aperture problems may have to be reconsidered. A quantitative generalization of the obtained results is subject to further research.

Chapter 8

Single-phase flow in saturated porous media

8.1 Introduction

This chapter is devoted to the study of different physical processes which all lead to the phenomenon usually denoted as *hydrodynamic dispersion*, i.e. the broadening of the concentration distribution of a solute in a liquid. As described in detail in chapter 2, several microscopic physical processes, like e.g. molecular diffusion, adsorption, holdup or microscopic velocity fluctuations can generate the macroscopic phenomenon of hydrodynamic dispersion. The scientific challenge is to get a quantitative understanding of the relations between the material properties and parameters of processes on the microscale and the effective parameters of macroscopic phenomena. The experimental technique presented in chapter 3 provides the opportunity to simultaneously measure 3D microscopic and macroscopic transport of a tracer dye in a porous medium, and therefore offers the prospect of gaining rewarding insights into the processes on different scales.

At first the technique is used in section 8.2 to measure the coefficients of molecular diffusion from the dispersion of the tracer dyes in porous medium with stagnant liquids. Section 8.3 then presents the measurement and interpretation of time-dependent longitudinal and transverse dispersion coefficients for different flow rates, solids and liquids. Then the availability of spatially and temporally highly resolved data is utilized to study the relation of the macroscopic dispersion coefficients to the porous structure and physical processes like holdup and adsorption on the microscale. Finally a summary and conclusions are given in section 8.4.

As already mentioned in chapter 5, the measurements do not provide any absolute concentration values. Consequently the concentrations given in this chapter are denoted by dimensionless numbers that have no physical relevance.

8.2 Molecular diffusion

For the evaluation of the results obtained in the following sections and for their comparison with literature values the knowledge of the respective coefficients of molecular diffusion D_m is indispensable. The diffusion coefficient is part of several dimensionless parameters like e.g. Peclet number $Pe = \frac{vd}{D_m}$, Schmidt number $Sc = \frac{\nu}{D_m}$ and the ratios $\frac{D_L}{D_m}$ and $\frac{D_T}{D_m}$ (see chapter

2). Since for the solvent-solute combinations used in this work no data could be found in the literature, an appropriate method for their estimation had to be found. As described in section 2.3.3, the dispersion of the solute in a porous medium with stagnant liquid phase $D(\text{Pe} = 0)$ can be related to the diffusion in the pure liquid D_m via equation 2.33. Further use is made of the dependence of the diffusion coefficient on the viscosity as explicated in section 2.2: therefore the diffusion coefficient has to be measured only once for each dye, the values for other weight percentages or mixing ratios of the solvents are then calculated using the Stokes-Einstein-equation 2.8.

For each dye a cuvette made of plexiglass with a volume of $25 \times 40 \times 25 \text{ mm}^3$ was filled with refractive index matched solid and liquid and a small pulse of dyed liquid was injected. Then the 3D (relative) concentration distributions were measured each after $\Delta t = 0, 23, 121$ and 143.5 hours with the setup described in chapter 3. For each 3D distribution the variances in x-, y- and z-direction σ_x^2 , σ_y^2 and σ_z^2 were determined by a least squares fit of a gaussian distribution to the macroscopic 1D distributions $\bar{c}(x, t) = \sum_{yz} c(x, y, z, t)$, $\bar{c}(y, t) = \sum_{xz} c(x, y, z, t)$ and $\bar{c}(z, t) = \sum_{xy} c(x, y, z, t)$ as described in section 6.4. From the variances $\sigma_i^2(t)$ the dispersion coefficients D_i for $\text{Pe} = 0$ are calculated as

$$D_i(\text{Pe} = 0) = \frac{1}{2} \frac{d\sigma_i^2(t)}{dt} \quad \text{with } i = x, y, z, \quad (8.1)$$

where the derivative is calculated from a least squares straight line fit of the $\sigma_i^2(t)$. Finally the coefficient of molecular diffusion D_m is calculated as the geometric mean

$$D_m = \frac{1}{\tau} (D_x D_y D_z)^{1/3}, \quad (8.2)$$

with the tortuosity τ defined in section 2.3.3. It should be noted that the relations 2.33, refo-stokeseinstein and 8.2 can not be regarded as exact but serve as approximations. Therefore the results obtained with these equations are considered as estimates and no uncertainties are given.

8.2.1 Nile Red

Figure 8.1 shows the dye distributions of Nile Red in a porous medium of silicone oil and plexiglass at four different times. From this data the temporal evolutions of the variances in x-, y- and z-direction were calculated as described above and plotted in figure 8.2. The slopes of the straight line fits are comparable and thus indicate isotropic diffusion. The vertical shifts stem from an anisotropic initial distribution. Table 8.1 shows the values for D_x , D_y and D_z calculated with equation 8.1, the tortuosity τ calculated with equation 2.33 and D_m calculated with equation 8.2. The Schmidt number $\text{Sc} = \frac{\nu}{D_m}$ is then calculated with the value for the kinematic viscosity from table 3.3. With the relation for the dependence of molecular diffusion from dynamic viscosity (values taken from table 3.3) given by the Stokes-Einstein-equation 2.8 the values for D_m and Sc are then converted for the silicone oil mixture used in combination with fused silica. As will be shown in section 8.3.6, Nile Red adsorbs on the surface of fused silica, and therefore the experimental determination of molecular diffusivity for this combination with the present method becomes rather unfeasible because it would have to quantitatively account for the effect of adsorption.

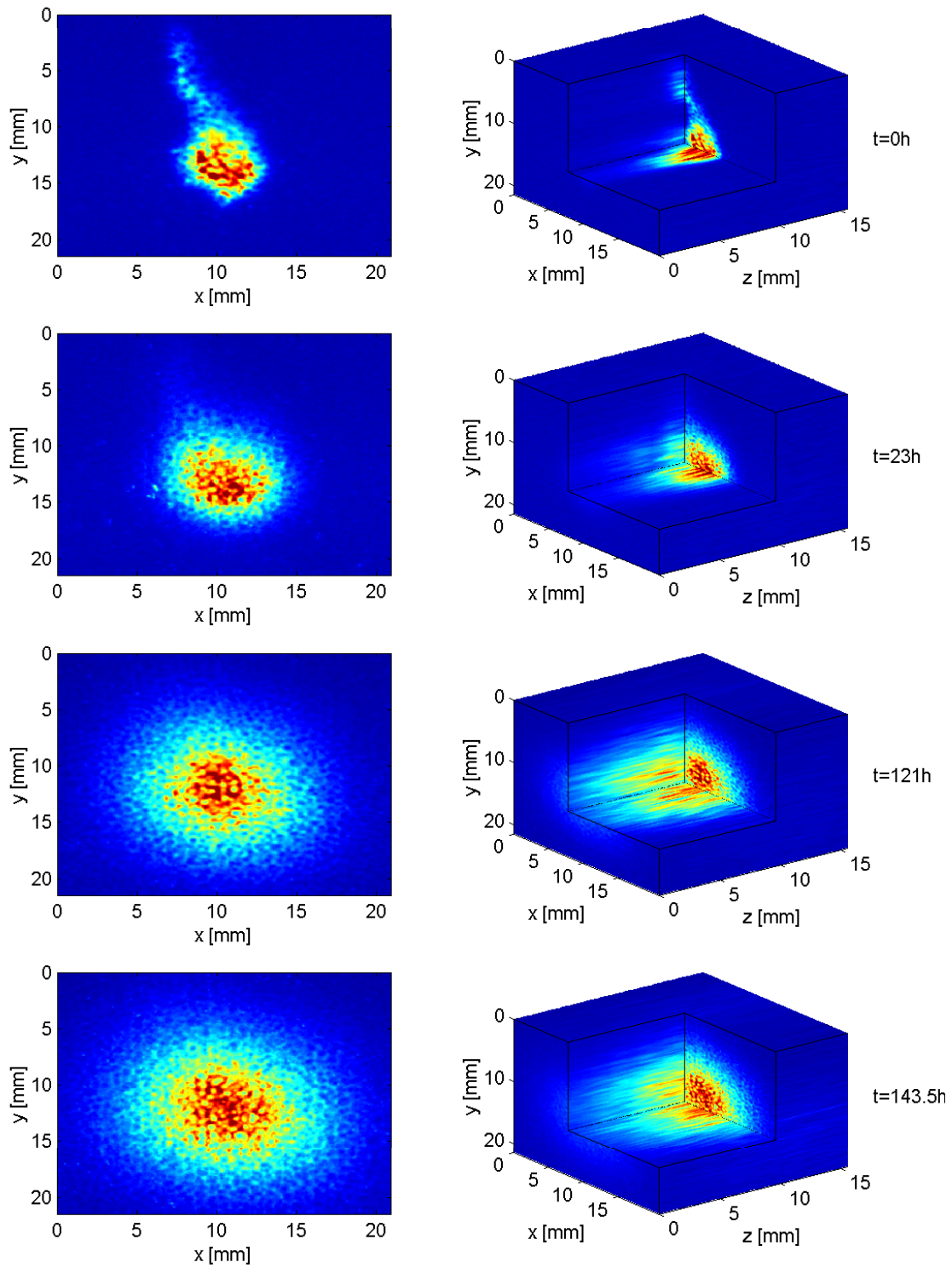


Figure 8.1: Dispersion of Nile Red in a porous medium of plexiglass and a stagnant silicone oil mixture. The images on the left show the 2D distributions at $z = 10$ mm for $\Delta t = 0, 23, 121$ and 143.5 hours. The corresponding 3D distributions are shown on the right. The trace of the cannula pulled out after dye injection is visible in the images for $\Delta t = 0$.

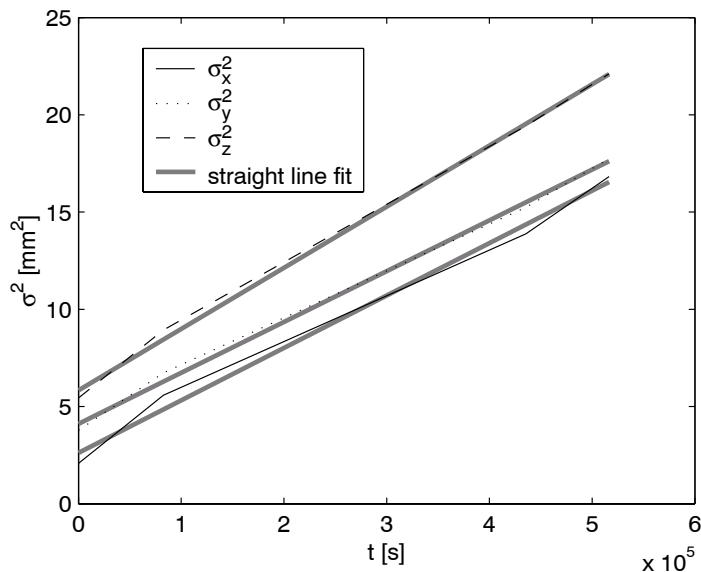


Figure 8.2: Temporal evolution of the variance in x-, y- and z-direction for the Nile Red distributions shown in figure 8.1.

8.2.2 Alexa Fluor 488

The dispersion of Alexa Fluor 488 in a porous medium of zinc chloride aqueous solution and fused silica is depicted in figure 8.3. It is cognizable from these images that the diffusion is anisotropic. This is further quantified by the temporal evolutions of the variances in x-, y- and z-direction plotted in figure 8.4 and the corresponding dispersion coefficients given in table 8.1. Since the dispersion coefficients in the horizontal directions, D_x and D_z , are significantly higher than the vertical coefficient D_y , this can be readily explained by density fluctuations and / or layered structures. Again the tortuosity τ is calculated with equation 2.33 for the estimation of D_m with equation 8.2 and $Sc = \frac{\nu}{D_m}$ is calculated with the value for the viscosity from table 3.3.

8.3 Hydrodynamic dispersion

The measurements of hydrodynamic dispersion presented in this section have been made using the $8 \times 4 \times 4 \text{ cm}^3$ horizontal flow cell sketched and pictured in figures 3.3 and 3.5. After the application of the desired flow rate and the injection of a pulse of dyed liquid, a 3D volume scan of the dye concentration was performed every 30 seconds as described in section 3.3. The spatial resolution of the measurements was $70 \mu\text{m} \times 70 \mu\text{m}$ parallel to the laser plane and 0.4 mm, as defined by the increments of the translation stage, in the out-of-plane direction. The effective resolution in the out-of-plane direction is however rather given by the width of the laser sheet of ca. 0.5-1 mm. The so obtained 4D image set consisting of $1300 \times 600 \times 90 \times n_t$ (n_t denoting the number of successive volume scans) 8-bit intensity values was then at first geometrically and radiometrically calibrated and corrected for systematic and statistical errors using the methods described in chapter 5. The corrected 4D data set, representing the relative dye concentrations at the real world coordinates (x, y, z) and times t , was then

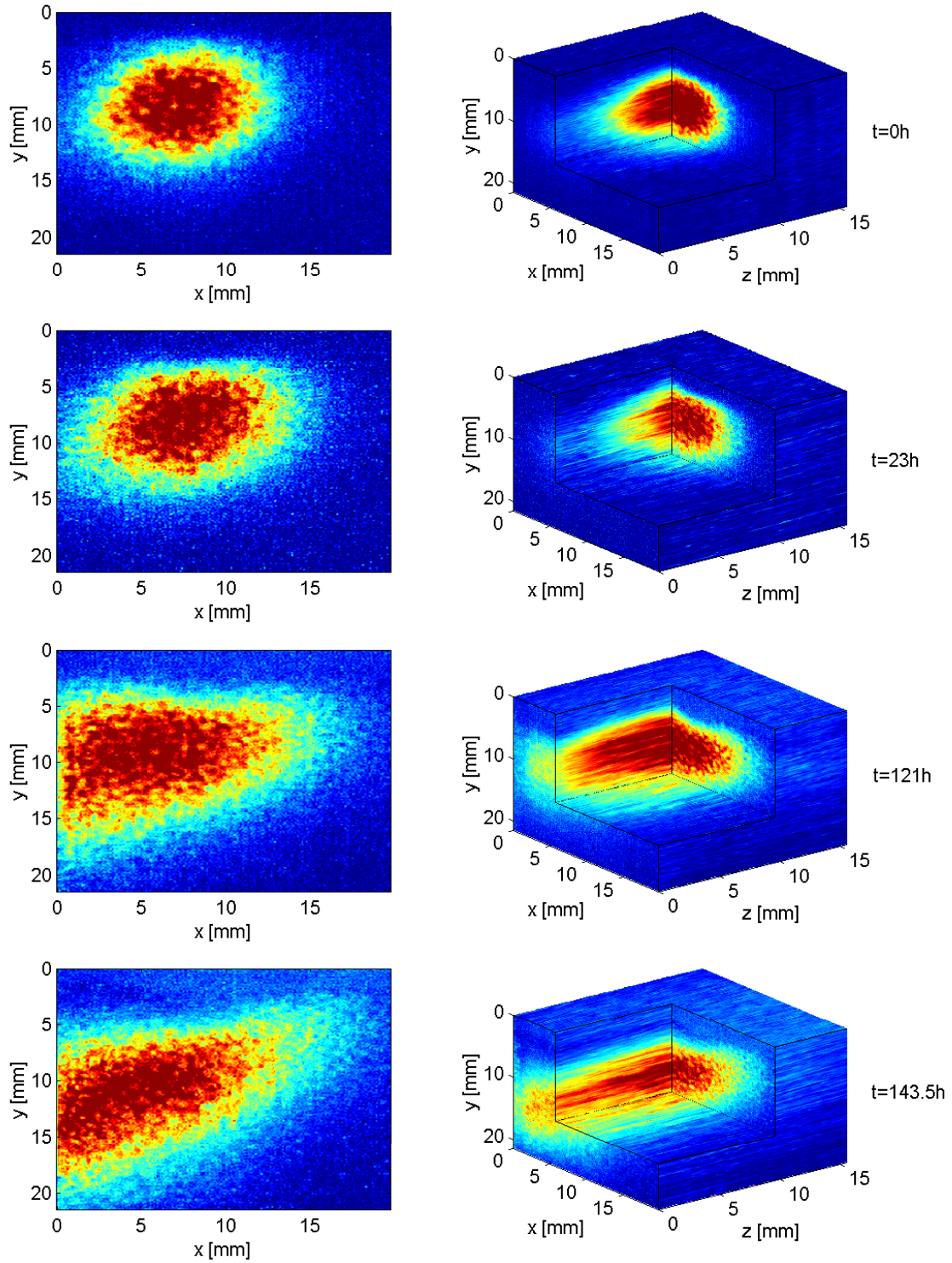


Figure 8.3: Dispersion of Alexa Fluor 488 in a porous medium of fused silica and a stagnant ZnCl_2 aqueous solution. The images on the left show the 2D distributions at $z = 14$ mm for $\Delta t = 0, 23, 121$ and 143.5 hours. The corresponding 3D distributions are shown on the right.

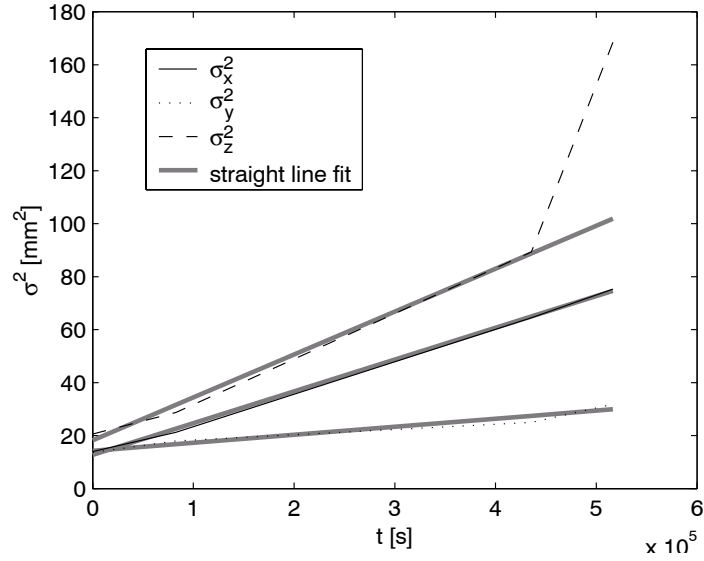


Figure 8.4: Temporal evolution of the variance in x-, y- and z-direction for the Alexa Fluor 488 distributions shown in figure 8.3. For the straight line fit of $\sigma_z(t)$ only the first three times were taken into account because then the dye reached the border of the cuvette in z-direction and the distribution strongly differed from a gaussian.

	Nile Red + silicone oil + plexiglass	Nile Red + silicone oil + fused silica	Alexa Fluor 488 + ZnCl ₂ solution + fused silica
D_x [mm ² /s]	$1.35 \cdot 10^{-5}$	-	$6.00 \cdot 10^{-5}$
D_y [mm ² /s]	$1.31 \cdot 10^{-5}$	-	$1.52 \cdot 10^{-5}$
D_z [mm ² /s]	$1.57 \cdot 10^{-5}$	-	$8.10 \cdot 10^{-5}$
τ	0.72	0.78	0.78
D_m [mm ² /s]	$1.96 \cdot 10^{-5}$	$9.58 \cdot 10^{-5}$	$5.36 \cdot 10^{-5}$
Sc	$5 \cdot 10^6$	$2 \cdot 10^5$	$7 \cdot 10^4$

Table 8.1: Results for the dispersion coefficients in a stagnant liquid D_x , D_y and D_z , tortuosity τ , coefficients of molecular diffusion D_m and Schmidt number Sc for the solid-liquid combinations used in this work.

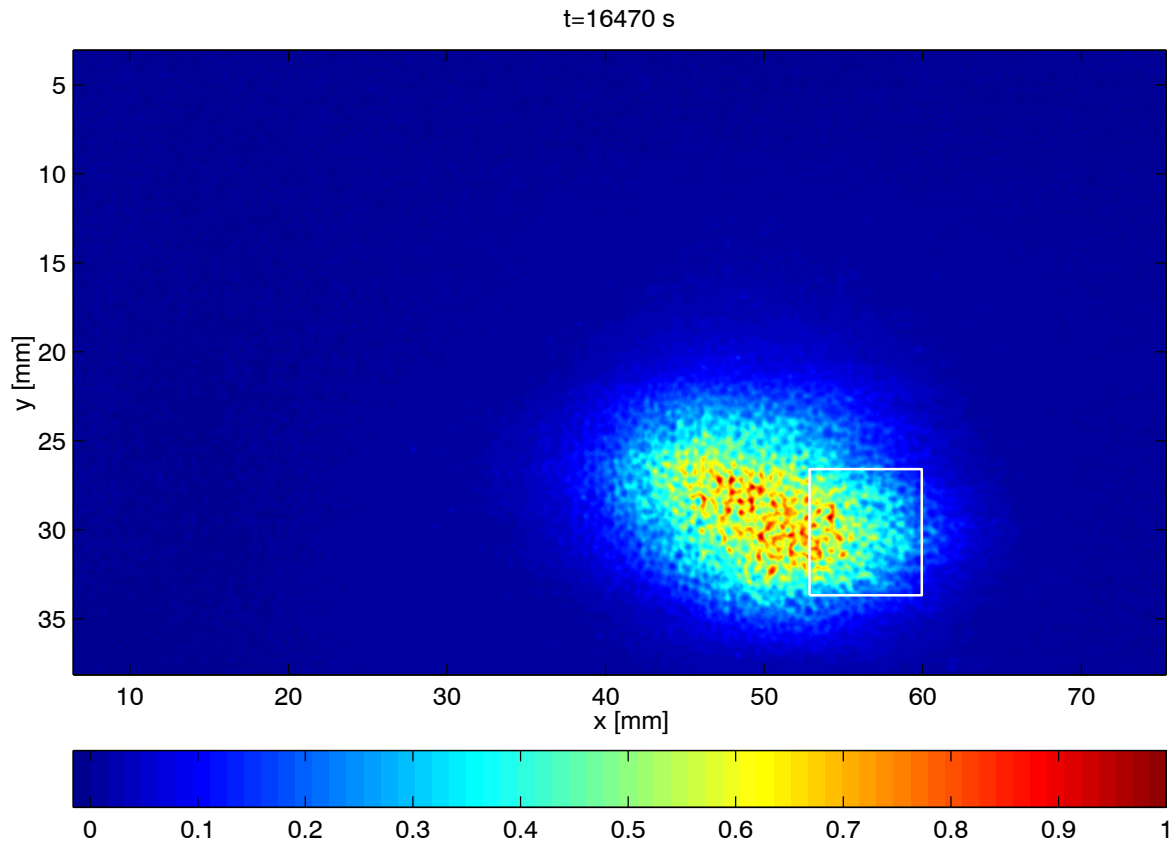


Figure 8.5: 2D dye concentration distribution at $t=16470$ s and $z=20$ mm taken from the experiment A2 (see table 8.3) with plexiglass and silicone oils. The temporal evolution in the area indicated by the white square is shown in figure 8.6.

the basis for the evaluations presented below in this section. Figures 8.5, 8.6, 8.7 and 8.8 exemplarily show different visualizations of a typical suchlike data set.

Four series of dye transport measurements using different combinations of solids and liquids as specified in table 8.2 have been performed. Series A aimed at the coverage of a large Peclet number range, while in series B the same solid-liquid combination was used to study the reversibility of transport phenomena through so-called *echo experiments*, i.e. experiments with a reversal of the flow direction after a certain mean transport distance. Series C and D were then measured in order to investigate the effect of the variation of solid, liquid and fluorescent dye. A combination of plexiglass and ZnCl_2 aqueous solution was not feasible due to the low acid resistance of plexiglass.

8.3.1 Correlation functions of porous media

In this section it will be shown how the dye transport measurements can be used to estimate geometrical properties of the employed porous media. A commonly used approach for the estimation of geometrical properties in porous media is the application of correlation functions,

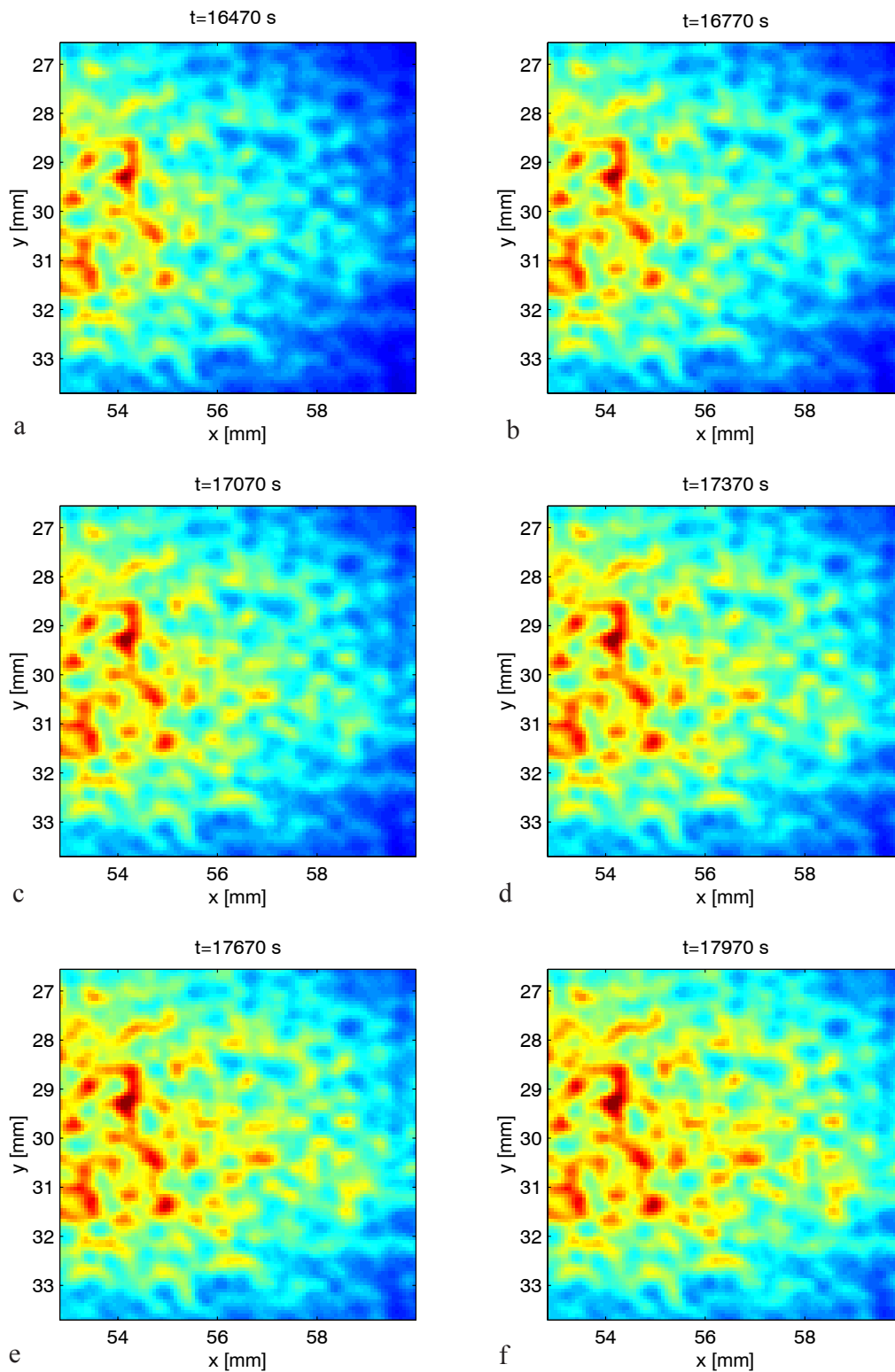


Figure 8.6: Temporal evolution of the dye concentration in an area of 100×100 pixel à $70 \times 70 \mu\text{m}^2$ corresponding to the $7 \times 7 \text{ mm}^2$ square shown in figure 8.5. The time between two consecutive images is 300 s corresponding to 10 3D volume scans.

Series	Solid	Liquid	Pe	Comment
A	Plexiglass	84 wt.% DC 550 + 16 wt.% DC 556	$33 < Pe < 6680$	
B	Plexiglass	84 wt.% DC 550 + 16 wt.% DC 556	$316 < Pe < 1116$	with reversal of flow direction
C	Fused silica	58 wt.% $ZnCl_2$ aqueous solution	$Pe = 52, 194$	
D	Fused silica	98 wt.% DC 556 + 2 wt.% DC 200	$Pe = 180$	Adsorption

Table 8.2: Specification of solids, liquids and Peclet number ranges used for the four series of dye transport measurements. The properties of solids, liquids and associated dyes are detailed in chapter 3.

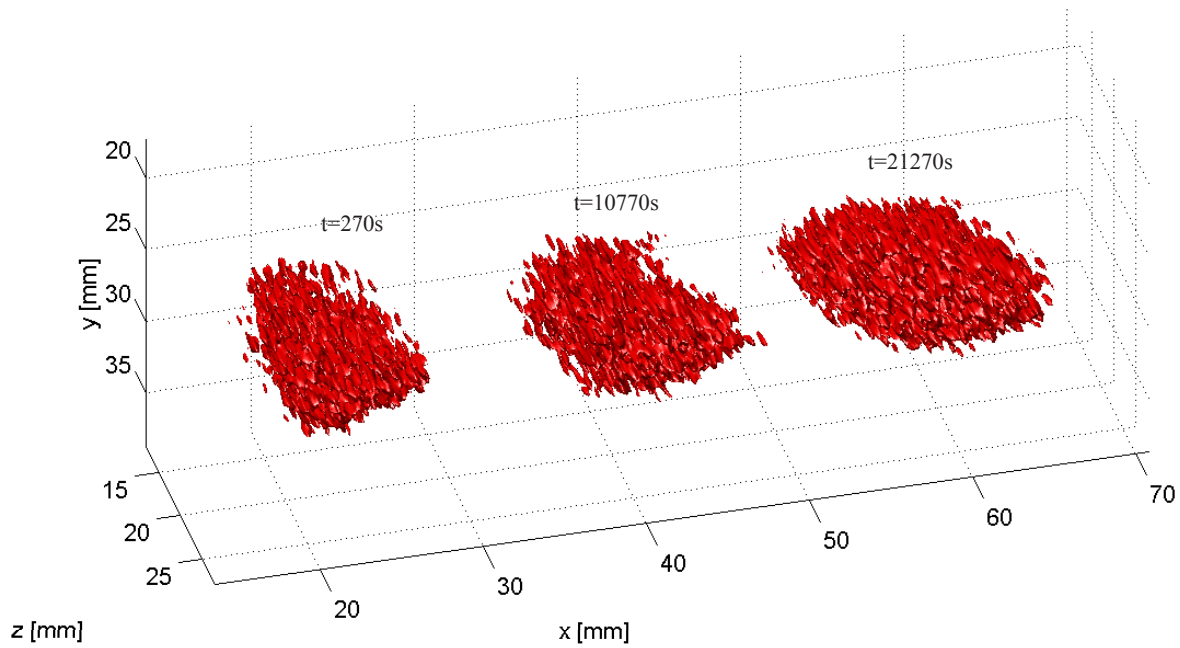


Figure 8.7: Isoconcentration surface plot of the experiment A2 (see table 8.3) for three times $t=270$ s, $t=10770$ s and $t=21270$ s. The isoconcentrations are 40% of the respective maximum concentrations. Figure 8.8 shows an alternative visualization of the same data.

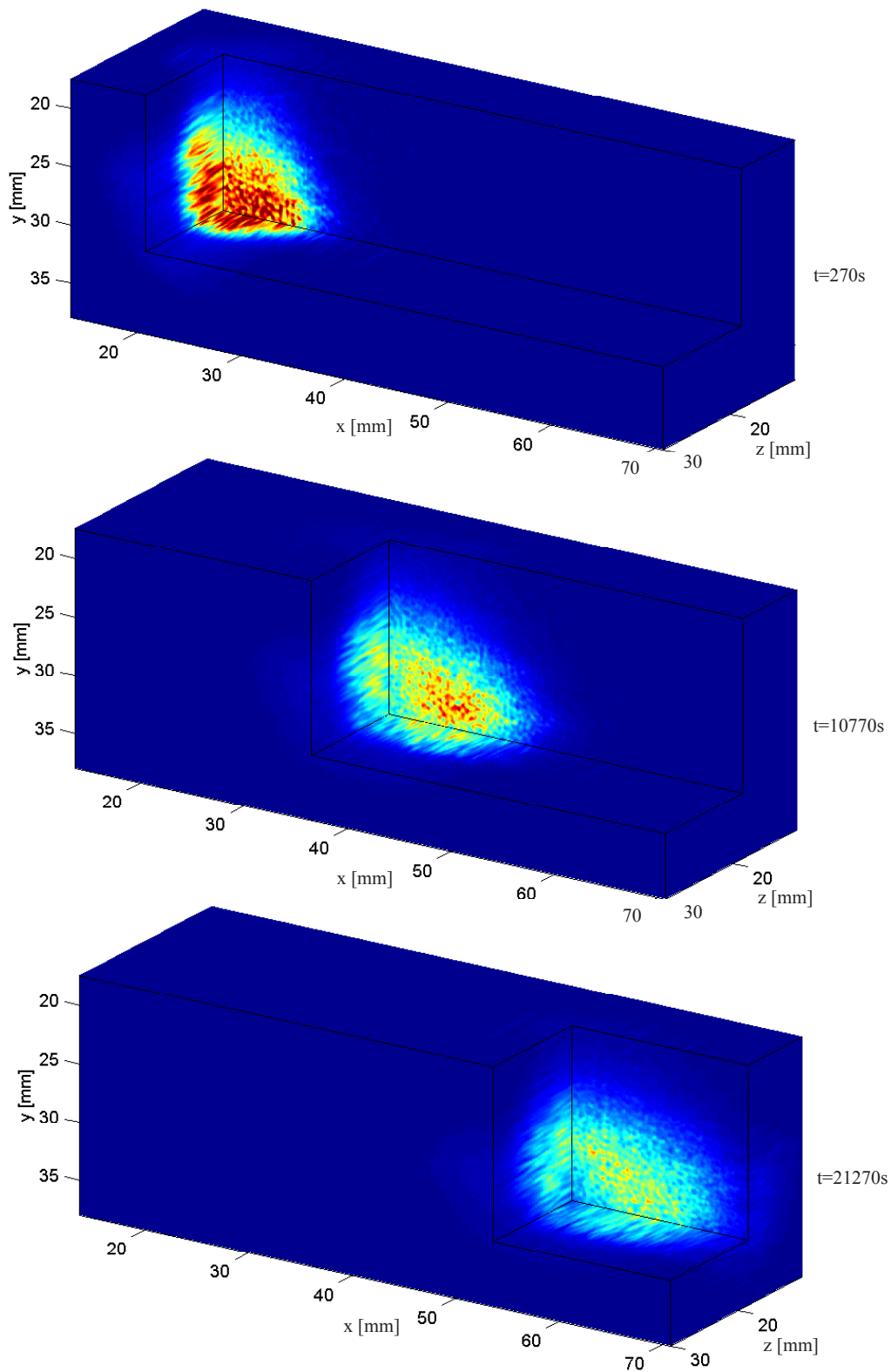


Figure 8.8: 3D dye concentration distributions of the experiment A2 (see table 8.3) at $t=270$ s, $t=10770$ s and $t=21270$ s corresponding to the isosurface visualization in figure 8.7.

mainly the two-point correlation functions

$$C_{ff}(\vec{x}_1, \vec{x}_2) = \langle (f(\vec{x}_1) - \langle f(\vec{x}_1) \rangle)(f(\vec{x}_2) - \langle f(\vec{x}_2) \rangle) \rangle \quad (8.3)$$

and

$$R_{ff}(\vec{x}_1, \vec{x}_2) = \frac{C_{ff}(\vec{x}_1, \vec{x}_2)}{\sqrt{C_{ff}(\vec{x}_1, \vec{x}_1)C_{ff}(\vec{x}_2, \vec{x}_2)}}. \quad (8.4)$$

C_{ff} and R_{ff} are called the *autocovariance* and *autocorrelation* of the random function $f(\vec{x})$, and $\langle f(\vec{x}) \rangle$ denotes the ensemble average of f at the position \vec{x} . Since usually only one realization of the porous medium is available, the random function f is assumed to be ergodic and consequently the ensemble average $\langle f(\vec{x}) \rangle$ is replaced by the spatial average \bar{f} . If f is further assumed to be stationary, the correlation functions depend only on the difference vector $\vec{r} = \vec{x}_1 - \vec{x}_2$ and can then be written as

$$C_{ff}(\vec{r}) = (f(\vec{x}) - \bar{f})(\bar{f}(\vec{x} + \vec{r}) - \bar{f}), \quad (8.5)$$

$$R_{ff}(\vec{r}) = \frac{C_{ff}(\vec{r})}{C_{ff}(0)}. \quad (8.6)$$

As described in Berryman & Blair (1986), the shape of the 1D isotropic autocorrelation $C_{\phi\phi}(r)$ can be used to estimate the average particle size d (from the position of $\frac{\partial C_{\phi\phi}(r)}{\partial r} = 0$), the porosity $\phi = C_{\phi\phi}(0)$ and the internal surface area per unit volume $s = -4 \frac{\partial C_{\phi\phi}(r)}{\partial r} \Big|_{r=0}$ from the porosity function $\phi(\vec{x}) \in \{0, 1\}$. While for the suchlike estimation of ϕ and s the relation $\phi^2 \stackrel{!}{=} \phi$ must be valid and therefore an adequate threshold for binarization of the measured porosity function $0 < \phi(\vec{x})_{\text{meas}} < 1$ has to be found, the estimation of d from $C_{\phi\phi}(r)$ is rather uncritical as described below.

For the estimation of $\phi(\vec{x})$ from the measured dye concentrations $c(\vec{x}, t)$, the temporal average of the unchanged concentrations is divided by the temporal average of the spatially smoothed concentrations:

$$\phi(\vec{x}) \propto \frac{\frac{1}{n_t} \sum_{i=1}^{n_t} c(\vec{x}, t_i)}{\frac{1}{n_t} \sum_{i=1}^{n_t} h(\vec{x}) * c(\vec{x}, t_i)} \quad (8.7)$$

where $h(\vec{x})$ denotes a smoothing filter mask for averaging over an appropriate REV. The effect of smoothing is shown in figure 8.9a,b for an experiment with plexiglass (A2 from table 8.3) and a REV size of circa $(1.5 \text{ mm})^2$. After the temporal averaging and the division according to equation 8.7 the estimate of $\phi(\vec{x})$ shown in figure 8.9c is obtained. Figure 8.9d shows $\phi(\vec{x})$ obtained from an experiment with fused silica (C1 from table 8.3). Here the pore and particle sizes are apparently larger. If the denominator of equation 8.7 becomes small, i.e. when the temporal average of the intensity in the data at the position \vec{x} is too low, the result for $\phi(\vec{x})$ becomes instable, which can be seen at the corners and edges of figures 8.9c,d. The estimation of $\phi(\vec{x})$ is therefore restricted to the areas where a significant amount of tracer dye passed through.

From the so obtained estimates of $\phi(\vec{x})$ now the autocorrelation $R_{\phi\phi}(\vec{r})$ is calculated according to equations 8.5 and 8.6. Figures 8.10a,c show the results for plexiglass and fused silica, respectively. The corresponding 1D autocorrelations in x- and y-direction, $R_{\phi\phi}(x)$ and $R_{\phi\phi}(y)$, are shown in figures 8.10b,d. From these curves the mean particle sizes of the two materials, d_{PG} and d_{FS} are estimated from the location of the first maxima to $d_{\text{PG}} \approx 0.7 \text{ mm}$

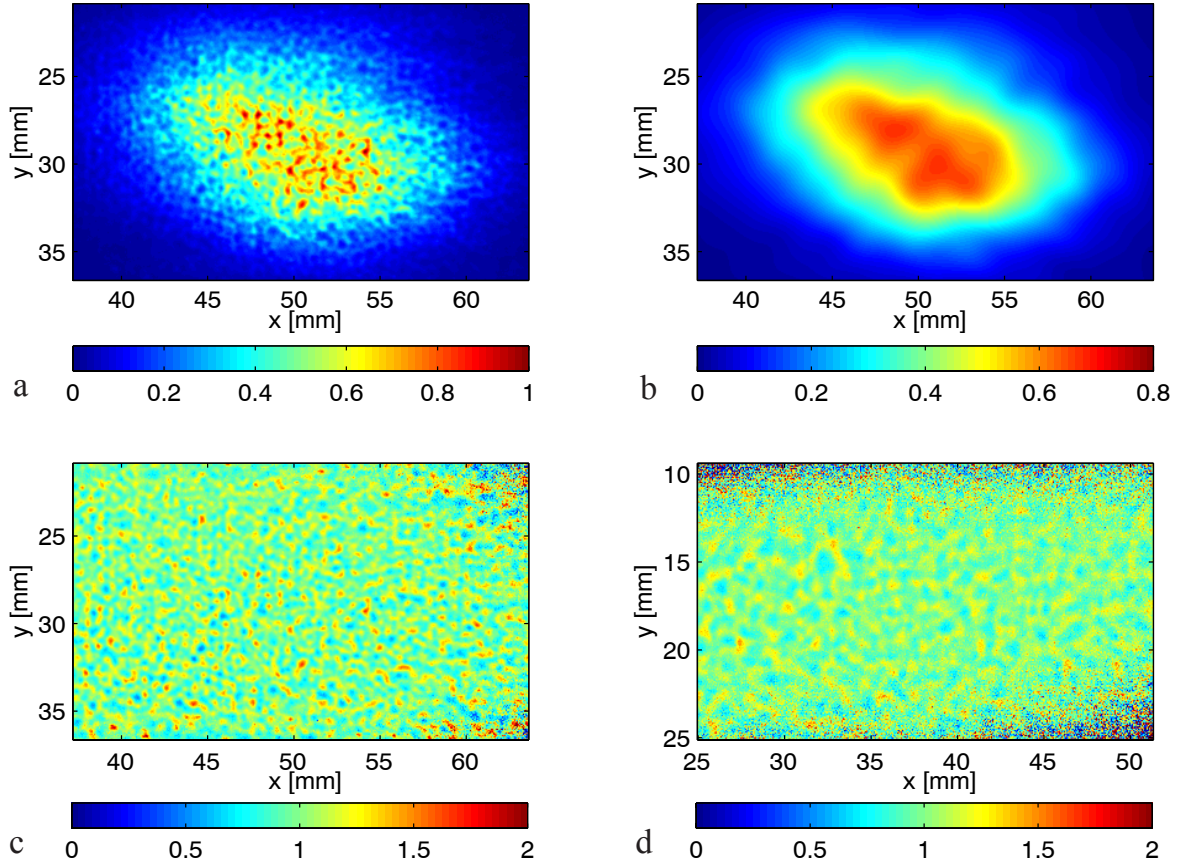


Figure 8.9: Estimation of the porosity $\phi(\vec{x})$ of packed plexiglass grains from the ratio of **a** the original image (taken from the experiment A2 at $t = 16470$ s and $z = 20$ mm) and **b** a smoothed version of the same image. The resulting distribution of $\phi(\vec{x})$ in **c** is obtained with the temporal averages according to equation 8.7. **d** The corresponding result for fused silica grains (taken from the experiment C1 at $z = 20$ mm) indicates larger pore and particle sizes.

and $d_{FS} \approx 1.15$ mm. In the following these values are used for the calculation of the Peclet number. For both materials the locations of the maxima in x- and y-direction are in good agreement, which indicates that no significant anisotropies are inherent in the pore structures.

8.3.2 Longitudinal and transverse dispersion coefficients

In the following now the estimation of the longitudinal and transverse dispersion coefficients from the measured 4D data sets $c(x, y, z, t)$ will be described. The first step towards the estimation of these effective macroscopic parameters is an appropriate averaging of the data over an adequate REV. As explained in section 6.2, the averaging over the yz -, xz - and xy -planes according to equations 6.4-6.6 leads to the macroscopic concentrations $\bar{c}(x, t)$, $\bar{c}(y, t)$ and $\bar{c}(z, t)$ which can each be modeled by a 1D convection-dispersion equation. From these averaged concentrations the temporal evolutions of $\bar{x}(t)$, $\bar{y}(t)$, $\bar{z}(t)$, $\sigma_x^2(t)$, $\sigma_y^2(t)$ and $\sigma_z^2(t)$ can

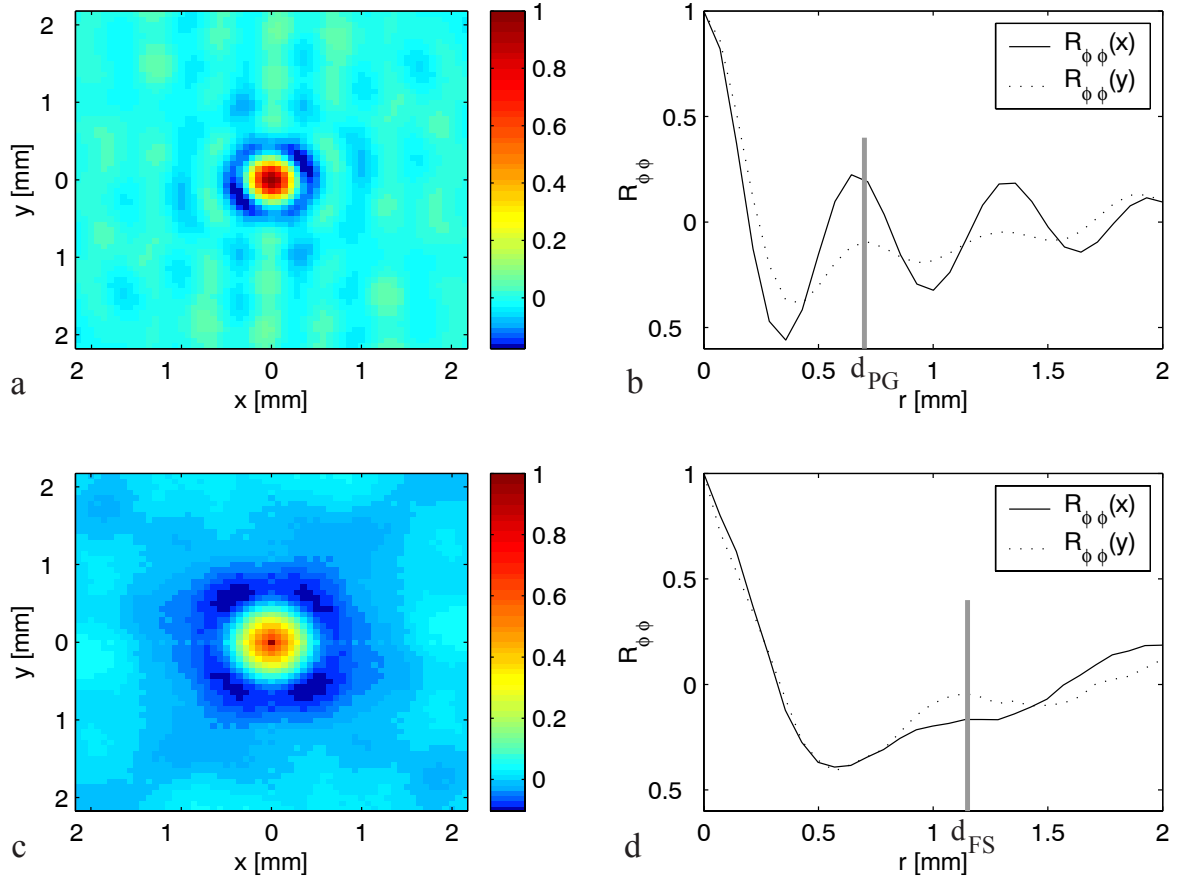


Figure 8.10: Autocorrelation $R_{\phi\phi}(\vec{r})$ for **a** packed plexiglass grains and **c** packed fused silica grains calculated from $\phi(\vec{x})$ in figure 8.9c+d using equations 8.5 and 8.6. From the first maxima of the corresponding 1D autocorrelations $R_{\phi\phi}(x)$ and $R_{\phi\phi}(y)$ in **b** and **d** the mean particle sizes are estimated to $d_{PG} \approx 0.7$ mm and $d_{FS} \approx 1.15$ mm.

then be computed by a least-squares fit of a solution of the 1D CDE as described in section 6.4. The spatial distributions of $\bar{c}(x, t)$, $\bar{c}(y, t)$ and $\bar{c}(z, t)$ at five different times are plotted in appendix B for all measurements of series A-C (see table 8.3). For the measurements of series B, the times before and after the reversal of flow direction, denoted as B1a / B2a and B1r / B2r respectively, have been evaluated individually. Additionally the accordingly obtained temporal evolutions of $\bar{x}(t)$, $\bar{y}(t)$, $\bar{z}(t)$, $\sigma_x^2(t)$, $\sigma_y^2(t)$ and $\sigma_z^2(t)$ are plotted over the complete measurement times.

Finally, the macroscopic velocities \bar{v}_x , \bar{v}_y and \bar{v}_z are estimated as

$$\bar{v}_x = \frac{d\bar{x}(t)}{dt}, \quad \bar{v}_y = \frac{d\bar{y}(t)}{dt}, \quad \bar{v}_z = \frac{d\bar{z}(t)}{dt}, \quad (8.8)$$

and the longitudinal and transverse dispersion coefficients D_L , D_{Ty} and D_{Tz} as

$$D_L = \frac{1}{2} \frac{d\sigma_x^2(t)}{dt}, \quad D_{Ty} = \frac{1}{2} \frac{d\sigma_y^2(t)}{dt}, \quad D_{Tz} = \frac{1}{2} \frac{d\sigma_z^2(t)}{dt}. \quad (8.9)$$

For the measurements shown in appendix B, the values of \bar{v}_x , \bar{v}_y , \bar{v}_z , D_L , D_{Ty} , D_{Tz} are calculated from a least squares fit of a straight line to the corresponding temporal evolution, like for e.g. for \bar{v}_x :

$$\chi^2 = \sum_{i=a}^b (\bar{x}(t_i) - (x_0 + \bar{v}_x t_i))^2 \stackrel{!}{=} \min. \quad (8.10)$$

The temporal range for these fits, $t_a < t < t_b$ was chosen in the way that for all measurements the same range in x-direction is covered, i.e. $\bar{x}(t_a) \approx 24$ mm and $\bar{x}(t_b) \approx 67$ mm. These temporal ranges and the resulting straight lines are illustrated by the gray lines. A more detailed discussion of the temporal evolutions of $\bar{x}(t)$, $\bar{y}(t)$, $\bar{z}(t)$, $\sigma_x^2(t)$, $\sigma_y^2(t)$ and $\sigma_z^2(t)$ is given in section 8.3.3.

The so obtained results for \bar{v}_x , \bar{v}_y , \bar{v}_z , D_L , D_{Ty} , D_{Tz} and $Pe = \frac{\bar{v}_x d}{D_m}$, using d from section 8.3.1 and D_m from section 8.2 are listed in table 8.3. The results of series D are addressed separately in section 8.3.6, since here adsorption contributes significantly to the dye transport, which therefore cannot be described by a usual 1D CDE. The provided errors were calculated from the mean residual $\overline{\chi^2}$ and the inverse of the hessian matrix D as described in section 6.5. For the least squares fit 8.10 of \bar{v}_x for instance this leads to:

$$\text{cov}_{\vec{p}} = \overline{\chi^2} \left(\frac{1}{2} D \right)^{-1} \quad \text{with} \quad \vec{p} = \begin{pmatrix} x_0 \\ \bar{v}_x \end{pmatrix}, \quad \overline{\chi^2} = \frac{1}{b-a+1} \chi^2 \quad \text{and} \quad D_{ij} = \frac{\partial^2 \chi^2}{\partial p_i \partial p_j}. \quad (8.11)$$

As expected, the relative errors increase if the temporal evolution deviates from a linear progression, if the statistical fluctuations become significant or if the number of time steps $n_t = b - a + 1$ decreases like in the experiments with high flow rates.

Longitudinal dispersion

Figure 8.11a shows the dependence of the measured coefficients of longitudinal dispersion on the Peclet number. In order to compare experiments with different D_m , the longitudinal dispersion is quantified, as is customary in the literature, by the dimensionless ratio of D_L to D_m . Many efforts have been made during the last decades in order to find an analytical expression for a functional dependence $D_L(Pe)$ (see Koch & Brady (1985) and the reviews in Sahimi (1993) and Fried & Combarous (1971)). In the recent literature mainly the two relations discussed below are used.

As described in section 2.3.3, the asymptotic value of D_L can be related to the contributions from molecular diffusion, mechanical dispersion, boundary-layer dispersion and holdup dispersion through the equation

$$\frac{D_L}{D_m} = \tau + \alpha Pe + \beta Pe \ln Pe + \gamma Pe^2. \quad (8.12)$$

The magnitude of $0 < \tau < 1$ can be neglected for $Pe > 10$ and is therefore set to $\tau = \frac{2}{3}$ in the following. The values of α , β and γ have then been obtained from a least squares fit to the data shown in figure 8.11a. The result, denoted as *Model 1*, apparently provides a good approximation of the data. Table 8.4 compares the obtained values to results from the literature. The obtained value for α has a high uncertainty because the term αPe is mainly important for low Pe , where no data for D_L is available. Maier *et al.* (2000) have obtained their results from lattice boltzmann simulations, which did not consider holdup dispersion,

	\bar{v}_x [mm/s]	\bar{v}_y [mm/s]	\bar{v}_z [mm/s]	Pe	Δh [cm]
A1	$(9.332 \pm 1) \cdot 10^{-4}$	$(2.02 \pm 2) \cdot 10^{-5}$	$(1.29 \pm 1) \cdot 10^{-5}$	33.327 ± 5	
A2	$(1.7067 \pm 3) \cdot 10^{-3}$	$(2.16 \pm 4) \cdot 10^{-5}$	$(1.23 \pm 4) \cdot 10^{-5}$	60.95 ± 1	
A3	$(2.0542 \pm 3) \cdot 10^{-3}$	$(3.72 \pm 5) \cdot 10^{-5}$	$(2.81 \pm 3) \cdot 10^{-5}$	73.36 ± 1	
A4	$(4.496 \pm 2) \cdot 10^{-3}$	$(8.1 \pm 3) \cdot 10^{-5}$	$(1.6 \pm 3) \cdot 10^{-5}$	160.56 ± 6	
A5	$(7.976 \pm 2) \cdot 10^{-3}$	$(1.19 \pm 3) \cdot 10^{-4}$	$(1.25 \pm 6) \cdot 10^{-4}$	284.84 ± 6	1.2
A6	$(8.433 \pm 7) \cdot 10^{-3}$	$(1.42 \pm 5) \cdot 10^{-4}$	$(1.04 \pm 2) \cdot 10^{-4}$	301.2 ± 3	
A7	$(1.736 \pm 2) \cdot 10^{-2}$	$(3.1 \pm 2) \cdot 10^{-4}$	$(4 \pm 2) \cdot 10^{-5}$	620.0 ± 5	2.7
A8	$(3.319 \pm 3) \cdot 10^{-2}$	$(3.1 \pm 4) \cdot 10^{-4}$	$(6 \pm 5) \cdot 10^{-5}$	1185 ± 1	5.6
A9	$(6.98 \pm 1) \cdot 10^{-2}$	$(1.4 \pm 2) \cdot 10^{-3}$	$(-1 \pm 1) \cdot 10^{-4}$	2494 ± 3	9.8
A10	$(9.22 \pm 2) \cdot 10^{-2}$	$(2.1 \pm 3) \cdot 10^{-3}$	$(-1 \pm 2) \cdot 10^{-4}$	3293 ± 7	13.8
A11	$(1.322 \pm 9) \cdot 10^{-1}$	$(2.4 \pm 3) \cdot 10^{-3}$	$(-1.7 \pm 3) \cdot 10^{-3}$	$(472 \pm 3) \cdot 10^1$	20.7
A12	$(1.381 \pm 9) \cdot 10^{-1}$	$(2.2 \pm 3) \cdot 10^{-3}$	$(-1.3 \pm 6) \cdot 10^{-3}$	$(493 \pm 3) \cdot 10^1$	20.7
A13	$(1.839 \pm 7) \cdot 10^{-1}$	$(2.3 \pm 5) \cdot 10^{-3}$	$(-2 \pm 5) \cdot 10^{-4}$	$(657 \pm 2) \cdot 10^1$	27.8
A14	$(1.870 \pm 4) \cdot 10^{-1}$	$(1.3 \pm 2) \cdot 10^{-3}$	$(-2 \pm 1) \cdot 10^{-3}$	$(668 \pm 2) \cdot 10^1$	27.8
B1a	$(8.841 \pm 6) \cdot 10^{-3}$	$(1.53 \pm 5) \cdot 10^{-4}$	$(1.3 \pm 2) \cdot 10^{-4}$	315.7 ± 2	1.2
B1r	$(-8.28 \pm 2) \cdot 10^{-3}$	$(-1.07 \pm 5) \cdot 10^{-4}$	$(-1.8 \pm 2) \cdot 10^{-4}$	295.6 ± 6	
B2a	$(3.104 \pm 2) \cdot 10^{-2}$	$(6.0 \pm 4) \cdot 10^{-4}$	$(5.7 \pm 8) \cdot 10^{-4}$	1108.5 ± 7	5.6
B2r	$(-3.13 \pm 2) \cdot 10^{-2}$	$(-6.24 \pm 3) \cdot 10^{-4}$	$(-6.4 \pm 6) \cdot 10^{-4}$	1116 ± 7	
C1	$(2.421 \pm 1) \cdot 10^{-3}$	$(-2.34 \pm 1) \cdot 10^{-4}$	$(7.18 \pm 5) \cdot 10^{-5}$	51.93 ± 2	
C2	$(9.04 \pm 3) \cdot 10^{-3}$	$(9.3 \pm 1) \cdot 10^{-4}$	$(2.03 \pm 8) \cdot 10^{-4}$	194.0 ± 7	

	D_L [mm ² /s]	D_{T_y} [mm ² /s]	D_{T_z} [mm ² /s]
A1	$(7.81 \pm 2) \cdot 10^{-4}$	$(2.119 \pm 5) \cdot 10^{-4}$	$(4.55 \pm 2) \cdot 10^{-4}$
A2	$(2.184 \pm 3) \cdot 10^{-3}$	$(-7.6 \pm 5) \cdot 10^{-6}$	$(4.587 \pm 9) \cdot 10^{-4}$
A3	$(2.135 \pm 4) \cdot 10^{-3}$	$(1.58 \pm 3) \cdot 10^{-4}$	$(6.60 \pm 1) \cdot 10^{-4}$
A4	$(6.42 \pm 1) \cdot 10^{-3}$	$(-6 \pm 1) \cdot 10^{-5}$	$(1.214 \pm 5) \cdot 10^{-3}$
A5	$(1.128 \pm 5) \cdot 10^{-2}$	$(5.44 \pm 5) \cdot 10^{-4}$	$(1.53 \pm 2) \cdot 10^{-3}$
A6	$(1.29 \pm 1) \cdot 10^{-2}$	$(5.1 \pm 3) \cdot 10^{-4}$	$(1.64 \pm 5) \cdot 10^{-3}$
A7	$(2.87 \pm 2) \cdot 10^{-2}$	$(-6 \pm 1) \cdot 10^{-4}$	$(3.1 \pm 1) \cdot 10^{-3}$
A8	$(6.23 \pm 6) \cdot 10^{-2}$	$(7 \pm 2) \cdot 10^{-4}$	$(7.3 \pm 2) \cdot 10^{-3}$
A9	$(1.59 \pm 1) \cdot 10^{-1}$	$(-3.9 \pm 4) \cdot 10^{-3}$	$(1.21 \pm 6) \cdot 10^{-2}$
A10	$(2.14 \pm 3) \cdot 10^{-1}$	$(-4.6 \pm 7) \cdot 10^{-3}$	$(1.4 \pm 1) \cdot 10^{-2}$
A11	$(3.3 \pm 2) \cdot 10^{-1}$	$(-9 \pm 7) \cdot 10^{-4}$	$(2.2 \pm 1) \cdot 10^{-2}$
A12	$(2.9 \pm 2) \cdot 10^{-1}$	$(-2 \pm 1) \cdot 10^{-3}$	$(3.0 \pm 4) \cdot 10^{-2}$
A13	$(4.7 \pm 1) \cdot 10^{-1}$	$(2.3 \pm 2) \cdot 10^{-2}$	$(2.7 \pm 4) \cdot 10^{-2}$
A14	$(4.56 \pm 7) \cdot 10^{-1}$	$(3 \pm 3) \cdot 10^{-3}$	$(2.5 \pm 3) \cdot 10^{-2}$
B1a	$(1.286 \pm 2) \cdot 10^{-2}$	$(1.0 \pm 3) \cdot 10^{-4}$	$(2.3 \pm 2) \cdot 10^{-3}$
B1r	$(1.132 \pm 6) \cdot 10^{-2}$	$(2.12 \pm 4) \cdot 10^{-3}$	$(-1.5 \pm 2) \cdot 10^{-3}$
B2a	$(5.68 \pm 4) \cdot 10^{-2}$	$(2 \pm 3) \cdot 10^{-4}$	$(2.0 \pm 1) \cdot 10^{-2}$
B2r	$(5.40 \pm 8) \cdot 10^{-2}$	$(5.2 \pm 2) \cdot 10^{-3}$	$(-1.5 \pm 1) \cdot 10^{-2}$
C1	$(4.5 \pm 1) \cdot 10^{-3}$	$(2.121 \pm 7) \cdot 10^{-3}$	$(1.74 \pm 1) \cdot 10^{-3}$
C2	$(3.5 \pm 2) \cdot 10^{-3}$	$(3 \pm 1) \cdot 10^{-5}$	$(4.33 \pm 6) \cdot 10^{-3}$

Table 8.3: Results for mean velocities and longitudinal and transverse dispersion coefficients from the experiments of series A, B and C. The digits after \pm denote the error related to the last digit of the result.

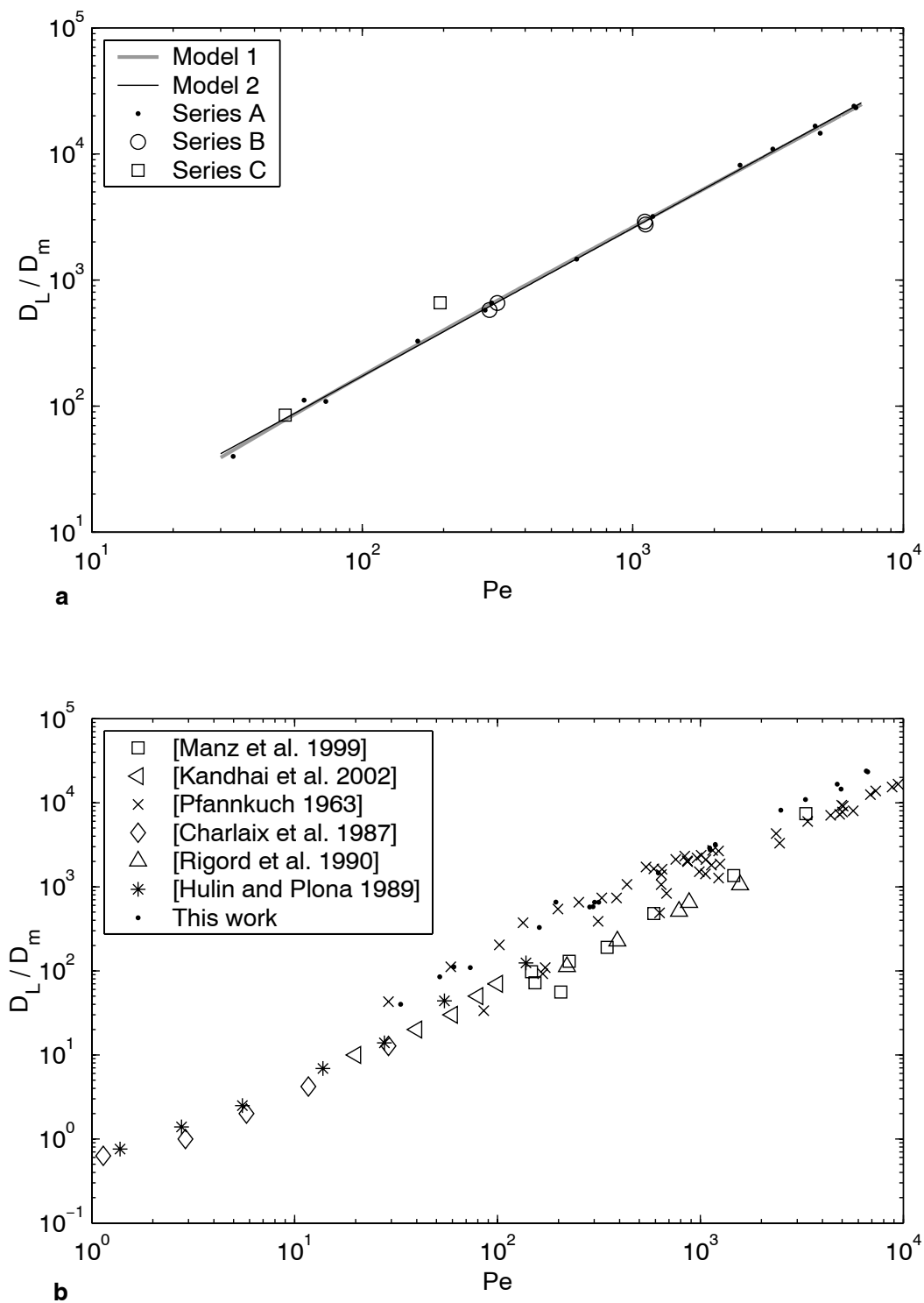


Figure 8.11: **a** Coefficients of longitudinal dispersion obtained from measurements of series A, B and C. The solid lines represent the least squares approximations of the models for $D_L(Pe)$ given by equations 8.12 and 8.13. **b** Comparison with results from NMR measurements (Manz *et al.* (1999) and Kandhai *et al.* (2002)) and classical breakthrough experiments (Pfannkuch (1963), Charlaix *et al.* (1987), Rigord *et al.* (1990) and Hulin & Plona (1989)).

Reference	α	β	γ	Pe range
Maier <i>et al.</i> (2000)	0.25	0.03	0	$1 < \text{Pe} < 5000$
Kandhai <i>et al.</i> (2002)	0.153 ± 9	0.080 ± 5	$(1.7 \pm 2) \cdot 10^{-3}$	$0.1 < \text{Pe} < 100$
This work	0.0 ± 2	0.37 ± 4	$(3 \pm 1) \cdot 10^{-5}$	$33 < \text{Pe} < 6680$

Table 8.4: Parameters of the functional dependence $D_L(\text{Pe})$ given by equation 8.12 for unconsolidated bead packings obtained from lattice-boltzmann simulations (Maier *et al.*, 2000), NMR measurements (Kandhai *et al.*, 2002) and the experimental data given in table 8.3. The digits after \pm denote the error related to the last digit of the result.

and therefore γ was set to zero. From the comparison of the results for α and β it is obvious that these simulations do not agree with the measurements of this work. The results of Kandhai *et al.* (2002), which were found from NMR measurements, also differ strongly from the results of this work. There is a general trend that the values for D_L obtained from NMR measurements are about one order of magnitude lower than the values from other methods, a finding which has been reported by several authors (see e.g. Kandhai *et al.* (2002), Maier *et al.* (2000), Manz *et al.* (1999) and Seymour & Callaghan (1997)). This disagreement is confirmed by the results of this work. The results for α , β and γ obtained from the measurements of this work agree with theoretical considerations predicting that the major contribution to D_L in this regime comes from boundary-layer dispersion, which is quantified by the parameter β (Koch & Brady (1985), Sahimi (1993)). A further discussion about the possible influence of holdup dispersion is given in section 8.3.5.

Another model which is commonly used to describe $D_L(\text{Pe})$ for $\text{Pe} > 5$ is the power-law relationship

$$\frac{D_L}{D_m} = \alpha \text{Pe}^n \quad (8.13)$$

Although there is no direct physical motivation for this relation, it has been found to provide a good approximation of experimental results. The consistence of this model, denoted as *Model 2* in figure 8.11a, with the data of this work is apparently well. Table 8.5 lists the values of α and n found from the data of this work and by other authors. n compares reasonably with the result of Manz *et al.* (1999) obtained with NMR and agrees well with the result of Dullien (1992), which was calculated from a compilation of measured dispersion coefficients from several authors. It also agrees with the compilation of α 's and n 's in Gist *et al.* (1990), where most results for n are in the range $1.1 < n < 1.22$. A distinctly higher value of $n = 1.29$ was found by Coelho *et al.* (1997) from numerical studies. Whereas n seems to be consistent for a large range of flow rates and grain size distributions, the results of Gist *et al.* (1990) indicate that α is much more sensitive to the pore structure and the amount of heterogeneities of the unconsolidated bead packing. This finding is confirmed by the below discussed comparison of data from the literature shown in figure 8.11b.

If one assumes that a functional relationship for $D_L(\text{Pe})$ like equation 8.12 or 8.13 must be valid, the errors for D_L and Pe given in table 8.3 do not suffice to explain the deviations of the experimental data from the fitted curves $D_L(\text{Pe})$ (the errors are so small that they cannot be identified from the logarithmic diagram 8.11a). However, these errors only account for the uncertainties of the respective individual measurements. The possible variance of D_L due to heterogeneities in the porous medium, which will be induced by the varying initial distributions used in the experiments (see appendix B), is not contained in the given errors

Reference	α	n
Manz <i>et al.</i> (1999)	-	1.12 ± 2
Coelho <i>et al.</i> (1997)	0.26	1.29
Gist <i>et al.</i> (1990)	0.46-3.9	0.93-1.22
Dullien (1992)	-	1.2
This work	0.77 ± 8	1.18 ± 2

Table 8.5: Parameters of the power-law dependence for $D_L(\text{Pe})$ given by equation 8.13 obtained for unconsolidated bead packings reported by various authors and found from the experimental data given in table 8.3. The digits after \pm denote the error related to the last digit of the result.

and may serve as an explanation for the aforementioned deviations.

Finally a comparison of experimental results for D_L from different authors is given in figure 8.11b. The values of Manz *et al.* (1999) and Kandhai *et al.* (2002) are obtained with NMR techniques, whereas the others were found from breakthrough curve measurements. Obviously the results of this work compare best with those of Pfannkuch (1963), which cover a similar range of Peclet numbers. A possible reason for the comparatively low values of other experiments could be that the transport distance is too short to reach the asymptotic value as discussed in Han *et al.* (1985).

Transverse dispersion

Only few measurements of transverse dispersion coefficients have been reported in the literature until now. Figure 8.12 shows two compilations of results for unconsolidated bead packings reprinted from Han *et al.* (1985) and Delgado & Guedes de Carvalho (2001). None of these works, mostly performed in the 1960's using conductivity probes to measure the transverse breakthrough distribution, has made a distinction between transverse dispersions in the vertical and horizontal direction. To the authors knowledge the PLIF measurements performed in this work are the first to simultaneously measure transverse dispersion in the vertical and horizontal direction. Additionally the present technique allows for highly resolved measurements of the temporal evolutions of $\sigma_y^2(t)$ and $\sigma_z^2(t)$ which are discussed in section 8.3.3.

Figures 8.13a,b show the semilogarithmic plots of the measured transverse dispersion coefficients in the vertical (D_{Ty}) and horizontal (D_{Tz}) direction given in table 8.3. The comparison of these two plots reveals a significantly different behavior of vertical and horizontal transverse dispersion: whereas D_{Tz} shows a considerable increase with Pe, which becomes even more evident from the double-logarithmic plot shown in figure 8.13c, D_{Ty} remains essentially constant near zero over the whole range of Pe, with the variance of D_{Ty} growing with Pe.

Two possible reasons have to be considered for an explanation of this anisotropic behavior:

- Anisotropy in the structure of the porous medium.
- Anisotropic external forces like gravity, which is directed in vertical direction and could therefore lead to a decrease of D_{Ty} via a density gradient in the fluid.

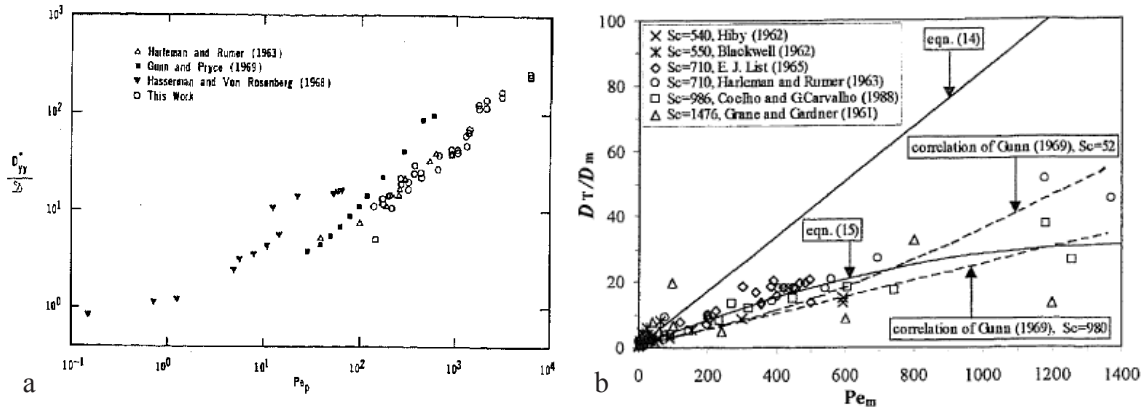


Figure 8.12: Compilations of measured transverse dispersion coefficients in unconsolidated bead packings reprinted from **a** Han *et al.* (1985) and **b** Delgado & Guedes de Carvalho (2001).

A first argument against the first hypothesis are the results about the pore structure obtained in section 8.3.1: no anisotropies between vertical and horizontal direction are identifiable from figures 8.9c+d, and the vertical and horizontal correlation lengths found from figures 8.10b+d show no appreciable differences. A second argument in favor of the second hypothesis are the findings presented in section 8.3.4.

In figure 8.13c the measured values of D_{Tz} are fitted to a power-law analog to equation 8.13:

$$\frac{D_{Tz}}{D_m} = \alpha Pe^n. \quad (8.14)$$

The parameters are estimated to $\alpha = 0.7 \pm 2$ and $n = 0.87 \pm 3$. The value of n agrees well with the value of $n = 0.9$ obtained by Sahimi (1993) from a compilation of results from several authors. Harleman & Rumer (1963) have found a value of $n = 0.7$ from experimental observations, and the numerical studies of Coelho *et al.* (1997) yielded a value of $n = 0.72$.

Finally figure 8.14 compares the measured values to the recent results of Manz *et al.* (1999) obtained with a NMR technique and Delgado & Guedes de Carvalho (2001) using mass transfer measurements from a buried flat wall aligned with the flow. The latter found the following relationship for $Sc \geq 550$ and $Pe < 1400$:

$$\frac{D_T}{D_m} = 0.71 + 0.0425Pe - 1.48 \cdot 10^{-5}Pe^2. \quad (8.15)$$

Both cited works agree reasonably with the vertical transverse dispersions coefficients of this work.

Hydraulic conductivity

For the experiments of series A and C, using plexiglass grains for the porous matrix and a silicone oil mixture as a fluid, the estimated velocities v_x and the measured differences Δh of the liquid heights at the inlet and outlet of the horizontal flow cell, given in table 8.3 and

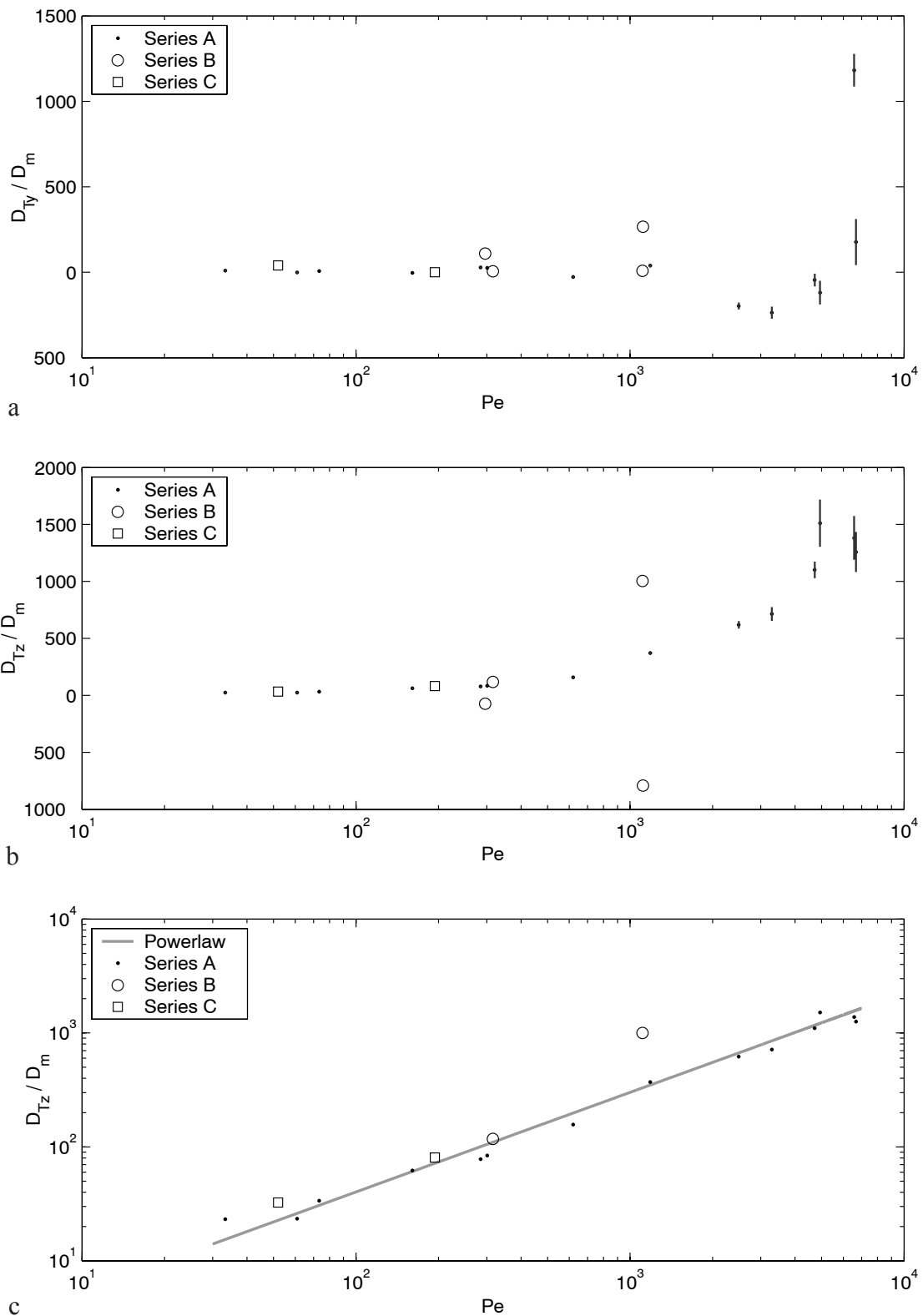


Figure 8.13: Semilogarithmic plot of measured transverse dispersion coefficients in **a** vertical and **b** horizontal direction. **c** double-logarithmic plot of horizontal transverse dispersion coefficients with least squares fit of the power-law relation 8.14.

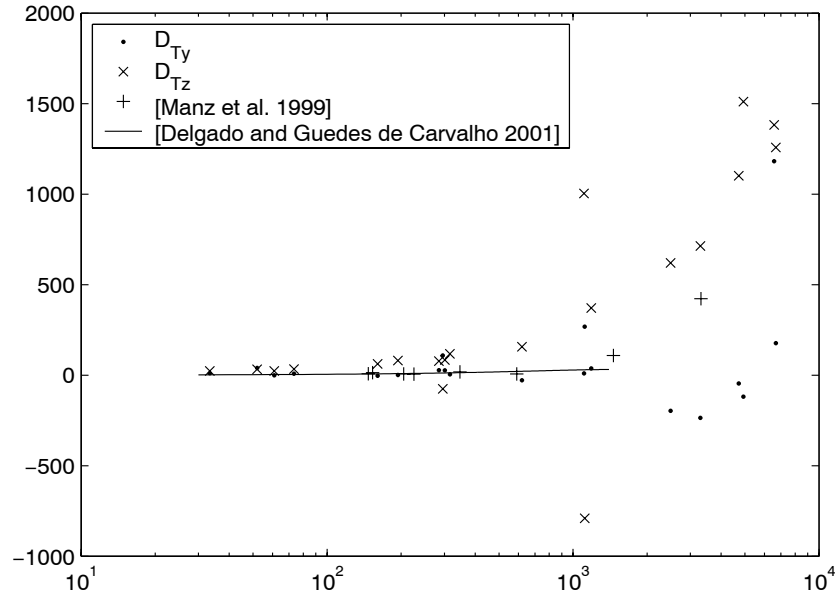


Figure 8.14: Comparison of the measured coefficients of transverse dispersion with literature data.

plotted in figure 8.15, can be used to estimate the hydraulic conductivity K , defined by the relation between the volumetric flux j_x and the hydraulic gradient $\frac{d\psi}{dx}$

$$j_x = -K \frac{d\psi}{dx}. \quad (8.16)$$

From the slope of the least squares straight line fit shown in figure 8.15, estimated to $\frac{\Delta v_x}{\Delta(\Delta h)} = (6.62 \pm 6) \cdot 10^{-4} \frac{1}{s}$, the hydraulic conductivity K can then be calculated as:

$$K = \frac{\Delta v_x}{\Delta(\Delta h)} \frac{\phi_{\text{plexiglass}} \Delta x}{g \rho_{\text{siliconeoil}}} = (6.62 \pm 6) \cdot 10^{-4} \frac{1}{s} \frac{0.37 \cdot 80 \text{ mm}}{9.81 \text{ ms}^{-2} \cdot 1.05 \text{ gcm}^{-3}} = (1.90 \pm 2) \cdot 10^{-9} \frac{\text{m}^3 \text{ s}}{\text{kg}}. \quad (8.17)$$

The value of the alternatively defined hydraulic conductivity $K^* = \rho g K$ (see e.g. Roth (1996a)) is given by

$$K^* = \rho_{\text{siliconeoil}} g K = (1.96 \pm 2) \cdot 10^{-5} \frac{\text{m}}{\text{s}}. \quad (8.18)$$

8.3.3 Temporal evolution of mean and variance

Until now a linear temporal increase of the mean positions $\bar{x}(t)$, $\bar{y}(t)$, $\bar{z}(t)$ and variances $\sigma_x^2(t)$, $\sigma_y^2(t)$, $\sigma_z^2(t)$ was assumed in order to estimate the velocities \bar{v}_x , \bar{v}_y , \bar{v}_z and dispersion coefficients D_L , D_{Ty} , D_{Tz} . In the following a closer look will be taken at the temporal evolutions of mean and variance which are plotted in appendix B and whose availability is one of the main features of the present experimental technique.

The comparative study of the characteristic temporal behaviors of the respective mean positions and variances shown in appendix B leads to the following observations:

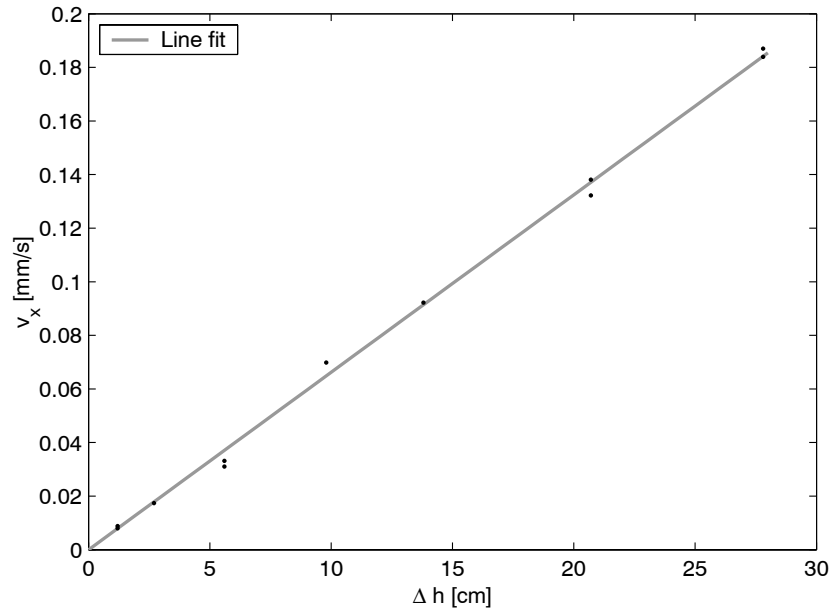


Figure 8.15: Estimated velocities v_x of series A and C given in table 8.3 as a function of the corresponding liquid height differences Δh . The least squares fit of a straight line is used for the estimation of the hydraulic conductivity.

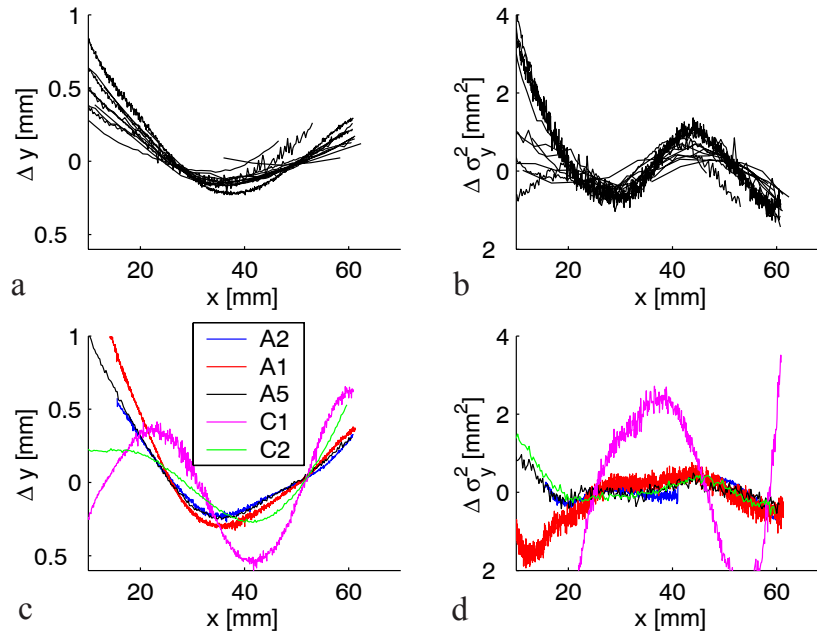


Figure 8.16: Indication for the influence of the porous structure from the deviations of **a** mean position $\bar{y}(t)$ and **b** variance $\sigma_y^2(t)$ from the corresponding straight line fit for the experiments of series A and B. **c** and **d** show the deviant behaviors of experiments A1, A2 and A5 and a comparison with C1 and C2.

- As expected the increase of the mean positions $\bar{x}(t)$ in flow direction is strictly linear.
- Apart from some small fluctuations at the beginning, the increase of $\sigma_x^2(t)$ is generally strictly linear. This indicates that the longitudinal dispersion has reached an asymptotic regime.
- The mean positions in vertical direction $\bar{y}(t)$ show significant variations. A possible explanation is discussed below.
- The vertical variances $\sigma_y^2(t)$ typically exhibit a strong increase at the beginning followed by a pronounced fluctuating behavior, indicating that no asymptotic regime has been reached over the length of the flow cell.
- The mean positions in z-direction $\bar{z}(t)$ are characterized by low fluctuations and small linear trends.
- The variances in z-direction $\sigma_z^2(t)$ typically show a strong increase at the beginning followed by a linear increase, indicating an asymptotic regime.

An intuitive approach to explain the fluctuations of $\bar{y}(t)$ and $\sigma_y^2(t)$ is the presence of heterogeneities, which can hardly be avoided in the construction of an unconsolidated bead packing. To confirm this hypothesis, the deviations between \bar{y} and σ_y^2 and their corresponding straight line fits, $\Delta y = \bar{y} - \bar{y}_{\text{linefit}}$ and $\Delta\sigma_y^2 = \sigma_y^2 - \sigma_{y\text{linefit}}^2$ have been plotted over the mean position in x-direction. The uniform behavior of the curves for series A and B shown in figure 8.16a,b strongly indicates that the deviations are mainly caused by the spatial structure of the porous medium. However, there are few exceptions which are shown in figure 8.16c,d: for $\bar{x} < 40$ mm, the shape of $\Delta\sigma_y^2$ of the experiments A1, A2 and A5 shows some deviant behavior, which might be caused by their deviant initial distributions. As expected the curves for the experiments C1 and C2 have a differing shape since they were measured in a completely different porous medium.

The possible reasons for the different behaviors of transverse dispersion in vertical and horizontal direction, like the stronger vertical fluctuations and the higher horizontal dispersion coefficients D_{Tz} are discussed in sections 8.3.2 and 8.3.4.

8.3.4 Reversibility

The idea behind echo dispersion experiments is the visualization of the effects of heterogeneities inherent in the porous medium through a reversal of flow direction after a certain travel distance. Whereas heterogeneities smaller than the size of the tracer plume lead to an irreversible broadening of the concentration distribution, structures larger than the plume size result in a reversible contribution to the temporal evolution of the mean position and variance.

Two echo dispersion experiments, denoted as B1 and B2, have been made using different flow rates. For both experiments, a heterogeneous initial distribution has been realized by the application of two adjacent tracer pulses. For this reason the dye distributions will not reach their asymptotic gaussian shape during the experiments, and the effect of heterogeneities will be more pronounced. The temporal evolutions of the 1D concentration distributions are shown separately for the times before and after the reversal of flow direction in figures B.15-B.18.

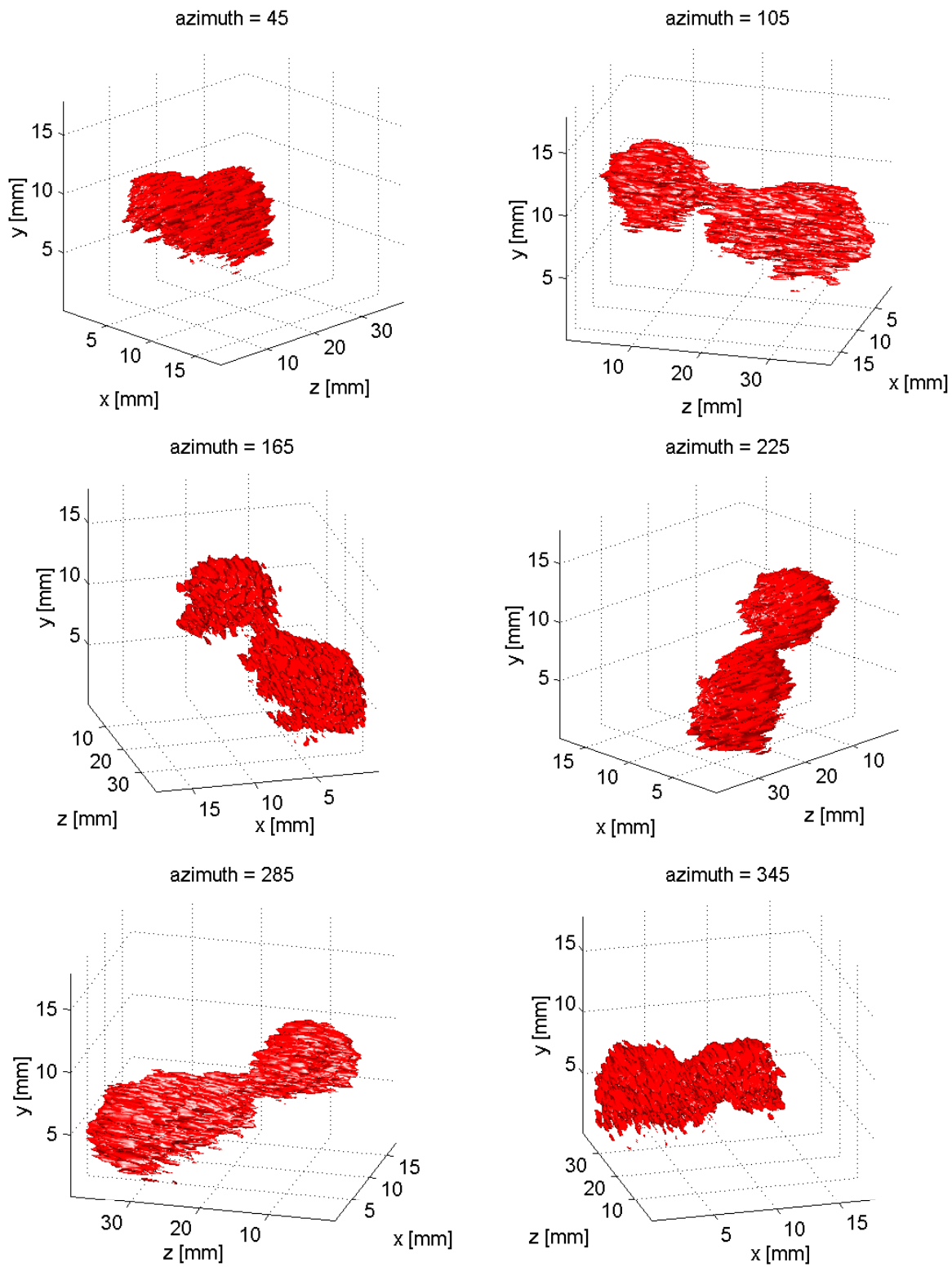


Figure 8.17: Isosurface plots from different angles of the 3D dye concentration distribution of the echo dispersion experiment B1 at $t = 0$ s.

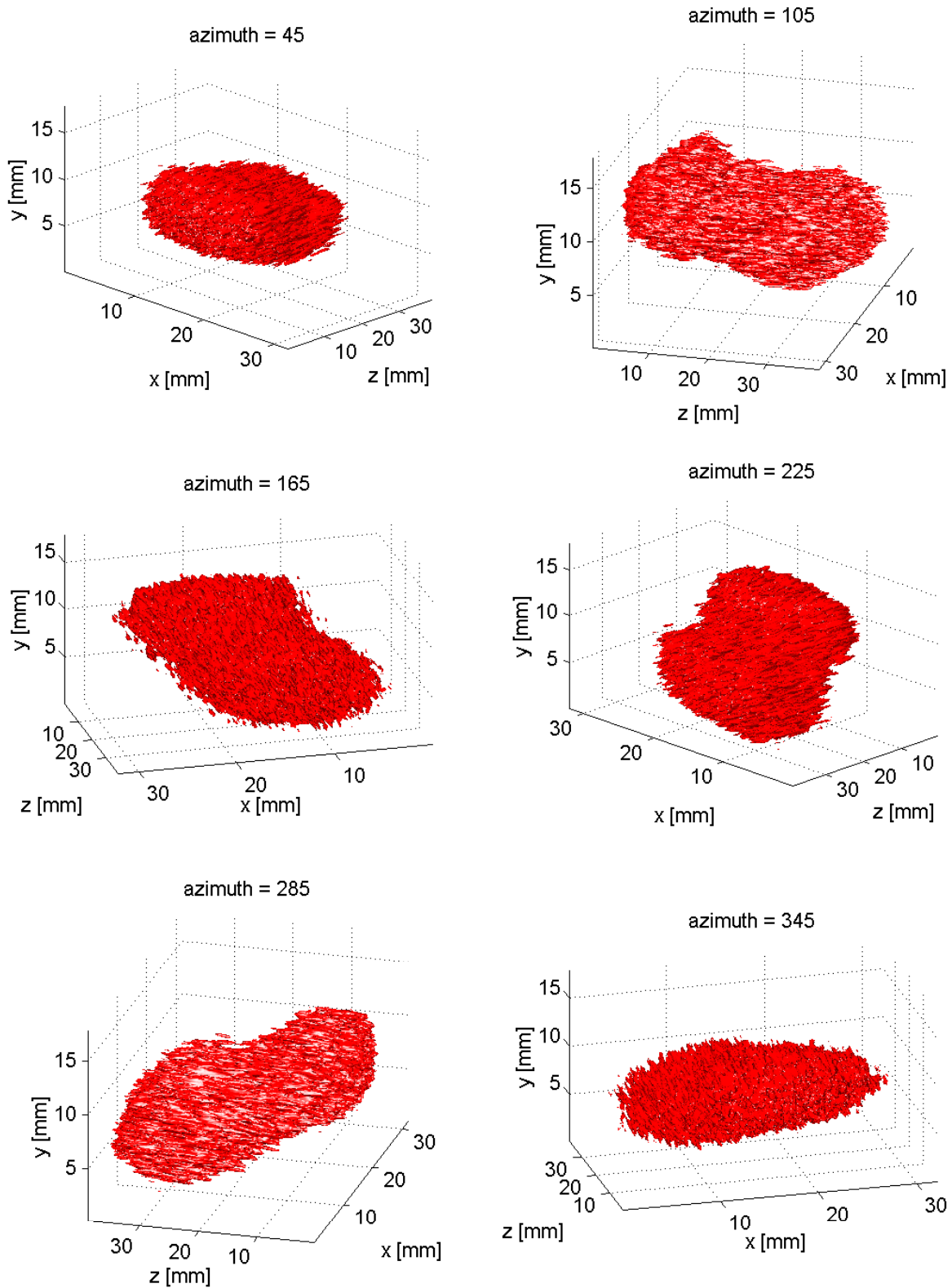


Figure 8.18: Isosurface plots from different angles of the 3D dye concentration distribution of the echo dispersion experiment B1 at $t = 10470$ s.

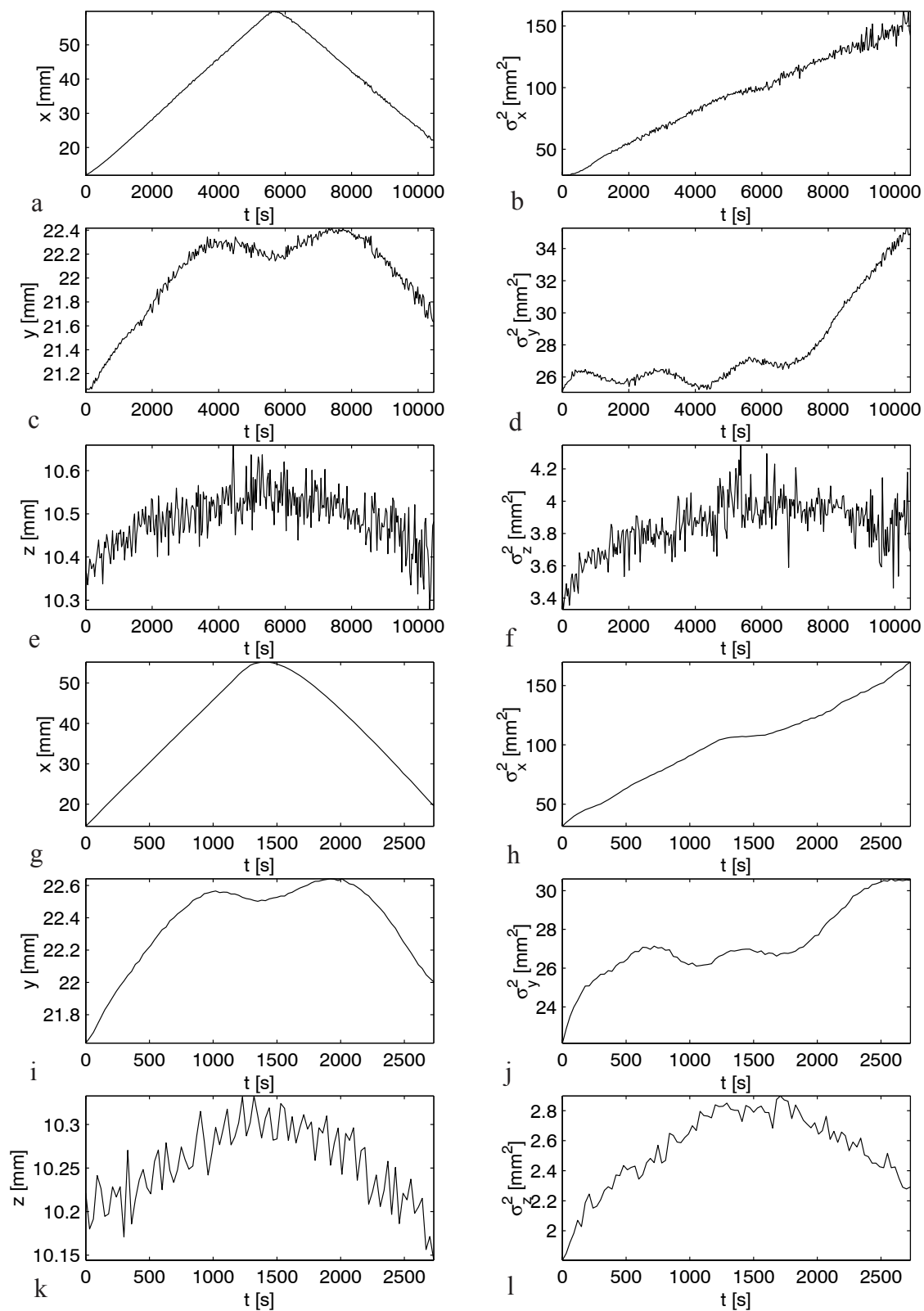


Figure 8.19: Temporal evolutions of mean and variance in x-, y- and z-direction for the echo dispersion experiments B1 (a-f) and B2 (g-l).

Figures 8.17 and 8.18 show visualizations of the 3D dye concentration distribution at the start and at the end of the experiment B1, respectively. From a comparison of these distributions, the effect of the irreversible part of the dispersion, mainly the broadening of the distribution in x-direction, is obvious. For a more detailed study of the dispersion mechanisms, the temporal evolutions of the mean positions and variances in x-, y- and z-direction have been plotted for both experiments in figure 8.19. From the respective evolutions of the mean position in flow direction, shown in figure 8.19a,g, the time of the reversal of flow direction is readily identifiable. Bearing in mind this point of time, the examination of the evolutions of $\bar{x}(t)$, $\bar{y}(t)$, $\bar{z}(t)$, $\sigma_x^2(t)$, $\sigma_y^2(t)$ and $\sigma_z^2(t)$ leads to the following observations:

- The evolutions of the mean positions $\bar{x}(t)$, $\bar{y}(t)$ and $\bar{z}(t)$ are nearly fully reversible. This is a strong indication for the hypothesis that the occurred displacements in y- and z-direction are caused by heterogeneities inherent in the porous medium. The evolutions of $\bar{y}(t)$ are superimposed by an additional increasing trend, which indicates the presence of additional forces in the vertical direction.
- The variances in flow direction $\sigma_x^2(t)$ show a linear increase both before and after the flow reversal. Consequently the longitudinal dispersion is mostly dominated by irreversible mechanisms. However, the dispersion coefficients for the receding flow are somewhat lower than those for the advancing flow (see table 8.3), which is a further indication for a reversible effect from larger heterogeneities.
- The transverse dispersion in horizontal direction $\sigma_z^2(t)$ is nearly completely reversible, with the corresponding dispersion coefficients for the receding flow becoming negative. Again this indicates the presence of heterogeneities.
- The evolutions of the vertical transverse variance $\sigma_y^2(t)$ are characterized by some low fluctuations and an additional significant increase during the receding flow. While the fluctuations can be explained by heterogeneities, the significant increase can only be explained by additional forces acting in the vertical direction, as for instance a density gradient in the fluid.

As a conclusion, the echo dispersion experiments provided a beneficial opportunity to study and separate the effects of reversible and irreversible processes on macroscopic dispersion. Additionally, the presence of an additional process, which cannot be related to the structure of the porous medium, could be identified. This finding confirms the hypothesis that the asymmetry between vertical and horizontal dispersion found in sections 8.3.2 and 8.3.3 is caused by an external force as discussed at the end of section 8.3.2.

8.3.5 Holdup dispersion

The scaling of the coefficient of longitudinal dispersion $D_L(\text{Pe})$ with the Peclet number in the range $50 < \text{Pe} < 7000$ according to a power-law $D_L \propto \text{Pe}^n$ with $n \approx 1.2$, which was found from the experiments of this work in agreement with previous results as described in section 8.3.2, still lacks a physical explanation. Koch & Brady (1985) have provided a quantitative theory describing the effects of boundary-layer dispersion and holdup dispersion, which can explain the observed power-law behavior over a certain Pe range. However, they deplore that "this holdup dispersion is not detectable from the presently available experimental data". Over the last decade the upcoming techniques of NMR and MRI have revealed some detailed

insights into the flow processes in unconsolidated bead packings: Sederman *et al.* (1997) have found significant variations of the local flow rate within the pore space of packed beds, and Kandhai *et al.* (2002) have used permeable spheres to study the influence of stagnant zones on the dispersion in a packed bed, finding "that holdup dispersion in porous media may be more important than assumed in many cases". The numerical studies of Reynolds *et al.* (2000) using a Lattice-Boltzmann formulation yielded a power-law distribution for the normalized local kinetic energy of the steady flow field for low Reynolds numbers $Re < 14$. They conclude that "this indicates that the stagnant zones play a significant role in transport through the packed bed".

With its high spatial and temporal resolution, the present technique is the first to provide the opportunity for a direct quantitative observation of holdup dispersion processes. This is accomplished by the analysis of the spatio-temporal concentration distributions as exemplified for the experiment A6 in figure 8.20. In figure 8.20a the y - t concentration distribution is shown at the position $x = 27.9$ mm / $z = 32$ mm for 15.9 mm $< y < 28.7$ mm and 600 s $< t < 8100$ s. From this illustration the existence of so-called *dead end pores* or *stagnant zones* can be directly recognized. The fact that the tracer dye can enter and leave these pores only by diffusion but not through convection leads to a significantly slower decay of the dye concentration after the major tracer plume has passed, than in pores with convective transport. This behavior can be identified at the four locations indicated by arrows. The process of holdup dispersion in a stagnant zone can be analyzed in more detail from the comparison of the temporal evolutions at two adjacent locations as shown in figure 8.20b. Whereas for $t < 3000$ s both pores show a similar behavior as it would be expected from convective-diffusive transport, the concentration at $y = 23.6$ mm exhibits a significantly slower decay. Consequently the pore structure at this location consists of both a zone with convective-diffusive transport and a zone with solely diffusive transport.

Figure 8.20c shows 1D concentration distribution in x -direction $\bar{c}(x)$ (see equation 6.4) for the same experiment at $t = 3000$ s together with the least squares fit of a gaussian distribution. As indicated the measured distribution is characterized by a slight tail, i.e. a decay of $\bar{c}(x)$ for $x \rightarrow 0$ which is slower than that of a gaussian. Such tails are obtained from practically all breakthrough experiments measuring $\bar{c}(x_{\text{outlet}}, t)$ at the outlet of a flow cell. However, such experiments cannot make any statement about the physical process which is the origin of the tail. Possible origins are heterogeneities of any scale, boundary effects caused by the container walls (see Maier *et al.* (2002)), adsorption on the surface of the solid and holdup in stagnant zones. With the present experimental technique, which can simultaneously measure the microscopic transport processes as shown in figure 8.20a,b as well as the macroscopic transport from the averaged distributions $\bar{c}(x, t)$ shown in figure 8.20c, the physical origin of the macroscopic tail in figure 8.20c can be directly attributed to microscopic holdup dispersion processes.

In section 8.3.2 it was found that the longitudinal dispersion coefficient $D_L(\text{Pe})$ scales with the Peclet number Pe according to a power-law given by equation 8.13 with an exponent $n \approx 1.2$. The physical origin of this power-law behavior is still under discussion (Manz *et al.* (1999)). The above findings seem to indicate that a major contribution to the power-law behavior comes from holdup dispersion. However, a model which considers only a combination of mechanical dispersion and holdup dispersion,

$$\frac{D_L}{D_m} = \tau + \alpha \text{Pe} + \gamma \text{Pe}^2, \quad (8.19)$$

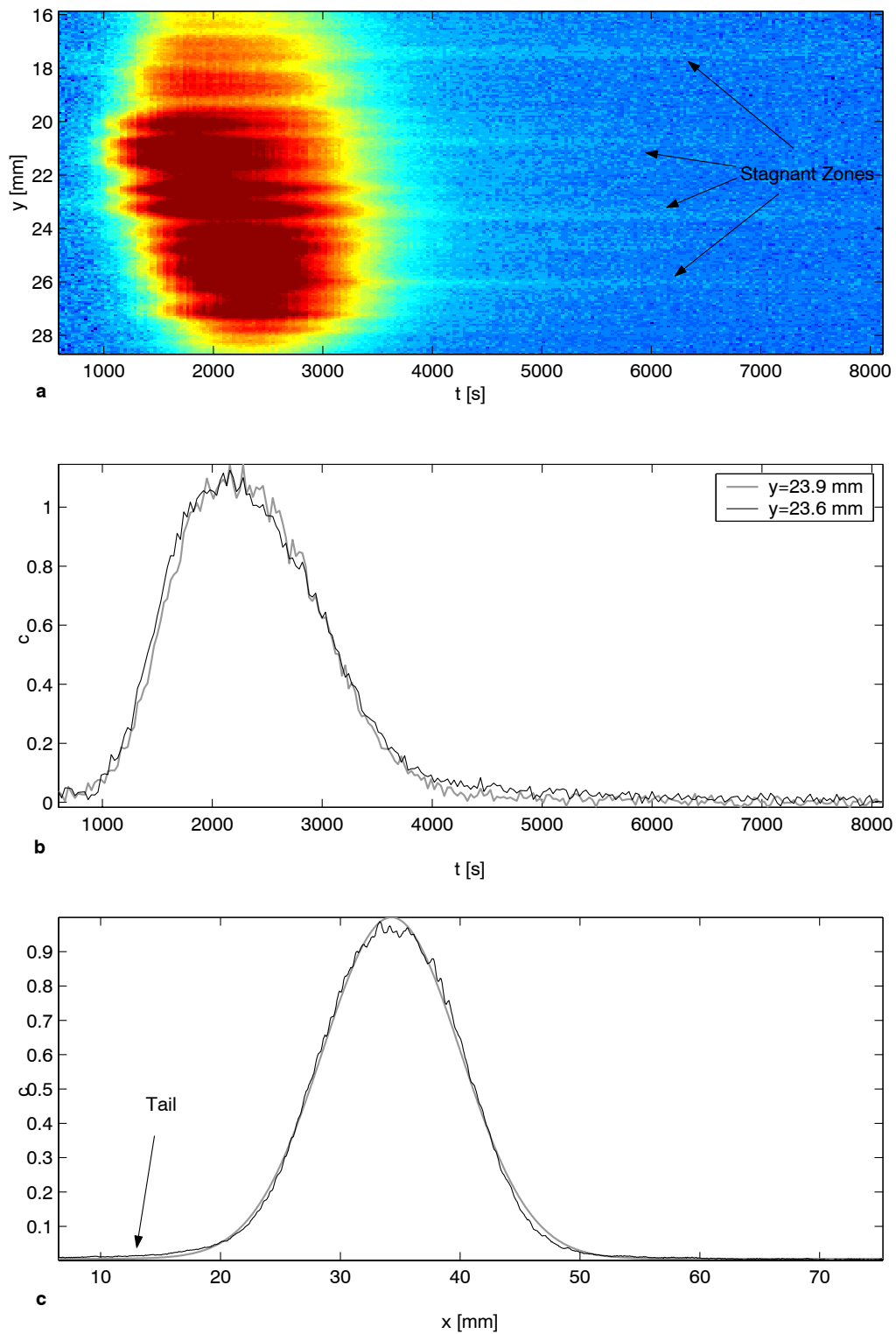


Figure 8.20: **a** Temporal evolution of dye concentrations at $x = 27.9$ mm / $z = 32$ mm for 15.9 mm $< y < 28.7$ mm and 600 s $< t < 8100$ s in experiment A6. The stagnant can be recognized by their long tails. **b** Comparison of the temporal evolutions at $y = 23.6$ mm and $y = 23.9$ mm. **c** Macroscopic averaged distribution $\bar{c}(x)$ at $t = 3000$ s.

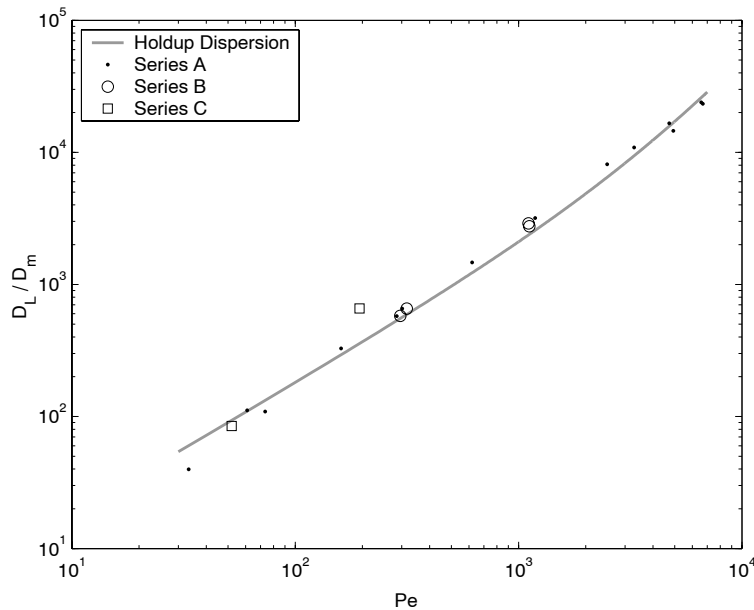


Figure 8.21: Least squares fit of the holdup dispersion model 8.19 to the measured longitudinal dispersion coefficients given in table 8.3. A comparison with figure 8.11a indicates that this model doesn't suffice to describe the observed data.

cannot describe the measured behavior as sufficiently as the models 8.12 and 8.13, as it can be seen from a comparison of figure 8.11a and figure 8.21. A possible explanation of this inconsistency is that the stagnant zones found from the data shown in figure 8.20a,b are not strictly separated from the zones with convective transport. If there is some kind of transition between these two zones, the behavior could be described by a contribution $\beta Pe \ln Pe$ which is analog to that from boundary-layer dispersion. This would then agree with the finding in section 8.3.2 that a major contribution comes from boundary-layer dispersion. This hypothesis is confirmed by the power-law distribution of the local kinetic energy for the steady flow field in a close-packed fixed bed of spheres found by Reynolds *et al.* (2000) from numerical studies. Further research is necessary to reveal these mechanisms.

8.3.6 Adsorption

In the experiment of series D a combination of fused silica grains and silicone oil together with Nile Red as a fluorescent dye was used as specified in table 8.2. The 2D dye concentration distributions obtained in this experiment are shown for three different times in figure 8.22. The strong tails that are visible in these images can also be found in the corresponding macroscopic concentration distributions $\bar{c}(x, t)$ shown in figure 8.23a. Apparently these distributions cannot be described by a classical convection-dispersion equation since there must be an additional physical process that leads to these significant tails. As already discussed in section 8.3.5 this microscopic physical process cannot be identified from the macroscopic concentrations $\bar{c}(x, t)$. However, the analysis of the microscopic spatio-temporal distribution shown in figure 8.23b provides the opportunity for a characterization of the underlying physical process. In contrast to the distribution shown in figure 8.20a, where longer tails could

only be observed at few isolated locations, which were then identified as stagnant zones, the y - t -distribution in figure 8.23a exhibits these long tails over the whole y -range. This finding, which can also be seen from the x - y -distributions in figure 8.22, indicates that the process that causes the immobility of a fraction of the dye molecules is uniformly active everywhere in the medium. Therefore the tails in the macroscopic distributions $\bar{c}(x, t)$ can be attributed neither to holdup dispersion nor to heterogeneities or boundary wall effects, and the only remaining reasonable explanation is the adsorption of the dye on the solid surface.

In principle the measured macroscopic 1D distributions $\bar{c}(x, t)$ can be described by a mobile-immobile model according to equations 6.2-6.3, where the immobile fraction of the liquid phase is represented by the dye molecules adsorbed on the solid surface. Numerical solutions of this set of coupled partial differential equations are available for the case that the initial distribution $\bar{c}(x, t = 0 \text{ s})$ is given by a δ -distribution $\delta(x)$. The parameters of the model can then be obtained from a least-squares minimization of the differences between model and data as described in section 6.4.

For an accurate representation of the data however the exact knowledge of the initial concentration distribution is necessary. This is demonstrated in figure 8.23c for $t = 1470 \text{ s}$, where the fit of the mobile-immobile model was made using two different initial distributions. Whereas the fit with the assumed δ -distribution is not able to describe $\bar{c}(x)$ for $x < 25 \text{ mm}$, an alternative fit with an adapted initial distribution provides a satisfactory description. Since the actual initial distribution of the experiment wasn't available because the measurement was started shortly after the injection of the tracer pulse, a slightly shifted and squeezed version of $\bar{c}(x, t = 0 \text{ s})$ shown in figure 8.23a was used as an initial distribution for this fit. The consistence with the data is obvious and indicates the applicability of the employed model.

8.4 Summary and conclusions

In this chapter the PLIF method described in chapter 3 was used to study the dispersion of fluorescent dyes in refractive index matched porous media. With this method the temporal evolution of the 3D dye concentration distribution inside the flow cell could be measured with a high spatial and temporal resolution. Through the analysis of this highly resolved data the following major achievements have been made:

- The longitudinal and transversal dispersion coefficients have been precisely measured over a large range of Peclet numbers. These are the first simultaneous measurements of longitudinal and transverse dispersion of a 3D dye pulse in an unconsolidated bead packing. Furthermore, the method provides the measurement of the temporal evolution of the dye concentration distribution with an unprecedented spatial and temporal resolution.
- The observed dependence of the coefficients of longitudinal dispersion on the Peclet number obeys a power-law with an estimated exponent $n = 1.18 \pm 0.02$, which is in agreement with previous studies.
- The measurements provide the first simultaneous separate determination of the transverse dispersion coefficients in vertical and horizontal direction. A significantly deviant behavior between these two directions was found. The analysis of the corresponding temporal evolutions of the means and variances, and the characterization of the separately obtained porous structure, provided an indication that this phenomenon is not

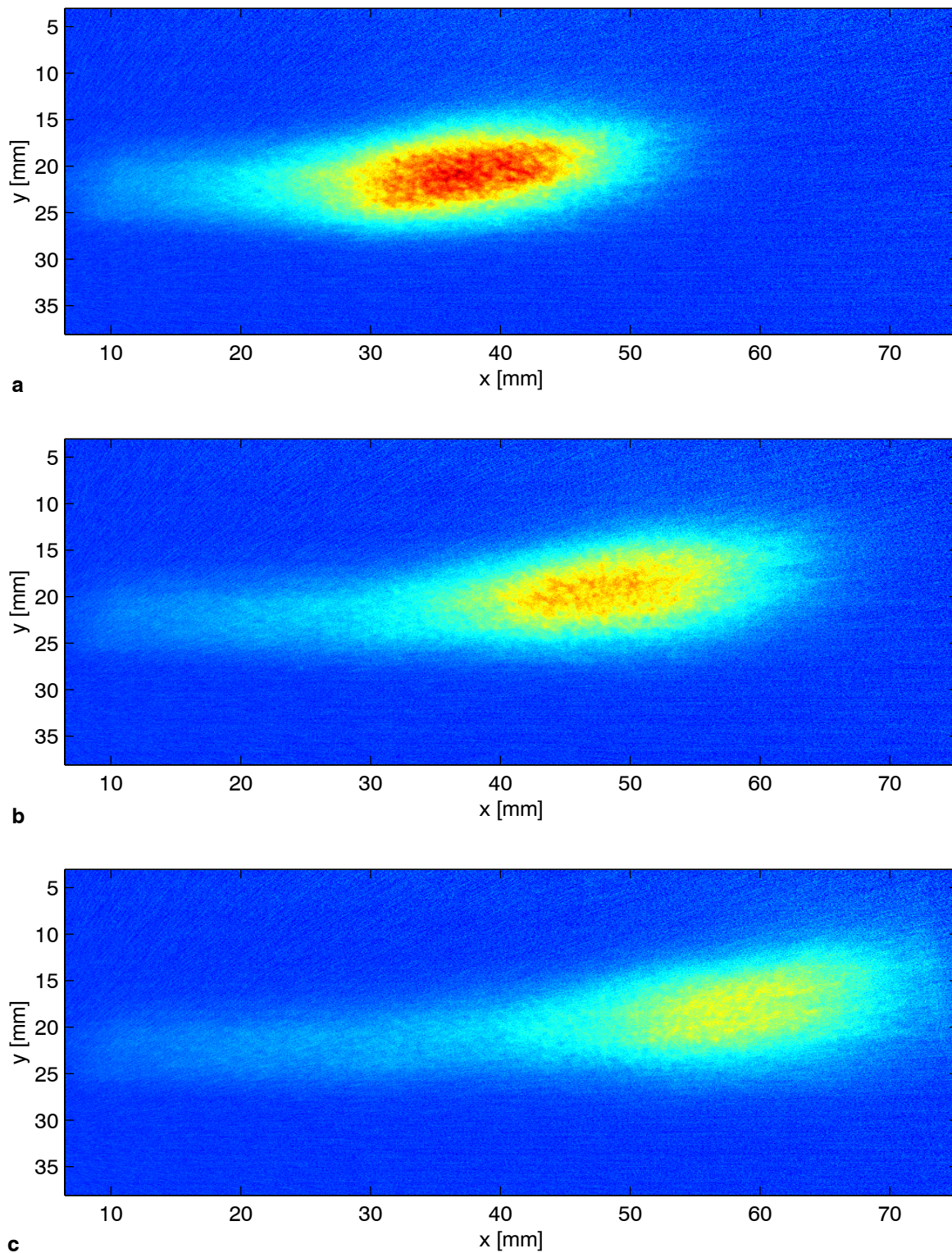


Figure 8.22: 2D dye concentration distributions $\bar{c}(x, y) = \sum_z c(x, y, z)$ for experiment D at **a** $t = 1470$ s, **b** $t = 2220$ s and **c** $t = 2970$ s. The tails indicate the adsorption of the dye on the solid surface.

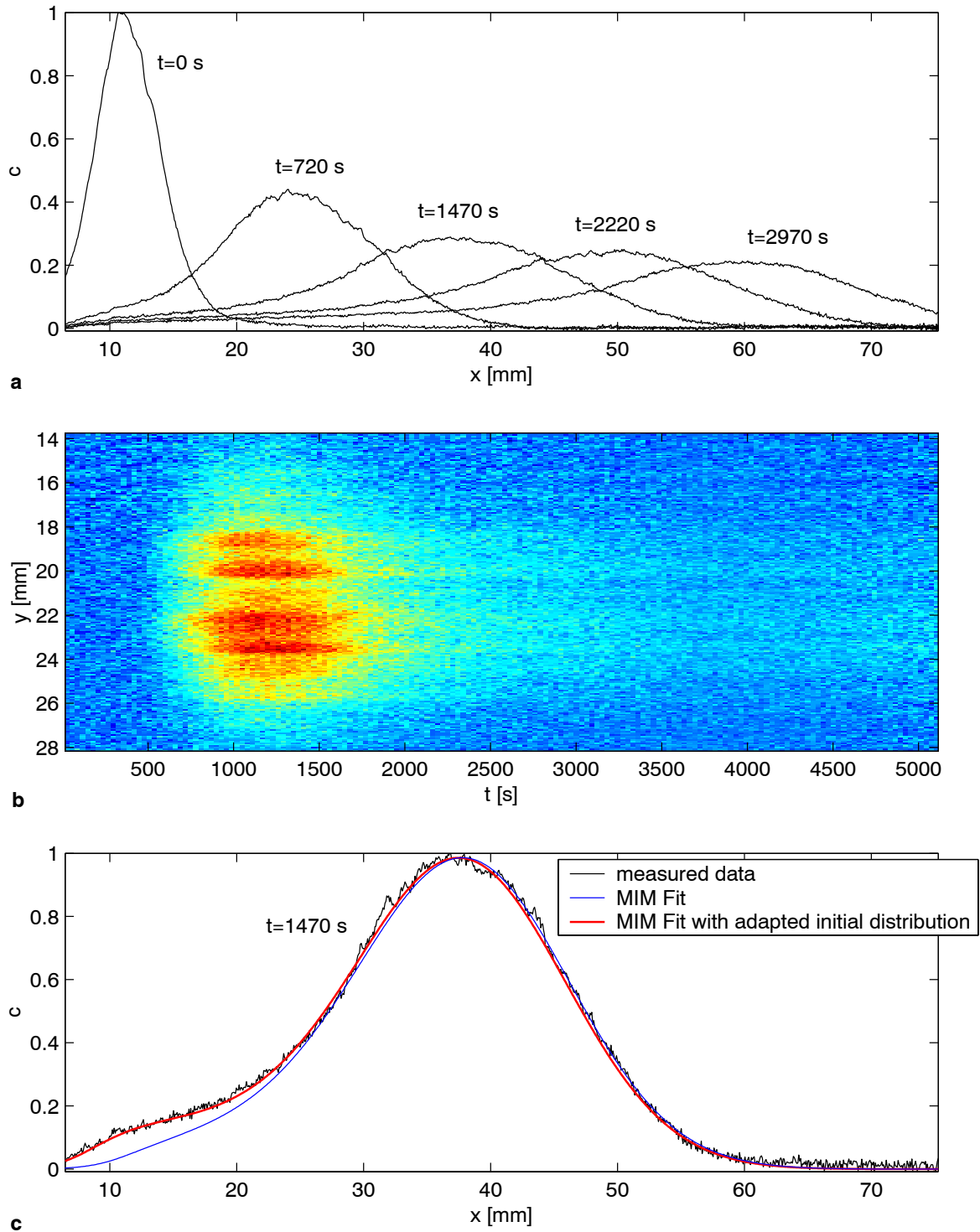


Figure 8.23: **a** Macroscopic averaged dye concentration distributions $\bar{c}(x)$ for the experiment of series D at five different times. **b** Temporal evolution of dye concentrations at $x = 33.1$ mm / $z = 28$ mm for 13.8 mm $< y < 28.1$ mm and 0 s $< t < 5070$ s. **c** Fit of a mobile-immobile model to the measured data at $t = 1470$ s using different initial distributions.

caused by anisotropies in the pore structure but induced by gravity through a density gradient in the liquid. This hypothesis is further confirmed by the analysis of the reversible and irreversible portion of the dispersion in echo dispersion experiments.

- The analysis of the microscopic spatio-temporal concentration distributions provided the first direct evidence for the presence of stagnant zones in unconsolidated bead packings. These stagnant zones lead to observable tails in the corresponding macroscopic concentration distributions and are a likely candidate for the explanation of the power-law behavior of the longitudinal dispersion coefficients.
- The transport of *Nile Red* as a tracer dye in a porous medium made up of fused silica grains and silicone oil as a solvent, resulted in macroscopic distributions with large tails. Through the analysis of the corresponding microscopic concentrations these tails could be related to the effect of the adsorption of the tracer dye on the solid surface of the porous medium.

Chapter 9

Flow of two immiscible liquids in a porous medium

9.1 Introduction

In this chapter the PLIF technique described in chapter 3 is used to simultaneously visualize the flow of two immiscible liquids in a refractive index matched porous medium. The realization and the obtained results of such an experiment are presented in section 9.2. As described already in section 3.6, the absorption and emission spectra of the two fluorescent dyes used to visualize the respective liquid phases show a certain overlap, which leads to a correlation in the measured intensities representing the two liquids. Therefore in section 9.3 a method is presented for the compensation of this undesirable effect, followed by a presentation of the data corrected in this way. Finally a summary and conclusions are given in section 9.4.

9.2 Immiscible displacement of oil by water

In the following the usage of the PLIF method presented in chapter 3 for the visualization of a displacement process of two immiscible liquids will be demonstrated. The two liquids employed here are the DC 550 / DC 556 silicone oil mixture and the ZnCl_2 aqueous solution, which are specified in section 3.5. Since in this experiment the desired information was not the concentration of the dyes but the respective liquid phase saturations, both liquids were uniformly dyed with Nile Red and Alexa Fluor 488 (see section 3.6), respectively. The porous medium was made up of the fused silica grains specified in section 3.4, which were embedded in the vertical flow cell shown in figures 3.3b and 3.4. The volume scans of the respective fluorescent light intensities were accomplished alternately, with the filter wheel switching between the two optical bandpass filters (550 ± 20 nm and 600 ± 20 nm) after each volume scan. The time for a volume scan of both fluorescence intensity distributions was 60 s.

At the beginning of the experiment the porous medium was completely saturated with the dyed silicone oil mixture. Then the zinc chloride aqueous solution, which has a significantly higher density than the silicone oil (see table 3.3), was injected from the bottom of the flow cell with a mean velocity in the liquid phase of 0.0023 mm/s. The displacement of the silicone oil by the aqueous solution was then recorded with a temporal resolution of one volume scan per minute during the following 90 minutes. The spatial resolution of the measurement was approximately $80 \mu\text{m} \times 80 \mu\text{m}$ parallel to the laser plane and 0.4 mm, as defined by the

increments of the translation stage, in the out-of-plane direction. The effective resolution in the out-of-plane direction is however rather given by the width of the laser sheet of ca. 0.5-1 mm.

The measured light intensities of Nile Red and Alexa Fluor 488, respectively, are shown in figure 9.1 for three different times. Each plot represents a volume subset of $20 \times 20 \times 20 \text{ mm}^3$. Due to the uniform dye concentrations in each liquid, the image data represents the volumetric contents of the silicone oil (figure 9.1a, c and e) and the aqueous phase (figure 9.1b, d and f). In figure 9.1b, d and f the separation between the lower region, where the aqueous phase has nearly completely displaced the oil and the upper region, which is still completely filled with, is visible. Figure 9.1a, c and e firstly show the residual oil saturation, which consists of little disconnected 'blobs' that have been trapped during the inflow of the aqueous solution in the lower regions. Secondly the parts of the oil-filled regions which adjoin water-filled areas are visible, whereas the oil at the top of the volume is only weakly fluorescing. This is an effect of the overlapping absorption and emission spectra of the two dyes, as mentioned above. A method for the correction of this effect is presented in the next section.

9.3 Compensation of spectral overlap

In this section a method for the compensation of the undesirable effects stemming from the spectral overlap of the emission spectrum of Alexa Fluor 488 and the absorption spectrum of Nile Red is presented. As discussed in the previous section, this effect leads to the phenomenon that the distribution of the silicone oil is clearly visible in the regions which are in the vicinity of water-filled areas, where the Nile Red is excited by the Alexa Fluor 488, whereas the silicone oil is nearly invisible in regions far from the aqueous solution.

The assumption that the Nile Red is excited both by the laser and by fluorescing Alexa Fluor 488 in the vicinity of the silicone oil can be described by the following set of equations: the measured light intensities $I_{\text{NileRed}}(x, y, z)$ and $I_{\text{AlexaFluor}}(x, y, z)$, quantifying the fluorescence emission of Nile Red and Alexa Fluor 488 in the 3D volume element at the position $(x, y, z)^T$ are related to the laser light intensity $s_{\text{Laser}}(x, y, z)$ through

$$I_{\text{AlexaFluor}}(x, y, z) = k_{\text{AlexaFluor}} \cdot s_{\text{Laser}}(x, y, z) \cdot c_{\text{AlexaFluor}}(x, y, z) \quad \text{and} \quad (9.1)$$

$$\begin{aligned} I_{\text{NileRed}}(x, y, z) &= k_{\text{NileRed}} \cdot s_{\text{Laser}}(x, y, z) \cdot c_{\text{NileRed}}(x, y, z) \\ &+ (h * I_{\text{AlexaFluor}}(x, y, z)) \cdot c_{\text{NileRed}}(x, y, z). \end{aligned} \quad (9.2)$$

$c_{\text{AlexaFluor}}(x, y, z)$ and $c_{\text{NileRed}}(x, y, z)$ denote the respective dye concentrations related to the volume element at the position $(x, y, z)^T$, and the constants $k_{\text{AlexaFluor}}$ and k_{NileRed} represent the effects of measurement geometry and quantum efficiency. While equation 9.1 and the first term of equation 9.2 describe the excitation of the dyes by the laser light, the second term of equation 9.2 describes the excitation of Nile Red by the fluorescence emission of neighboring Alexa Fluor 488. The shape of the neighborhood is defined by the convolution kernel h . If, as a first approximation, the laser intensity $s_{\text{Laser}}(x, y, z)$ is assumed to be constant throughout the medium, the desired concentration $c_{\text{NileRed}}(x, y, z)$ is given by

$$c_{\text{NileRed}}(x, y, z) = \frac{I_{\text{NileRed}}(x, y, z)}{k_{\text{NileRed}} s_{\text{Laser}} + h * I_{\text{AlexaFluor}}(x, y, z)}. \quad (9.3)$$

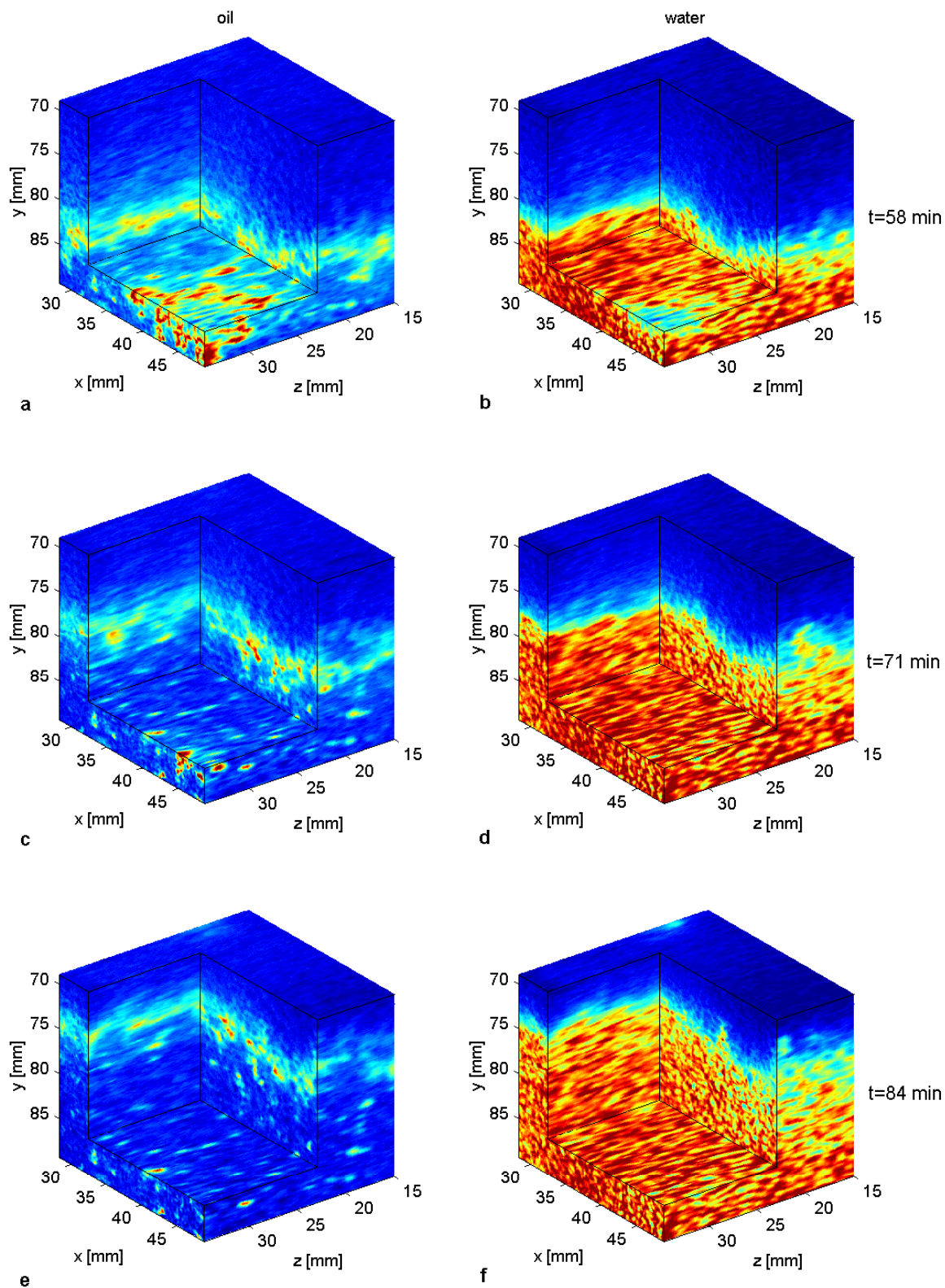


Figure 9.1: Volume subsets of $20 \times 20 \times 20 \text{ mm}^3$ showing the fluorescence emission intensities of Nile Red (a, c, e) and Alexa Fluor 488 (b, d, f) measured at three different times during the displacement of oil by water.

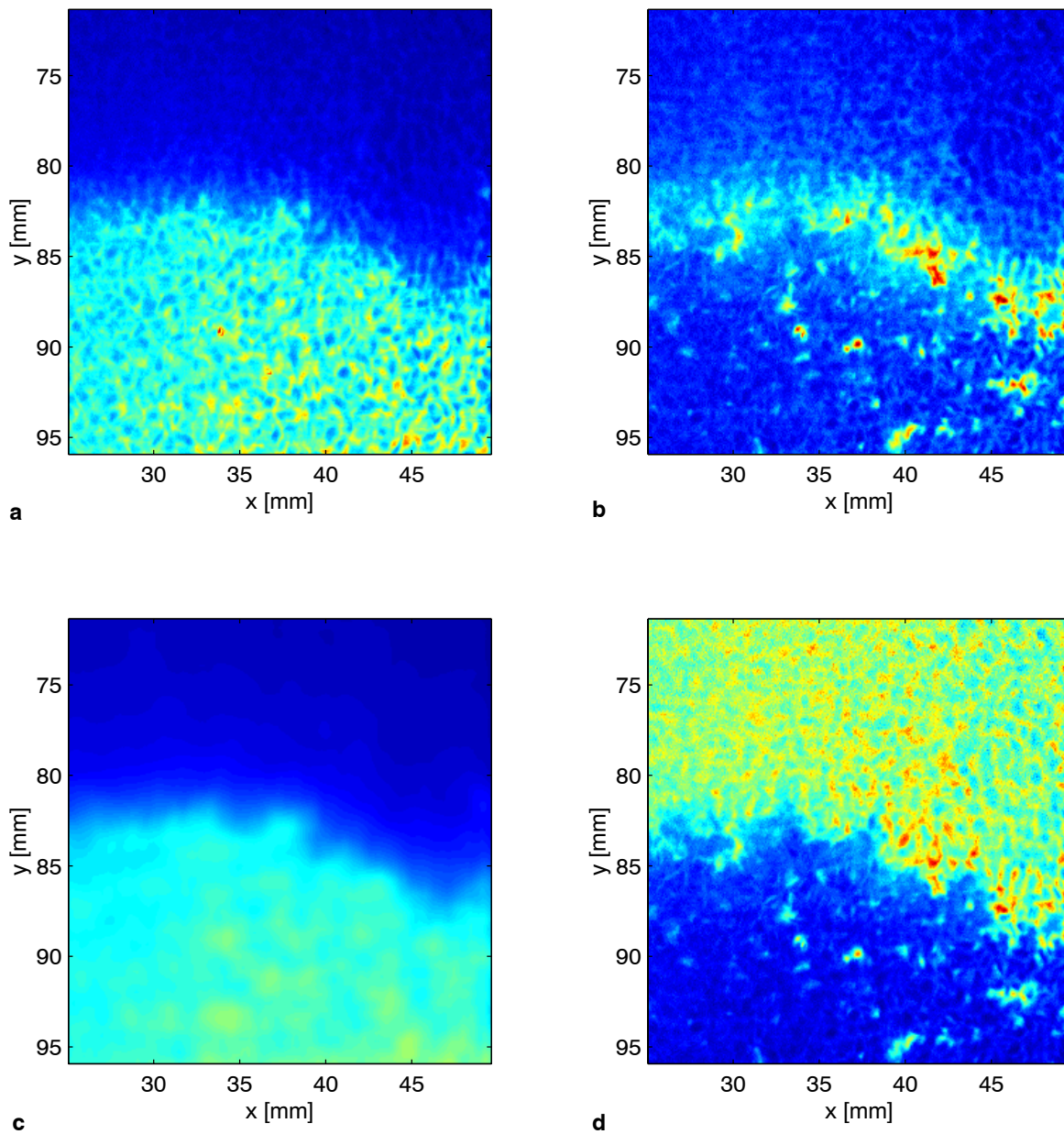


Figure 9.2: Correction of the measured intensities of Nile Red according to equation 9.3. **a** Originally measured fluorescent light intensities of Alexa Fluor 488 and **b** Nile Red in a region of $25 \times 25 \text{ mm}^2$ at $z = 33 \text{ mm}$ and $t = 58 \text{ min}$. **c** Alexa Fluor 488 distribution convoluted with a gaussian filter. **d** Corrected Nile Red distribution showing a homogeneous saturation in the upper region compared to the original distribution in **b**. All results are normalized to $0 < c < 1$.

The application of this equation for the correction of the spectral overlap is illustrated in figure 9.2. The normalized measured light intensities of Alexa Fluor 488 and Nile Red in a region of $25 \times 25 \text{ mm}^2$ are shown in figure 9.2a,b. As discussed above, the spectral overlap leads to the phenomenon that the distribution of silicone oil shown in figure 9.2b is only visible in the vicinity of the aqueous solution entering from the bottom of the flow cell, and not in upper regions ($y < 80 \text{ mm}$). Figure 9.2c shows the convoluted intensity $h * I_{\text{AlexaFluor}}(x, y, z)$ with the convolution kernel h chosen as a gaussian filter with variance $\sigma = 0.8 \text{ mm}$. This corresponds to the intuitive assumption that the excitation of Nile Red by the fluorescence emission of Alexa Fluor 488 decreases with distance, and the range of this interaction is characterized by σ . Finally, the corrected distribution of Nile Red, calculated according to equation 9.3, is shown in figure 9.2d. The additive constant $k_{\text{NileRed}} s_{\text{Laser}}$ in equation 9.3 has been chosen to 0.07. Both the shape of h and the value of $k_{\text{NileRed}} s_{\text{Laser}}$ have been found by trial and error with the objective of a preferably homogeneous Nile Red distribution in the upper regions ($y < 80 \text{ mm}$). Both parameters turned out to be not very critical, in the sense that their variation causes only slight changes in the resulting Nile Red distribution. The improvement over the original data in figure 9.2b is obvious.

Although the so obtained corrected Nile Red distribution appears quite reasonable, it is not presumed that these results allow for any exact evaluation of physical quantities. Even though the approach for the correction according to equation 9.3 is physically motivated, the parameters h and $k_{\text{NileRed}} s_{\text{Laser}}$ lack a physical justification. Furthermore all data presented in this chapter are relative concentrations, and consequently all illustrations show normalized concentration distributions $0 < c(x, y, z, t) < 1$.

However, the corrected results give an insightful visualization and allow for a qualitative study of the 3D microscopic processes during the imbibition of an aqueous phase into an oil saturated porous medium. Figure 9.3 shows the corrected version of the data shown in the 3D visualization of figure 9.1, which can now be regarded as the respective relative saturations of the wetting and nonwetting phase. A more detailed visualization of the imbibition process in a 2D subset of approximately $12 \times 12 \text{ mm}^2$ is shown in figures 9.4 and 9.5. The formation and shape of the residual oil saturation in the form of so-called *blobs* can be readily observed. Interestingly the oil saturation often decreases in regions which are apparently disconnected from the major fraction of the oil, as indicated by the errors at $t = 51 \text{ min}$, $t = 55 \text{ min}$ and $t = 56 \text{ min}$. Possible explanations are connections in the out-of-plane direction or the displacement of the blobs due to buoyant forces. The latter microscopic effect is responsible for typically observed macroscopic phenomena like the hysteresic behaviour of so-called *capillary pressure-saturation relations*.

9.4 Summary and conclusions

In the previous sections the measurement and analysis of the flow of two immiscible liquids during an imbibition process has been described. From the thereby obtained results the following conclusions can be drawn:

- Through the employment of appropriate solids, liquids and fluorescent dyes, the PLIF technique described in chapter 3 is the first high-resolution matching-index method for the simultaneous visualization of the 3D pore-scale flow of two immiscible liquids in a porous medium.

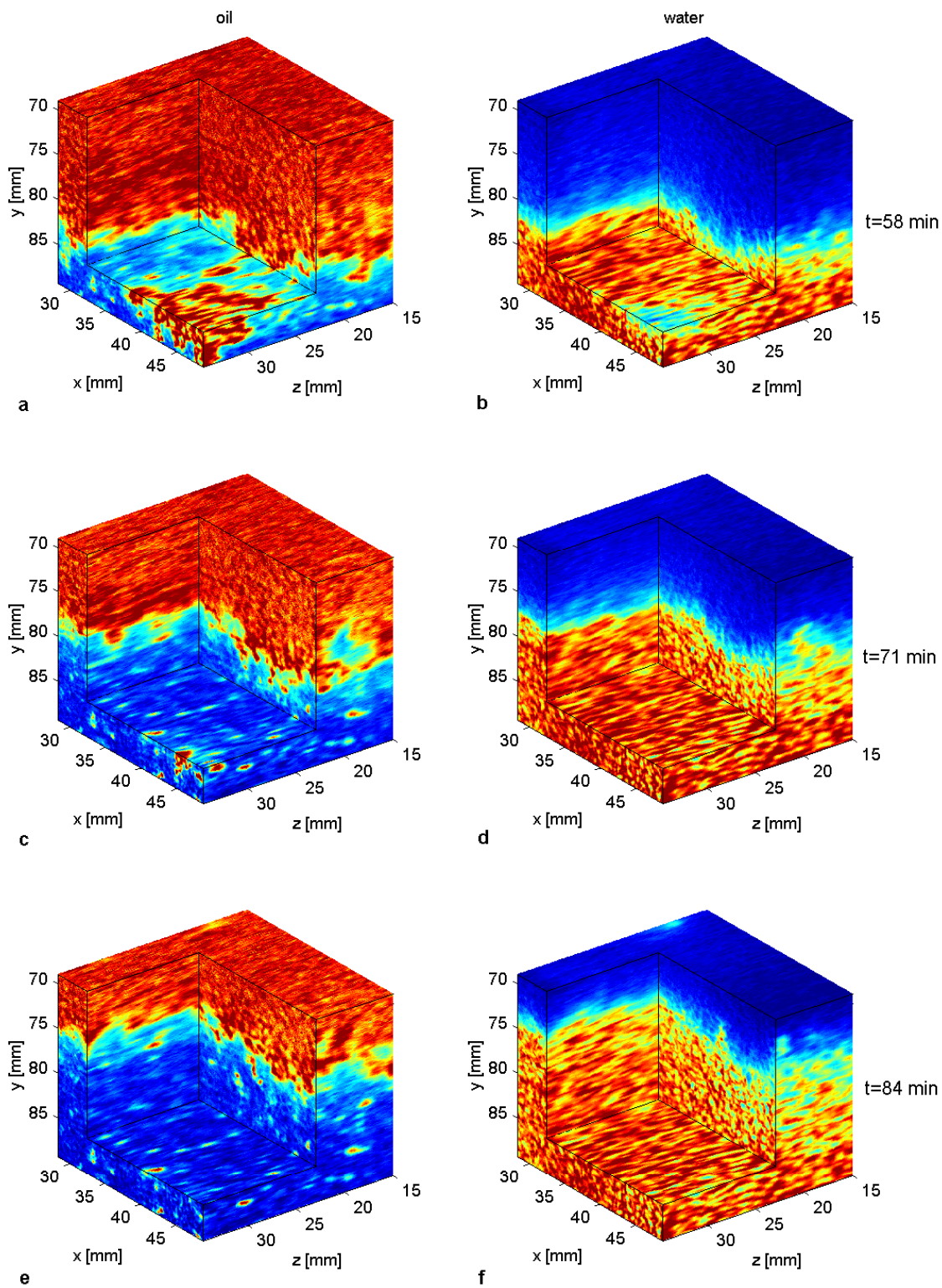


Figure 9.3: Volume subsets of $20 \times 20 \times 20 \text{ mm}^3$ representing the relative saturations of silicone oil (a, c, e) and zinc chloride aqueous solution (b, d, f) at three different times during the imbibition of the aqueous solution. This data has been obtained from the original data shown in figure 9.1 through the correction according to equation 9.3.

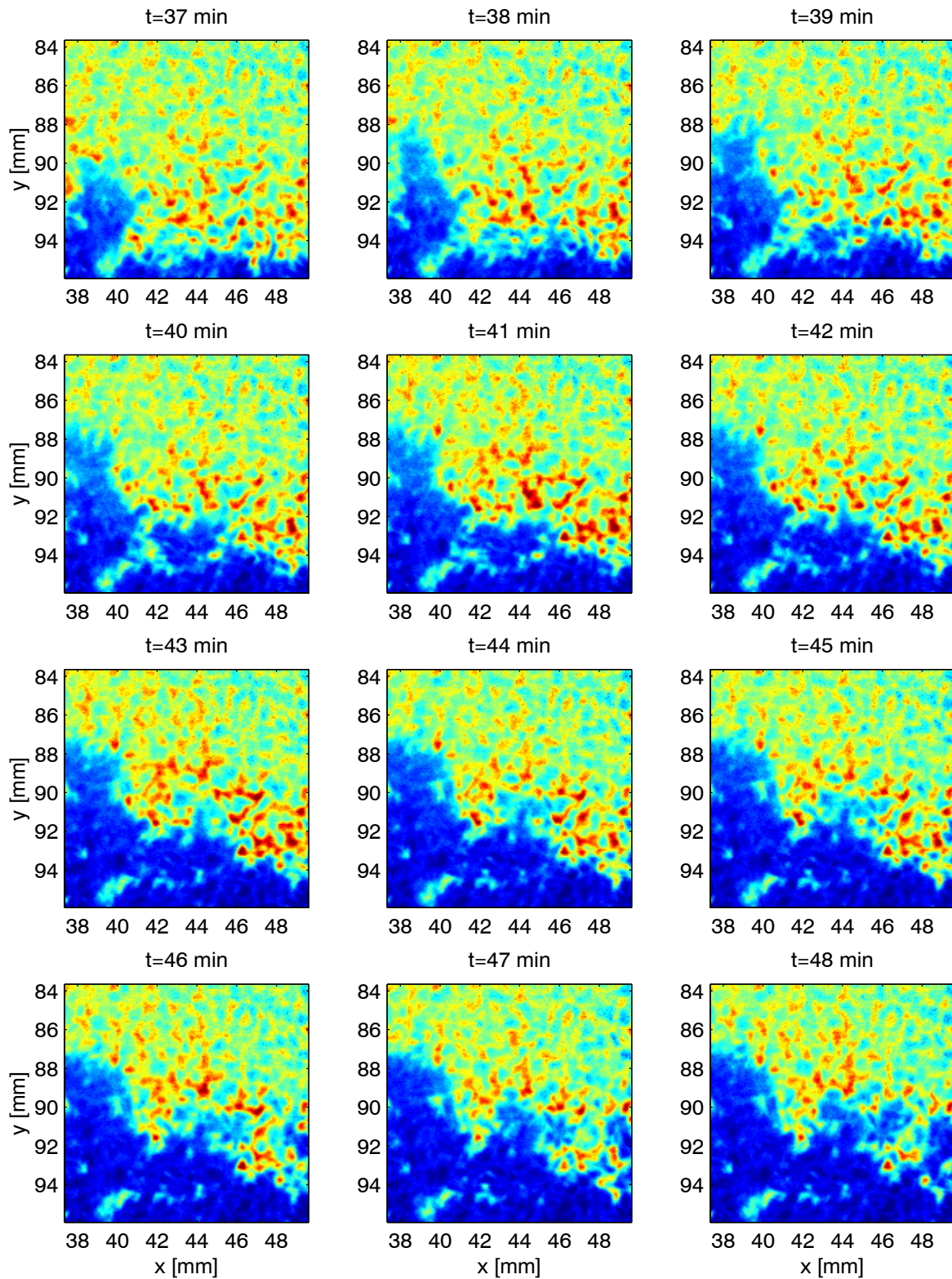


Figure 9.4: Temporal evolution of the silicone oil distribution during the imbibition of the aqueous phase from the bottom in an area of $12 \times 12 \text{ mm}^2$ at $z = 33 \text{ mm}$. The continuation is shown in figure 9.5.

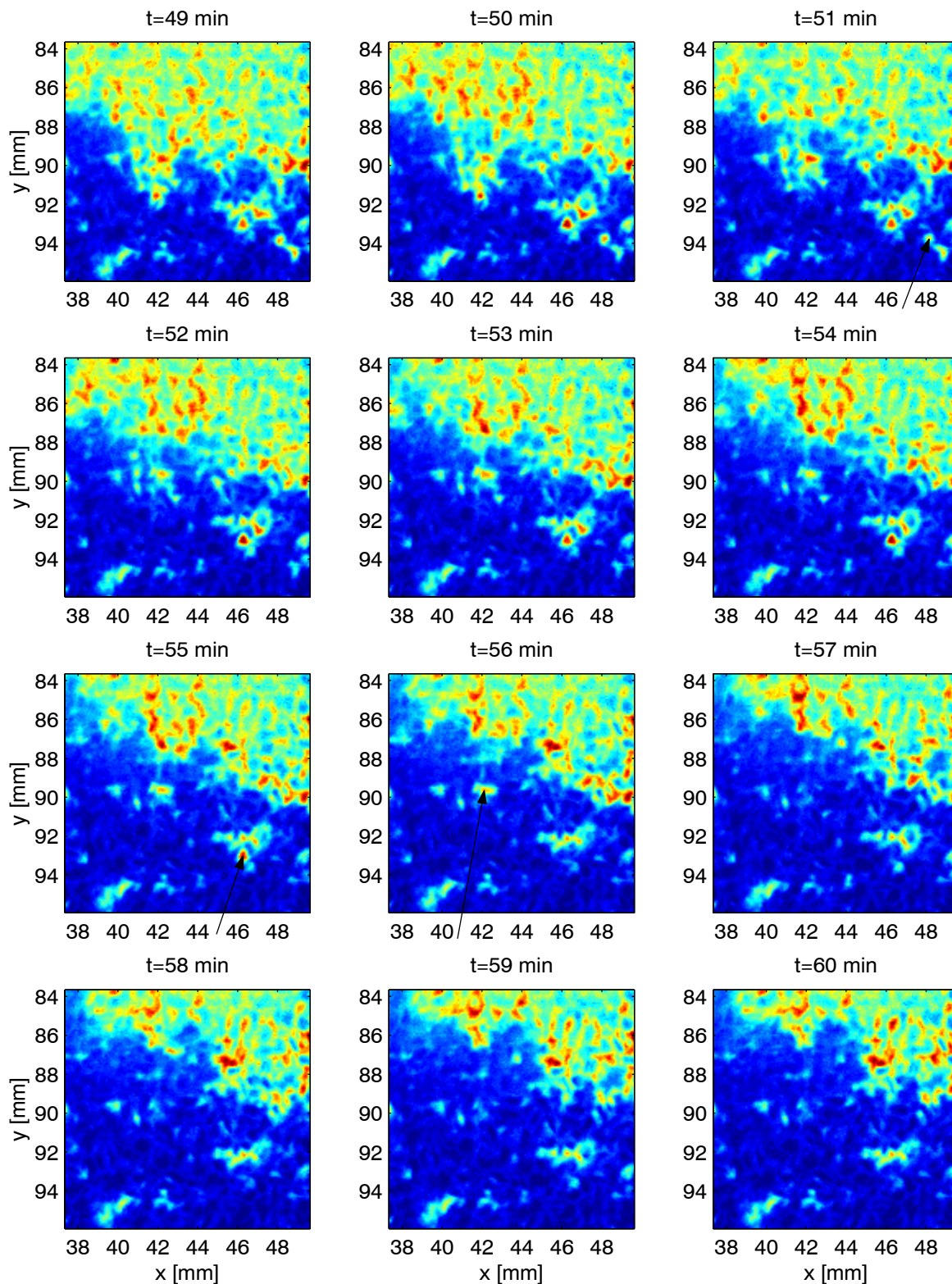


Figure 9.5: Continuation of the time series of silicone oil distributions shown in figure 9.4. The arrows at $t = 51$ min, $t = 55$ min and $t = 56$ min indicate displacements of apparently disconnected blobs.

- The effects caused by the spectral overlap of the absorption and emission spectra of the two fluorescent dyes could be qualitatively corrected through a physically motivated inverse transformation.
- The analysis of the corrected results provides detailed insights into the microscopic 3D flow processes during the displacement of a nonwetting phase by an invading wetting phase liquid. The formation of disconnected areas of residual oil, a microscopic process which has strong impact on macroscopic phenomena like the hysteresis of capillary pressure-saturation relations, can be investigated with a high spatial and temporal resolution.

Chapter 10

Summary and conclusions

In the present work valuable new insights have been gained into the flow and transport in porous media. The highly accurate measurements have been accomplished by the development of both novel experimental techniques as well as new numerical methods for data processing and parameter estimation.

The following major achievements have provided the basis for the capability of the experimental method:

- The acquisition of an appropriate combination of solids, liquids and fluorescent dyes for the composition of transparent and optically homogeneous porous media.
- The employment of capable imaging hardware, light source and optical components.
- The adoption and application of a method for the highly precise matching of refractive indices.

These developments led to the following unique features of the present technique:

- The capability of measuring dye concentrations in an array of $1300 \times 600 \times 100$ volume elements every 30 seconds.
- The availability of two immiscible liquids in order to study two-phase flow.
- The availability of two different solid materials in order to study the influence of solid-liquid interactions.

A further basis for the quality of the obtained results are the following achievements in the field of image processing:

- A detailed analysis of possible systematic and statistical errors has led to a sophisticated combination of algorithms for image preprocessing.
- A method for the local parameter estimation has been applied for the first time to the estimation of temporally and spatially resolved dispersion tensors.
- Based on a detailed analysis of accuracy using synthetic data sets, a new confidence measure has been found for the local parameter estimation method.

- The commonly used approach for the parameter regularization in case of an aperture problem has been extended by an additional physically based constraint, so that the obtained results are unbiased and physically reasonable.

The accomplished measurements and subsequent data analysis have led to the following major results:

- The measurements represent the first simultaneous estimation of the longitudinal as well as both transversal dispersion coefficients over a large range of Peclet numbers.
- For the longitudinal dispersion coefficients, a dependence on the Peclet number according to a power-law with an exponent $n \approx 1.2$ has been found.
- The values of the horizontal transversal dispersion coefficients are significantly higher than those in vertical direction. A detailed analysis of the influence of the porous structure leads to the conclusion that the porous structure cannot be solely responsible for this behavior.
- The analysis of the temporal evolution of microscopic dye concentration patterns provided the first direct evidence for the existence of stagnant zones in the liquid phase, which have an important effect on the dispersion and are a potential explanation for the power-law behavior of longitudinal dispersion.
- The phenomenon of adsorption could be clearly identified and visualized from the microscopic spatio-temporal dye patterns.
- The method has been used for the first simultaneous visualization of 3D pore-scale flow of two immiscible liquids in a porous medium.

Appendix A

Cubic smoothing splines

A.1 Introduction

Suppose a series of data values $y_i, i = 1..n$ is measured at discrete times t_i and we want to describe this timeseries by a regression model $f(t)$ under the assumption of additive noise e_i :

$$y_i = f(t_i) + e_i, \langle e_i \rangle = 0, \langle e_i e_j \rangle = \delta_{ij} \sigma^2. \quad (\text{A.1})$$

The problem then is to find $f(t)$ from the data y_i .

If there are any prior assumptions on the process generating f , one can in some cases find a parametric functional form $f(t; \vec{p})$, whose parameters $\vec{p} = (p_1, p_2, ..p_m)^T$ can then be estimated by a least squares method. If the underlying process is too complex or is not known, e.g. when the intention of the analysis is to learn about the process, $f(t; \vec{p})$ cannot be determined. This is the case in the analysis of the timeseries of concentrations $c(X, Y, Z, t_i)$ at a position (X, Y, Z) (see chapters 5 and 8 and figure A.1), where processes like convection, diffusion, dispersion, adsorption and also the initial distribution play a role. In these situations non-parametric approaches are used, where no prior specification of a parametric functional form of f is required. Here we use an approach known as cubic smoothing splines, which is described in the following sections.

A.2 Roughness penalty approach

One method for non-parametric regression is the so-called roughness penalty approach (for a complete description see Green & Silverman (1994)). The idea is that the roughness of the sought function should be minimal. The roughness of a twice-differentiable curve $g(t)$ can be measured by its integrated squared second derivative $\int (\frac{\partial^2 g}{\partial t^2})^2 dt$. On the other hand also the goodness-of-fit, i.e. the residual sum of squares $\sum_{i=1}^n (y_i - g(t_i))^2$ should be minimal.

The roughness penalty approach to estimate $f(t)$ in equation A.1 from given y_i can then be stated as follows:

Given any twice-differentiable function $g(t)$ defined on $[a, b]$, and a smoothing parameter $\lambda > 0$, define the penalty functional

$$S(g) = \sum_{i=1}^n (y_i - g(t_i))^2 + \lambda \int_a^b (\frac{\partial^2 g}{\partial t^2})^2 dt. \quad (\text{A.2})$$

The function \hat{g} is defined as the minimizer of $S(g)$ over all twice-differentiable functions g . Whereas the first term in $S(g)$ measures the difference between $g(t_i)$ and y_i , the second is proportional to the roughness of g . In other words, the function \hat{g} is the smoothest function that achieves a certain given degree of fidelity (determined by the smoothing parameter λ) to the data y_i .

Now it can be shown (Green & Silverman, 1994) that the function \hat{g} which minimizes $S(g)$ is a cubic spline with knots at the times t_i . A cubic spline is piecewise polynomial of third degree in each of the intervals between adjacent t_i with the polynomial pieces grafted together so that the first two derivatives of the are continuous. For a given λ , fast algorithms for the calculation of \hat{g} are available (for a description see Green & Silverman (1994)).

A.3 Estimation of the smoothing parameter λ

The smoothing parameter λ controls the relative importance of the roughness of g and the difference between $g(t_i)$ and y_i . For $\lambda \rightarrow 0$, \hat{g} tends to an exact interpolation of the data y_i , whereas for $\lambda \rightarrow \infty$, \hat{g} converges to a straight line fit. In other words, the degrees of freedom of \hat{g} are (continuously!) decreasing with growing λ .

In figure A.1 the measured time-series of concentrations $y_i = c(X, Y, Z, t_i)$ at two fixed positions (X_1, Y_1, Z_1) and (X_2, Y_2, Z_2) are shown together with the estimates of \hat{g} for different values of λ . The noise in the two time-series has the same level whereas the signal strength and thus the signal-to-noise ratio is higher by a factor of about 6 for the left time-series. It is obvious that for both time-series the estimate \hat{g} changes from a nearly exact interpolation for $\lambda = 1$ to an approximately second-order ($\lambda = 10^7$) and first order ($\lambda = 10^9$) polynomial, as discussed above. Furthermore it is visible that the apparently optimal value for λ is different for the two time-series. Whereas for the left time series the fit for $\lambda = 100$ seems optimal, for the right time series the fit for $\lambda = 5000$ is best. This is due to their different signal strength and thereby different integral of the squared second derivative.

There are several procedures available to choose the smoothing parameter λ from the data, mainly based on cross-validation methods (for descriptions see Craven & Wahba (1979), Wecker & Ansley (1983) and Green & Silverman (1994)). Here we use a direct approach which is based on the assumption that the time-series $c(X, Y, Z, t_i)$ for different (X, Y, Z) differ mainly in amplitude and little in shape. Then the integral of the squared second derivative is approximately proportional to the squared maximum of g :

$$\int_a^b \left(\frac{\partial^2 g}{\partial t^2}\right)^2 dt \approx c_1(\max(g))^2 \quad (\text{A.3})$$

and the residual sum of squares is constant:

$$\sum_{i=1}^n (y_i - g(t_i))^2 = c_2. \quad (\text{A.4})$$

The value of λ is then determined by

$$\frac{\lambda}{1} = \frac{c_2}{c_1(\max(g))^2} \quad (\text{A.5})$$

$$\lambda = \frac{c_2}{c_1(\max(g))^2} = \frac{\lambda_*}{(\max(g))^2}, \quad (\text{A.6})$$

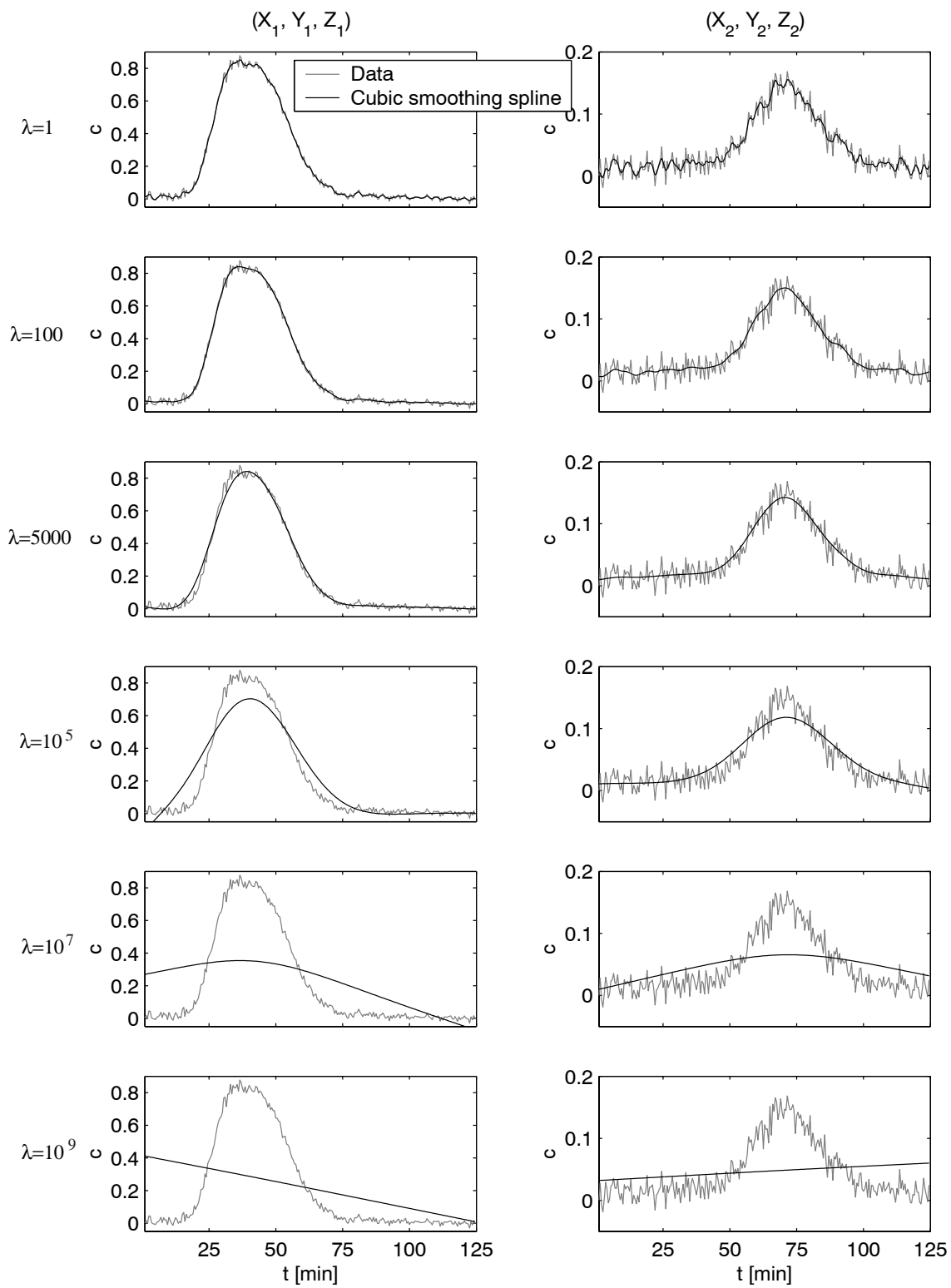


Figure A.1: Cubic smoothing splines for two time-series of concentrations calculated with different smoothing parameters λ .

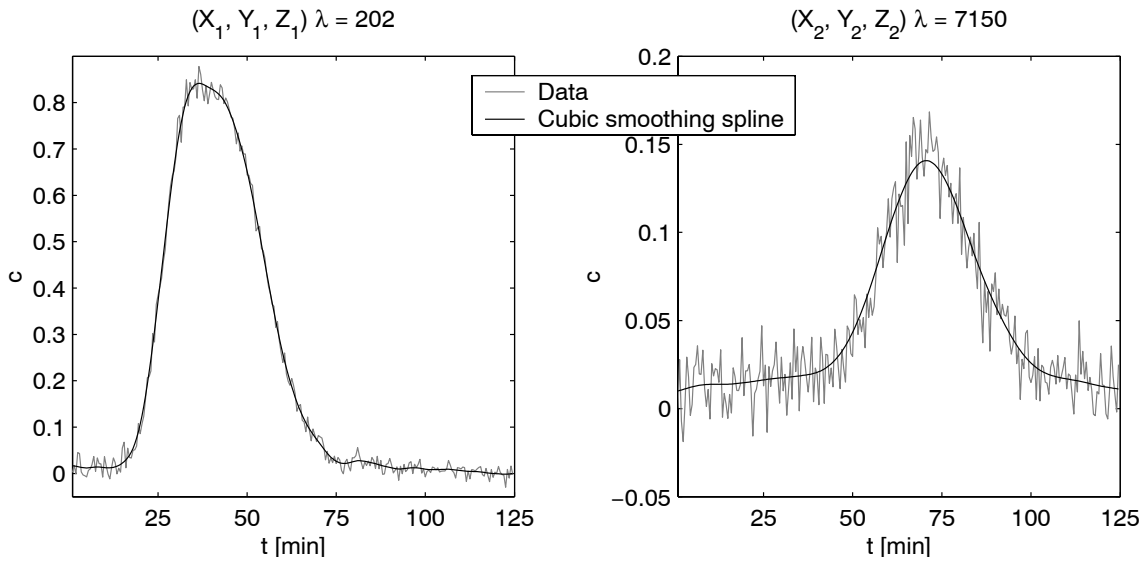


Figure A.2: Cubic smoothing splines for two time-series of concentrations calculated with adaptive smoothing parameters for $\lambda_* = 150$.

where λ_* is constant for all (X, Y, Z) and is chosen manually. The results for the two time-series from figure A.1 calculated with $\lambda_* = 150$ are shown in figure A.2.

Appendix B

Concentration Profiles

The following diagrams provide a detailed graphical representation of the temporal evolution of the tracer dye concentration profiles for the experiments of series A-D. The specifications of the individual experiments are given in table 8.2 and 8.3. For each experiment, the respective normalized 1D concentration distributions in x-, y- and z-direction are plotted for five different times. Additionally for the distributions in x-direction the corresponding least squares approximations of a gaussian distribution are plotted. For the echo dispersion experiments of series B, the temporal evolutions of the 1D concentration distributions are shown separately for the times before and after the reversal of flow direction, denoted as B1a / B2a and B1r / B2r.

Subsequently the temporal evolutions of the mean and the variance of the concentration distributions in x-, y- and z-direction, $\bar{x}(t)$, $\bar{y}(t)$, $\bar{z}(t)$, $\sigma_x^2(t)$, $\sigma_y^2(t)$ and $\sigma_z^2(t)$, are plotted with the maximal temporal resolution, i.e. 30 s per volume scan. The least squares fits of a straight line, which have been used to estimate the velocities \bar{v}_x , \bar{v}_y , \bar{v}_z and dispersion coefficients D_L , D_{Ty} , D_{Tz} as described in section 8.3.2, are indicated by the gray lines.

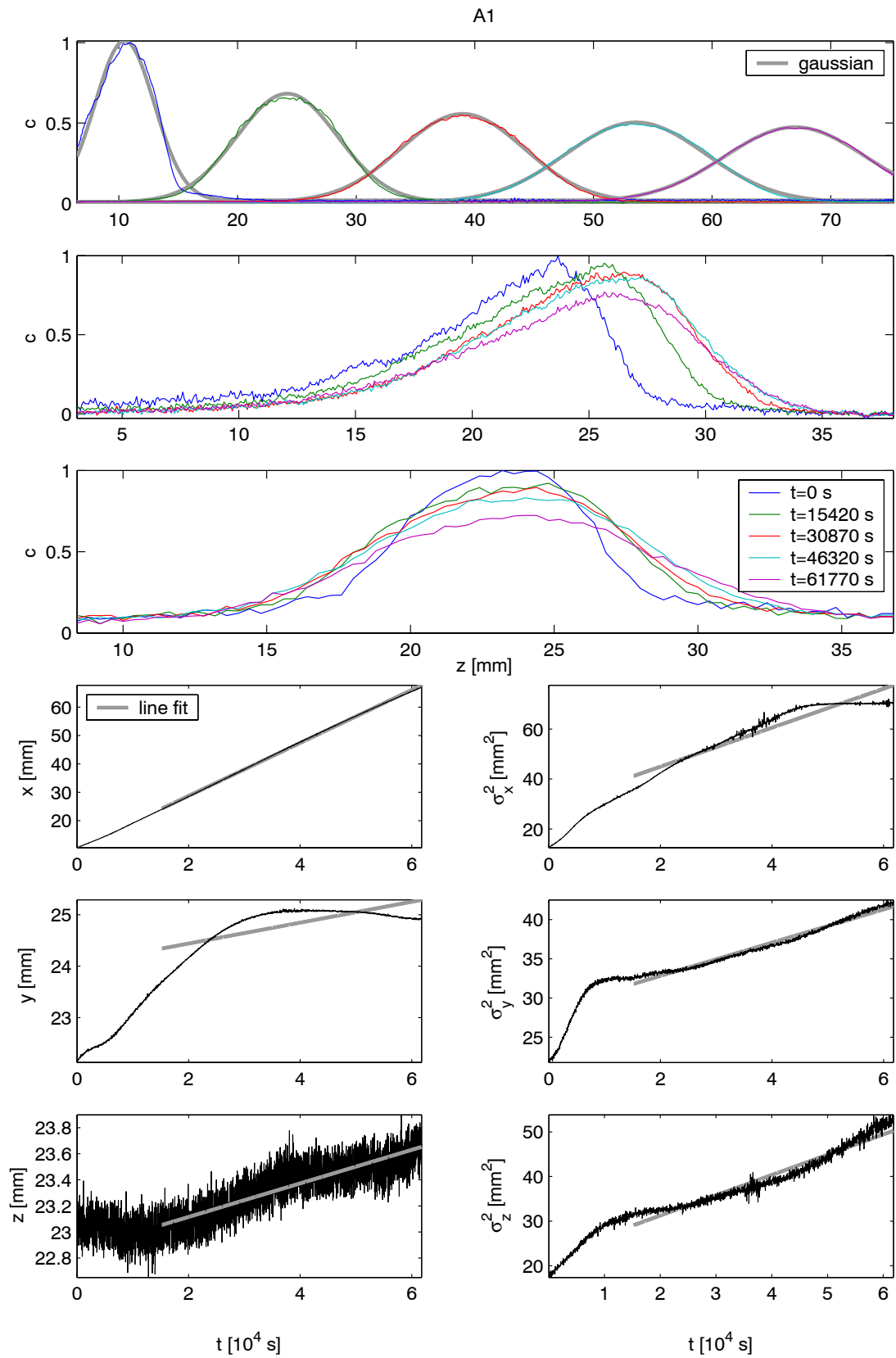


Figure B.1: Experiment A1.

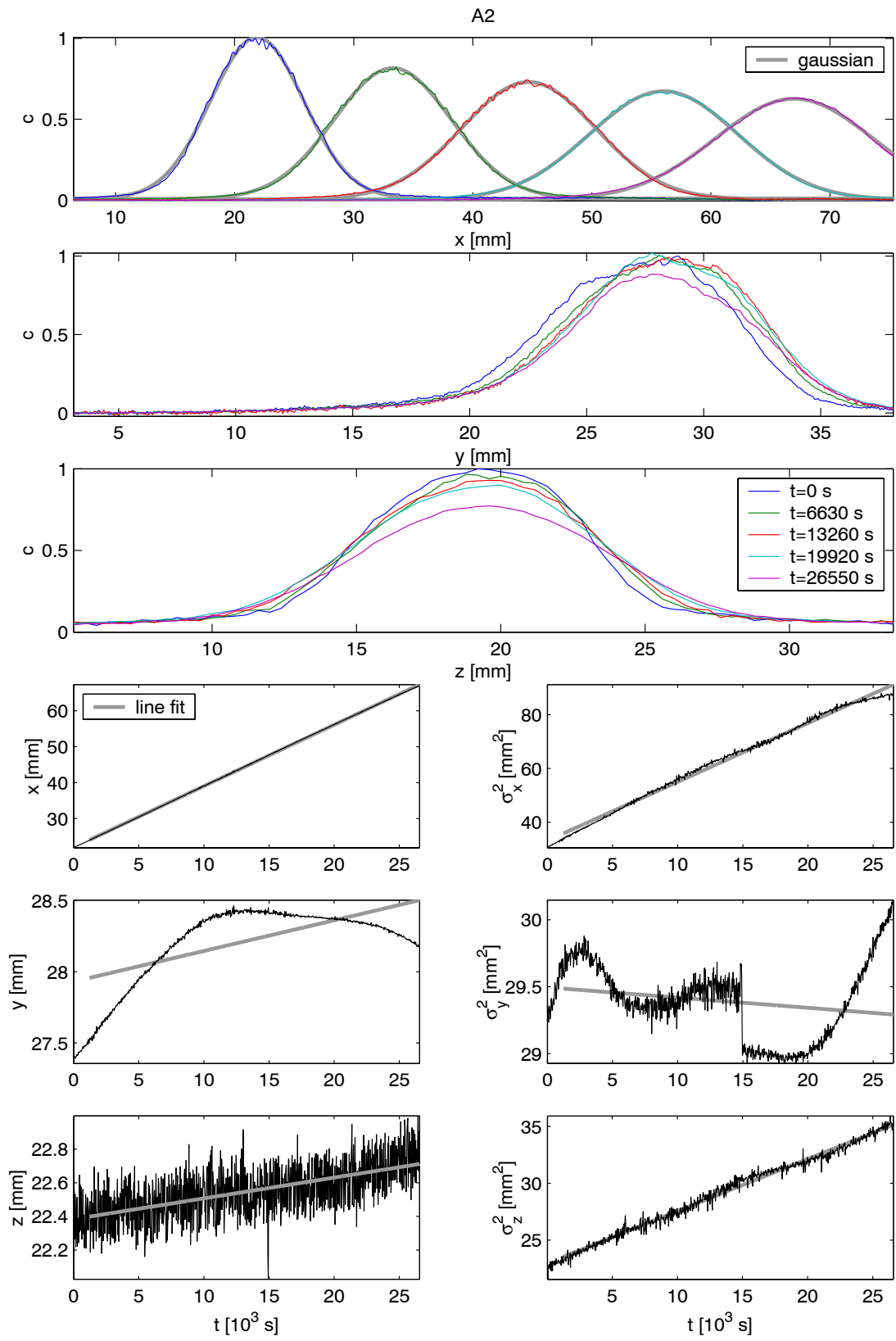


Figure B.2: Experiment A2.

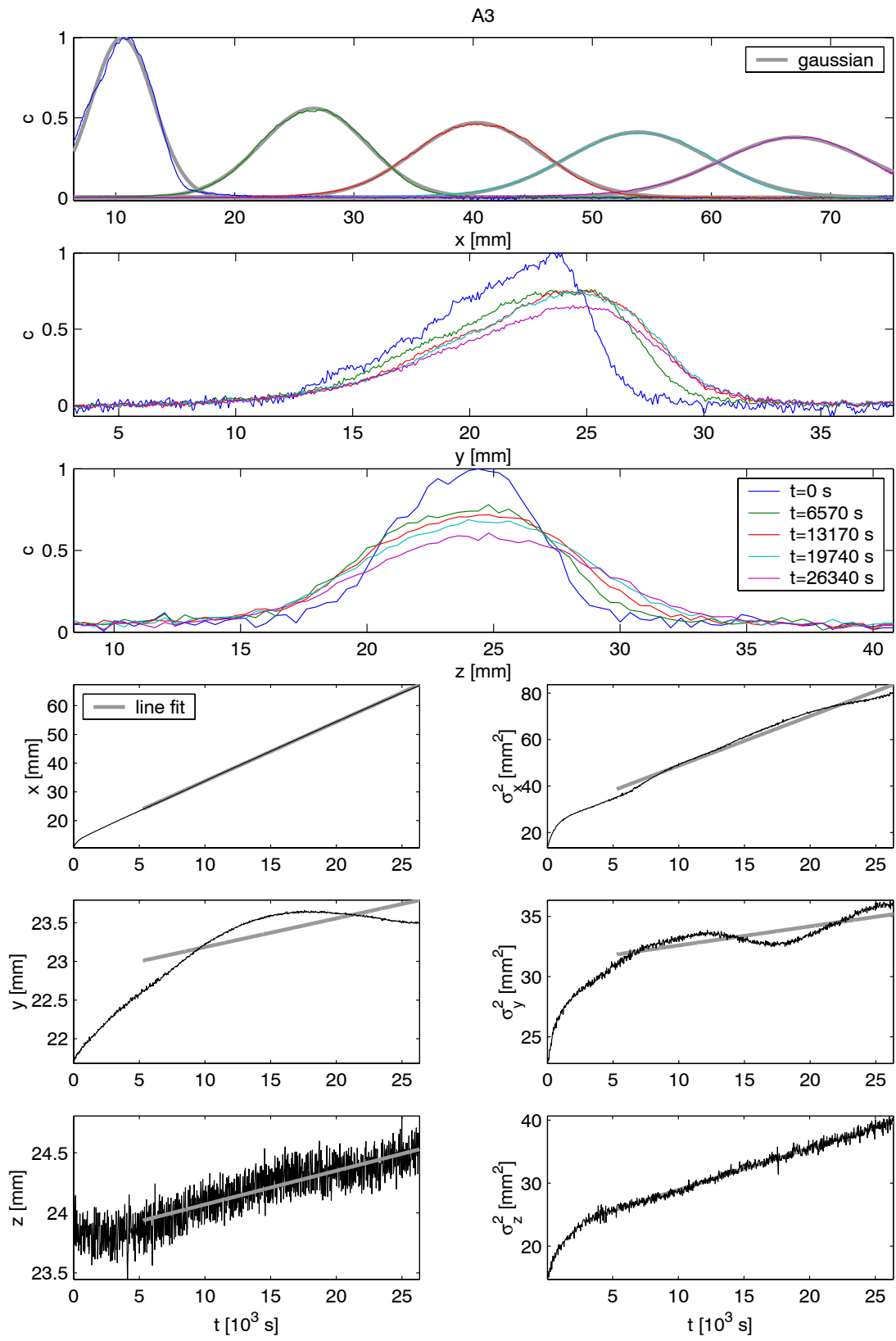


Figure B.3: Experiment A3.

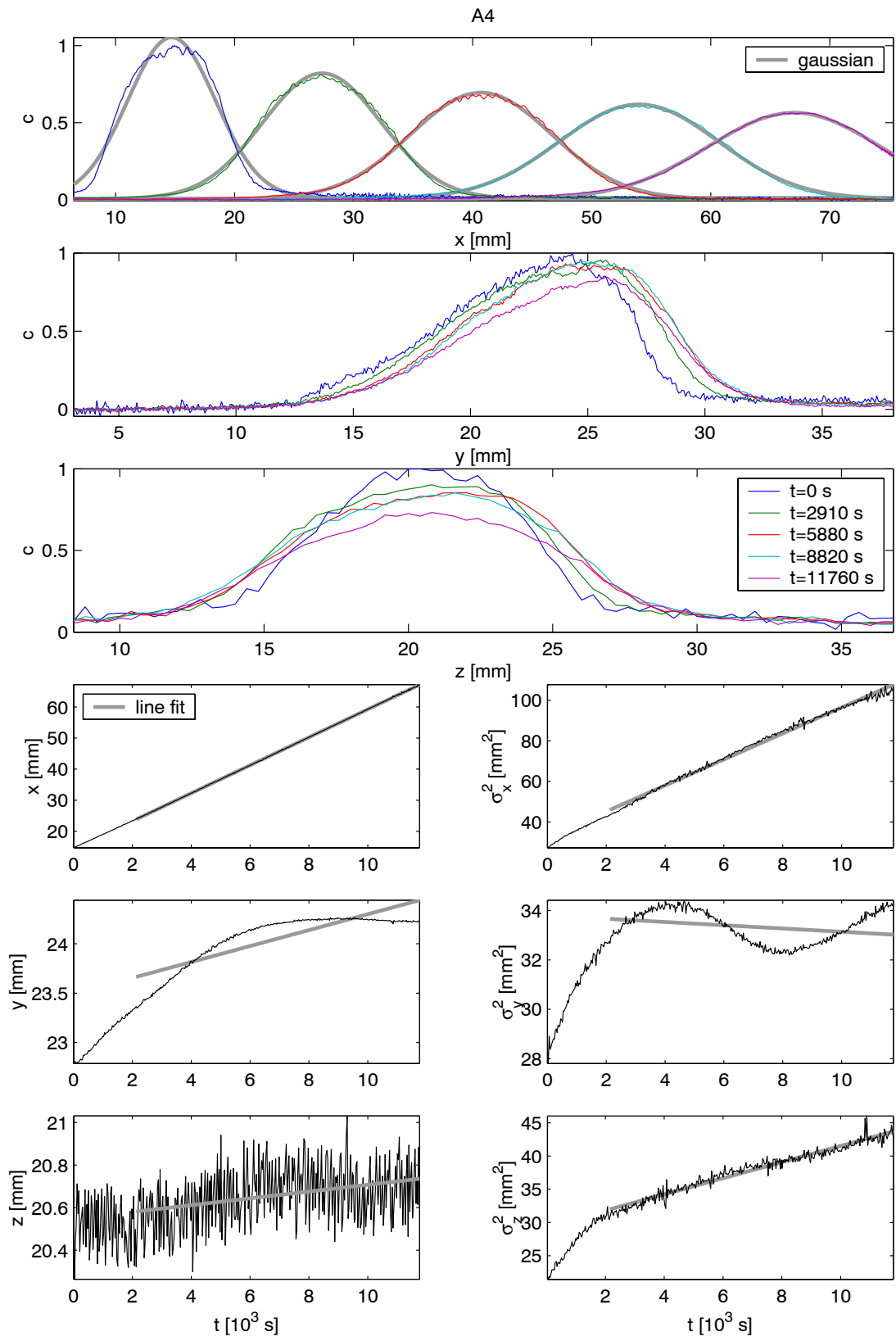


Figure B.4: Experiment A4.

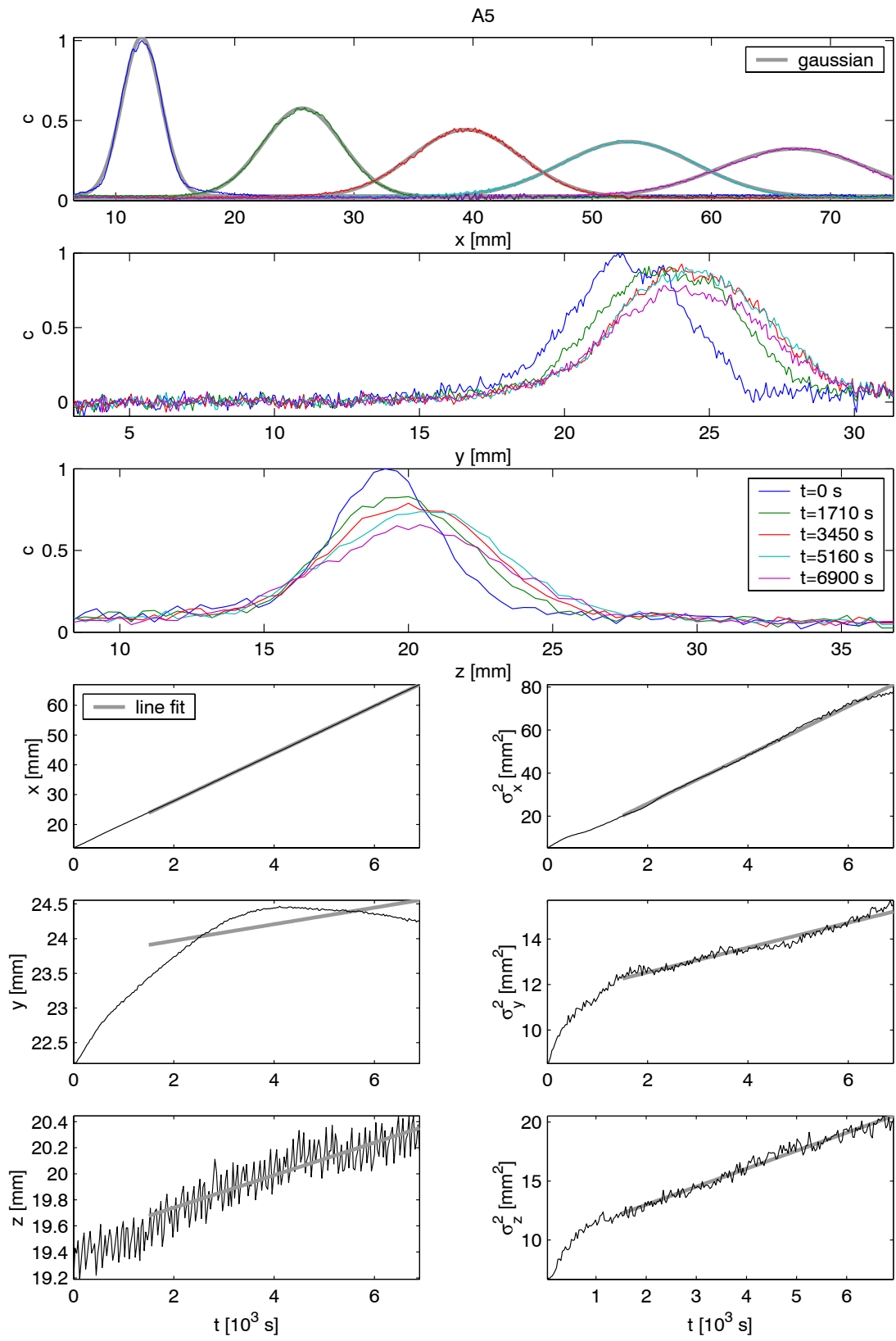


Figure B.5: Experiment A5.

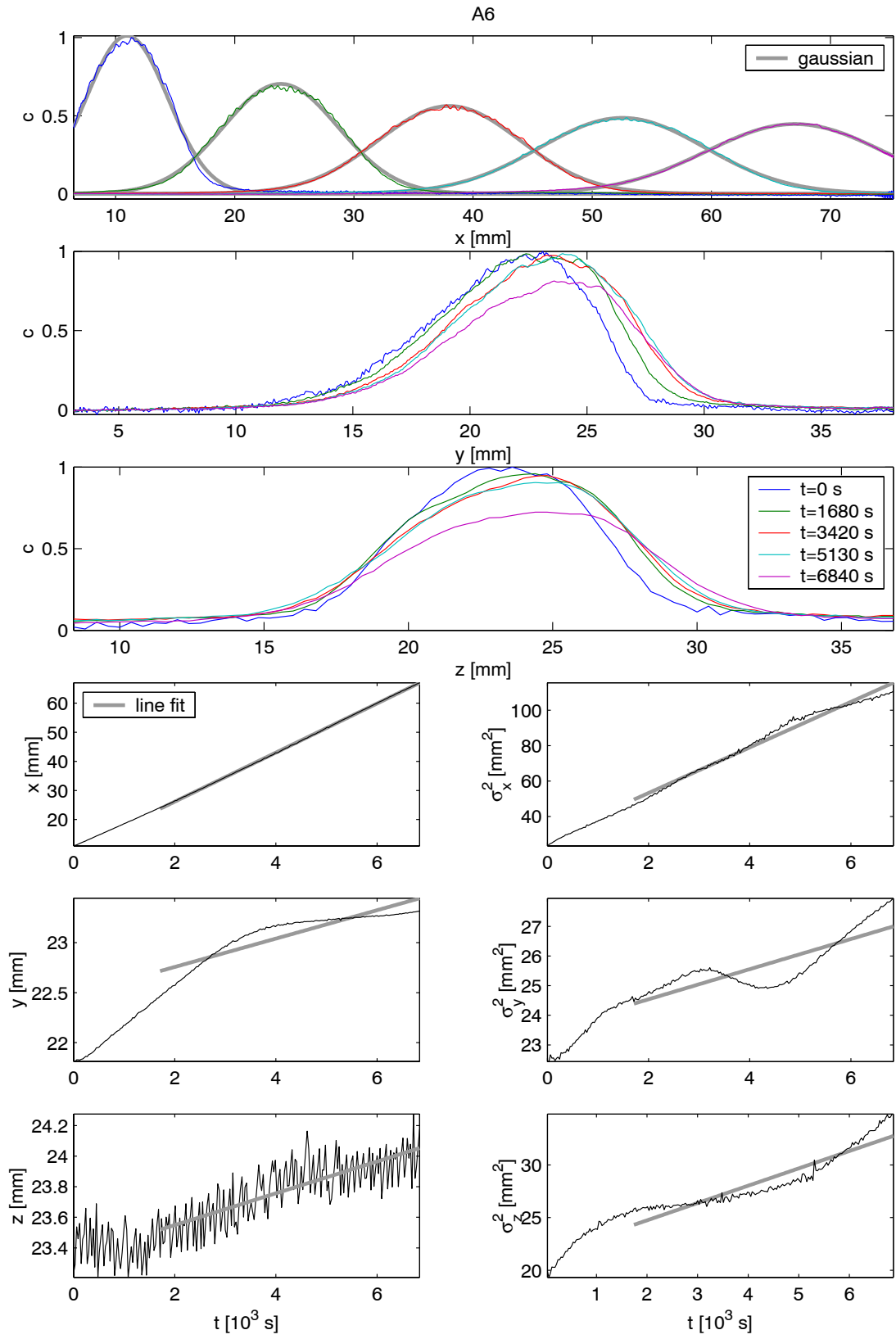


Figure B.6: Experiment A6.

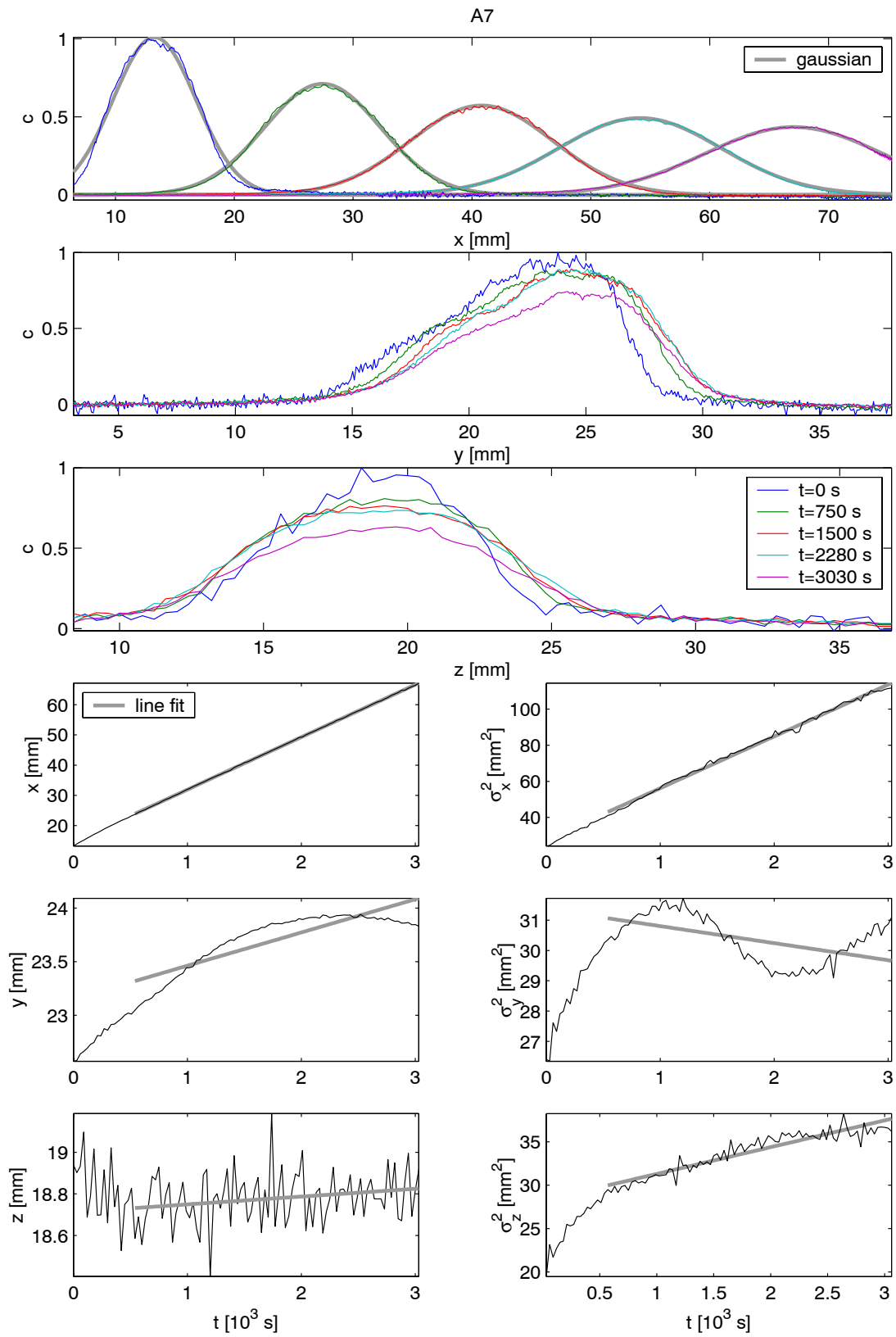


Figure B.7: Experiment A7.

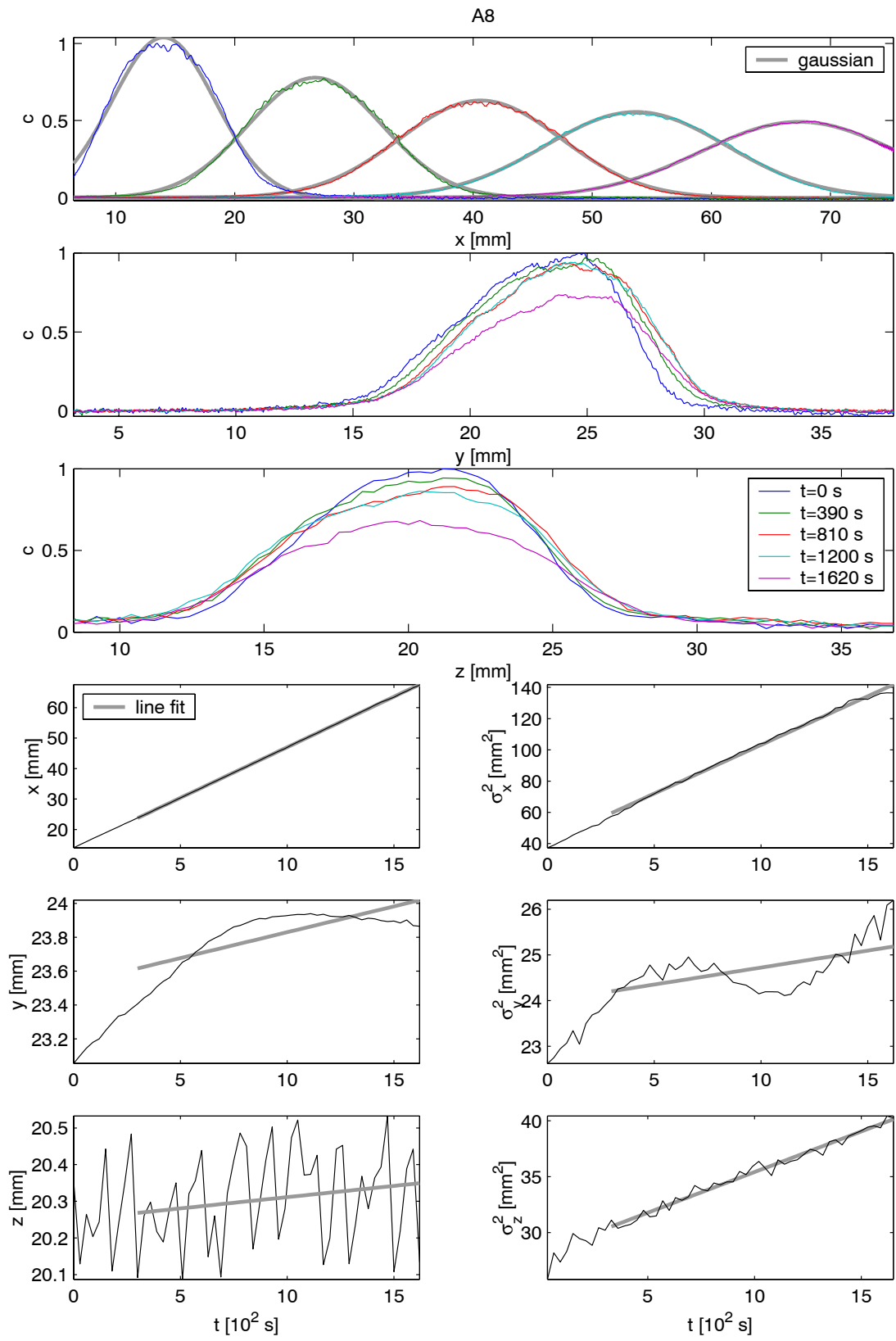


Figure B.8: Experiment A8.

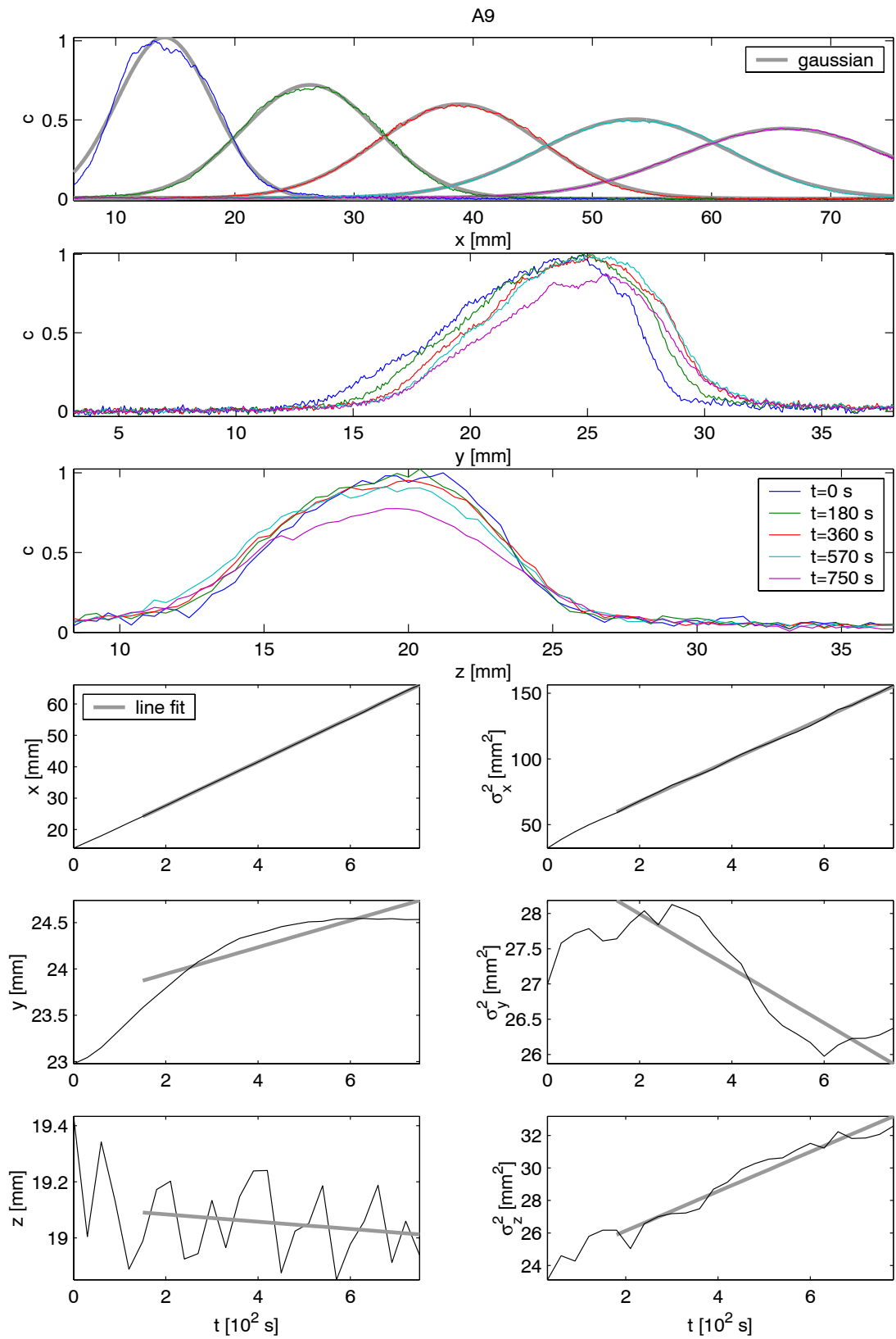


Figure B.9: Experiment A9.

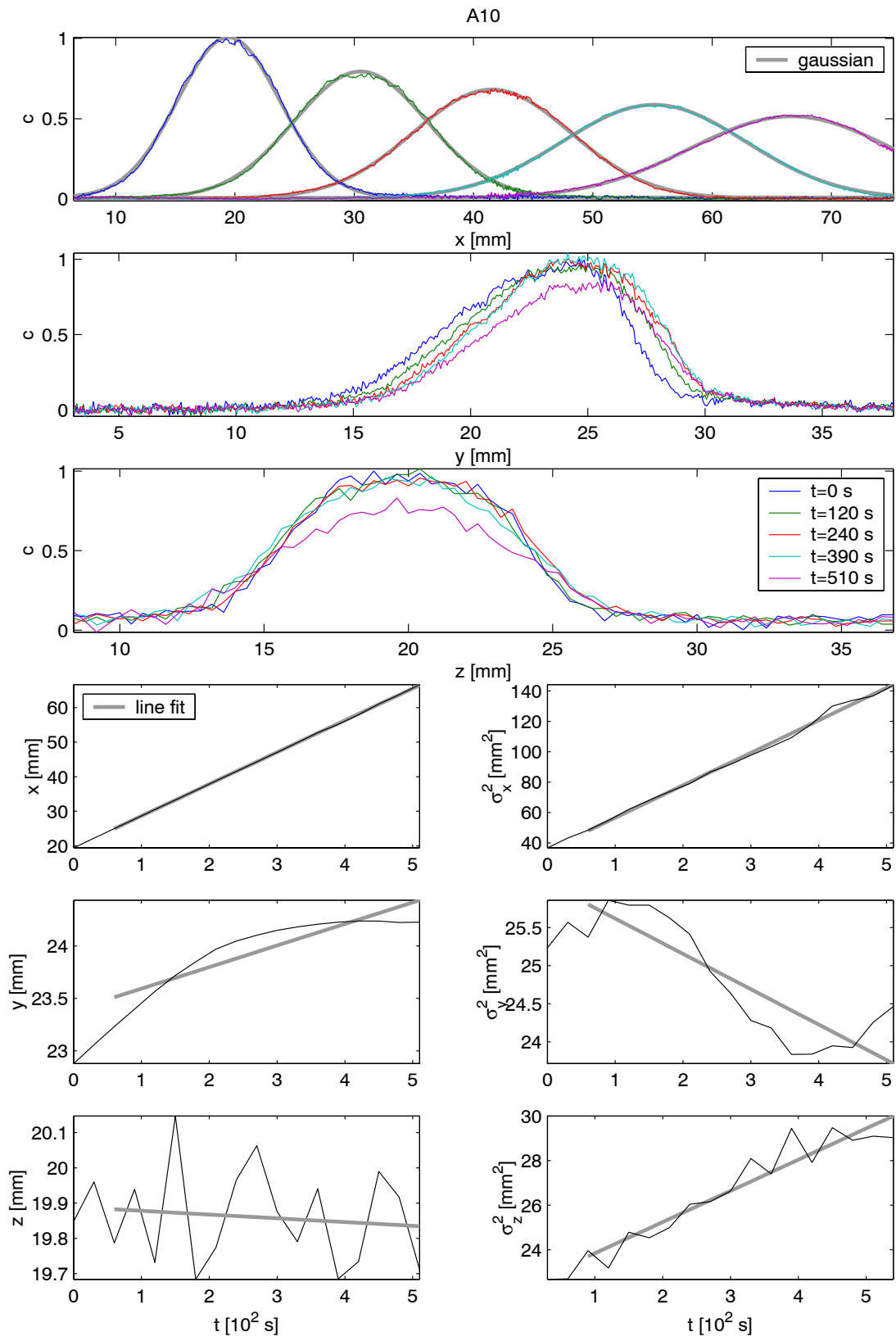


Figure B.10: Experiment A10.

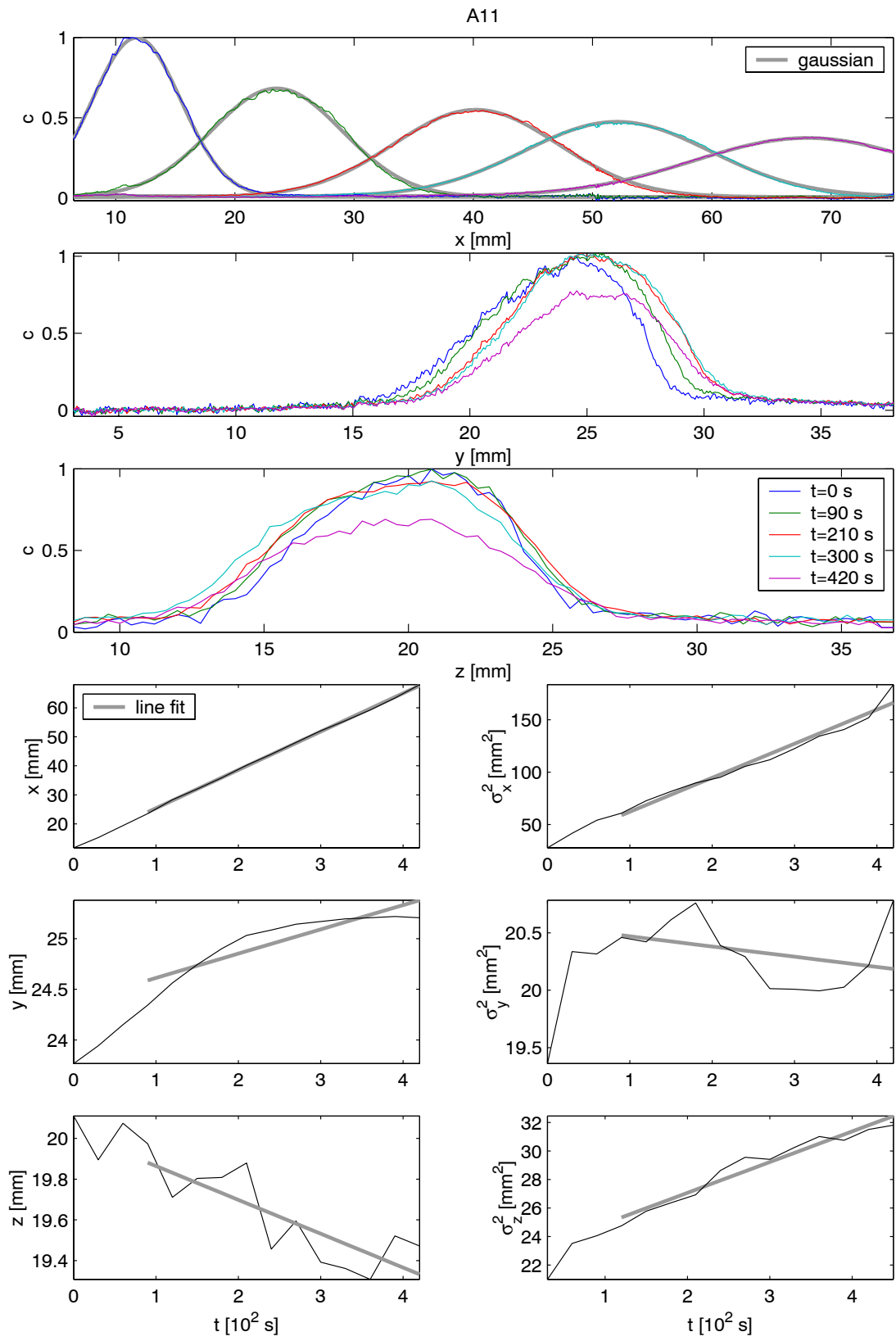


Figure B.11: Experiment A11.

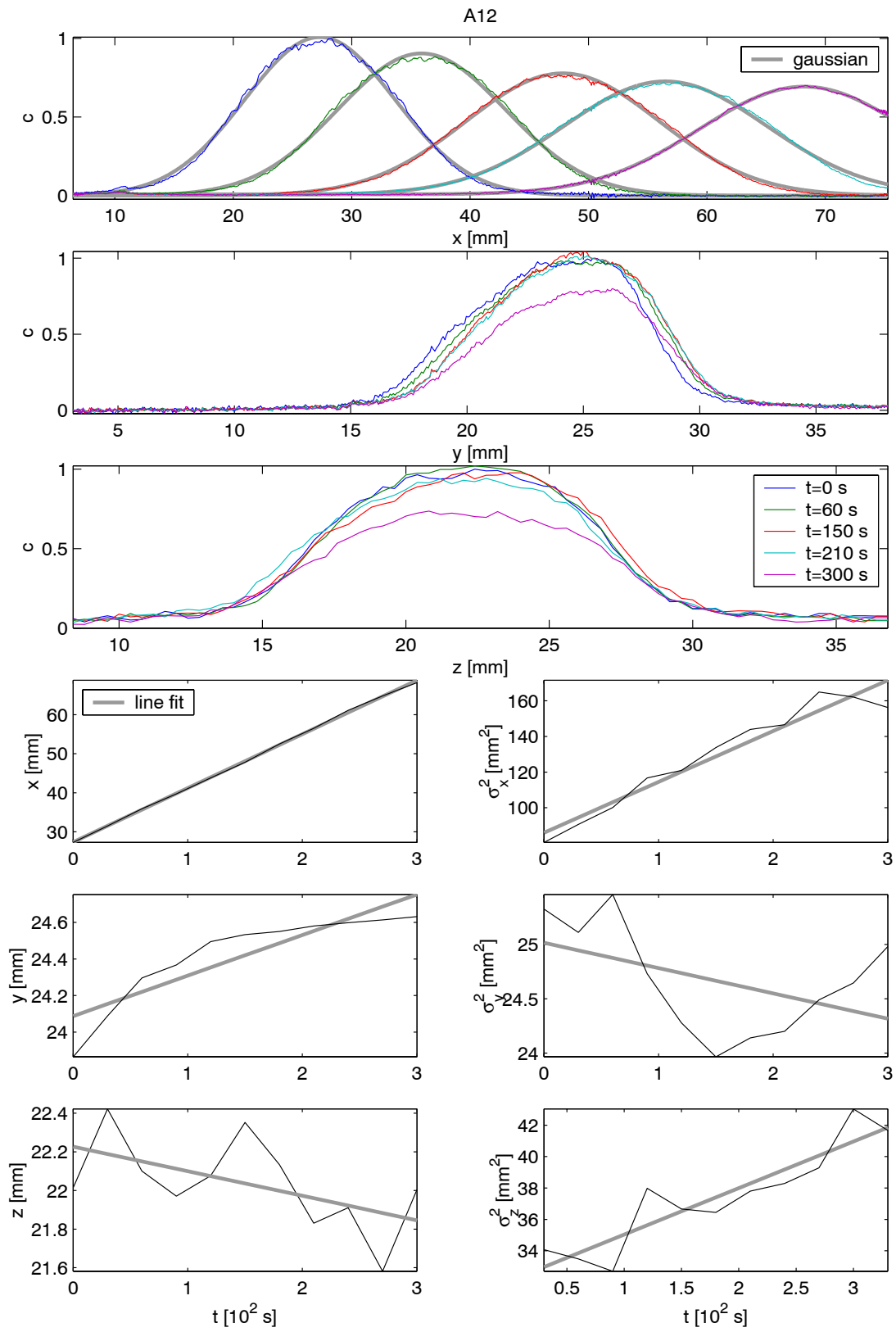


Figure B.12: Experiment A12.

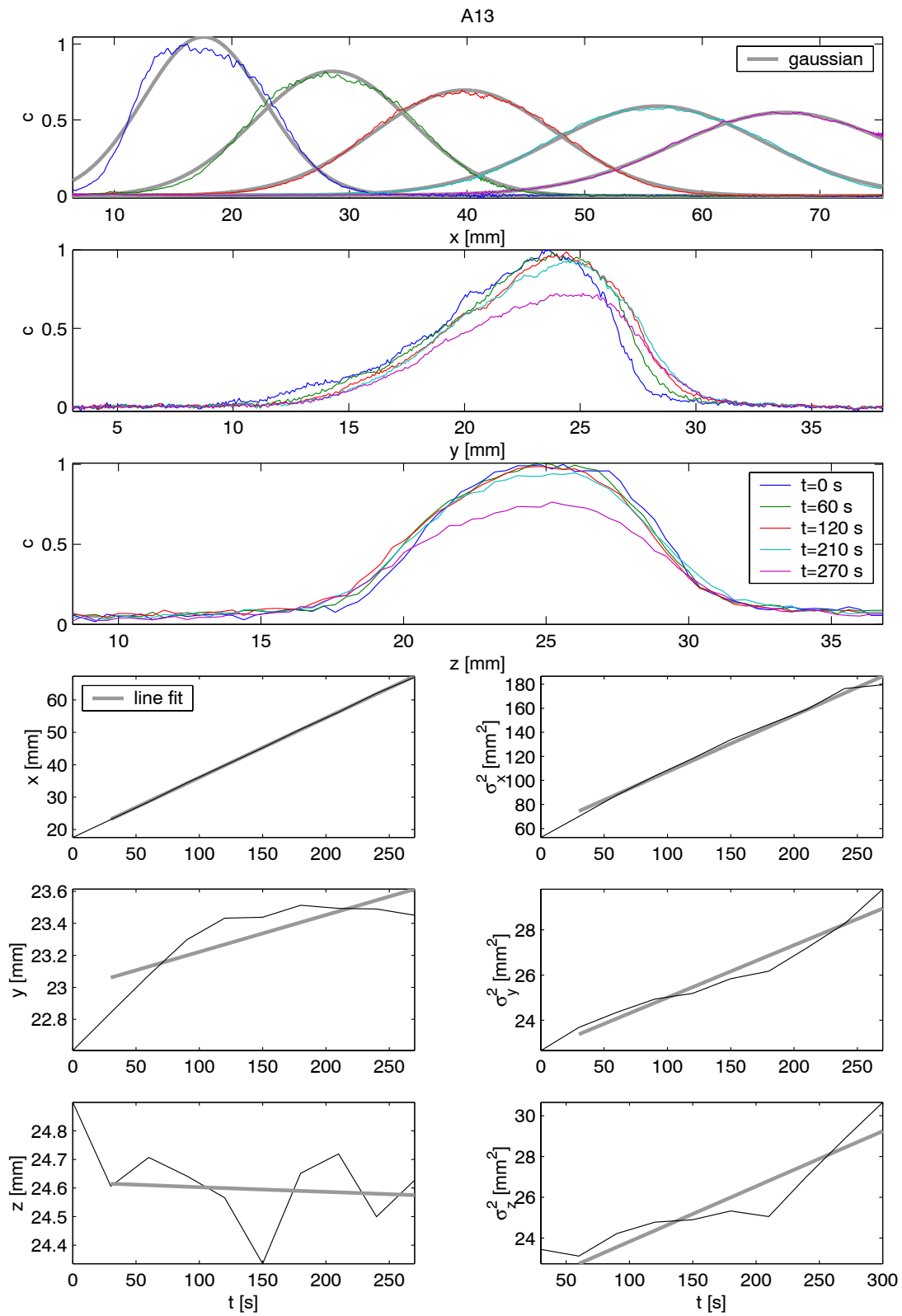


Figure B.13: Experiment A13.

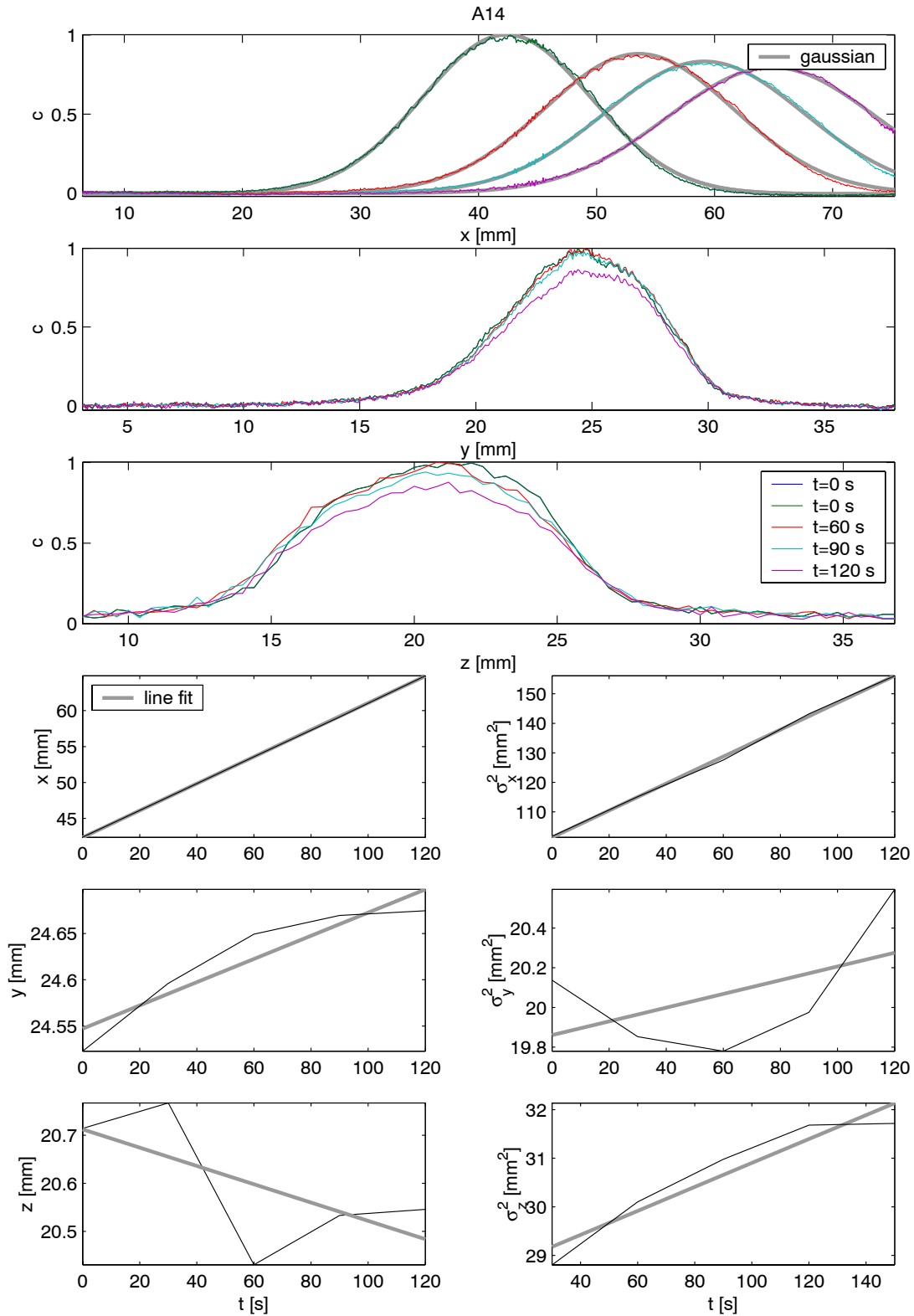


Figure B.14: Experiment A14.

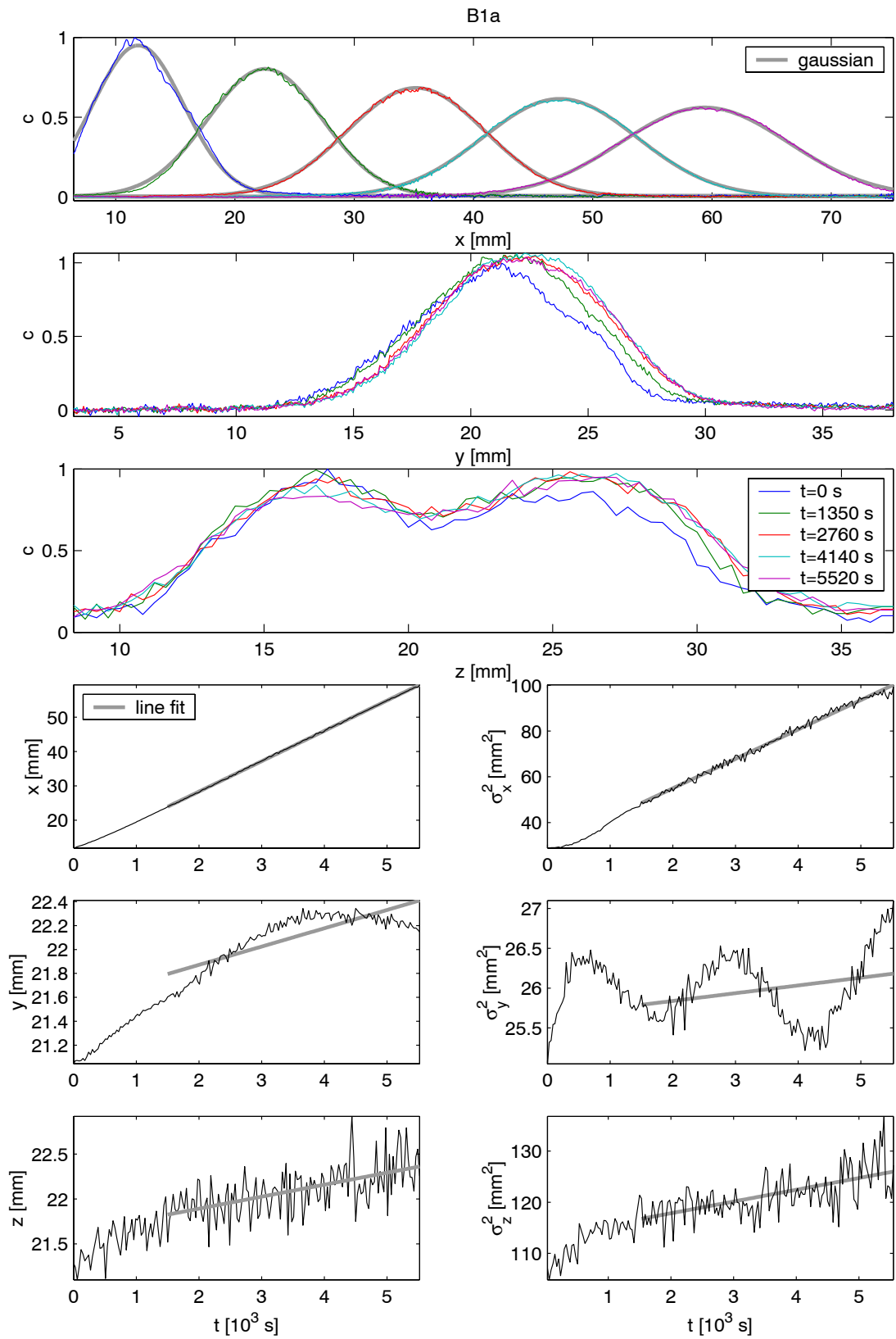


Figure B.15: Experiment B1a.

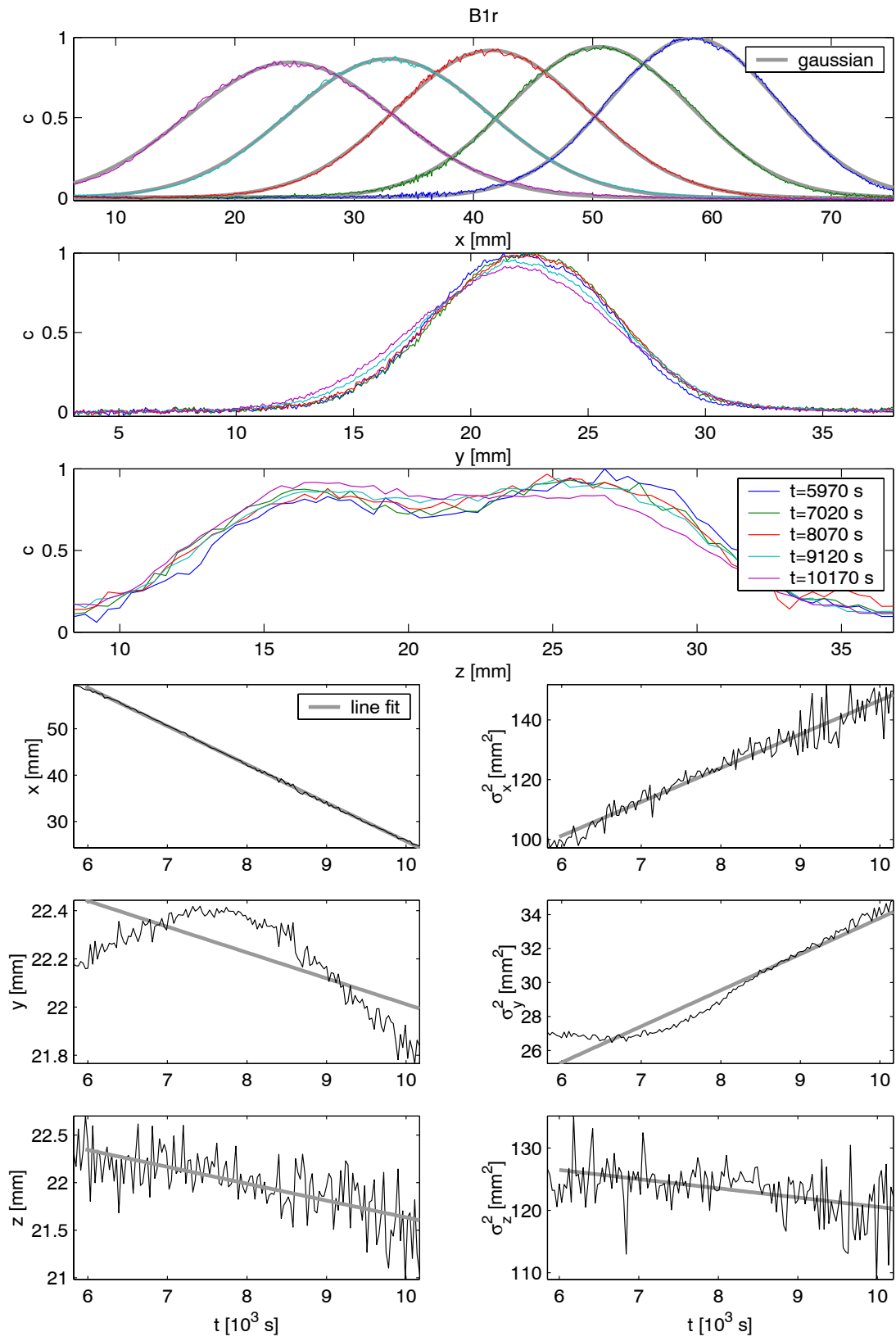


Figure B.16: Experiment B1r.

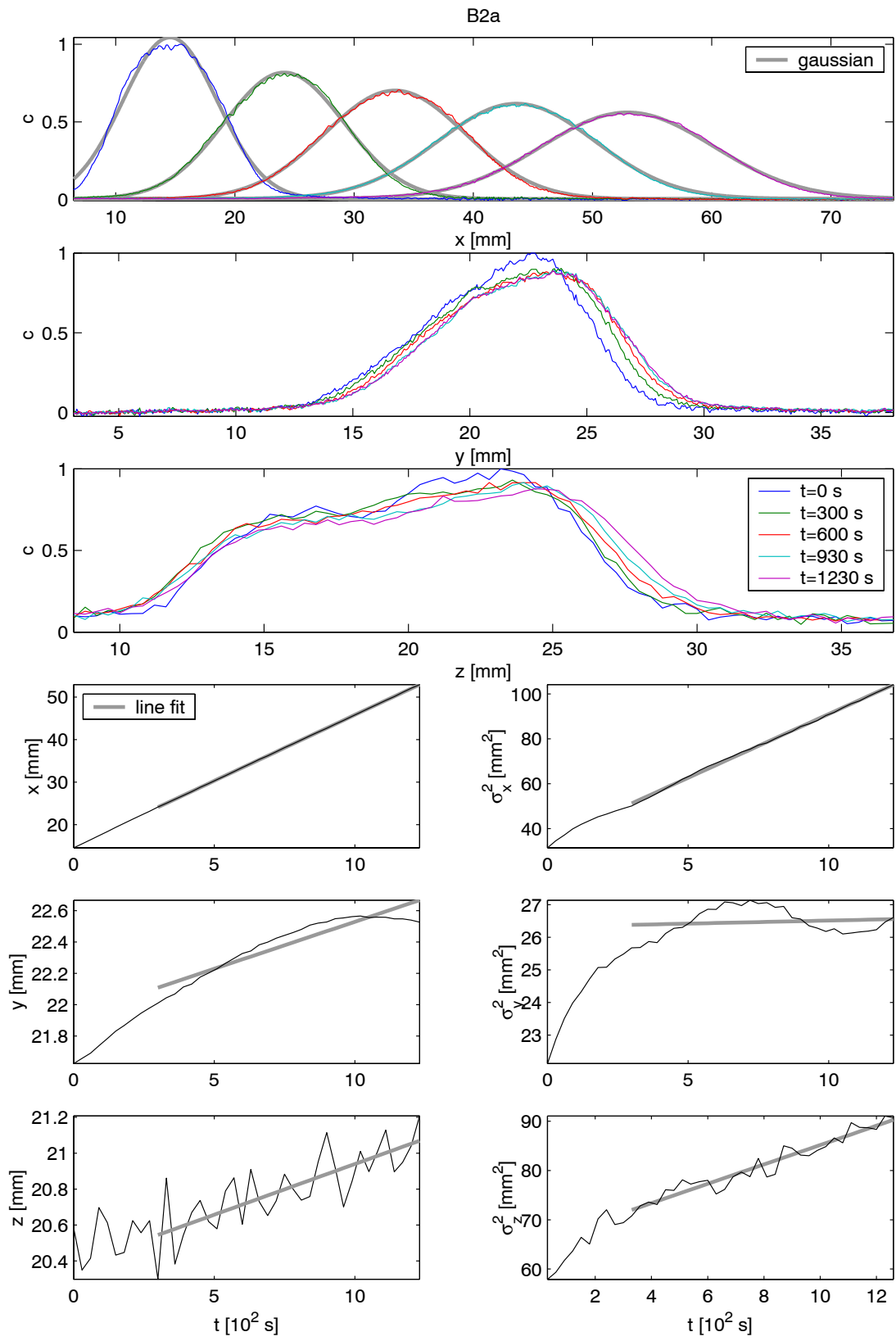


Figure B.17: Experiment B2a.

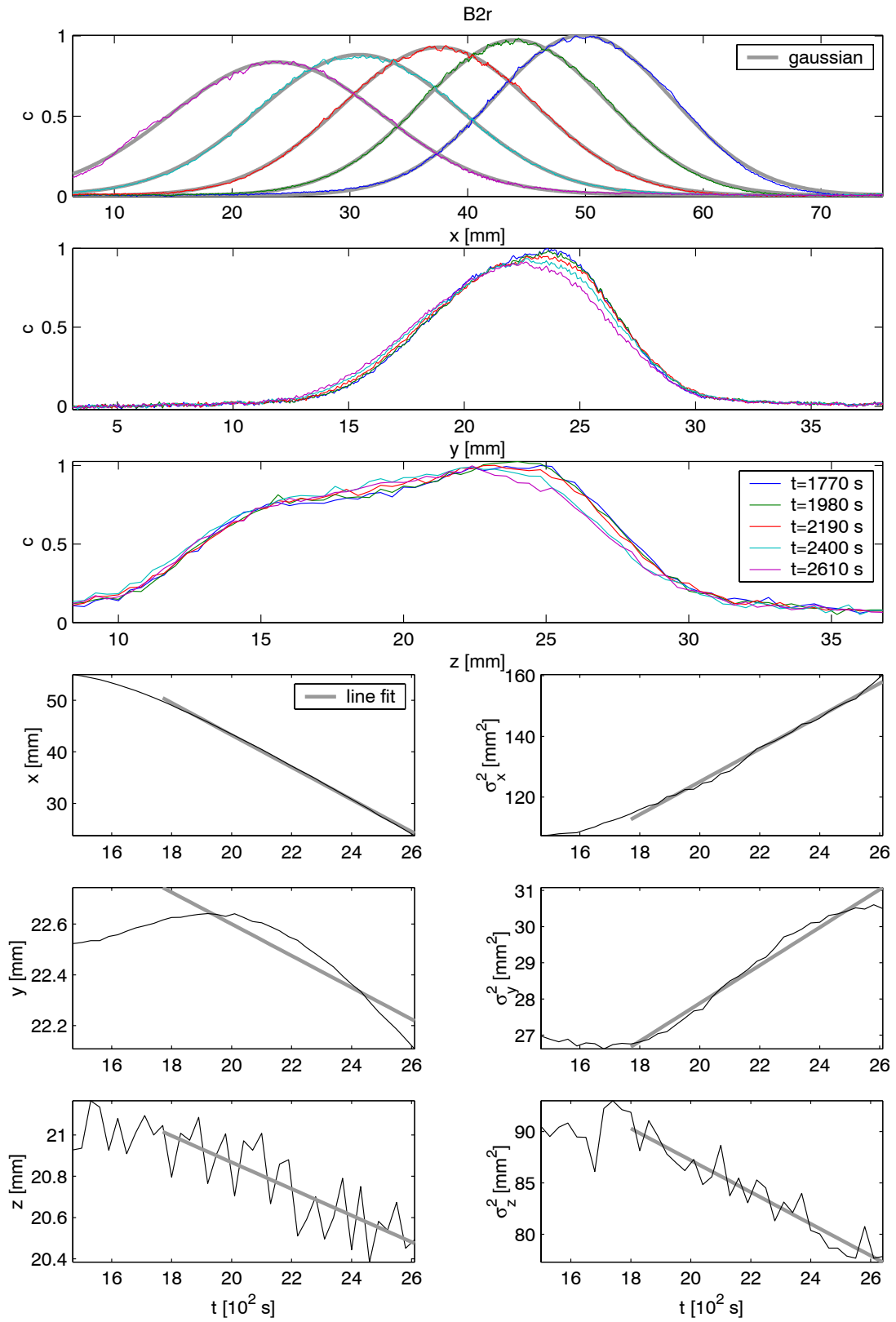


Figure B.18: Experiment B2r.

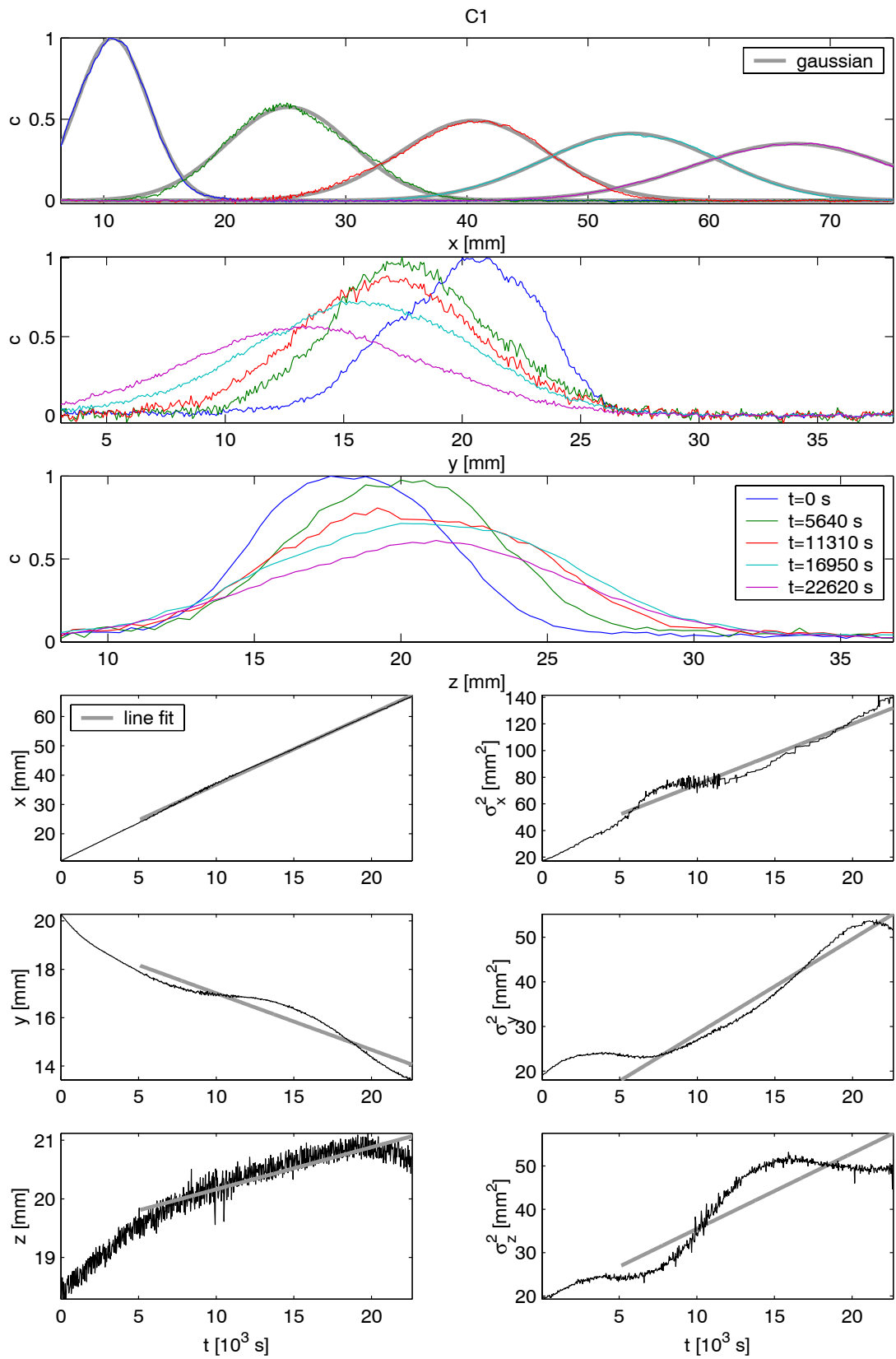


Figure B.19: Experiment C1.

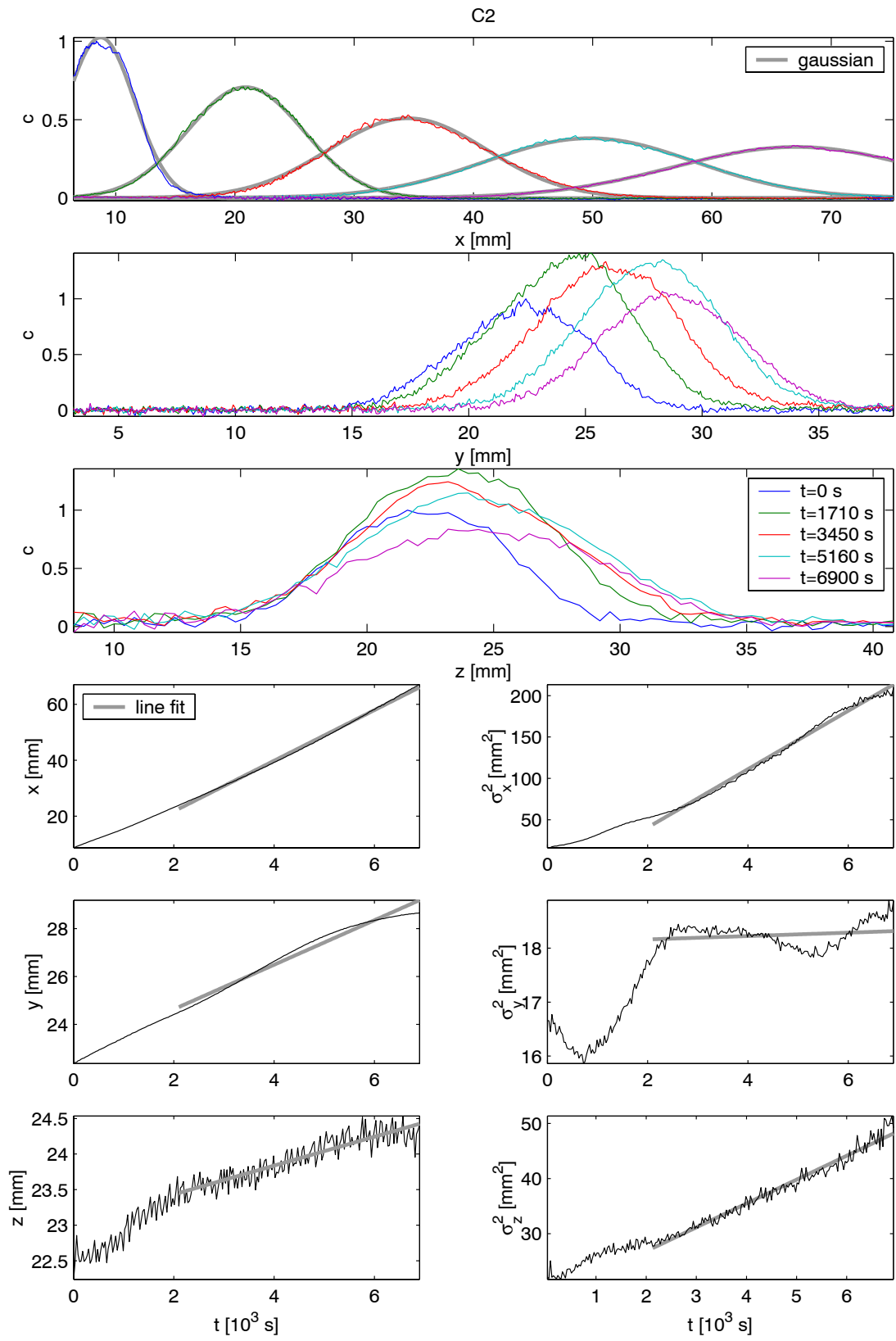


Figure B.20: Experiment C2.

Bibliography

- Adamson, A.W. (1997). *Physical chemistry of surfaces*. Wiley, New York, sixth edn.
- Azzam, M.I.S. & Dullien, F.A.L. (1977). Flow in tubes with periodic step changes in diameter: a numerical solution. *Chemical Engineering Science*, **32**, 1445–1455.
- Basler (1998). *Basler A113/A113P/A113C/A113CP High Resolution Progressive Scan Camera User's Manual*. Basler Vision Technologies GmbH.
- Beims, U. (1983). Planung, Durchführung und Auswertung von Gütepumpversuchen. *Zeitschrift für angewandte Geologie*, **29**.
- Berryman, J.G. & Blair, S.C. (1986). Use of digital image analysis to estimate fluid permeability of porous materials: Application of two-point correlation functions. *Journal of Applied Physics*, **60**, 1930–1938.
- Brown, R. (1828). On the existence of active molecules in organic and inorganic bodies. *The Philosophical Magazine and Annals of Philosophy*, **4**, 161–173.
- Buckingham, E. (1914). On physically similar systems: Illustrations of the use of dimensional equations. *Physical Review*, **4**, 345–376.
- Budwig, R. (1994). Refractive index matching methods for liquid flow investigations. *Experiments in Fluids*, **17**, 350–355.
- Burdett, I.D., Webb, D.R. & Davies, G.A. (1981). A new technique for studying dispersion flow, holdup and axial mixing in packed extraction columns. *Chemical Engineering Science*, **36**, 1915–1919.
- Capuani, F., Frenkel, D. & Lowe, C.P. (2003). Velocity fluctuations and dispersion in a simple porous medium. *Physical Review E*, **67**, 056306 1–8.
- Cargille (1999). *Siloxane data sheet*. Cargille Laboratories Inc.
- Charlaix, E., Hulin, J.P. & Plona, T.J. (1987). Experimental study of tracer dispersion in sintered glass porous materials of variable compaction. *Physics of Fluids*, **30**, 1690–1698.
- Christiansen, C. (1884). Untersuchungen über die optischen Eigenschaften von fein vertheilten Körpern T. 1. *Ann. Phys. Chem., ser. 3*, **23**, 298–306.
- Coats, K.H. & Smith, B.D. (1964). Dead-end pore volume and dispersion in porous media. *Society of Petroleum Engineers Journal*, **4**, 73–84.

- Coelho, D., Thovert, J.F. & Adler, P.M. (1997). Geometrical and transport properties of random packings of spheres and aspherical particles. *Physical Review E*, **55**, 1959–1978.
- Coleman, T.F. & Li, Y. (1996). An interior trust region approach for nonlinear minimization subject to bounds. *SIAM Journal on Optimization*, **6**, 418–445.
- Craven, P. & Wahba, G. (1979). Smoothing noisy data with spline functions. *Numerische Mathematik*, **31**, 377–403.
- Delgado, J.M.P.Q. & Guedes de Carvalho, J.R.F. (2001). Measurement of the coefficient of transverse dispersion in flow through packed beds for a wide range of values of the schmidt number. *Transport in Porous Media*, **44**, 165–180.
- Dentz, M., Kinzelbach, H., Attinger, S. & Kinzelbach, W. (2003). Numerical studies of the transport behavior of a passive solute in a two-dimensional incompressible random flow field. *Physical Review E*, **67**, 046306 1–10.
- Dow Corning (1996a). *Product Information Dow Corning 550 Fluid*. Dow Corning Europe.
- Dow Corning (1996c). *Product Information Dow Corning 710 Fluid*. Dow Corning Europe.
- Dow Corning (1998b). *Product Information Dow Corning 556 Cosmetic Grade Fluid*. Dow Corning Europe.
- Dow Corning (1999d). *Produktinformation Dow Corning 200 Fluid*. Dow Corning GmbH.
- Dullien, F.A.L. (1992). *Porous Media: Fluid Transport and Pore Structure*. Academic Press, New York, 2nd edn.
- Einstein, A. (1905). Über die von der molekularkinetischen Theorie der Wärme geforderte Bewegung von in ruhenden Flüssigkeiten suspendierten Teilchen. *Annalen der Physik*, **17**, 549–560.
- Einstein, A. (1906). Eine neue Bestimmung der Moleküldimensionen. *Annalen der Physik*, **19**, 289–306.
- Fick, A. (1855). Über Diffusion. *Poggendorff's Annalen der Physik und Chemie*, **94**, 59–86.
- Fried, J.J. & Combarous, M.A. (1971). Dispersion in porous media. *Advances in Hydroscience*, **7**, 169–282.
- Ghauharali, R.I., Müller, M., Buist, A.H., Sosnowski, T.S., Norris, T.B., Squier, J. & Brakenhoff, G.J. (1997). Optical saturation measurements of fluorophores in solution with pulsed femtosecond excitation and two-dimensional ccd camera detection. *Applied Optics*, **36**, 4320–4328.
- Gist, G.A., Thompson, A.H., Katz, A.J. & Higgins, R.L. (1990). Hydrodynamic dispersion and pore geometry in consolidated rock. *Physics of Fluids A*, **2**, 1533–1544.
- Goodfellow (1999). *Material Safety Data Sheet Polymethylmethacrylate Powder*. Goodfellow England.

- Green, P.J. & Silverman, B.W. (1994). *Nonparametric regression and generalized linear models: a roughness penalty approach*. Chapman and Hall, London.
- Grimmett, G.R. & Stirzaker, D.R. (2001). *Probability and Random Processes*. Oxford University Press, 3rd edn.
- Han, N., Bhakta, J. & Carbonell, R.G. (1985). Longitudinal and lateral dispersion in packed beds: Effect of column length and particle size distribution. *AIChE Journal*, **31**, 277–288.
- Hänsler, E. (2001). *Statistische Signale*. Springer, Berlin, 3rd edn.
- Harleman, D.R.F. & Rumer, R.R. (1963). Longitudinal and lateral dispersion in an isotropic porous medium. *Journal of Fluid Mechanics*, **16**, 385–394.
- Haugland, R.P. (2001). *Handbook of Fluorescent Probes and Research Products*. Molecular Probes Inc., eighth edn.
- Haußecker, H., Garbe, C., Spies, H. & Jähne, B. (1999). A total least squares framework for low-level analysis of dynamic scenes and processes. In *DAGM*, 240–249, Springer, Bonn, Germany.
- Hense, C.R. (1987). The christiansen filter - a centennial retrospective review. *Glastechnische Berichte*, **60**, 89–111, 140–160.
- Hulin, J.P. & Plona, T.J. (1989). Echo tracer dispersion in porous media. *Physics of fluids A*, **1**, 1341–1347.
- Jähne, B. (2002). *Digital image processing*. Springer, Berlin, Germany, 5th edn.
- Jin, Y. & Jury, W.A. (1996). Characterizing the dependence of gas diffusion coefficient on soil properties. *Soil Science Society of America Journal*, **60**, 66–71.
- Kandhai, D., Hlushkou, D., Hoekstra, A.G., Soot, P.M.A., Van As, H. & Tallarek, U. (2002). Influence of stagnant zones on transient and asymptotic dispersion in macroscopically homogeneous porous media. *Physical Review Letters*, **88**, 234501 1–4.
- Kerr, P.F. (1977). *Optical mineralogy*. McGraw Hill, 4th edn.
- Koch, D.L. & Brady, J.F. (1985). Dispersion in fixed beds. *Journal of Fluid Mechanics*, **154**, 399–427.
- Lowe, C.P. & Frenkel, D. (1996). Do hydrodynamic dispersion coefficients exist? *Physical Review Letters*, **77**, 4552–4555.
- Madison (1999). *Zinc chloride solution product sheet*. Madison Industries, Inc.
- Maier, R.S., Kroll, D.M., Bernard, R.S., Howington, S.E., Peters, J.F. & Davis, H.T. (2000). Pore-scale simulation of dispersion. *Physics of Fluids*, **12**, 2065–2079.
- Maier, R.S., Kroll, D.M., Bernard, R.S., Howington, S.E., Peters, J.F. & Davis, H.T. (2002). Enhanced dispersion in cylindrical packed beds. *Philosophical Transactions of the Royal Society London A*, **360**, 497–506.

- Manz, B., Alexander, P. & Gladden, L.F. (1999). Correlations between dispersion and structure in porous media probed by nuclear magnetic resonance. *Physics of Fluids*, **11**, 259–267.
- Millington, R.J. & Quirk, J.P. (1960). Transport in porous media. In *7th International Congress of Soil Science, Madison, WI*.
- Montemagno, C.D. & Gray, W.G. (1995). Photoluminescent volumetric imaging: A technique for the exploration of multiphase flow and transport in porous media. *Geophysical research letters*, **22**, 425–428.
- Moroni, M. & Cushman, J.H. (2001). Three-dimensional particle tracking velocimetry studies of the transition from pore dispersion to fickian dispersion for homogeneous porous media. *Water Resources Research*, **37**, 873–884.
- Mühlich, M. & Mester, R. (1999). Subspace methods and equilibration in computer vision. Tech. Rep. XP-TR-C-21, Computer vision group, Institute for Applied Physics, Goethe-Universität Frankfurt am Main, Germany.
- Narrow, T.L., Yoda, M. & Abdel-Khalik, S.I. (2000). A simple model for the refractive index of sodium iodide aqueous solutions. *Experiments in Fluids*, **28**, 282–283.
- Nestares, O., Fleet, D.J. & Heeger, D.J. (2000). Likelihood functions and confidence bounds for total-least-squares problems. In *IEEE Conference on Computer Vision and Pattern Recognition, Hilton Head, South Carolina, vol. I*, 523–530.
- Paus, L. (1997). Ausbreitungsverhalten von CKW in der ungesättigten und gesättigten Bodenzone. In *12. DEHEMA-Fachgespräch Umweltschutz: Möglichkeiten und Grenzen der Reinigung kontaminierter Grundwässer*, 113–140.
- Peurrung, L.M., Rashidi, M. & Kulp, T.J. (1995). Measurement of porous medium velocity fields and their volumetric averaging characteristics using particle tracking velocimetry. *Chemical Engineering Science*, **50**, 2243–2253.
- Pfannkuch, H.O. (1963). Contribution a l'étude des déplacements de fluides miscibles dans un milieu poreux. *Revue de l'institut français du pétrole*, **XVIII**, 215–270.
- Press, W.H., Teukolsky, S.A., Vetterling, W.T. & Flannery, B.P. (1992). *Numerical Recipes in C*. Cambridge University Press.
- Rage, T. (1996). *Studies of Tracer Dispersion and Fluid Flow in Porous Media*. Ph.D. thesis, University of Oslo.
- Rashidi, M., Peurrung, L., Tompson, A.F.B. & Kulp, T.J. (1996). Experimental analysis of pore-scale flow and transport in porous media. *Advances in Water Resources*, **19**, 163–180.
- Renn, J. (1997). Einsteins controversy with drude and the origin of statistical mechanics: a new glimpse from the "love letters". *Archive for history of exact sciences*, **51**, 315–354.
- Reynolds, A.M., Reavell, S.V. & Harral, B.B. (2000). Flow and dispersion through a close-packed fixed bed of spheres. *Physical Review E*, **62**, 3632–3639.
- Rigord, P., Calvo, A. & Hulin, J.P. (1990). Transition to irreversibility for the dispersion of a tracer in porous media. *Physics of Fluids A*, **2**, 681–687.

- Roth, K. (1996a). Lecture notes in soil physics. Tech. rep., Institute of Soil Science, University of Hohenheim, Stuttgart.
- Roth, K. (1996b). Transport analysis package. Tech. rep., Institut für Bodenkunde, University of Hohenheim.
- Saffman, P.G. (1959). A theory of dispersion in porous media. *Journal of Fluid Mechanics*, **6**, 321–349.
- Sahimi, M. (1993). Flow phenomena in rocks: from continuum models to fractals, percolation, cellular automata, and simulated annealing. *Reviews of Modern Physics*, **65**, 1393–1534.
- Scharr, H. (2000). *Optimale Operatoren in der Digitalen Bildverarbeitung*. Ph.D. thesis, University of Heidelberg, Heidelberg, Germany.
- Schott (2001). *Fused silica data sheet*. Schott Lithotec AG, Mainz, Germany.
- Sederman, A.J., Johns, M.L., Bramley, A.S., Alexander, P. & Gladden, L.F. (1997). Magnetic resonance imaging of liquid flow and pore structure within packed beds. *Chemical Engineering Science*, **52**, 2239–2250.
- Seymour, J.D. & Callaghan, P.T. (1997). Generalized approach to NMR analysis of flow and dispersion in porous media. *AIChE Journal*, **43**, 2096–2111.
- Spies, H. (2001). *Analysing Dynamic Processes in Range Data Sequences*. Ph.D. thesis, University of Heidelberg, Heidelberg, Germany.
- Strutt, J.W. (1899). Transparency and opacity. *Nature*, **60**, 64–65.
- Taylor, G. (1953). Dispersion of soluble matter in solvent flowing slowly through a tube. *Proceedings of the Royal Society of London A*, **219**, 186–203.
- Torquato, S., Truskett, T.M. & Debenedetti, P.G. (2000). Is random close packing of spheres well defined? *Physical Review Letters*, **84**, 2064–2067.
- Tritton, D. (1988). *Physical Fluid Dynamics*. Oxford Science Publications, 2nd edn.
- Van Huffel, S. & Vandewalle, J. (1991). *The Total Least Squares Problem - Computational Aspects and Analysis*. Society for Industrial and Applied Mathematics, Philadelphia.
- Waxler, R.M., Horowitz, D. & Feldman, A. (1979). Optical and physical parameters of plexiglas 55 and lexan. *Applied Optics*, **18**, 101–104.
- Weast, R.C. (1974). *CRC Handbook of Chemistry and Physics*. CRC Press, 55th edn.
- Wecker, W.E. & Ansley, C.F. (1983). The signal extraction approach to nonlinear regression and spline smoothing. *Journal of the American Statistical Association*, **78**, 81–89.

Acknowledgements

I gratefully acknowledge the persevering support of Prof. Roth in all important issues, his philanthropic attitude and the interesting discussions.

I thank Prof. Jähne for his initial effort for the realization of this project, for the provision with experimental resources and for the possibility to work in an inspiring environment in the field of digital image processing.

I am grateful to the members of the image processing research group at the IWR and the soil physics group at the IUP for the warm and stimulating atmosphere during the last years.

In particular I want to thank Erik Bock, Mark Wenig, Hagen Spies, Torsten Bone, Günther Balschbach, Angelika Gassama, Andreas Bayer, Rainer Zimmermann and the members of the workshop and the satellite group at the IUP for the support in many technical issues and for the proofreading of this work.

Finally I want to express my gratitude to my family for their support during this work.